UNIVERSIDADE DE SÃO PAULO
Escola de Engenharia de São Carlos

Multi-scale modelling of materials with voids based on second-order computational homogenisation at finite strains: numerical analysis, experimental investigation and applications in architected structures

Modelagem multi-escala de materiais com vazios baseada em homogeneização computacional de segunda ordem em deformações finitas: análise numérica, investigação experimental e aplicações em estruturas arquitetadas

Wanderson Ferreira dos Santos

PhD Thesis - Postgraduate Program in Civil Engineering (Structural Engineering) at the São Carlos School of Engineering, University of São Paulo

Wanderson Ferreira dos Santos

Multi-scale modelling of materials with voids based on second-order computational homogenisation at finite strains: numerical analysis, experimental investigation and applications in architected structures

PhD thesis submitted in partial fulfillment of the requirements for the degree of Doctor in Science - Postgraduate Program in Civil Engineering (Structural Engineering) at the São Carlos School of Engineering, University of São Paulo.

Área de concentração: Structures

Advisor: Prof. Sergio Persival Baroncini Proença

Co-advisors: Prof. Francisco Manuel Andrade Pires and Dr. Igor André Rodrigues Lopes

São Carlos

2025

Index card prepared by User Service at “Prof. Dr. Sergio Rodrigues Fontes Library” at EESC/USP

Santos, Wanderson Ferreira dos
S237m Multi-scale modelling of materials with voids based on second-order computational homogenisation at finite strains: numerical analysis, experimental investigation and applications in architected structures / Wanderson Ferreira dos Santos; advisor Sergio Persival Baroncini Proença; co-advisors Francisco Manuel Andrade Pires and Igor André Rodrigues Lopes -- São Carlos, 2025.

Doctoral (Dissertation) - Graduate Program in Civil Engineering (Structural Engineering) -- São Carlos School of Engineering, at University of São Paulo, 2025.

1. Materials with voids. 2. Architected structures. 3. Multi-scale modelling. 4. Second-order computational homogenisation. 5. Experimental investigation. I. Título.

Prepared by Eduardo Graziosi Silva- CRB-8/8907

ACKNOWLEDGEMENTS

First of all, I would like to thank my parents for their unwavering support and unconditional paternal love throughout every moment of my life.

I would like to thank my advisor Prof. Sergio Persival Baroncini Proença for his guidance throughout the PhD thesis. I am also grateful for the knowledge shared in the postgraduate courses, which contributed significantly to my academic development.

I would like to express my deep gratitude to Prof. Francisco Manuel Andrade Pires and Dr. Igor André Rodrigues Lopes for their co-supervision of my PhD thesis. My time in Porto and the continuation of our collaboration in Brazil were essential for the development of this work. I acquired valuable knowledge about how to conduct high-quality research in Computational Mechanics. Professor Francisco and Dr. Igor are examples of researchers that I intend to follow in my academic career. In particular, I would like to thank Dr. Igor for his friendship and the good times on my trip to Guimarães, where I had the happy opportunity to meet his family. I am immensely grateful to have met and collaborated with members of the research group CM2S – Computational Multi-Scale Modelling of Solids and Structures. I had the pleasure of learning and sharing good times with António, Rui, Francisca, Miguel, Guilherme, Tiago and José.

I would like to express my gratitude to Profa. Zilda de Castro Silveira and PhD candidate Alina de Souza Leão Rodrigues for their valuable collaboration. It was a pleasure to accept the challenge of dealing with experimental investigation, which significantly contributed to my academic development. Moreover, I extend my gratitude to Prof. Marcelo Aparecido Chinelatto and MSc Ricardo Gomes Pereira for their important support in conducting the experimental tests.

I would like to thank Prof. Eduardo Alberto Fancello and Prof. Edson Denner Leonel for their participation in my doctoral qualification exam, as well as for their valuable comments and suggestions on my work.

I would like to thank Prof. Jose Julio de Cerquira Pituba for the motivation and knowledge he shared during my undergraduate studies in Civil Engineering at the Federal University of Goiás. Prof. Julio played a fundamental role in the beginning of my academic journey.

I would like to thank Prof. Ayrton Ribeiro Ferreira for the knowledge he shared through valuable research conversations, and, above all, for his friendship.

I would like to thank all my friends and PhD colleagues, especially Welington, Daniel, Luiz, Ellon, Lucas Ribeiro, Hebert, Péricles, Lucas Almeida and Leonardo. We shared many moments of friendship, which made my PhD journey more enjoyable, filled with laughter and great stories to remember.

I would like to thank everyone at the Department of Structural Engineering, São Carlos School of Engineering, University of São Paulo. In particular, I want to thank Dr. Dorival Piedade Neto for his valuable contributions regarding the computational aspects.

Finally, I would like to thank the Coordination for the Improvement of Higher Education Personnel Foundation for the funding provided to my PhD thesis, especially regarding my doctoral internship in Portugal under the Institutional Internationalization Program. I would also like to thank the Faculty of Engineering of the University of Porto for the infrastructure provided during my time in Porto.

"The mind, once stretched by a new idea, never returns to its original dimensions"
Often attributed to Oliver Wendell Holmes Sr.

ABSTRACT

SANTOS, W.F. dos **Multi-scale modelling of materials with voids based on second-order computational homogenisation at finite strains: numerical analysis, experimental investigation and applications in architected structures**. 2025. 238p. Thesis (Doctor) - São Carlos School of Engineering, University of São Paulo, São Carlos, 2025.

Architected materials with voids include cellular and lattice structures, as well as exotic mechanical metamaterials with innovative properties, enabling the development of lightweight structures for specific and multifunctional engineering applications. The mechanical behaviour of these artificial materials can be challenging due to their intriguing properties and the presence of higher-order effects that often can not be adequately predicted by Cauchy continuum mechanics, encompassing strain localisation, size effects, and complex deformation modes. Moreover, the design of geometries to program material properties across multiple scales often leads to complex morphologies, making architected materials difficult to fabricate using conventional manufacturing methods. In this context, the present contribution combines conceptual formulation, numerical simulations, and an experimental approach (using additive manufacturing) for the multi-scale investigation of architected structures. A new second-order computational homogenisation formulation and its numerical implementation are proposed for investigating natural and architected materials in the presence of voids. The macro-scale is described by a second gradient continuum theory in the finite strain regime, and the micro-scale is modelled by the concept of Representative Volume Element (RVE) within the Cauchy continuum mechanics. The Method of Multi-scale Virtual Power is employed to link the two scales, ensuring a variationally consistent scale transition. In the developed formulation, the kinematical quantities are defined only in the solid domain of the RVE, and a new homogenisation relation is postulated for the second-order gradient, allowing for the consideration of voids in the RVE domain and its outer boundary. The kinematic constraints are imposed on the RVE by the Lagrange multiplier method and particularised for minimal (lower bound), periodic and direct (upper bound) conditions. It is demonstrated that the homogenised macroscopic stress tensors can be expressed in terms of the Lagrange multipliers. The finite element method is adopted to obtain approximate solutions corresponding to micro and macro equilibrium states. The Newton–Raphson method is employed to solve the non-linear systems of equations that describe equilibrium at both scales The consistent macroscopic tangents required for coupled multi-scale simulations are derived. The applicability and accuracy of the second-order computational strategy is assessed in several carefully chosen numerical examples of porous solids and architected materials accounting for two and three-dimensional simulations. Micro-scale numerical examples are presented to show deformation modes that can be captured by the second-order computational approach. Coupled multi-scale simulations are performed to demonstrate the robustness and predictive capacity of the second-order computational homogenisation approach for modelling thin-walled architected structures, encompassing numerical examples of cellular and lattice materials as well as metamaterials with second-order deformation modes, coupling deformation mechanisms and size effects. Regarding the experimental approach, polymeric architected structures are fabricated using additive manufacturing technology (known as 3D printing) and subjected to mechanical testing. In particular, a novel mechanical metamaterial exhibiting tension-induced undulation and cellular beams under bending with size effects are 3D-printed using Fused Deposition Modelling with a commercially available amorphous thermoplastic. The experimental data from mechanical tests are compared with numerical results from different computational modelling options, including coupled multi-scale analyses and single-scale models at the macro-scale. Finally, the advantages and challenges of integrating 3D printing with different numerical modelling strategies are discussed towards the design and fabrication of architected polymeric materials with complex geometries and intricate mechanical behaviour.

Keywords: Materials with voids. Architected structures. Multi-scale modelling. Second-order computational homogenisation. Experimental investigation.

RESUMO

SANTOS, W.F. dos **Modelagem multi-escala de materiais com vazios baseada em homogeneização computacional de segunda ordem em deformações finitas: análise numérica, investigação experimental e aplicações em estruturas arquitetadas**. 2025. 238p. Tese (Doutorado) - Escola de Engenharia de São Carlos, Universidade de São Paulo, São Carlos, 2025.

Materiais arquitetados com vazios incluem estruturas celulares e treliçadas, bem como metamateriais mecânicos exóticos com propriedades inovadoras, permitindo o desenvolvimento de estruturas leves para aplicações específicas e multifuncionais em engenharia. O comportamento mecânico desses materiais artificiais pode ser desafiador devido às suas propriedades intrigantes e à existência de efeitos de ordem superior que não podem ser adequadamente previstos pela mecânica do contínuo clássica, abrangendo localização de deformações, efeitos de tamanho e modos de deformação complexos. Além disso, o design de geometrias para programar as propriedades do material em múltiplas escalas frequentemente gera morfologias complexas, tornando as estruturas arquitetadas difíceis de fabricar com métodos convencionais de manufatura. Neste contexto, a presente contribuição combina formulação conceitual, simulações numéricas e uma abordagem experimental (usando manufatura aditiva) para a investigação multi-escala de estruturas arquitetadas. Uma nova formulação de homogeneização computacional de segunda ordem e sua implementação numérica são propostas para investigar materiais naturais e arquitetados na presença de vazios. A macro-escala é descrita por uma teoria contínua do segundo gradiente no regime de deformações finitas, e a micro-escala é modelada pelo conceito de Elemento de Volume Representativo (EVR) usando a mecânica clássica de Cauchy. O Método da Potência Virtual Multi-escala é empregado para vincular as duas escalas, garantindo uma transição de escala variacionalmente consistente. Na formulação desenvolvida, as quantidades cinemáticas são definidas apenas no domínio sólido do EVR e uma nova relação de homogeneização é postulada para o gradiente de segunda ordem, permitindo consideração de vazios no domínio do EVR e sua fronteira externa. As restrições cinemáticas são impostas no EVR pelo método dos multiplicadores de Lagrange e particularizadas para condições mínimas (limite inferior), periódica e direta (limite superior). Demonstra-se que os tensores de tensão macroscópicos homogenizados podem ser expressos em termos dos multiplicadores de Lagrange. O método dos elementos finitos é adotado para obter soluções aproximadas correspondentes aos estados de equilíbrio micro e macro. O método de Newton-Raphson é empregado para resolver os sistemas de equações não lineares que descrevem o equilíbrio em ambas as escalas As tangentes macroscópicas consistentes necessárias para as simulações multi-escala acopladas são derivadas. A aplicabilidade e a precisão da estratégia computacional de segunda ordem são avaliadas em vários exemplos numéricos cuidadosamente escolhidos de sólidos porosos e materiais arquitetados, considerando simulações bidimensionais e tridimensionais. Exemplos numéricos em micro-escala são apresentados para mostrar os modos de deformação que podem ser capturados pela abordagem computacional de segunda ordem. Simulações multi-escala acopladas são realizadas para demonstrar a robustez e a capacidade preditiva da abordagem de homogeneização computacional de segunda ordem para modelar estruturas arquitetadas de paredes finas, abrangendo exemplos numéricos de materiais celulares e de treliçados bem como metamateriais com modos de deformação de segunda ordem, mecanismos de deformação acoplados e efeitos de tamanho. Quanto à abordagem experimental, estruturas arquitetadas poliméricas são fabricadas utilizando a tecnologia de manufatura aditiva (conhecida como impressão 3D) e submetidas a testes mecânicos. Em particular, um novo metamaterial mecânico exibindo ondulação induzida por tensão e estruturas celulares sob flexão com efeitos de tamanho são impressos em 3D utilizando Modelagem por Deposição Fundida com um termoplástico amorfo comercialmente disponível. Os dados experimentais dos testes mecânicos são comparados com os resultados numéricos de diferentes opções de modelagem computacional, incluindo análises multi-escala acopladas e modelos de escala única na macro-escala. Por fim, as vantagens e desafios de integrar a impressão 3D com diferentes estratégias de modelagem numérica são discutidos em direção ao design e fabricação de materiais poliméricos arquitetados com geometrias complexas e comportamento mecânico intricado.

Palavras-chave: Materiais com vazios. Estruturas arquitetadas. Modelagem multi-escala. Homogeneização computacional de segunda ordem. Investigação experimental.

CONTENTS

APPENDIX 235

1 INTRODUCTION

1.1 Context

1.1.1 Architected materials with voids: metamaterials, lattice and cellular structures

Architected structures are micro-architected materials with macroscopic mechanical behaviour governed by morphology designed at multiple length scales (e.g., meso-scale, micro-scale and/or nano-scale architecture), as well as their material composition. Then, artificial structures can be rationally designed to achieve superior mechanical performance and outstanding physical properties beyond those provided by conventional natural materials. In this context, lightweight materials such as foams, mechanical metamaterials, lattice and cellular structures, can be explored across a wide range of structural components and advanced applications in diverse engineering fields such as construction, automotive, and aerospace industries (e.g., see Chica and Alzate (2019), Tay and Lankarani (2014) and Smeets *et al.* (2021)). Moreover, applications in the biomedical field can also be mentioned (Savio *et al.*, 2018; Pais; Belinha; Alves, 2023).

In particular, cellular and lattice structures offer valuable features and beneficial capabilities, including:

- (i) high mechanical strength and stiffness combined with low density: Schaedler *et al.* (2011), Meza, Das and Greer (2014), Zheng *et al.* (2014), Zhang *et al.* (2019), Andersen, Wang and Sigmund (2021), Yavas *et al.* (2022), Wang *et al.* (2022);
- (ii) energy absorption: Song *et al.* (2019), Chen *et al.* (2020), Alberdi *et al.* (2020), Guo *et al.* (2021), Zhang *et al.* (2022), Cheng *et al.* (2023), Yin *et al.* (2023);
- (iii) vibration control: Syam *et al.* (2018) and Rifaie, Abdulhadi and Mian (2022);
- (iv) thermal management: Catchpole-Smith *et al.* (2019) and Sajjad *et al.* (2022);
- (v) sound absorption: An *et al.* (2021), Li *et al.* (2021) and Li *et al.* (2023).

Furthermore, lightweight structures, particularly valuable in terms of their sustainability, can be designed by reducing material usage and energy consumption (Nazir *et al.*, 2019; Wu *et al.*, 2023a). Other important information, remarkable properties and applications, can be found in Fleck and Ashby (2010), Pan, Han and Lu (2020), Qi, Jiang and Yang (2021), Benedetti *et al.* (2021), Yin *et al.* (2023), and Wang *et al.* (2024). Therefore, these advanced structures can be utilised in various high-performance applications, delivering exceptional material efficiency.

Metamaterials are an intriguing class of engineered materials with exotic properties and unique capabilities, commonly not found in natural materials. This class of improved materials can provide particular properties and/or remarkable behaviours such as:

- (a) negative Poisson's ratio or auxetic materials: Lakes (1987), Bertoldi *et al.* (2010), Babaee *et al.* (2013), Mukhopadhyay and Adhikari (2016), Mizzi *et al.* (2018), Su, Wu and Shi (2022), Zhang *et al.* (2022), Liu *et al.* (2023), and Li *et al.* (2023);
- (b) metamaterials with negative compressibility: Baughman *et al.* (1998), Lakes *et al.* (2012), Gatt and Grima (2008), and Nicolaou and Motter (2012);
- (c) pattern transformations or multi-stable mechanical metamaterials: Mullin (2007), Bertoldi *et al.* (2008), Bertoldi *et al.* (2010), Gao *et al.* (2018), and VAN BREE *et al.* (2020);
- (d) ultralight, ultrastiff mechanical metamaterials: Zheng *et al.* (2014), Bauer, Schwaiger and Kraft (2016), Li and Gao (2016), and Guo Yang Wu and Wei (2024);
- (e) twisting under uniaxial forces: Frenzel, Kadic and Wegener (2017), Fernandez-Corbaton *et al.* (2019), Zhong *et al.* (2019), Qi *et al.* (2020), Wang and Liu (2020), Xu *et al.* (2023), Lemkalli *et al.* (2023), and Zhang *et al.* (2024); and
- (f) negative thermal expansion: Wang *et al.* (2016), Li, Yang and Lu (2019), and Zhang and Sun (2024).

Thus, innovative materials with tailored and often unprecedented mechanical behaviours are achieved through deliberate material design (Jiao *et al.*, 2023). This class of materials has multifunctional applications, including high stiffness-to-weight and/or high strength-to-weight ratios (Zheng *et al.*, 2014), vibration control (Dalela; Balaji; Jena, 2022; Rifaie; Abdulhadi; Mian, 2022; Zhang *et al.*, 2023), biomedical applications (Wang *et al.*, 2023; Chen *et al.*, 2024), energy absorption and dissipation (Mohsenizadeh *et al.*, 2018; Jiang *et al.*, 2023; Chen *et al.*, 2023), among others. Further details on mechanical metamaterials and their applications can be found in Yu *et al.* (2018), Surjadi *et al.* (2019), Wu *et al.* (2019), and Jiao *et al.* (2023).

Architected structures, particularly those with thin-walled elements, exhibit complex mechanical behaviour, comprising stress concentration and strain localisation mechanisms, as well as boundary layer phenomena and size effects (Iltchev *et al.*, 2015; Korshunova *et al.*, 2021; Pham; Hütter, 2021; Hosseini; Niiranen, 2022; Kladovasilakis *et al.*, 2022). Moreover, more sophisticated strategies may be required to deal with complicated deformation modes of mechanical metamaterials, higher strain gradients and high curvatures, among others. In particular, some works have been developed to investigate size effects in architected structures and metamaterials under: (i) bending: see Yoder, Thompson and Summers (2018), Khakalo, Balobanov and Niiranen (2018), Yang and Müller (2021), Hosseini and Niiranen (2022), Sarhil *et al.* (2023) and Yang *et al.* (2021); and (ii) axial tension/compression-induced-torsion: see Duan, Wen and Fang (2018), Khakalo, Balobanov and Niiranen (2018), Zheng *et al.* (2019), Ziemke *et al.* (2019), Frenzel *et al.* (2021) and Xu *et al.* (2023). Therefore, the modelling and design of such structures are challenging due to the complicated previously mentioned phenomena that arise in the mechanical and constitutive behaviour of these advanced materials. Finally, it is worth mentioning that obstacles still remain in the manufacture of micro-architected materials characterised by intricate geometries across the scales.

1.1.2 Multi-scale modelling based on second-order computational homogenisation

Regarding numerical simulations of architected structures with voids, a standard approach involves single-scale models or DNS models, where the solid part at the micro-architecture level is explicitly discretised into fine elements. For a periodic architected structure, the DNS model, consisting of an array of unit cells, is represented through the finite element discretisation of all unit cells. However, a large number of unit cells may result in a substantial number of finite elements and, consequently, degrees of freedom, particularly in three-dimensional simulations. Although the DNS finite element models show good agreement with the experimental results, the numerical simulations can be computationally expensive and even prohibitive for complete modelling of complex architected structures in industrial applications (Tekoglu; Onck, 2005; Iltchev *et al.*, 2015).

An alternative for modelling architected structures is to use FE^2 multi-scale approaches based on computational homogenisation, where finite element simulations are performed to model both the macro- and micro-scales. The macro-scale structure is assumed to be a homogenised continuum with effective constitutive behaviour derived from average-based homogenisation theory applied to the micro-scale fields. In this coupled strategy, each integration point of the macro-scale mesh is associated with the micro-scale through the concept of the Representative Volume Element (RVE), whose geometry and distribution of constituents must be statistically representative of the microstructure. FE^2 multi-scale models based on computational homogenisation are valuable for investigating cellular materials, lattice structures, and metamaterials.

Over the last years, first- and second-order homogenisation-based multi-scale strategies have been explored to model the non-homogeneous solids. In first-order approaches, the Cauchy continuum theory or first gradient-based continuum mechanics is assumed to govern both the macro-scale and the micro-scale. In this case, first-order effects associated with tension/compression and shear deformation modes predominate at the micro-scale. Moreover, size effects are not captured due to the absence of a scale parameter. Therefore, consistent results from first-order strategies require the validity of the Principle of Scale

Separation, where the characteristic macro-scale length must be much smaller than the characteristic RVE length.

To overcome the limitations of first-order strategies, the so-called generalised continuum theory or higher-order continuum mechanics emerges as an interesting option for multi-scale modelling architected materials, allowing for the consideration of size effects and localisation phenomena (Weeger, 2021; Yang *et al.*, 2022; Sarhil *et al.*, 2023). Different approaches based on generalised continuum theory have been employed in the investigation of metamaterials and architected structures, such as: (i) Micromorphic continuum theory: Rokoš *et al.* (2019), Biswas, Poh and Shedbale (2020), Rokoš *et al.* (2020), VAN BREE *et al.* (2020) and Sarhil *et al.* (2023); (ii) Cosserat or micropolar theories: Feyel (2003), Kumar and McDowell (2004), Alavi *et al.* (2022), Reis and Ganghoffer (2012), Yoder, Thompson and Summers (2018), Duan, Wen and Fang (2018) and Lemkalli *et al.* (2023); (iii) Asymptotic homogenisation method: Yang *et al.* (2020), Yang and Müller (2021), Yang *et al.* (2022), Vazic and Newell (2023) and Yang *et al.* (2021).

In the context of generalised continuum theories, multi-scale strategies based on second-order computational homogenisation are interesting for modelling architected materials displaying high-order effects. In the pioneering works of Kouznetsova (2002) and Kouznetsova, Geers and Brekelmans (2002), the standard second-order approach incorporates the second-gradient continuum theory in the modelling of the macro-scale, while maintaining the classical continuum theory at the micro-scale. Next, the implementation and computational aspects of a fully coupled micro–macro second-order computational homogenisation scheme suitable for the multi-scale modelling of macroscopic localisation and size effects has been described by Kouznetsova, Geers and Brekelmans (2004a). The formulation of Kouznetsova was focused on periodic boundary conditions on the RVE outer boundary. Later, Kaczmarczyk, Pearce and Bićanić (2008) extended this formulation to enforcement of generalised boundary conditions for the RVE, including direct displacement (upper bound) and traction (lower bound) boundary conditions. Specific works on microstructural size effects in second-order computational homogenisation were performed by Kouznetsova, Geers and Brekelmans (2004b) and Kaczmarczyk, Pearce and Bićanić (2010). Larsson and Diebels (2007) showed a higher order homogenisation procedure for multi-scale analysis scheme based on non-linear micropolar kinematics. Luscher (2010), Luscher, McDowell and Bronkhorst (2010) and Luscher, McDowell and Bronkhorst (2012) developed a hierarchical multi-scale approach based on second-order homogenisation, where orthogonality conditions were explored to define the microscopic constraints, encompassing a volume constraint over the RVE. Jänicke and Steeb (2012) discussed on minimal loading conditions for higher-order numerical homogenisation schemes. Nguyen and Noels (2014) investigated the micro-buckling of thin components and macroscopic localisation for cellular materials, where the continuous Galerkin method was employed to solve the strain gradient continuum at the macro-scale (Nguyen; Becker; Noels, 2013).

Yvonnet, Auffray and Monchiet (2020) proposed a computational homogenisation procedure for modelling elastic structures of materials with effective anisotropic strain-gradient behaviour. Weeger (2021) presented a numerical homogenisation method for computing the effective second gradient constitutive models of cubic beam-lattice metamaterials. Wu *et al.* (2023b) studied non-linear cellular materials and metamaterials using a second-order computational homogenisation strategy, employing an equivalent homogenised volume to model strain-gradient effects.

In particular, important theoretical contributions were proposed by Blanco *et al.* (2016a), where the Method of Multi-scale Virtual Power (Blanco *et al.*, 2016b) was explored for the derivation of a second-order mechanical model, including inertia and body force effects in the scale transition. Using the Method of Multi-scale Virtual Power, Lopes and Pires (2022a) proposed a variationally consistent multi-scale framework based on second-order computational homogenisation at finite strains for composite structures. Within this context, Lopes and Pires (2022b) performed an assessment of multi-scale models based on second-order computational homogenisation. Under assumptions of standard second-order computational homogenisation, the resulting macro-length scale parameter depends only of the RVE length, i.e., no length-scale parameter is introduced at the RVE level due to the size of the micro-constituents. Nevertheless, the multi-scale description of solids may require the regularisation of strain localisation at the micro-scale. For this purpose, a more general formulation must be employed with advanced constitutive laws to better describe the micro-scale behaviour. In this case, fully second-order computational homogenisation can be explored by introducing the second-gradient continua at both macro- and micro-scales. For example, second-order computational homogenisation schemes with higher-order theory at the macro- and micro-levels were proposed by Lesičar, Tonković and Sorić (2017) (small strain setting) and Lopes and Pires (2022c) (finite strains context). In addition, Schmidt *et al.* (2022) developed a computational homogenisation framework for investigating higher-order continua, incorporating first-, second-, and third-order effects at both micro- and macro-scales, using isogeometrical analysis.

Second-order homogenisation approaches are suitable to predict the constitutive behaviour of porous solids subjected to complex strain paths, such as those resulting from bending and torsion-like loadings. Furthermore, the presence of voids can trigger macroscopic localisation, which results in significant strain gradients that can only be addressed in a multi-scale framework with higher-order theories. In this context, Kouznetsova (2002), Kouznetsova, Geers and Brekelmans (2002), Kouznetsova, Geers and Brekelmans (2004b), Kouznetsova, Geers and Brekelmans (2004b) and other similar approaches (e.g., Kaczmarczyk, Pearce and Bićanić (2008)) investigated porous materials. Within these formulations, no volume constraint is considered in the RVE domain, which allows an easier numerical treatment of RVEs containing voids. However, the lack of a volumetric constraint in Kouznetsova's formulation can result in problems due to excessive deformation near the

RVE corners, leading to unphysical and mesh dependent results (see deails in Luscher, McDowell and Bronkhorst (2012) and Lopes and Pires (2022b)). Luscher (2010) and Luscher, McDowell and Bronkhorst (2012) studied the behaviour of porous solids with a second-order homogenisation formulation that includes a volume constraint in the entire RVE domain. Nevertheless, the RVE models employed do not contain a finite element mesh for the entire domain. Thus, the required volume constraint defined in the formulation is not numerically verified. Due to the same reason, the formulation proposed by Lopes and Pires (2022a) is also not suitable for investigating porous media. Therefore, a more natural way to consistently investigate porous materials is to define the kinematics only over the RVE solid part, since it is not possible to impose the volume constraint over the void domain.

1.1.3 Experimental and numerical investigations of 3D-printed architected materials

Regarding the fabrication of architected structures, Spadaccini (2019) highlights challenging aspects related to the morphological complexity of many three-dimensional structures, multiple length scales, the possibility of incorporating different material constituents, and the overall manufacturing throughput. The above-mentioned characteristics reveal limitations of conventional manufacturing technologies for fabricating more advanced architected structures, leading to highly complex and costly structure-based designs (Nazir *et al.*, 2019). The support of additive manufacturing techniques, also known as 3D printing, has contributed to the development of architected materials with complex designs and shapes, encompassing sophisticated structures at different length scales (Surjadi *et al.*, 2019). At small length scales, additive manufacturing has enabled the fabrication of micro- and nano-lattices with complex geometries and unit cell sizes ranging from tens of nanometers to submicrometers (Bauer *et al.*, 2017; Zhang *et al.*, 2020). Thus, advancements in 3D printing technology have made the design and manufacturing of metamaterials with exceptional mechanical properties more feasible (Yang *et al.*, 2024). As presented by Kladovasilakis *et al.* (2022), the range of studies on additive manufacturing with architected materials covers various sectors, such as civil engineering (Tiwari; Pratapa; Santhanam, 2024), automotive (Tilley *et al.*, 2024), aerospace (Ferro *et al.*, 2018; Opgenoord; Willcox, 2021), and biomedical applications (Mahmoud; Elbestawi, 2017; Ataollahi, 2023).

One of the most commonly used 3D printing techniques for producing architected cellular materials or mechanical metamaterials, particularly at the meso- and macro-scales, involves the direct extrusion of material onto a substrate or bed through a nozzle (Surjadi *et al.*, 2019). For example, Fusion Deposition Modelling (FDM) is an attractive manufacturing process for customised structures made from polymeric architected materials (Cuan-Urquizo; Silva, 2023), combining ease of manufacturing and cost efficiency to produce lightweight components with suitable mechanical performance. In this 3D printing technology, a solid filament is heated to its melting point and extruded onto a flat table through a nozzle. Specifically, thermoplastic polymeric materials have been extensively investigated as feedstocks for FDM 3D printing of architected structures, covering their design, fabrication, testing, and modelling (Almesmari *et al.*, 2023). Further details on FDM-based 3D printing of cellular, lattice, and porous mechanical metamaterials can be found in Cuan-Urquizo and Silva (2023).

Given the complexity of dealing with architected materials, the combination of experimental and computational strategies represents a promising alternative for investigating these advanced structures, coupling the advantages of each approach to achieve the desired mechanical properties. This coupled approach enables the achievement of desired mechanical properties and expands their applications in various industries. In this context, Aziz *et al.* (2021) investigated size effects on the mechanical properties of 3D-printed polymer body-centred cubic lattice structures, coupling mechanical experiments and classical finite element analyses. Korshunova *et al.* (2021) studied the bending behaviour of additively manufactured steel powder octet-truss lattice structures through experimental validation and numerical modelling via finite element analysis and the Finite Cell Method, incorporating higher-order continuum theories to account for size effects. Furthermore, multi-scale simulations based on computational homogenisation methods are particularly interesting for modelling the macroscopic effective behaviour of the architected structures, incorporating detailed information about the material's micro-architecture. For instance, Molavitabrizi *et al.* (2023) combined a second-order homogenisation approach with experimental verification to evaluate size effects in additively polymer manufactured lattice materials under bending. Zhmaylo *et al.* (2023) compared the numerical results from finite element homogenisation and DNS models with experimental data for additively manufactured lattice metamaterials made from powder materials, observing a good correlation between the different approaches. Therefore, coupling of experiments on additively manufactured polymeric materials with numerical simulations based on finite element methods provides a powerful approach for designing mechanically efficient architected materials.

1.2 Objectives

1.2.1 Main objective

The main objective is to investigate the mechanical behaviour of architected materials with voids through multi-scale modelling based on second-order computational homogenisation under finite strains. To validate the numerical modelling, an experimental programme was conceived to fabricate and test physical samples of architected structures.

1.2.2 Specific objectives

The specific objectives are listed below:

(a) The extension of the multi-scale variational formulation for second-order homogenisation at finite strains proposed by Lopes and Pires (2022a) to model natural and artificial materials in the presence of voids. This requires the postulation of a new homogenisation relation for the second-order gradient and the definition of kinematic quantities only in the solid part of the RVE domain.

(b) The development of a discrete multi-scale formulation based on second-order homogenisation and its numerical implementation in an in-house finite element programme.

(c) Micro-scale numerical simulations of two- and three-dimensional RVEs under second-order deformation modes (e.g., torsion and bending) of materials with linear elastic constitutive law, including the effective constitutive behaviour of porous solids and architected materials (lattice and cellular structures as well as metamaterials).

(d) FE^2 multi-scale numerical simulations to investigate the mechanical behaviour of two- and three-dimensional architected materials, accounting for deformation mode coupling and size effects, where a linear elastic law is assumed to model the constitutive behaviour.

(e) Investigation across scales of a novel 3D-printed polymer mechanical metamaterial displaying tension-induced undulation, coupling manufacturing and experimentation of the exotic architected structure and numerical simulations via different computational modelling approaches (DNS model and first-order multi-scale model), assuming an elasto-plastic constitutive behaviour.

(f) Analysis of the mechanical behaviour of 3D-printed polymer architected materials under bending with size effects, encompassing the experimental investigation and numerical simulations through different modelling options (DNS models as well as first- and second-order multi-scale models).

1.3 Motivation

As previously discussed, architected materials have been extensively explored to achieve specific or extreme macroscopic properties and enhanced functional structures. However, computational modelling of the mechanical behaviour of these artificial materials is still challenging due to the existence of higher-order effects that cannot be adequately captured by classical linear continuum mechanics For instance, the presence of coupled deformation mechanisms and/or size effects are some features observed in recent metamateriais, celullar solids and lattice structures. In this regard, the generalised continua theories may provide an improved description of the more complex overall behaviour, offering a consistent alternative for investigating solid structures exhibiting outstanding and/or extraordinary properties.

In this PhD thesis, a new consistent second-order homogenisation formulation at finite strains is proposed for the multi-scale modelling of porous and architected solids. The formulation is based on the Method of Multi-Scale Virtual Power, where equilibrium equations and homogenisation relations are derived using straightforward variational arguments. Under finite strain setting, second-gradient continuum is defined at the macro-scale and a Cauchy continuum is established at the micro-scale. In particular, a new expression for the kinematic homogenisation of the second-order gradient is postulated, considering that the kinematics is defined exclusively in the solid part of the RVE domain. Thus, three different sets of micro-scale kinematic constraints over the RVE can derived based on the variational arguments: minimal (lower bound), periodic, and direct (upper bound).

In particular, the enrichment of the continuum description through second-gradient elasticity enables us to consider second-order deformation modes, including: (i) bending and twist commonly observed in engineering applications, (ii) more complex and/or exotic deformation mechanisms (e.g., coupling deformation modes in mechanical metamaterials). The consideration of the finite strain hypothesis is important for dealing with higher strain gradients and high curvatures. A scale parameter is naturally incorporated into the second-order formulation, allowing us to capture size effects in architected structures. Thus, multi-scale problems that exhibit higher-order effects can be investigated using the new second-order strategy based on computational homogenisation. The second-order approach can be compared with the classical first-order approach and DNS finite element models, allowing for the assessment of the advantages and limitations of each modelling approach. Therefore, this contribution advances towards a more sophisticated modelling of the intricate behaviour of architected materials.

Furthermore, the combination of experimental and numerical investigations enables the assessment of the advantages and challenges of integrating 3D printing and modelling options to enhance the design and fabrication processes of architected materials with intricate geometries tailored for specific applications. This approach allows for precise control over material properties, unlocking superior mechanical performance and functionality. It is worth mentioning that recent advances in additive manufacturing technology have opened up new possibilities for the development of sophisticated micro-architected materials. Moreover, the manufacturing method adopted here is versatile and affordable, extending its applicability to cellular and lattice structures with diverse microstructural designs. This flexibility paves the way for expanding potential applications and enhancing the capabilities of these innovative materials in a wide range of engineering fields.

1.4 Computational framework

The discrete second-order multi-scale formulation for solids containing voids was implemented using the Fortran 90 language within an in-house finite element program named Links - Large Strain Implicit Non-Linear Analysis of Solids Linking Scales (see Figure 1). Links has been developed by the research group called CM2S – Computational Multi-Scale Modelling of Solids and Structures (see Figure 2) - coordinated by Professor Francisco Manuel Andrade Pires from the Faculty of Engineering, University of Porto. In the context of multi-scale strategies based on computational homogenisation, Links enables the numerical simulation of the mechanical behaviour of solids through micro-scale and FE^2 analyses at finite strains. Moreover, Links allows the simulation of multi-scale problems using first-order scheme (Lopes; Ferreira; Pires, 2021) and second-order approaches (Lopes; Pires, 2022a; Lopes; Pires, 2022d). It is worth noting that parallel computing strategies have been implemented to reduce computational cost of coupled multi-scale analyses (Lopes; Pires; Reis, 2018). All numerical simulations of this PhD thesis are performed using Links. Finally, the open-source software ParaView is employed for post-processing visualisation.

Figure 1 – Logo of the in-house finite element program Links.

Source: Lopes (2019).

Figure 2 – Logo of the research group CM2S.

Source: Lopes (2019).

1.5 Thesis layout

In summary, the outline of the doctoral thesis is organised as follows.

- Chapter 2 presents an overview of the main aspects of first- and second-order multi-scale modelling based on computational homogenisation.
- Chapter 3 presents the second-order computational homogenisation formulation for porous solids at finite strains, based on the Method of Multi-Scale Virtual Power. The kinematical quantities are defined only in the solid domain of the RVE, and a new homogenisation relation is postulated for the second-order gradient. Volumetric constraints naturally arise at the micro-scale considering the solid domain of the RVE. The formulation in light of variational principles allows the derivation of kinematic constraints that define the direct, periodic and minimal multi-scale models.
- Chapter 4 shows the finite element solution of the micro-scale discrete equilibrium problem for all multi-scale models, where the Newton–Raphson scheme is employed for the iterative solution of the corresponding non-linear systems of equations. Implementation aspects are also described in detail, including the determination of the constraint and homogenisation matrices, along with the consistent tangents.
- Chapter 5 reports micro-scale simulations with results associated with the homogenised constitutive behaviour of RVEs under second-order deformation modes. In this context, two-dimensional and three-dimensional numerical examples are presented to highlight the generality and some particularities of the new formulation developed in the present contribution.
- Chapter 6 presents several challenging coupled two-dimensional and three-dimensional numerical examples to assess the robustness and predictive capability of the multi-scale second-order homogenisation strategy to capture second-order effects in architected structures with linear elastic constitutive law. In particular, carefully chosen multi-scale applications are explored for investigating mechanisms associated with deformation mode coupling and size effects. The numerical results of the second-order strategy are compared with those of the first-order strategy and DNS models, as well as with experimental data found in the literature.
- Chapter 7 presents an brief introduction to the additive manufacturing process, focusing on FDM technology and its application in polymeric architected materials. Thus, considerations regarding 3D printing are provided to contextualise the manufacturing process employed in the experimental investigation.
- Chapter 8 investigates the exotic mechanical behaviour of a novel 3D-Printed polymer metamaterial made from a commercially available amorphous thermoplastic, encompassing experimentation and assessment of the predictive capacity of different

computational modelling approaches. Architected structures displaying tension-induced undulation mechanical behaviour are manufactured by FDM-based 3D printing. The architected structures are tested in laboratory experiments at different displacement rates. The mechanical behaviour is addressed in detail, encompassing the investigation of strength and failure mechanisms. Cyclic tests are also conducted to examine the mechanical behaviour of the polymeric architected structure with respect to residual displacements resulting from plastic strains. Three-dimensional elasto-plastic numerical simulations are conducted using DNS models and FE^2 multi-scale simulations based on first-order computational homogenisation.

- Chapter 9 combines mechanical testing and advanced modelling strategies by finite elements to capture size effects in the mechanical behaviour of additively manufactured polymer lattice beams under bending. The lattice structures are manufactured using the FDM 3D printing technique. Architected structures with different unit cell sizes and morphologies are tested through three-point bending experiments. Numerical simulations are performed using an in-house finite element code, employing two modelling options: (i) DNS finite element models, and (ii) Coupled multi-scale strategies based on first- and second-order computational homogenisation.
- Chapter 10 summarises the main contributions and conclusions of the investigation, along with perspectives for future research.

It is worth highlighting that most of the work developed in this PhD thesis has been published or submitted for publication in international journals. In this context, the text is based on the combination of the contributions presented in the following papers:

SANTOS, W. F. et al. Second-order multi-scale modelling of natural and architected materials in the presence of voids: Formulation and numerical implementation. **Computer Methods in Applied Mechanics and Engineering**, v. 416, 116374, Copyright Elsevier, 2023.

SANTOS, W. F. et al. Exploring novel mechanical metamaterials: Unravelling deformation mode coupling and size effects through second-order computational homogenisation. **International Journal of Solids and Structures**, v. 292, 112724, Copyright Elsevier, 2024.

SANTOS, W. F. et al. Analysis of a novel 3d-printed mechanical metamaterial with tension-induced undulation: experimental and numerical investigations. **Under Review**, 2025a.

SANTOS, W. F. et al. Three-point bending of 3D-printed polymer architected materials with size effects: manufacturing, testing and numerical modelling. **Under Review**, 2025b.

Finally, some developments of this PhD thesis were also presented at international scientific events:

- SANTOS, W. F. et al. A second-order computational homogenisation approach for investigating porous materials. In: **VII ECCOMAS Young Investigators Conference (YIC 2023)**, Porto, 2023.
- SANTOS, W. F. et al. Multi-scale modelling of metamaterials via second-order computational homogenisation. In: **9th European Congress on Computational Methods in Applied Sciences and Engineering (ECCOMAS 2024)**, Lisbon, 2024.
- SANTOS, W. F. et al. Multi-scale modelling of deformation-coupling and size effects in mechanical metamaterials. In: **Congress on Numerical Methods in Engineering 2024 (CMN 2024)**, Aveiro, 2024.

2 A BRIEF OVERVIEW OF MULTI-SCALE MODELLING BASED ON FIRST- AND SECOND-ORDER HOMOGENISATION

Constitutive models formulated with phenomenological observations have been important in the context of Computational Mechanics for investigating the macroscopic behaviour of several materials (natural and artificial). However, the global behaviour of many non-homogeneous materials, including micro-architected structures and porous media, is controlled by the complex phenomena that occur at the lower scales and their interaction mechanisms. In this case, the phenomenological constitutive models become inefficient, since their physical representation requires the introduction of numerous variables to be identified experimentally. Thus, the representation physical interactions at microscopic scales are difficult to be captured with exclusively macroscopic models.

Alternatively, multi-scale theories enable more representative and precise descriptions of mechanical and constitutive behaviour of complex materials across scales. Such approaches are based on the understanding of the physical phenomena that occur at the lower scales of the material and on its effect on the upper scales. The macroscopic behaviour is obtained from the successive coupling between scales, transferring the information found in the immediately inferior scales to the superior ones. Thus, multi-scale modelling allows the reduction of uncertainties in many phenomenological constitutive models and provides more realistic responses.

In particular, multi-scale strategies based on first- and second-order computational homogenisation have been widely explored to investigate non-homogeneous media. To better understand the differences and hypotheses of each approach, first- and second-order homogenisation schemes are briefly addressed below. For further details, readers are encouraged to consult the works developed by Geers, Kouznetsova and Brekelmans (2003), Kanouté *et al.* (2009), Geers, Kouznetsova and Brekelmans (2010), Nguyen, Stroeven and Sluys (2011), Saeb, Steinmann and Javili (2016), Geers *et al.* (2017), Matouš *et al.* (2017), Otero, Oller and Martinez (2018) and Lopes and Pires (2022d).

2.1 Considerations on multi-scale approach based on first-order homogenisation

Figure 3 presents an illustrative scheme of multi-scale approach based on first-order homogenisation for a non-homogeneous solid. In this case, two scales are considered for the multi-scale representation of the non-homogeneous material: (i) the macro-scale or macro-continuum with characteristic length L and domain Ω, and (ii) the micro-scale model based on the RVE concept with characteristic length l_μ and domain Ω_μ. Note that each macro-point of the macro-continuum is modelled through an RVE, which incorporates the presence of voids observed at the micro-scale. It is important to highlight that the

RVE must be statistically representative of the material's microstructure, capturing the specific characteristics of its constituents, such as size, morphology, distribution, volume fraction, and constitutive properties. Moreover, $\boldsymbol{u_0}$ and $\boldsymbol{t_0}$ denote the Newman and Dirichlet boundary conditions, respectively, applied at the macro-scale.

Figure 3 – First-order multi-scale modelling of a non-homogeneous material.

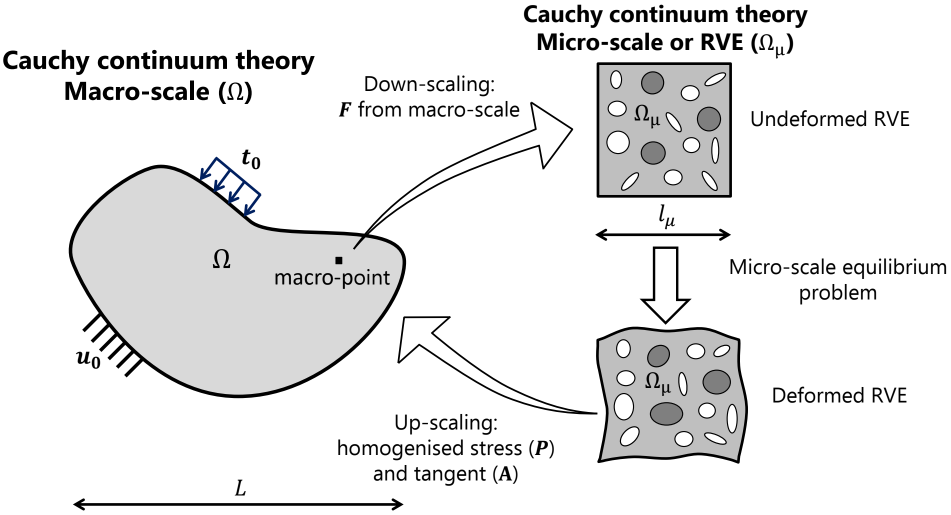

Source: The author.

In the first-order approach, the Cauchy continuum theory (first gradient-based) is assumed for both scales (i.e., macro-scale and micro-scale). Regarding the mechanical behaviour, the loading programme applied at the macro-scale ($\boldsymbol{t_0}$) results in macroscopic fields of displacement, strain, and stress. In the context of finite strains, the deformation gradient $\boldsymbol{F}$ from macro-scale is incorporated into the RVE model in the down-scaling process. The RVE equilibrium problem is solved using convenient boundary conditions, which define different multi-scale models. For example, the subsequent multi-scale models can be derived: (i) uniform traction boundary condition (lower bound); (ii) periodic boundary displacement fluctuations; (iii) linear boundary displacements (upper bound). Theory and applications involving these first-order multi-scale models can be found in Perić *et al.* (2011) (small strains) and Lopes, Ferreira and Pires (2021) (finite strains). Afterwards, the homogenisation process allows obtaining the first Piola-Kirchhoff stress tensor $\boldsymbol{P}$ (the energetic conjugate of $\boldsymbol{F}$). The homogenised constitutive consistent tangent A, required to solve the non-linear macroscopic equilibrium problem (e.g., using the Newton–Raphson method), is given by

$$\mathsf{A} = \frac{\partial \boldsymbol{P}}{\partial \boldsymbol{F}}. \tag{2.1}$$

Finally, in the downscaling process, the effective constitutive behaviour at the macro-point is updated based on the homogenised response of the RVE. The transition process between scales (i.e., down-scaling and up-scaling) continues until global equilibrium at the macro-scale is achieved.

In first-order theories, RVE deformation modes are predominantly associated with tension/compression and shear (e.g. see the components of $\boldsymbol{F}$ imposed on RVEs in Figure 4). On the one hand, since no scale parameter is introduced in this type of approach, the first-order formulation cannot capture size effects observed in structures with high-order effects (Geers *et al.*, 2009). Thus, the effective constitutive behaviour of the material is not affected by solely changing the size scale of a given RVE morphology. On the other hand, the change in the RVE size combined with alterations in its morphology influences the homogenised constitutive behaviour, where an RVE incorporating more heterogeneities generally provides more realistic responses. Therefore, the effective constitutive behaviour of the RVE is influenced by parameters such as the properties of the constituents and their interaction mechanisms, including morphology, distribution, and volume fraction. Furthermore, first-order homogenisation schemes are not suitable for the analysis of localisation problems, since large spatial gradients at the macro-scale cannot be modelled (Geers; Kouznetsova; Brekelmans, 2010). It is important to highlight that the applicability of first-order theories requires the Principle of Scale Separation to be satisfied for a multi-scale problem, where the characteristic RVE length must be infinitely smaller than the characteristic macrostructural length (i.e., $l_\mu \ll L$).

Figure 4 – First-order deformation modes - (b), (c), and (d) - for a three-dimensional RVE with a unidirectional void of circular cross-section.

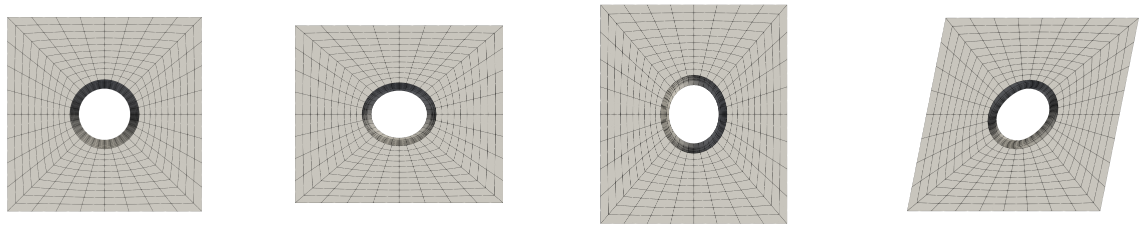

(a) Undeformed RVE. (b) Tension: F_{11}. (c) Compression: F_{11}. (d) Shear: F_{12}.

Source: The author.

In general, the well-known first-order homogenisation schemes are based on the so-called Hill–Mandel Principle (Bishop; Hill, 1951; Mandel, 1971). In summary, this principle establishes the macroscopic stress power equals the volume average of the microscopic stress power over Ω_μ (i.e., a bridge between scales is created through energetic consistency). First-order homogenisation schemes have been explored in FE^2 multi-scale computational strategies, i.e., with finite element simulations at both macro- and micro-scales. Over the years, some works employing this approach include Feyel (1999), Feyel and Chaboche (2000), Terada and Kikuchi (2001), Kouznetsova, Brekelmans and Baaijens (2001), Miehe and Koch (2002), Souza, Allen and Kim (2008), Souza and Allen (2010) and Perić *et al.* (2011), for instance. In a more recent context, it is also worth mentioning the works involving the Method of Multi-scale Virtual Power (Blanco *et al.*, 2016b), a generalisation of the well-known Hill–Mandel Principle, such as SOUZA NETO *et al.* (2015) and Lopes, Ferreira and Pires (2021). In this case, equilibrium equations and homogenisation relations are obtained by straightforward variational arguments.

2.2 Considerations on multi-scale approach based on second-order homogenisation

Generalised continuum theories, such as second gradient or strain gradient models (Mindlin, 1965) and micropolar/Cosserat (Cosserat; Cosserat, 1909) or micromorphic continua (Eringen; Suhubi, 1964a; Eringen; Suhubi, 1964b; Eringen, 1968; Forest, 2009), are attractive alternatives to describe size and localisation effects that cannot be suitably modelled by the classical continuum mechanics (Forest, 2002; Weeger, 2021). In general, generalised continuum theories involve the introduction of additional degrees of freedom or higher-order gradients of the displacement field to model the behaviour of materials with higher-order effects in a more realistic manner. In this context, second-order homogenisation approaches, which incorporate a second-gradient continuum to enhace the material description across the scales, have shown to be an interesting alternative for computational modelling of non-homogeneous materials (see Kouznetsova, Geers and Brekelmans (2002), Luscher, McDowell and Bronkhorst (2012) and Lopes and Pires (2022d)). Second-order multi-scale constitutive models based on computational homogenisation can be divided into two classes: standard second-order homogenisation (discussed bellow) and fully second-order homogenisation (see detail in Lopes and Pires (2022c)).

In the standard second-order scheme, the macro-scale is enriched with second-gradient continuum theory, while the micro-scale still maintains the Cauchy continuum theory (see Figure 5). In the down-scaling process, the deformation descriptors $\boldsymbol{F}$ and $\mathbf{G}$ (second gradient of the displacements) are inserted into the RVE model. An RVE equilibrium problem must also be solved with micro-scale constraints imposed over the RVE, where distinct models can be defined for the multi-scale strategy. For instance, the second-order approach presented by Lopes and Pires (2022a) enables the definition of the following multi-scale models: (i) minimal constraint (lower bound); (ii) periodic constraint; (iii) direct constraint (upper bound). The homogenisation procedure enables the recovery of the conjugate stresses $\boldsymbol{P}$ and $\mathbf{Q}$ (higher-order stress tensor), as well as the respective consistent tangents ($\mathbf{A}$, $\mathbf{A}_{\mathbf{G}}$, $\mathbf{H}$, and $\mathbf{H}_{\boldsymbol{F}}$). Following the approach presented by Lopes and Pires (2022a), the additional homogenised consistent tangents involving $\mathbf{Q}$ and $\mathbf{G}$ (i.e., $\mathbf{A}_{\mathbf{G}}$, $\mathbf{H}$, and $\mathbf{H}_{\boldsymbol{F}}$) can be derived by

$$\mathbf{A}_{\mathbf{G}} = \frac{\partial \boldsymbol{P}}{\partial \mathbf{G}}, \tag{2.2}$$

$$\mathbf{H} = \frac{\partial \mathbf{Q}}{\partial \mathbf{G}}, \tag{2.3}$$

$$\mathbf{H}_{\boldsymbol{F}} = \frac{\partial \mathbf{Q}}{\partial \boldsymbol{F}}, \tag{2.4}$$

while the consistent tangent that relates $\boldsymbol{F}$ and $\boldsymbol{P}$ (i.e., $\mathbf{A}$) is obtained from Equation 2.1.

Figure 5 – Second-order multi-scale modelling of a non-homogeneous material.

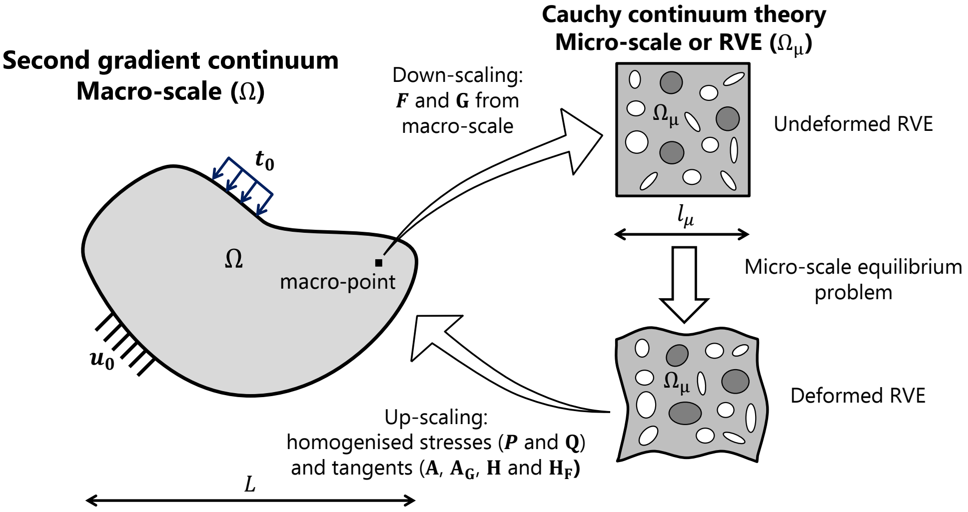

Source: The author.

As illustrated in Figure 6, the second-order computational homogenisation approach enables the capture of deformation modes related to $\mathbf{G}$, including extensional, trapezoidal, curvature, and twisting/torsion modes, which appear due to the presence of significant macroscopic strain gradients. It is worth mentioning that several engineering problems involve bending (i.e., trapezoidal and curvature modes) and torsion, which are disregarded in the first-order theory. Note that $\mathbf{A_G}$, $\mathbf{H}$, and $\mathbf{H}_{\boldsymbol{F}}$ enable the coupling of more complex deformation modes, relating first- and second-order effects, for example. In particular, the coupling of deformation modes can be crucial in the investigation of mechanical metamaterials. As reported in Frenzel, Kadic and Wegener (2017) and Xu *et al.* (2023), metamaterials with twist induced by uniaxial forces are examples coupling first- and second-order effects.

Figure 6 – Second-order deformation modes - (b), (c), (d) and (e) - for a three-dimensional RVE with a unidirectional void of circular cross-section.

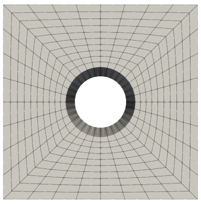

(a) Undeformed RVE.

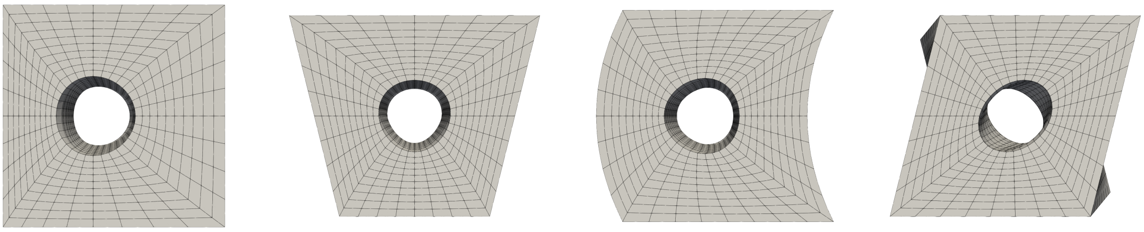

(b) Extensional: G_{111}. (c) Trapezoidal: G_{112}. (d) Curvature: G_{122}. (e) Torsion: G_{123}.

Source: The author.

Furthermore, the Principle of Scale Separation is relaxed and the characteristic length scale parameter is naturally incorporated in the formulation (Lopes; Pires, 2022d). Thus, the second-order strategy can capture size effects, where the effective constitutive behaviour of the material is influenced by changes in the size scale of a given RVE morphology. Lopes and Pires (2022d) also report that second-order approaches allow the regularisation of moderate localisation.

Therefore, second-order schemes allow to account for higher-order deformation gradients at the macro-scale and the size effects of the RVE. Several works in the context of second-order strategies are presented in Subsection 1.1.2, encompassing FE^2 multi-scale computational strategies. An overview with more details can be found in Lopes and Pires (2022d), including a discussion on distinct formulations and a guide for their implementation.

3 MULTI-SCALE MODELLING OF POROUS MATERIALS BASED ON SECOND-ORDER COMPUTATIONAL HOMOGENISATION

A new second-order computational homogenisation formulation at finite strains, suitable for the multi-scale simulation of natural and architected materials containing voids, is proposed below. It is worth noting that this formulation was published in Santos *et al.* (2023). Let us consider the multi-scale setting shown in Figure 7, where the finite strain regime is adopted for both the macro-scale (Ω) and the micro-scale (Ω_μ). The macro-scale continuum (characteristic length L) is described by second gradient theory. The micro-scale or RVE (characteristic length l_μ) is governed by a standard (first gradient) continuum mechanics. It is worth mentioning that the generality of the new formulation allows taking into account the presence of voids inside the RVE and also on its outer contour, a feature of many architected materials.

In the proposed framework, the macroscopic displacement $\boldsymbol{u}_M$, the macroscopic deformation gradient $\boldsymbol{F}$, and the second gradient of the displacements $\mathbf{G}$ are inserted in the micro-scale model. After solving the micro-scale equilibrium problem, the homogenisation procedure allows us to recover the respective conjugate stresses accounted for the deformation descriptors in the strain energy density function at the macro-scale, i.e., the first Piola–Kirchhoff stress tensor $\boldsymbol{P}$ (associated with $\boldsymbol{F}$) and the higher-order stress tensor $\mathbf{Q}$ (related to $\mathbf{G}$). Furthermore, respective consistent tangents ($\mathbf{A}$, $\mathbf{A}_\mathbf{G}$, $\mathbf{H}$, and $\mathbf{H}_{\boldsymbol{F}}$) also need to be obtained for coupled multi-scale analysis.

Figure 7 – Representation of the multi-scale setting for second-order homogenisation.

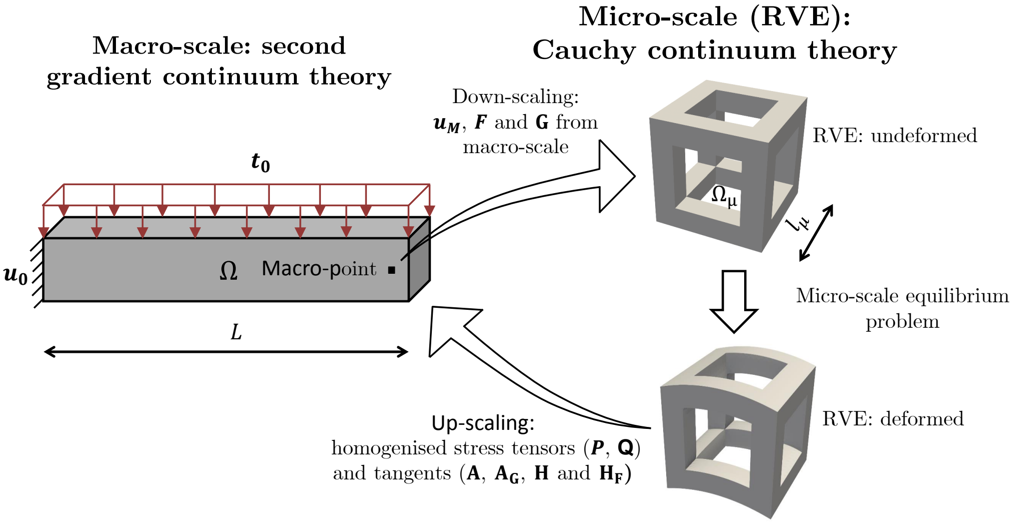

Source: The author.

The second-order computational homogenisation approach enables the capture of second-order deformation modes related to bending (trapezoidal and curvature) and twisting/torsion (see Figure 6), which are present in many architected structures. On the other hand, first-order homogenisation strategies predominantly capture deformation modes related to tension/compression and shear (see Figure 4). Furthermore, the present second-order formulation keeps a characteristic length scale parameter associated with the RVE length that is naturally included in the formulation.

The approach is based on the *Method of the Multi-Scale Virtual Power*, which relies on two main pillars: (i) the definition of the multi-scale kinematics, by postulating the kinematic insertion and kinematic homogenisation, whose compatibility leads to the kinematic admissibility, and (ii) the statement of the *Principle of Multi-Scale Virtual Power*, which is the basis to define the micro-scale equilibrium problem and the procedure for stresses homogenisation.

3.1 Multi-scale kinematics

3.1.1 Preliminary notations and definitions

For convenience, some definitions and notations are presented below. Let us consider the RVEs of a porous solid and architected materials presented in Figure 8. The total domain Ω_μ of each RVE is composed of the solid portion Ω_μ^s and the voids portion Ω_μ^v:

$$\Omega_\mu = \Omega_\mu^s \bigcup \Omega_\mu^v. \tag{3.1}$$

The outer boundary of the RVE, denoted by $\partial\Omega_\mu$, is given by

$$\partial\Omega_\mu = \partial\Omega_\mu^{s,b} \bigcup \partial\Omega_\mu^{v,b}, \tag{3.2}$$

where $\partial\Omega_\mu^{s,b}$ represents the outer boundary of the solid part and $\partial\Omega_\mu^{v,b}$ is the outer boundary of the porous portion.

Still, regarding the nomenclature for the boundaries, $\partial\Omega_\mu^{s,v}$ indicates the boundary of the voids. Thus, the boundary of the solid portion $\partial\Omega_\mu^s$ is given by

$$\partial\Omega_\mu^s = \partial\Omega_\mu^{s,b} \bigcup \partial\Omega_\mu^{s,v}. \tag{3.3}$$

Finally, the outer boundary of the solid part $\partial\Omega_\mu^{s,b}$ is calculated as

$$\partial\Omega_\mu^{s,b} = \partial\Omega_\mu^s \bigcap \partial\Omega_\mu. \tag{3.4}$$

Figure 8 – RVEs of a porous solid and architected materials , in which $\boldsymbol{N}$ is the normal at the outer RVE boundary and $\boldsymbol{N}^v$ is the normal at the void boundaries.

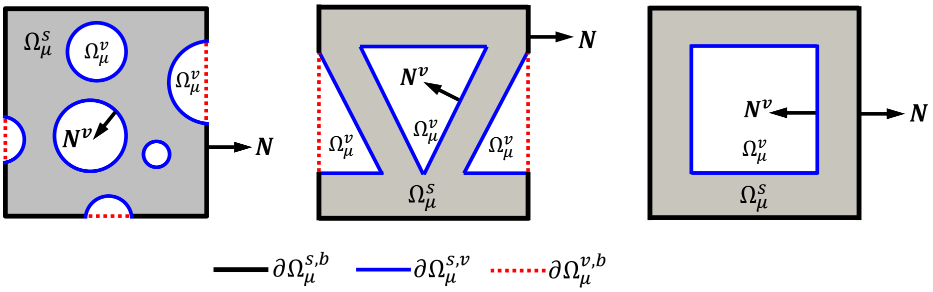

Source: The author.

3.1.2 Kinematic insertion

The micro-scale displacement is assumed to be a function of the macro-scale quantities by the kinematic insertion. In the context of second-order computational homogenisation approaches, an expression based on Taylor's expansion of the macroscopic displacement field is adopted to approximate the micro-scale counterpart. It accounts for the macroscopic second derivatives (Kouznetsova, 2002; Luscher, 2010), with an additional term proposed by Blanco *et al.* (2016a):

$$\boldsymbol{u}_\mu\left(\boldsymbol{Y}\right) = \boldsymbol{u}_M + \left(\boldsymbol{F} - \boldsymbol{I}\right) \cdot \boldsymbol{Y} + \frac{1}{2}\mathbf{G} : \left(\boldsymbol{Y} \otimes \boldsymbol{Y} - \boldsymbol{J}\right) + \tilde{\boldsymbol{u}}\left(\boldsymbol{Y}\right), \quad \forall \boldsymbol{Y} \in \Omega_\mu^s, \tag{3.5}$$

where $\boldsymbol{Y}$ denotes the vector of RVE reference coordinates and $\tilde{\boldsymbol{u}}$ is the micro displacement fluctuation field. Note that the kinematic insertion is only defined for the solid domain. The symbol $\boldsymbol{J}$ denotes the second-order moment of volume tensor:

$$\boldsymbol{J} = \frac{1}{V_\mu^s} \int_{\Omega_\mu^s} \boldsymbol{Y} \otimes \boldsymbol{Y} dV, \tag{3.6}$$

where $V_\mu^s = \left|\Omega_\mu^s\right|$ indicates the volume occupied by the solid domain Ω_μ^s. Moreover, V_μ^s is obtained by subtracting the void volume V_μ^v from the total volume V_μ, i.e., $V_\mu^s = V_\mu - V_\mu^v$.

Furthermore, the microscopic deformation gradient is derived from Equation (3.5):

$$\boldsymbol{F}_\mu\left(\boldsymbol{Y}\right) = \nabla_Y \boldsymbol{u}_\mu\left(\boldsymbol{Y}\right) + \boldsymbol{I} = \boldsymbol{F} + \mathbf{G} \cdot \boldsymbol{Y} + \nabla_Y \tilde{\boldsymbol{u}}\left(\boldsymbol{Y}\right), \quad \forall \boldsymbol{Y} \in \Omega_\mu^s. \tag{3.7}$$

Finally, without loss of generality, it is conveniently assumed that the origin of the micro coordinate system is located at the centroid of the solid part of the RVE, $\boldsymbol{Y}_{CG}$:

$$\boldsymbol{Y}_{CG} = \frac{1}{V_\mu^s} \int_{\Omega_\mu^s} \boldsymbol{Y} dV, \tag{3.8}$$

such that the following expression must be valid:

$$\int_{\Omega_\mu^s} \boldsymbol{Y} dV = \mathbf{0}. \tag{3.9}$$

3.1.3 Kinematic homogenisation

The kinematic homogenisation procedure establishes how macro-scale kinematical descriptors ($\boldsymbol{u}_M$, $\boldsymbol{F}$ and $\mathbf{G}$) are recovered based on the volume averaging of the micro-scale kinematic quantities. In this context, the homogenisation related to the macro-scale displacement vector is postulated to be given by:

$$\boldsymbol{u}_M = \frac{1}{V_\mu^s} \int_{\Omega_\mu^s} \boldsymbol{u}_\mu dV. \tag{3.10}$$

The homogenisation formula related to the first macro-deformation gradient is based on the volume averaging of its micro-scale counterpart, in the solid part of the RVE, since no kinematics is defined for the voids:

$$\boldsymbol{F} = \frac{1}{V_\mu^s}\left[\int_{\Omega_\mu^s} \boldsymbol{F}_\mu dV - \int_{\partial\Omega_\mu^{s,v}} \tilde{\boldsymbol{u}} \otimes \boldsymbol{N}^v dA - \int_{\partial\Omega_\mu^{s,b}} \tilde{\boldsymbol{u}} \otimes \bar{\boldsymbol{N}} dA\right], \tag{3.11}$$

with $\boldsymbol{N}^v$ denoting the normal unit vector at the void inner boundary (see Figure 8), and $\bar{\boldsymbol{N}}$ denoting a constant mean normal in the solid part of the RVE boundary $\partial\Omega_\mu^{s,b}$, which will be addressed in Remark 2.

Remark 1. *Equations (3.10) and (3.11) have been proposed by Rocha et al. (2018) and Feijóo et al. (2023) to study RVEs containing random voids in the boundary in the context of first-order homogenisation. Some non-classical aspects of the homogenisation relation that has been postulated need to be explained in detail. Firstly, the volume average (Equation (3.10)) has been defined for the displacement field, considering only the solid part of the RVE, Ω_μ^s, instead of Ω_μ, which is coherent since the kinematic insertion is defined only in the RVE matrix (Equation (3.5)). Secondly, the homogenisation of the deformation gradient has also been established in Equation (3.11) using only the solid part of the RVE domain. Note that this definition results in a volume integral over the solid part of the RVE volume (associated with $\boldsymbol{F}_\mu$) and additional terms in the form of boundary integrals associated with the fluctuations $\tilde{\boldsymbol{u}}$. Thirdly, the definition of the insertion for the solid part leads to the appearance of the second term of Equation (3.11) in order to accommodate the fluctuations over the solid-void boundary $\partial\Omega_\mu^{s,v}$ (see further details in Rocha et al. (2018)).*

Remark 2. *The last term of Equation (3.11) proposed by Rocha et al. (2018) and Feijóo et al. (2023), which is associated with a vector denoted by $\bar{\boldsymbol{N}}$, emerges by the fact that the homogenisation formula postulated must be such that no spurious macro-scale gradient should occur when considering a constant displacement fluctuation field (i.e., $\tilde{\boldsymbol{u}} = \boldsymbol{c}$) in the modelling of materials with random voids reaching the RVE boundary. As shown in Appendix A.1, the imposition of $\tilde{\boldsymbol{u}} = \boldsymbol{c}$ in Equation (3.11) results in Equation (A.3), which can be rewritten as:*

$$\int_{\partial\Omega_\mu^{s,b}} \bar{\boldsymbol{N}} dA = \int_{\partial\Omega_\mu^{s,b}} \boldsymbol{N} dA, \tag{3.12}$$

where $\boldsymbol{N}$ denotes the normal unit vector at the RVE outer solid boundary (see Figure (8)).

Since $\bar{\boldsymbol{N}}$ is a constant vector, Equation (3.12) can be rewritten as:

$$\bar{\boldsymbol{N}} = \frac{1}{A_\mu^{s,b}} \int_{\partial\Omega_\mu^{s,b}} \boldsymbol{N} dA, \tag{3.13}$$

where $A_\mu^{s,b} = \left|\partial\Omega_\mu^{s,b}\right| = \int_{\partial\Omega_\mu^{s,b}} dA$ denotes the surface area of the outer solid part, and it is shown that $\bar{\boldsymbol{N}}$ is the mean normal. Thus, the boundary integral associated with $\bar{\boldsymbol{N}}$ maintains the kinematical consistency in the homogenisation related to the first macro-deformation gradient (Feijóo et al., 2023). In addition, the mean normal term vanishes for a periodic material.

Since the problem at the micro-scale is still a first-order problem, the homogenised second gradient cannot be defined as the volume averaging its micro-scale counterpart, which would lead to higher-order constraints. Therefore, the homogenisation formula for the second gradient is postulated as follows:

$$\begin{aligned}\mathbf{G} =& \frac{1}{V_\mu^s}\left[\int_{\Omega_\mu^s} \nabla_Y \boldsymbol{u}_\mu \otimes \boldsymbol{Y}\cdot\boldsymbol{J}^{-1} dV - \int_{\partial\Omega_\mu^{s,v}} \tilde{\boldsymbol{u}}\otimes \boldsymbol{N}^v \otimes \boldsymbol{Y}\cdot \boldsymbol{J}^{-1} dA\right. \\ &\left. - \int_{\partial\Omega_\mu^{s,b}} \tilde{\boldsymbol{u}} \otimes \bar{\bar{\boldsymbol{X}}}\cdot\boldsymbol{J}^{-1}dA\right],\end{aligned} \tag{3.14}$$

where $\bar{\bar{\boldsymbol{X}}}$ is a constant second-order tensor. Regarding Equation (3.14), two major characteristics are worth to be remarked. First, the boundary void-solid integral (i.e., associated with $\partial\Omega_\mu^{s,v}$) arises to account for the effect of fluctuations on the void boundaries due to the fact that the kinematics is defined only over the solid part of the RVE. Second, the homogenisation formula for $\mathbf{G}$ (Equation (3.14)) must also avoid spurious macro-scale second gradient when considering a uniform displacement fluctuation field. In this context, the integral on the RVE outer solid boundary ($\partial\Omega_\mu^{s,b}$) related to $\bar{\bar{\boldsymbol{X}}}$ aims to remove spurious macro-scale second gradients induced by $\tilde{\boldsymbol{u}} = \boldsymbol{c}$ (arbitrary constant field) for porous RVEs. As demonstrated in Appendix A.2, the enforcement of $\tilde{\boldsymbol{u}} = \boldsymbol{c}$ in Equation (3.14) results in Equation (A.7), which can be rewritten as:

$$\int_{\partial\Omega_\mu^{s,b}} \bar{\bar{\boldsymbol{X}}} dA = \int_{\partial\Omega_\mu^{s,b}} \boldsymbol{N}\otimes\boldsymbol{Y} dA - V^s \boldsymbol{I}, \tag{3.15}$$

where $\boldsymbol{I}$ is the second-order identity tensor.

Since $\bar{\bar{\boldsymbol{X}}}$ is defined as a constant tensor, the following expression can be obtained:

$$\bar{\bar{\boldsymbol{X}}} = \frac{1}{A_\mu^{s,b}}\int_{\partial\Omega_\mu^{s,b}} \boldsymbol{N}\otimes\boldsymbol{Y} dA - \frac{1}{A_\mu^{s,b}} V^s \boldsymbol{I}. \tag{3.16}$$

Therefore, the boundary integral related to $\bar{\bar{\boldsymbol{X}}}$ was added to Equation (3.14) to ensure the kinematical consistency in the homogenisation of the second macro-deformation gradient.

3.1.4 Kinematic admissibility

The compatibility between kinematic insertion and kinematic homogenisation is ensured through constraints that must be imposed at the RVE level. Ensuring the conservation of the displacement field, Equation (3.5) into (3.10) results in:

$$\begin{aligned}&\boldsymbol{u}_M = \boldsymbol{u}_M + (\boldsymbol{F}-\boldsymbol{I})\cdot\frac{1}{V_\mu^s}\int_{\Omega_\mu^s}\boldsymbol{Y} dV + \frac{1}{2}\mathbf{G} : \left[\frac{1}{V_\mu^s}\int_{\Omega_\mu^s}(\boldsymbol{Y}\otimes\boldsymbol{Y})\, dV - \boldsymbol{J}\right] + \frac{1}{V_\mu^s}\int_{\Omega_\mu^s}\tilde{\boldsymbol{u}} dV \Leftrightarrow \\ &(\boldsymbol{F}-\boldsymbol{I})\cdot\frac{1}{V_\mu^s}\int_{\Omega_\mu^s}\boldsymbol{Y} dV + \frac{1}{2}\mathbf{G} : \left[\frac{1}{V_\mu^s}\int_{\Omega_\mu^s}(\boldsymbol{Y}\otimes\boldsymbol{Y})\, dV - \boldsymbol{J}\right] + \frac{1}{V_\mu^s}\int_{\Omega_\mu^s}\tilde{\boldsymbol{u}} dV = \boldsymbol{0}.\end{aligned} \tag{3.17}$$

Taking into account the definition presented in Equations (3.6) and (3.9), Equation (3.17) yields:

$$\int_{\Omega_\mu^s} \tilde{\boldsymbol{u}} dV = \mathbf{0}. \tag{3.18}$$

Including the definition of the micro-displacements gradient that results from kinematic homogenisation, Equation (3.7), into Equation (3.11), taking into account Equation (3.9), results in:

$$\begin{gathered}
\boldsymbol{F} = \boldsymbol{F} + \frac{1}{V_\mu^s}\left[\boldsymbol{\mathsf{G}} \cdot \int_{\Omega_\mu^s} \boldsymbol{Y} dV + \int_{\Omega_\mu^s} \nabla_Y \tilde{\boldsymbol{u}} dV - \int_{\partial\Omega_\mu^{s,v}} \tilde{\boldsymbol{u}} \otimes \boldsymbol{N}^v dA - \int_{\partial\Omega_\mu^{s,b}} \tilde{\boldsymbol{u}} \otimes \bar{\boldsymbol{N}} dA\right] \Leftrightarrow \\
\int_{\Omega_\mu^s} \nabla_Y \tilde{\boldsymbol{u}} dV - \int_{\partial\Omega_\mu^{s,v}} \tilde{\boldsymbol{u}} \otimes \boldsymbol{N}^v dA - \int_{\partial\Omega_\mu^{s,b}} \tilde{\boldsymbol{u}} \otimes \bar{\boldsymbol{N}} dA = \mathbf{0}.
\end{gathered} \tag{3.19}$$

The first term can be expressed as a boundary integral, and developed taking into account that $\partial\Omega_\mu^s = \partial\Omega_\mu^{s,b} \bigcup \partial\Omega_\mu^{s,v}$:

$$\int_{\Omega_\mu^s} \nabla_Y \tilde{\boldsymbol{u}} dV = \int_{\partial\Omega_\mu^s} \tilde{\boldsymbol{u}} \otimes \boldsymbol{N} dA = \int_{\partial\Omega_\mu^{s,b}} \tilde{\boldsymbol{u}} \otimes \boldsymbol{N} dA + \int_{\partial\Omega_\mu^{s,v}} \tilde{\boldsymbol{u}} \otimes \boldsymbol{N}^v dA. \tag{3.20}$$

Therefore, Equation (3.19) may be rewritten as

$$\begin{gathered}
\int_{\partial\Omega_\mu^{s,b}} \tilde{\boldsymbol{u}} \otimes \boldsymbol{N} dA + \int_{\partial\Omega_\mu^{s,v}} \tilde{\boldsymbol{u}} \otimes \boldsymbol{N}^v dA - \int_{\partial\Omega_\mu^{s,v}} \tilde{\boldsymbol{u}} \otimes \boldsymbol{N}^v dA - \int_{\partial\Omega_\mu^{s,b}} \tilde{\boldsymbol{u}} \otimes \bar{\boldsymbol{N}} dA = \mathbf{0} \Leftrightarrow \\
\int_{\partial\Omega_\mu^{s,b}} \tilde{\boldsymbol{u}} \otimes \left(\boldsymbol{N} - \bar{\boldsymbol{N}}\right) dA = \mathbf{0},
\end{gathered} \tag{3.21}$$

which is a constraint enforced on the external solid boundary only, where the kinematics is actually defined.

Remark 3. *Regarding Equation (3.21), it is interesting to note that in the case of RVEs without voids intersecting the boundary (i.e., $\partial\Omega_\mu^{v,b} = \emptyset$): $\partial\Omega_\mu^{s,b} = \partial\Omega_\mu$, and $\bar{\boldsymbol{N}} = \mathbf{0}$. Thus, the conventional minimal kinematic constraint, typically defined in first-order homogenisation schemes, is recovered as a limiting case:*

$$\int_{\partial\Omega_\mu} \tilde{\boldsymbol{u}} \otimes \boldsymbol{N} dA = \mathbf{0}. \tag{3.22}$$

Likewise, inserting Equation (3.7) into Equation (3.14) leads to

$$\begin{aligned}
\boldsymbol{\mathsf{G}} = \frac{1}{V_\mu^s}\Bigg[&\int_{\Omega_\mu^s} (\boldsymbol{F} - \boldsymbol{I}) \otimes \boldsymbol{Y} \cdot \boldsymbol{J}^{-1} dV + \int_{\Omega_\mu^s} \boldsymbol{\mathsf{G}} \cdot \boldsymbol{Y} \otimes \boldsymbol{Y} \cdot \boldsymbol{J}^{-1} dV + \int_{\Omega_\mu^s} \nabla_Y \tilde{\boldsymbol{u}} \otimes \boldsymbol{Y} \cdot \boldsymbol{J}^{-1} dV \\
&- \int_{\partial\Omega_\mu^{s,v}} \tilde{\boldsymbol{u}} \otimes \boldsymbol{N}^v \otimes \boldsymbol{Y} \cdot \boldsymbol{J}^{-1} dA - \int_{\partial\Omega_\mu^{s,b}} \tilde{\boldsymbol{u}} \otimes \bar{\bar{\boldsymbol{X}}} \cdot \boldsymbol{J}^{-1} dA\Bigg].
\end{aligned} \tag{3.23}$$

Including the definition of the second-order moment of volume given by Equation (3.6) and Equation (3.9), the above equation is simplified to

$$\int_{\Omega_\mu^s} \nabla_Y \tilde{\boldsymbol{u}} \otimes \boldsymbol{Y} \cdot \boldsymbol{J}^{-1} dV - \int_{\partial\Omega_\mu^{s,v}} \tilde{\boldsymbol{u}} \otimes \boldsymbol{N}^s \otimes \boldsymbol{Y} \cdot \boldsymbol{J}^{-1} dA - \int_{\partial\Omega_\mu^{s,b}} \tilde{\boldsymbol{u}} \otimes \bar{\bar{\boldsymbol{X}}} \cdot \boldsymbol{J}^{-1} dA = \boldsymbol{0}. \tag{3.24}$$

After integration by parts, the first term may be split into a volumetric and a boundary integral component:

$$\begin{aligned}\int_{\Omega_\mu^s} \nabla_Y \tilde{\boldsymbol{u}} \otimes \boldsymbol{Y} \cdot \boldsymbol{J}^{-1} dV &= \int_{\partial\Omega_\mu^s} (\tilde{\boldsymbol{u}} \otimes \boldsymbol{N} \otimes \boldsymbol{Y}) \cdot \boldsymbol{J}^{-1} dA - \int_{\Omega_\mu^s} \tilde{\boldsymbol{u}} dV \otimes \boldsymbol{J}^{-1} \\ &= \int_{\partial\Omega_\mu^{s,b}} (\tilde{\boldsymbol{u}} \otimes \boldsymbol{N} \otimes \boldsymbol{Y}) \cdot \boldsymbol{J}^{-1} dA + \int_{\partial\Omega_\mu^{s,v}} (\tilde{\boldsymbol{u}} \otimes \boldsymbol{N}^s \otimes \boldsymbol{Y}) \cdot \boldsymbol{J}^{-1} dA \\ &- \int_{\Omega_\mu^s} \tilde{\boldsymbol{u}} dV \otimes \boldsymbol{J}^{-1}.\end{aligned} \tag{3.25}$$

Consequently, Equation (3.24) may be expressed as

$$\begin{aligned}&\int_{\partial\Omega_\mu^{s,b}} \tilde{\boldsymbol{u}} \otimes \boldsymbol{N} \otimes \boldsymbol{Y} \cdot \boldsymbol{J}^{-1} dA + \int_{\partial\Omega_\mu^{s,v}} (\tilde{\boldsymbol{u}} \otimes \boldsymbol{N}^s \otimes \boldsymbol{Y}) \cdot \boldsymbol{J}^{-1} dA - \int_{\Omega_\mu^s} \tilde{\boldsymbol{u}} dV \otimes \boldsymbol{J}^{-1} \\ &- \int_{\partial\Omega_\mu^{s,v}} \tilde{\boldsymbol{u}} \otimes \boldsymbol{N}^s \otimes \boldsymbol{Y} \cdot \boldsymbol{J}^{-1} dA - \int_{\partial\Omega_\mu^{s,b}} \tilde{\boldsymbol{u}} \otimes \bar{\bar{\boldsymbol{X}}} \cdot \boldsymbol{J}^{-1} dA = \boldsymbol{0},\end{aligned} \tag{3.26}$$

which is simplified to

$$\int_{\partial\Omega_\mu^{s,b}} \tilde{\boldsymbol{u}} \otimes \left(\boldsymbol{N} \otimes \boldsymbol{Y} - \bar{\bar{\boldsymbol{X}}}\right) \cdot \boldsymbol{J}^{-1} dA - \int_{\Omega_\mu^s} \tilde{\boldsymbol{u}} dV \otimes \boldsymbol{J}^{-1} = \boldsymbol{0}. \tag{3.27}$$

Finally, since the volumetric term of Equation (3.27) becomes null due to the constraint of Equation (3.18), it is possible to assume that the boundary terms are satisfied independently, i.e.:

$$\int_{\partial\Omega_\mu^{s,b}} \tilde{\boldsymbol{u}} \otimes \left(\boldsymbol{N} \otimes \boldsymbol{Y} - \bar{\bar{\boldsymbol{X}}}\right) \cdot \boldsymbol{J}^{-1} dA = \boldsymbol{0} \Leftrightarrow \int_{\partial\Omega_\mu^{s,b}} \tilde{\boldsymbol{u}} \otimes \left(\boldsymbol{N} \otimes \boldsymbol{Y} - \bar{\bar{\boldsymbol{X}}}\right) dA = \boldsymbol{0}. \tag{3.28}$$

Remark 4. *Note that in the case of an RVE that does not contain voids, the solid boundary would coincide with the RVE boundary, thus* $V_\mu = V_\mu^s$*,* $\partial\Omega_\mu^{s,b} = \partial\Omega_\mu$*, and* $\partial\Omega_\mu^{s,v} = \emptyset$*. As a consequence* $\bar{\boldsymbol{N}} = \boldsymbol{0}$ *and* $\bar{\bar{\boldsymbol{X}}} = \boldsymbol{0}$*, since* $\partial\Omega_\mu^{s,b}$ *becomes a closed boundary, and the last two terms of Equation (3.11) and (3.14) turn to be null. Therefore, the present definitions of the homogenised deformation gradient* $\boldsymbol{F}$ *and second gradient* $\boldsymbol{\mathsf{G}}$ *recover their conventional counterparts in the absence of voids at the micro-scale.*

Remark 5. *In the case of an RVE without voids in its domain,* $\Omega_\mu^s = \Omega_\mu$*, Equation (3.24) could be rewritten as*

$$\int_{\Omega_\mu} \nabla_Y \tilde{\boldsymbol{u}} \otimes \boldsymbol{Y} \cdot \boldsymbol{J}^{-1} dV = \boldsymbol{0}, \tag{3.29}$$

with its decomposition in a boundary integral given by

$$\int_{\partial\Omega_\mu} \tilde{\boldsymbol{u}} \otimes \boldsymbol{N} \otimes \boldsymbol{Y} \cdot \boldsymbol{J}^{-1} dA - \int_{\Omega_\mu} \tilde{\boldsymbol{u}} dV \otimes \boldsymbol{J}^{-1} = \boldsymbol{0}, \tag{3.30}$$

which recovers the minimal constraint of Lopes and Pires (2022a). Moreover, the previous integral can be conveniently split into a boundary constraint

$$\int_{\partial\Omega_\mu} \tilde{\boldsymbol{u}} \otimes \boldsymbol{N} \otimes \boldsymbol{Y} \cdot \boldsymbol{J}^{-1} dA = \boldsymbol{0} \Leftrightarrow \int_{\partial\Omega_\mu} \tilde{\boldsymbol{u}} \otimes \boldsymbol{N} \otimes \boldsymbol{Y} dA = \boldsymbol{0}, \tag{3.31}$$

and a volumetric constraint

$$\int_{\Omega_\mu} \tilde{\boldsymbol{u}} dV \otimes \boldsymbol{J}^{-1} = \boldsymbol{0} \Leftrightarrow \int_{\Omega_\mu} \tilde{\boldsymbol{u}} dV = \boldsymbol{0}, \tag{3.32}$$

respectively.

It must be remarked that the models proposed by Lopes and Pires (2022a), Blanco et al. (2016a) and Luscher (2010) are not able to correctly deal with RVEs containing voids, since the resulting volumetric constraints must be applied in the whole RVE domain, even though there is no kinematics defined for the voids domain. Regarding the formulation proposed by Kouznetsova (2002), it only takes into account the boundary constraint of Equation (3.31) and there are no volumetric constraints. However, this lack of volume constraints leads to excessive deformation near the RVE corners (Luscher; McDowell; Bronkhorst, 2012; Lopes; Pires, 2022b).

3.2 Sets of admissible fluctuations

The set of admissible fluctuation displacements that satisfies the constraints of Equations (3.18), (3.21) and (3.28) may be defined by $\tilde{\mathcal{V}}$, such that $\tilde{\boldsymbol{u}} \in \tilde{\mathcal{V}}$ and $\delta\tilde{\boldsymbol{u}} \in \tilde{\mathcal{V}}$:

$$\begin{aligned} \tilde{\mathcal{V}} = \Bigg\{ & \tilde{\boldsymbol{u}} \text{ sufficiently regular in } \Omega_\mu^s, \int_{\partial\Omega_\mu^{s,b}} \tilde{\boldsymbol{u}} \otimes \left(\boldsymbol{N} - \bar{\boldsymbol{N}}\right) dA = \boldsymbol{0}, \\ & \int_{\partial\Omega_\mu^{s,b}} \tilde{\boldsymbol{u}} \otimes \left(\boldsymbol{N} \otimes \boldsymbol{Y} - \bar{\bar{\boldsymbol{X}}}\right) dA = \boldsymbol{0}, \int_{\Omega_\mu^s} \tilde{\boldsymbol{u}} dV = \boldsymbol{0} \Bigg\}. \end{aligned} \tag{3.33}$$

This represents the set of minimally constrained displacement fluctuation fields. However, more restrictive subsets may be conveniently defined. Following the constraints usually employed in first-order homogenisation models, null or periodic fluctuations on the RVE boundary may be defined as subsets of solutions that still satisfy the kinematic admissibility.

3.2.1 Periodic boundary condition

With regard to the periodic boundary conditions, it is here defined as

$$\tilde{\boldsymbol{u}}^+ = \tilde{\boldsymbol{u}}^- \Leftrightarrow \tilde{\boldsymbol{u}}\left(\boldsymbol{Y}^+\right) = \tilde{\boldsymbol{u}}\left(\boldsymbol{Y}^-\right), \quad \forall \boldsymbol{Y}^+ \in \partial\Omega_\mu^{s,b+}, \ \forall \boldsymbol{Y}^- \in \partial\Omega_\mu^{s,b-} \tag{3.34}$$

with + and - denoting opposite RVE boundaries, i.e., $\partial\Omega_\mu^{s,b+} = \partial\Omega_\mu^{s,b} \bigcap \partial\Omega_\mu^+$ and $\partial\Omega_\mu^{s,b-} = \partial\Omega_\mu^{s,b} \bigcap \partial\Omega_\mu^-$, such that

$$\boldsymbol{N}\left(\boldsymbol{Y}^+\right) = -\boldsymbol{N}\left(\boldsymbol{Y}^-\right), \quad \forall \boldsymbol{Y}^+ \in \partial\Omega_\mu^{s,b+}, \ \forall \boldsymbol{Y}^- \in \partial\Omega_\mu^{s,b-}. \tag{3.35}$$

Therefore, this boundary condition can only be applied to RVEs with voids intersecting the RVE boundary if there is a corresponding void intersection on the opposite side (see Figure 9); otherwise, Equation (3.35) is not verified. In this particular case, the mean normal $\bar{\boldsymbol{N}}$ is null by definition. Consequently, Equation (3.21) is automatically satisfied with the periodic constraint.

Figure 9 – Illustrative representation of periodic porous materials.

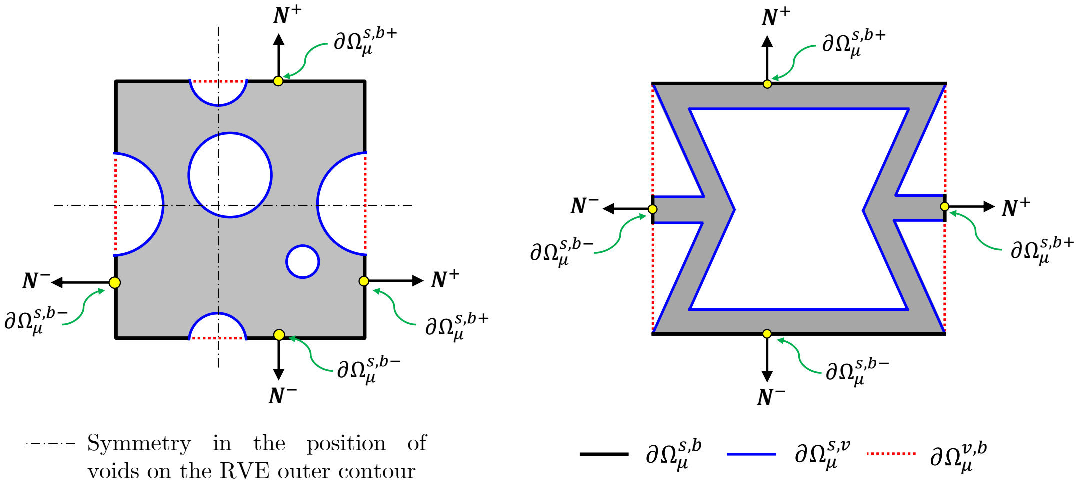

Source: The author.

Remark 6. *An approach to enforcing periodic boundary conditions on RVEs with non-periodic voids on the boundary is proposed by Nguyen et al. (2012). It consists on the definition of a global displacement interpolation on each RVE boundary surface. Nevertheless, this particular subject is out of the scope of the present contribution.*

Assuming RVEs with rectangular or cubic shapes, characterised by a constant normal vector on each surface, the introduction of the periodic condition in Equation (3.28) yields:

$$\int_{\partial\Omega_\mu^{s,b}} \tilde{u}_i \left(N_j Y_k - \bar{\bar{X}}_{jk}\right) dA = \int_{\partial\Omega_\mu^{s,b+,j}} \tilde{u}_i \left[\left(Y_k^+ - Y_k^-\right) - 2\bar{\bar{X}}_{jk}\right] dA = 0, \tag{3.36}$$

for each positive surface j, where index notation is conveniently applied to represent the expression. Moreover, the coordinates of a pair of points Y_k^+ and Y_k^- on a face with normal N_j are equal as long as $j \neq k$, or

$$\left(Y_k^+ - Y_k^-\right)_j = L_k \delta_{jk}, \tag{3.37}$$

where L_k is the undeformed RVE length in the direction k. Thus, since $\bar{\bar{X}}_{jk}$ is also a constant value, Equation (3.36) can be simplified to

$$\int_{\partial\Omega_\mu^{s,b+(j)}} \tilde{u}_i dA = 0. \tag{3.38}$$

After these considerations, the set of micro-scale solutions for the periodic boundary condition is defined by

$$\begin{aligned}\tilde{\mathcal{V}}^{per} = \Bigg\{ & \tilde{\boldsymbol{u}} \text{ sufficiently regular in } \Omega_\mu^s,\ \tilde{\boldsymbol{u}}\left(\boldsymbol{Y}^+\right) = \tilde{\boldsymbol{u}}\left(\boldsymbol{Y}^-\right), \int_{\Omega_\mu^s} \tilde{\boldsymbol{u}} dV = \boldsymbol{0}, \\ & \int_{\partial\Omega_\mu^{s,b+(i)}} \tilde{\boldsymbol{u}} dA = \boldsymbol{0}, \quad \text{for each positive surface } i \Bigg\}.\end{aligned} \tag{3.39}$$

In the case of RVEs without voids in its domain, this constraint is similar to the periodic constraint deduced by Lopes and Pires (2022a) and Luscher (2010).

3.2.2 Direct boundary condition

The direct boundary condition is defined by

$$\tilde{\boldsymbol{u}}\left(\boldsymbol{Y}\right) = \boldsymbol{0}, \quad \forall \boldsymbol{Y} \in \partial\Omega_\mu^{s,b}. \tag{3.40}$$

Consequently, the resulting set of admissible solutions is given by

$$\tilde{\mathcal{V}}^{dir} = \left\{ \tilde{\boldsymbol{u}} \text{ sufficiently regular in } \Omega_\mu^s,\ \tilde{\boldsymbol{u}}\left(\boldsymbol{Y}\right) = \boldsymbol{0},\ \forall \boldsymbol{Y} \in \partial\Omega_\mu^{s,b},\ \int_{\Omega_\mu^s} \tilde{\boldsymbol{u}} dV = \boldsymbol{0} \right\}. \tag{3.41}$$

Note that $\tilde{\mathcal{V}}^{dir} \subset \tilde{\mathcal{V}}^{per} \subset \tilde{\mathcal{V}}$, thus the solutions obtained with direct and periodic boundary conditions respect the minimal kinematic admissible constraint.

Subsection 3.3 presents the *Principle of Multi-scale Virtual Power* for the minimal constraint, containing the micro-scale equilibrium problem and the expressions for the stress homogenisation. Furthermore, the derivations for the periodic and direct constraints are shown in 3.4 and 3.5, respectively.

3.3 Principle of Multi-scale Virtual Power: minimal constraint

The *Principle of Multi-scale Virtual Power*, a generalisation of the well-known Hill-Mandel Principle, is employed to ensure the conservation of the virtual power in the scale transition. A dual formulation based on the Lagrange multiplier method is adopted here since: (i) the Lagrange multipliers are useful to understand the reactive nature of kinematic constraints (Blanco *et al.*, 2016a), (ii) this method has proven to be computationally efficient to enforce micro-scale constraints (Lopes; Ferreira; Pires, 2021), and (iii) the Lagrange multipliers can be directly related to the homogenised stresses. For the minimal constraint defined in Equation (3.33), the *Principle of Multi-Scale Virtual*

Power is expressed by

$$\begin{aligned} \boldsymbol{P} : \delta\boldsymbol{F} + \mathbf{Q} \vdots \delta\mathbf{G} = & \frac{1}{V_\mu}\Bigg[\int_{\Omega_\mu^s} \boldsymbol{P}_\mu : \left(\delta\boldsymbol{F} + \delta\mathbf{G}\cdot\boldsymbol{Y} + \nabla_Y \delta\tilde{\boldsymbol{u}}\right) dV \\ & -\delta\boldsymbol{\lambda}_{\boldsymbol{L}} : \left(\int_{\partial\Omega_\mu^{s,b}} \tilde{\boldsymbol{u}} \otimes \left(\boldsymbol{N} - \bar{\boldsymbol{N}}\right) dA\right) \\ & -\boldsymbol{\lambda}_{\boldsymbol{L}} : \left(\int_{\partial\Omega_\mu^{s,b}} \delta\tilde{\boldsymbol{u}} \otimes \left(\boldsymbol{N} - \bar{\boldsymbol{N}}\right) dA\right) \\ & -\delta\boldsymbol{\lambda}_{\mathbf{M}} \vdots \left(\int_{\partial\Omega_\mu^{s,b}} \tilde{\boldsymbol{u}} \otimes \left(\boldsymbol{N} \otimes \boldsymbol{Y} - \bar{\bar{\boldsymbol{X}}}\right) dA\right) \\ & -\boldsymbol{\lambda}_{\mathbf{M}} \vdots \left(\int_{\partial\Omega_\mu^{s,b}} \delta\tilde{\boldsymbol{u}} \otimes \left(\boldsymbol{N} \otimes \boldsymbol{Y} - \bar{\bar{\boldsymbol{X}}}\right) dA\right) \\ & - \int_{\Omega_\mu^s} \delta\boldsymbol{\lambda}_V \cdot \tilde{\boldsymbol{u}} dV - \int_{\Omega_\mu^s} \boldsymbol{\lambda}_V \cdot \delta\tilde{\boldsymbol{u}} dV \Bigg], \\ & \forall \left(\delta\boldsymbol{F}, \delta\mathbf{G}, \delta\tilde{\boldsymbol{u}}, \delta\boldsymbol{\lambda}_{\boldsymbol{L}}, \delta\boldsymbol{\lambda}_{\mathbf{M}}, \delta\boldsymbol{\lambda}_V\right). \end{aligned} \tag{3.42}$$

The Lagrange multipliers $\boldsymbol{\lambda}_V$, $\boldsymbol{\lambda}_{\boldsymbol{L}}$ and $\boldsymbol{\lambda}_{\mathbf{M}}$ are related to the constraints in Equations (3.18), (3.21) and (3.28), respectively.

3.3.1 Micro-scale equilibrium problem

The weak micro-equilibrium equation is obtained by setting $\delta\boldsymbol{F} = \mathbf{0}$ and $\delta\mathbf{G} = \mathbf{0}$ in Equation (3.42):

$$\begin{aligned} & \int_{\Omega_\mu^s} \boldsymbol{P}_\mu : \nabla_Y \delta\tilde{\boldsymbol{u}} dV \\ & - \delta\boldsymbol{\lambda}_{\boldsymbol{L}} : \left(\int_{\partial\Omega_\mu^{s,b}} \tilde{\boldsymbol{u}} \otimes \left(\boldsymbol{N} - \bar{\boldsymbol{N}}\right) dA\right) - \boldsymbol{\lambda}_{\boldsymbol{L}} : \left(\int_{\partial\Omega_\mu^{s,b}} \delta\tilde{\boldsymbol{u}} \otimes \left(\boldsymbol{N} - \bar{\boldsymbol{N}}\right) dA\right) \\ & - \delta\boldsymbol{\lambda}_{\mathbf{M}} \vdots \left(\int_{\partial\Omega_\mu^{s,b}} \tilde{\boldsymbol{u}} \otimes \left(\boldsymbol{N} \otimes \boldsymbol{Y} - \bar{\bar{\boldsymbol{X}}}\right) dA\right) \\ & - \boldsymbol{\lambda}_{\mathbf{M}} \vdots \left(\int_{\partial\Omega_\mu^{s,b}} \delta\tilde{\boldsymbol{u}} \otimes \left(\boldsymbol{N} \otimes \boldsymbol{Y} - \bar{\bar{\boldsymbol{X}}}\right) dA\right) \\ & - \delta\boldsymbol{\lambda}_V \cdot \int_{\Omega_\mu^s} \tilde{\boldsymbol{u}} dV - \boldsymbol{\lambda}_V \cdot \int_{\Omega_\mu^s} \delta\tilde{\boldsymbol{u}} dV = \mathbf{0} \\ & \forall \left(\delta\tilde{\boldsymbol{u}}, \delta\boldsymbol{\lambda}_{\boldsymbol{L}}, \delta\boldsymbol{\lambda}_{\mathbf{M}}, \delta\boldsymbol{\lambda}_V\right). \end{aligned} \tag{3.43}$$

Integrating by parts the first term of Equation (3.43):

$$\int_{\Omega_\mu^s} \boldsymbol{P}_\mu : \nabla_Y \delta\tilde{\boldsymbol{u}} dV = \int_{\partial\Omega_\mu^s} \boldsymbol{P}_\mu \cdot \boldsymbol{N} \cdot \delta\tilde{\boldsymbol{u}} dA - \int_{\Omega_\mu} \mathrm{div}_Y \left(\boldsymbol{P}_\mu\right) \cdot \delta\tilde{\boldsymbol{u}} dV, \tag{3.44}$$

and with $\partial\Omega_\mu^s = \partial\Omega_\mu^{s,b} \bigcup \partial\Omega_\mu^{s,v}$:

$$\begin{aligned} \int_{\Omega_\mu} \boldsymbol{P}_\mu : \nabla_Y \delta\tilde{\boldsymbol{u}} dV = & \int_{\partial\Omega_\mu^{s,b}} \boldsymbol{P}_\mu \cdot \delta\tilde{\boldsymbol{u}} \cdot \boldsymbol{N} dA + \int_{\partial\Omega_\mu^{s,v}} \boldsymbol{P}_\mu \cdot \delta\tilde{\boldsymbol{u}} \cdot \boldsymbol{N}^s dA \\ & - \int_{\Omega_\mu^s} \mathrm{div}_Y \left(\boldsymbol{P}_\mu\right) \cdot \delta\tilde{\boldsymbol{u}} dV. \end{aligned} \tag{3.45}$$

Substituting Equation (3.45) into Equation (3.43) and reorganising the terms:

$$
\begin{aligned}
&\int_{\partial\Omega_\mu^{s,b}} \left[\boldsymbol{P}_\mu \cdot \boldsymbol{N} - \boldsymbol{\lambda}_{\boldsymbol{L}} \cdot \left(\boldsymbol{N} - \bar{\boldsymbol{N}}\right) - \boldsymbol{\lambda}_{\mathsf{M}} : \left(\boldsymbol{N} \otimes \boldsymbol{Y} - \bar{\bar{\boldsymbol{X}}}\right)\right] \cdot \delta\tilde{\boldsymbol{u}} dA \\
&+ \int_{\partial\Omega_\mu^{s,v}} \left[\boldsymbol{P}_\mu \cdot \boldsymbol{N}^v\right] \cdot \delta\tilde{\boldsymbol{u}} dA - \int_{\Omega_\mu^s} \left(\mathrm{div}_Y\left(\boldsymbol{P}_\mu\right) + \boldsymbol{\lambda}_V\right) \cdot \delta\tilde{\boldsymbol{u}} dV \\
&- \delta\boldsymbol{\lambda}_{\boldsymbol{L}} : \left(\int_{\partial\Omega_\mu^{s,b}} \tilde{\boldsymbol{u}} \otimes \left(\boldsymbol{N} - \bar{\boldsymbol{N}}\right) dA\right) - \delta\boldsymbol{\lambda}_{\mathsf{M}} \vdots \left(\int_{\partial\Omega_\mu^{s,b}} \tilde{\boldsymbol{u}} \otimes \left(\boldsymbol{N} \otimes \boldsymbol{Y} - \bar{\bar{\boldsymbol{X}}}\right) dA\right) \\
&- \delta\boldsymbol{\lambda}_V \cdot \int_{\Omega_\mu^s} \tilde{\boldsymbol{u}} dV = \boldsymbol{0}, \quad \forall\left(\delta\tilde{\boldsymbol{u}}, \delta\boldsymbol{\lambda}_{\boldsymbol{L}}, \delta\boldsymbol{\lambda}_{\mathsf{M}}, \delta\boldsymbol{\lambda}_V\right).
\end{aligned}
\tag{3.46}
$$

By standard variational arguments, the strong equilibrium equations can be defined by:

$$\boldsymbol{P}_\mu \cdot \boldsymbol{N} = \boldsymbol{\lambda}_{\boldsymbol{L}} \cdot \left(\boldsymbol{N} - \bar{\boldsymbol{N}}\right) + \boldsymbol{\lambda}_{\mathsf{M}} : \left(\boldsymbol{N} \otimes \boldsymbol{Y} - \bar{\bar{\boldsymbol{X}}}\right) \text{ on } \partial\Omega_\mu^{s,b}, \tag{3.47}$$

$$\boldsymbol{P}_\mu \cdot \boldsymbol{N}^v = \boldsymbol{0} \quad \text{on} \quad \partial\Omega_\mu^{s,v}, \tag{3.48}$$

$$\mathrm{div}_Y\left(\boldsymbol{P}_\mu\right) = -\boldsymbol{\lambda}_V \quad \text{in} \quad \Omega_\mu^s, \tag{3.49}$$

$$\int_{\partial\Omega_\mu^{s,b}} \tilde{\boldsymbol{u}} \otimes \left(\boldsymbol{N} - \bar{\boldsymbol{N}}\right) dA = \boldsymbol{0}, \tag{3.50}$$

$$\int_{\partial\Omega_\mu^{s,b}} \tilde{\boldsymbol{u}} \otimes \left(\boldsymbol{N} \otimes \boldsymbol{Y} - \bar{\bar{\boldsymbol{X}}}\right) dA = \boldsymbol{0}, \tag{3.51}$$

$$\int_{\Omega_\mu^s} \tilde{\boldsymbol{u}} dV = \boldsymbol{0}. \tag{3.52}$$

3.3.2 First Piola-Kirchhoff stress homogenisation

The homogenised first Piola-Kirchhoff stress is obtained from the *Principle of Multi-scale Virtual Power* by setting $\delta\boldsymbol{\lambda}_{\boldsymbol{L}} = \boldsymbol{0}$, $\delta\boldsymbol{\lambda}_{\mathsf{M}} = \boldsymbol{0}$, $\delta\boldsymbol{\lambda}_V = \boldsymbol{0}$, $\delta\mathbf{G} = \boldsymbol{0}$ and $\delta\tilde{\boldsymbol{u}} = \boldsymbol{0}$ in Equation (3.42), resulting in

$$\boldsymbol{P} = \frac{1}{V_\mu} \int_{\Omega_\mu^s} \boldsymbol{P}_\mu dV. \tag{3.53}$$

The above expression is also found in first-order homogenisation and may be rewritten as:

$$\boldsymbol{P} = \frac{1}{V_\mu} \left[\int_{\partial\Omega_\mu^s} \boldsymbol{P}_\mu \cdot \boldsymbol{N} \otimes \boldsymbol{Y} dA - \int_{\Omega_\mu^s} \mathrm{div}_Y\left(\boldsymbol{P}_\mu\right) \otimes \boldsymbol{Y} dV\right]. \tag{3.54}$$

Considering $\partial\Omega_\mu^s = \partial\Omega_\mu^{s,b} \bigcup \partial\Omega_\mu^{s,v}$:

$$\boldsymbol{P} = \frac{1}{V_\mu} \left[\int_{\partial\Omega_\mu^{s,b}} \boldsymbol{P}_\mu \cdot \boldsymbol{N} \otimes \boldsymbol{Y} dA + \int_{\partial\Omega_\mu^{s,v}} \boldsymbol{P}_\mu \cdot \boldsymbol{N}^v \otimes \boldsymbol{Y} dA - \int_{\Omega_\mu^s} \mathrm{div}_Y\left(\boldsymbol{P}_\mu\right) \otimes \boldsymbol{Y} dV\right]. \tag{3.55}$$

Given the strong form of the micro-problem (Equations (3.47), (3.48) and (3.49)) for each integral of Equation (3.55), it is possible to rewrite as:

$$\boldsymbol{P} = \frac{1}{V_\mu}\left[\int_{\partial\Omega_\mu^{s,b}} \boldsymbol{\lambda}_{\boldsymbol{L}} \cdot \left(\boldsymbol{N} - \bar{\boldsymbol{N}}\right) \otimes \boldsymbol{Y} dA + \int_{\partial\Omega_\mu^{s,b}} \boldsymbol{\lambda}_{\mathbf{M}} : \left(\boldsymbol{N} \otimes \boldsymbol{Y} - \bar{\boldsymbol{X}}\right) \otimes \boldsymbol{Y} dA\right]. \tag{3.56}$$

Therefore, the homogenised First Piola-Kirchhoff stress can be determined from boundary integrals, including the Lagrange multipliers. This conclusion is interesting for the determination of the consistent macroscopic tangents in the context of a coupled multi-scale simulation by a simple and efficient numerical approach based on the concept of homogenisation matrices, which remain constant throughout the simulation.

3.3.3 Higher-order stress homogenisation

The homogenised higher-order stress tensor $\mathbf{Q}$ is determined by setting $\delta\boldsymbol{\lambda}_{\boldsymbol{L}} = \mathbf{0}$, $\delta\boldsymbol{\lambda}_{\mathbf{M}} = \mathbf{0}$, $\delta\boldsymbol{\lambda}_V = \mathbf{0}$, $\delta\boldsymbol{F} = \mathbf{0}$ and $\delta\tilde{\boldsymbol{u}} = \mathbf{0}$ in Equation (3.42):

$$\mathbf{Q} = \frac{1}{V_\mu}\int_{\Omega_\mu^s} \left(\boldsymbol{P}_\mu \otimes \boldsymbol{Y}\right)^S dV. \tag{3.57}$$

where the right symmetry of $\mathbf{G}$, only the symmetric part of the right-hand side of the above expression contributes to the higher-order stress tensor (Luscher, 2010; Blanco *et al.*, 2016a), is accounted for.

As demonstrated by Blanco *et al.* (2016b), this expression may be rewritten as:

$$\mathbf{Q} = \frac{1}{2V_\mu}\left[\int_{\partial\Omega_\mu^s} \boldsymbol{P}_\mu \cdot \boldsymbol{N} \otimes \boldsymbol{Y} \otimes \boldsymbol{Y} dA - \int_{\Omega_\mu^s} \mathrm{div}_Y\left(\boldsymbol{P}_\mu\right) \otimes \boldsymbol{Y} \otimes \boldsymbol{Y} dV\right], \tag{3.58}$$

and with $\partial\Omega_\mu^s = \partial\Omega_\mu^{s,b} \bigcup \partial\Omega_\mu^{s,v}$:

$$\begin{aligned}\mathbf{Q} = \frac{1}{2V_\mu}\Bigg[&\int_{\partial\Omega_\mu^{s,b}} \boldsymbol{P}_\mu \cdot \boldsymbol{N} \otimes \boldsymbol{Y} \otimes \boldsymbol{Y} dA + \int_{\partial\Omega_\mu^{s,v}} \boldsymbol{P}_\mu \cdot \boldsymbol{N}^v \otimes \boldsymbol{Y} \otimes \boldsymbol{Y} dA \\ &- \int_{\Omega_\mu^s} \mathrm{div}_Y\left(\boldsymbol{P}_\mu\right) \otimes \boldsymbol{Y} \otimes \boldsymbol{Y} dV\Bigg].\end{aligned} \tag{3.59}$$

Given the strong form of the micro-problem (Equations (3.47), (3.48) and (3.49)) for each integral of Equation (3.59), it can be expressed by:

$$\begin{aligned}\mathbf{Q} =&\frac{1}{2V_\mu}\left[\int_{\partial\Omega_\mu^{s,b}} \boldsymbol{\lambda}_{\boldsymbol{L}} \cdot \left(\boldsymbol{N} - \bar{\boldsymbol{N}}\right) \otimes \boldsymbol{Y} \otimes \boldsymbol{Y} dA + \int_{\partial\Omega_\mu^{s,b}} \boldsymbol{\lambda}_{\mathbf{M}} : \left(\boldsymbol{N} \otimes \boldsymbol{Y} - \bar{\boldsymbol{X}}\right) \otimes \boldsymbol{Y} \otimes \boldsymbol{Y} dA\right] \\ &+\frac{1}{2}\frac{V_\mu^s}{V_\mu}\boldsymbol{\lambda}_V \otimes \boldsymbol{J},\end{aligned} \tag{3.60}$$

where the homogenised higher-order stress tensor is determined from boundary integrals and an additional constant term, both encompassing the Lagrange multipliers. Thus, a simple and efficient numerical approach can also be explored to compute the consistent macroscopic tangents in the context of a multi-scale coupled analysis.

3.4 Principle of Multi-scale Virtual Power: periodic constraint

In the case of the periodic boundary condition, the *Principle of Multi-scale Virtual Power* is expressed by:

$$
\begin{aligned}
\boldsymbol{P} : \delta \boldsymbol{F} + \mathbf{Q} \vdots \delta \mathbf{G} = \frac{1}{V_\mu} \Bigg[& \int_{\Omega_\mu^s} \boldsymbol{P}_\mu : \left(\delta \boldsymbol{F} + \delta \mathbf{G} \cdot \boldsymbol{Y} + \nabla_Y \delta \tilde{\boldsymbol{u}} \right) dV \\
& - \int_{\partial \Omega_\mu^{s,b+}} \delta \boldsymbol{\lambda}_P \cdot \left(\tilde{\boldsymbol{u}}^+ - \tilde{\boldsymbol{u}}^- \right) dA \\
& - \int_{\partial \Omega_\mu^{s,b+}} \boldsymbol{\lambda}_P \cdot \left(\delta \tilde{\boldsymbol{u}}^+ - \delta \tilde{\boldsymbol{u}}^- \right) dA \\
& - \int_{\Omega_\mu^s} \delta \boldsymbol{\lambda}_V \cdot \tilde{\boldsymbol{u}} dV - \int_{\Omega_\mu^s} \boldsymbol{\lambda}_V \cdot \delta \tilde{\boldsymbol{u}} dV \\
& - \sum_{i=1}^{n_{i+}} \left(\delta \boldsymbol{\lambda}_{S_i} \cdot \int_{\partial \Omega_\mu^{s,b+(i)}} \tilde{\boldsymbol{u}} dA + \boldsymbol{\lambda}_{S_i} \cdot \int_{\partial \Omega_\mu^{s,b+(i)}} \delta \tilde{\boldsymbol{u}} dA \right) \Bigg], \\
& \forall \left(\delta \boldsymbol{F}, \delta \mathbf{G}, \delta \tilde{\boldsymbol{u}}, \delta \boldsymbol{\lambda}_P, \delta \boldsymbol{\lambda}_V, \boldsymbol{\lambda}_{S_i} \right),
\end{aligned}
\tag{3.61}
$$

where the Lagrange multipliers $\boldsymbol{\lambda}_P$, $\boldsymbol{\lambda}_{S_i}$ and $\boldsymbol{\lambda}_V$ are used to enforce the boundary and volumetric constraints presented in Equation (3.39).

3.4.1 Micro-scale equilibrium problem

The weak micro-equilibrium equation is defined as a consequence of the *Principle of Multi-scale Virtual Power*, by setting $\delta \boldsymbol{F} = \mathbf{0}$ and $\delta \mathbf{G} = \mathbf{0}$ in Equation (3.61). This results in

$$
\begin{aligned}
& \int_{\Omega_\mu^s} \boldsymbol{P}_\mu : \nabla_Y \delta \tilde{\boldsymbol{u}} dV \\
& - \int_{\partial \Omega_\mu^{s,b+}} \delta \boldsymbol{\lambda}_P \cdot \left(\tilde{\boldsymbol{u}}^+ - \tilde{\boldsymbol{u}}^- \right) dA - \int_{\partial \Omega_\mu^{s,b+}} \boldsymbol{\lambda}_P \cdot \left(\delta \tilde{\boldsymbol{u}}^+ - \delta \tilde{\boldsymbol{u}}^- \right) dA \\
& - \int_{\Omega_\mu^s} \delta \boldsymbol{\lambda}_V \cdot \tilde{\boldsymbol{u}} dV - \int_{\Omega_\mu^s} \boldsymbol{\lambda}_V \cdot \delta \tilde{\boldsymbol{u}} dV \\
& - \sum_{i=1}^{n_{i+}} \left(\delta \boldsymbol{\lambda}_{S_i} \cdot \int_{\partial \Omega_\mu^{s,b+(i)}} \tilde{\boldsymbol{u}} dA + \boldsymbol{\lambda}_{S_i} \cdot \int_{\partial \Omega_\mu^{s,b+(i)}} \delta \tilde{\boldsymbol{u}} dA \right) = \mathbf{0}, \\
& \forall \left(\delta \tilde{\boldsymbol{u}}, \delta \boldsymbol{\lambda}_P, \delta \boldsymbol{\lambda}_V, \delta \boldsymbol{\lambda}_{S_i} \right).
\end{aligned}
\tag{3.62}
$$

Following an approach similar to the one employed for the minimal constraint, the strong equilibrium equations are obtained and expressed by:

$$\begin{aligned}
\boldsymbol{P}_\mu \cdot \boldsymbol{N} &= \boldsymbol{\lambda}_P + \boldsymbol{\lambda}_{S_i} \quad \text{on each positive RVE face } \partial\Omega_\mu^{s,b+(i)}, && (3.63)\\
\boldsymbol{P}_\mu \cdot \boldsymbol{N} &= -\boldsymbol{\lambda}_P \quad \text{on} \quad \partial\Omega_\mu^{s,b-}, && (3.64)\\
\boldsymbol{P}_\mu \cdot \boldsymbol{N}^v &= \boldsymbol{0} \quad \text{on} \quad \partial\Omega_\mu^{s,v}, && (3.65)\\
\operatorname{div}_Y \left(\boldsymbol{P}_\mu\right) &= -\boldsymbol{\lambda}_V \quad \text{in} \quad \Omega_\mu^s, && (3.66)\\
\int_{\partial\Omega_\mu^{s,b+}} \left(\tilde{\boldsymbol{u}}^+ - \tilde{\boldsymbol{u}}^-\right) dA &= \boldsymbol{0}, && (3.67)\\
\int_{\Omega_\mu^s} \tilde{\boldsymbol{u}} dV &= \boldsymbol{0}, && (3.68)\\
\sum_{i=1}^{n_{i+}} \int_{\partial\Omega_\mu^{s,b+(i)}} \tilde{\boldsymbol{u}} dA &= \boldsymbol{0}, \quad \text{on each positive RVE face } \partial\Omega_\mu^{s,b+(i)}. && (3.69)
\end{aligned}$$

3.4.2 First Piola-Kirchhoff stress homogenisation

The expression for the homogenised Piola-Kirchhoff stress tensor is obtained from the *Principle of Multi-Scale Virtual Power* by defining $\delta\mathbf{G} = \mathbf{0}$, $\delta\boldsymbol{\lambda}_P = \mathbf{0}$, $\delta\boldsymbol{\lambda}_V = \mathbf{0}$, $\delta\boldsymbol{\lambda}_{S_i} = \mathbf{0}$ and $\delta\tilde{\boldsymbol{u}} = \mathbf{0}$ in Equation (3.61), which yields Equation (3.55). Given the strong form of the micro-problem, the homogenised $\boldsymbol{P}$ can be expressed in terms of boundary integrals of the Lagrange multipliers as:

$$\begin{aligned}
\boldsymbol{P} &= \frac{1}{V_\mu}\left[\sum_{i=1}^{n_{i+}}\left(\int_{\partial\Omega_\mu^{s,b+(i)}} (\boldsymbol{\lambda}_P + \boldsymbol{\lambda}_{S_i}) \otimes \boldsymbol{Y} dA\right) - \int_{\partial\Omega_\mu^{s,b-}} \boldsymbol{\lambda}_P \otimes \boldsymbol{Y} dA\right]\\
&= \frac{1}{V_\mu}\left[\sum_{i=1}^{n_{i+}} \boldsymbol{\lambda}_{S_i} \otimes \left(\int_{\partial\Omega_\mu^{s,b+(i)}} \boldsymbol{Y} dA\right) + \int_{\partial\Omega_\mu^{s,b+}} \boldsymbol{\lambda}_P \otimes \left(\boldsymbol{Y}^+ - \boldsymbol{Y}^-\right) dA\right].
\end{aligned} \tag{3.70}$$

Moreover, similarly to the minimal boundary condition, $\boldsymbol{P}$ can also be determined from boundary integrals, including the Lagrange multipliers.

3.4.3 Higher-order stress homogenisation

The homogenised higher-order stress tensor $\mathbf{Q}$ is determined by setting $\delta\boldsymbol{F} = \mathbf{0}$, $\delta\boldsymbol{\lambda}_P = \mathbf{0}$, $\delta\boldsymbol{\lambda}_V = \mathbf{0}$, $\delta\boldsymbol{\lambda}_{S_i} = \mathbf{0}$ and $\delta\tilde{\boldsymbol{u}} = \mathbf{0}$ in Equation (3.61), leading to Equation (3.59). Considering the strong equilibrium equations, the homogenised $\mathbf{Q}$ can also be expressed in terms of boundary integrals of the Lagrange multipliers by:

$$\begin{aligned}
\mathbf{Q} = \frac{1}{2V_\mu}&\left[\sum_{i=1}^{n_{i+}} \boldsymbol{\lambda}_{S_i} \otimes \left(\int_{\partial\Omega_\mu^{s,b+(i)}} \boldsymbol{Y} \otimes \boldsymbol{Y} dA\right)\right.\\
&\left. + \int_{\partial\Omega_\mu^{s,b+}} \boldsymbol{\lambda}_P \otimes \left(\boldsymbol{Y}^+ \otimes \boldsymbol{Y}^+ - \boldsymbol{Y}^- \otimes \boldsymbol{Y}^-\right) dA\right] + \frac{1}{2}\boldsymbol{\lambda}_V \otimes \boldsymbol{J}\frac{V_\mu^s}{V_\mu}.
\end{aligned} \tag{3.71}$$

Analogously to the minimal boundary condition, $\mathbf{Q}$ can be determined from boundary integrals and an additional constant term, both considering the Lagrange multipliers.

3.5 Principle of Multi-scale Virtual Power: direct constraint

For the direct boundary condition, the *Principle of Multi-scale Virtual Power* is expressed by:

$$\begin{aligned}\boldsymbol{P} : \delta\boldsymbol{F} + \boldsymbol{\mathsf{Q}}\,\vdots\,\delta\boldsymbol{\mathsf{G}} = \frac{1}{V_\mu}\Bigg[&\int_{\Omega^s_\mu} \boldsymbol{P}_\mu : \left(\delta\boldsymbol{F} + \delta\boldsymbol{\mathsf{G}}\cdot\boldsymbol{Y} + \nabla_Y\delta\tilde{\boldsymbol{u}}\right) dV \\ &- \int_{\partial\Omega^{s,b}_\mu} \delta\boldsymbol{\lambda}_D\cdot\tilde{\boldsymbol{u}}dA - \int_{\partial\Omega^{s,b}_\mu} \boldsymbol{\lambda}_D\cdot\delta\tilde{\boldsymbol{u}}dA \\ &- \int_{\Omega^s_\mu} \delta\boldsymbol{\lambda}_V\cdot\tilde{\boldsymbol{u}}dV - \int_{\Omega^s_\mu} \boldsymbol{\lambda}_V\cdot\delta\tilde{\boldsymbol{u}}dV\Bigg], \\ &\forall\left(\delta\boldsymbol{F}, \delta\boldsymbol{\mathsf{G}}, \delta\tilde{\boldsymbol{u}}, \delta\boldsymbol{\lambda}_D, \delta\boldsymbol{\lambda}_V\right),\end{aligned} \tag{3.72}$$

where the Lagrange multipliers $\boldsymbol{\lambda}_D$ and $\boldsymbol{\lambda}_V$ are used to enforce the constraints shown in Equation (3.41).

3.5.1 Micro-scale equilibrium problem

The weak micro-equilibrium equation is defined as a consequence of the *Principle of Multi-scale Virtual Power*, by setting $\delta\boldsymbol{F} = \boldsymbol{0}$ and $\delta\boldsymbol{\mathsf{G}} = \boldsymbol{0}$ in Equation (3.72). This results in

$$\begin{aligned}&\int_{\Omega^s_\mu} \boldsymbol{P}_\mu : \nabla_Y\delta\tilde{\boldsymbol{u}}dV - \int_{\partial\Omega^{s,b}_\mu} \delta\boldsymbol{\lambda}_D\cdot\tilde{\boldsymbol{u}}dA - \int_{\partial\Omega^{s,b}_\mu} \boldsymbol{\lambda}_D\cdot\delta\tilde{\boldsymbol{u}}dA \\ &- \int_{\Omega^s_\mu} \delta\boldsymbol{\lambda}_V\cdot\tilde{\boldsymbol{u}}dV - \int_{\Omega^s_\mu} \boldsymbol{\lambda}_V\cdot\delta\tilde{\boldsymbol{u}}dV = 0, \quad \forall\left(\delta\tilde{\boldsymbol{u}}, \delta\boldsymbol{\lambda}_D, \boldsymbol{\lambda}_V\right).\end{aligned} \tag{3.73}$$

The corresponding strong equilibrium equations are defined by:

$$\boldsymbol{P}_\mu\cdot\boldsymbol{N} = \boldsymbol{\lambda}_D \quad \text{on} \quad \partial\Omega^{s,b}_\mu, \tag{3.74}$$

$$\boldsymbol{P}_\mu\cdot\boldsymbol{N}^v = \boldsymbol{0} \quad \text{on} \quad \partial\Omega^{s,v}_\mu, \tag{3.75}$$

$$\operatorname{div}_Y\left(\boldsymbol{P}_\mu\right) = -\boldsymbol{\lambda}_V \quad \text{in} \quad \Omega^s_\mu, \tag{3.76}$$

$$\int_{\partial\Omega^{s,b}_\mu} \tilde{\boldsymbol{u}}dA = \boldsymbol{0}, \tag{3.77}$$

$$\int_{\Omega^s_\mu} \tilde{\boldsymbol{u}}dV = \boldsymbol{0}. \tag{3.78}$$

3.5.2 First Piola-Kirchhoff stress homogenisation

The expression for the homogenised first Piola-Kirchhoff stress tensor $(\boldsymbol{P})$ is obtained from the *Principle of Multi-Scale Virtual Power* by defining $\delta\boldsymbol{\mathsf{G}} = \boldsymbol{0}$, $\delta\boldsymbol{\lambda}_D = \boldsymbol{0}$,

$\delta\boldsymbol{\lambda}_V = \mathbf{0}$ and $\delta\tilde{\boldsymbol{u}} = \mathbf{0}$ in Equation (3.72), leading to Equation (3.55). Given the strong equilibrium equations, $\boldsymbol{P}$ can be rewritten in terms of a boundary integral of $\boldsymbol{\lambda}_D$ as:

$$\boldsymbol{P} = \frac{1}{V_\mu} \int_{\partial\Omega_\mu^{s,b}} \boldsymbol{\lambda}_D \otimes \boldsymbol{Y} dA. \tag{3.79}$$

Note that $\boldsymbol{P}$ can be determined from a boundary integral, including the respective Lagrange multiplier.

3.5.3 Higher-order stress homogenisation

The homogenised higher-order stress tensor ($\mathbf{Q}$) is determined by setting $\delta\boldsymbol{F} = \mathbf{0}$, $\delta\boldsymbol{\lambda}_D = \mathbf{0}$, $\delta\boldsymbol{\lambda}_V = \mathbf{0}$ and $\delta\tilde{\boldsymbol{u}} = \mathbf{0}$ in Equation (3.72), which leads to Equation (3.59). Considering the strong equilibrium equations, it can be expressed by:

$$\mathbf{Q} = \frac{1}{2V_\mu} \int_{\partial\Omega_\mu^{s,b}} \boldsymbol{\lambda}_D \otimes \boldsymbol{Y} \otimes \boldsymbol{Y} dA + \frac{1}{2}\frac{V_\mu^s}{V_\mu} \boldsymbol{\lambda}_V \otimes \boldsymbol{J}, \tag{3.80}$$

where only a boundary integral and an additional constant term, including the Lagrange multipliers, are needed. Moreover, $\mathbf{Q}$ can be determined from a boundary integral and an additional constant term, encompassing the respective Lagrange multipliers.

4 FINITE ELEMENT SOLUTION OF THE DISCRETE MICRO-SCALE EQUILIBRIUM PROBLEM

In this section, the finite element solution of the discrete micro-scale equilibrium problem is described for the minimal, periodic and direct models. The Newton–Raphson scheme is employed for the iterative solution of the corresponding non-linear systems of equations. In addition, implementation aspects related to the micro-constraints enforcement and the stress homogenisation are clarified. The numerical implementations written in Fortran 90 are carried out in an in-house finite element program named Large Strain Implicit Non-Linear Analysis of Solids Linking Scales (Links). Moreover, Links has been developed by the research group named Computational Multi-Scale Modelling of Solids (CM2S). The discrete formulation follows the recent publication developed by Santos *et al.* (2023).

4.1 Initial considerations

The displacements ($\boldsymbol{u}$) and coordinates ($\boldsymbol{Y}$) are approximated through their nodal values and interpolated with the corresponding shape functions ($\mathbf{H}$):

$$\boldsymbol{u} = \mathbf{H}\mathbf{u} \Rightarrow u_i = H_k \mathrm{u}_{ik}. \tag{4.1}$$

$$\boldsymbol{Y} = \mathbf{H}\mathbf{Y} \Rightarrow Y_i = H_k \mathrm{Y}_{ik}. \tag{4.2}$$

where $\mathbf{Y}$ and $\mathbf{u}$ indicate the nodal coordinates and the nodal displacements, respectively.

Analogously, displacement fluctuations can be approximated by:

$$\tilde{\boldsymbol{u}} = \mathbf{H}\tilde{\mathbf{u}} \Rightarrow \tilde{u}_i = H_k \tilde{\mathrm{u}}_{ik}. \tag{4.3}$$

The nodal displacement fluctuation vector $\tilde{\mathbf{u}}$ can be conveniently splitting according to the position of the nodes,

$$\tilde{\mathbf{u}} = \begin{Bmatrix} \tilde{\mathbf{u}}_i \\ \tilde{\mathbf{u}}_b \end{Bmatrix} \tag{4.4}$$

with $\tilde{\mathbf{u}}_i$ denoting the degrees of freedom of nodes in the interior of the RVE and $\tilde{\mathbf{u}}_b$ representing the outer surface degrees of freedom. In particular, split the nodes is interesting for the implementation of boundary integrals.

The first Piola-Kirchhoff tensor ($\boldsymbol{P}$) is the conjugate of the deformation gradient ($\boldsymbol{F}$). In turn, the higher-order stress tensor (Q) corresponds to the conjugate of the second-order deformation gradient tensor (G). Moreover, $\boldsymbol{F}$ and $\boldsymbol{P}$ are second-order tensors, while G and Q are third-order tensors. Regarding the implementation of the computational strategy, such tensors are stored in vector format. In this context, for two-dimensional problems:

$$\mathbf{F} = \left\{\begin{matrix} F_{11} \\ F_{21} \\ F_{12} \\ F_{22} \end{matrix}\right\}, \quad \mathbf{G} = \left\{\begin{matrix} \mathsf{G}_{111} \\ \mathsf{G}_{211} \\ \mathsf{G}_{121} \\ \mathsf{G}_{221} \\ \mathsf{G}_{112} \\ \mathsf{G}_{212} \\ \mathsf{G}_{122} \\ \mathsf{G}_{222} \end{matrix}\right\}, \quad \mathbf{P} = \left\{\begin{matrix} P_{11} \\ P_{21} \\ P_{12} \\ P_{22} \end{matrix}\right\}, \quad \mathbf{Q} = \left\{\begin{matrix} \mathsf{Q}_{111} \\ \mathsf{Q}_{211} \\ \mathsf{Q}_{121} \\ \mathsf{Q}_{221} \\ \mathsf{Q}_{112} \\ \mathsf{Q}_{212} \\ \mathsf{Q}_{122} \\ \mathsf{Q}_{222} \end{matrix}\right\}, \tag{4.5}$$

and for three-dimensional problems:

$$\mathbf{F} = \left\{\begin{matrix} F_{11} \\ F_{21} \\ F_{31} \\ F_{12} \\ F_{22} \\ F_{32} \\ F_{13} \\ F_{23} \\ F_{33} \end{matrix}\right\}, \quad \mathbf{G} = \left\{\begin{matrix} \mathsf{G}_{111} \\ \mathsf{G}_{211} \\ \mathsf{G}_{311} \\ \mathsf{G}_{121} \\ \mathsf{G}_{221} \\ \mathsf{G}_{321} \\ \mathsf{G}_{131} \\ \mathsf{G}_{231} \\ \mathsf{G}_{331} \\ \mathsf{G}_{112} \\ \mathsf{G}_{212} \\ \mathsf{G}_{312} \\ \mathsf{G}_{122} \\ \mathsf{G}_{222} \\ \mathsf{G}_{322} \\ \mathsf{G}_{132} \\ \mathsf{G}_{232} \\ \mathsf{G}_{332} \\ \mathsf{G}_{113} \\ \mathsf{G}_{213} \\ \mathsf{G}_{313} \\ \mathsf{G}_{123} \\ \mathsf{G}_{223} \\ \mathsf{G}_{323} \\ \mathsf{G}_{133} \\ \mathsf{G}_{233} \\ \mathsf{G}_{333} \end{matrix}\right\}, \quad \mathbf{P} = \left\{\begin{matrix} P_{11} \\ P_{21} \\ P_{31} \\ P_{12} \\ P_{22} \\ P_{32} \\ P_{13} \\ P_{23} \\ P_{33} \end{matrix}\right\}, \quad \mathbf{Q} = \left\{\begin{matrix} \mathsf{Q}_{111} \\ \mathsf{Q}_{211} \\ \mathsf{Q}_{311} \\ \mathsf{Q}_{121} \\ \mathsf{Q}_{221} \\ \mathsf{Q}_{321} \\ \mathsf{Q}_{131} \\ \mathsf{Q}_{231} \\ \mathsf{Q}_{331} \\ \mathsf{Q}_{112} \\ \mathsf{Q}_{212} \\ \mathsf{Q}_{312} \\ \mathsf{Q}_{122} \\ \mathsf{Q}_{222} \\ \mathsf{Q}_{322} \\ \mathsf{Q}_{132} \\ \mathsf{Q}_{232} \\ \mathsf{Q}_{332} \\ \mathsf{Q}_{113} \\ \mathsf{Q}_{213} \\ \mathsf{Q}_{313} \\ \mathsf{Q}_{123} \\ \mathsf{Q}_{223} \\ \mathsf{Q}_{323} \\ \mathsf{Q}_{133} \\ \mathsf{Q}_{233} \\ \mathsf{Q}_{333} \end{matrix}\right\}. \tag{4.6}$$

Furthermore, all Lagrange multipliers employed to enforce the micro-scale kinematic constraints are also stored in vector format.

The following matrices and vectors are presented only for three-dimensional problems, since two-dimensional problems are a particular case. For instance, the second-order moment of the volume tensor ($\boldsymbol{J}$) is given by

$$\boldsymbol{J} = \frac{1}{V_\mu^s} \begin{bmatrix} \int_{\Omega_\mu^s} Y_1 Y_1 dV & \int_{\Omega_\mu^s} Y_1 Y_2 dV & \int_{\Omega_\mu^s} Y_1 Y_3 dV \\ \int_{\Omega_\mu^s} Y_2 Y_1 dV & \int_{\Omega_\mu^s} Y_2 Y_2 dV & \int_{\Omega_\mu^s} Y_2 Y_3 dV \\ \int_{\Omega_\mu^s} Y_3 Y_1 dV & \int_{\Omega_\mu^s} Y_3 Y_2 dV & \int_{\Omega_\mu^s} Y_3 Y_3 dV \end{bmatrix}, \tag{4.7}$$

where k indicates the contribution of each node.

We conveniently assumed that the origin of the micro-coordinate system is located at the centroid of the solid part of the RVE. The expression for calculating the geometric centre of the RVE ($\boldsymbol{Y}_{CG}$) is given by

$$\boldsymbol{Y}_{CG} = \frac{1}{V_\mu^s} \begin{Bmatrix} \int_{\Omega_\mu^s} Y_1 dV \\ \int_{\Omega_\mu^s} Y_2 dV \\ \int_{\Omega_\mu^s} Y_3 dV \end{Bmatrix}. \tag{4.8}$$

Note that for the case of the coordinate centre located in the geometric centre of the RVE:

$$\int_{\Omega_\mu^s} \boldsymbol{Y} dV = \begin{Bmatrix} \int_{\Omega_\mu^s} Y_1 dV \\ \int_{\Omega_\mu^s} Y_2 dV \\ \int_{\Omega_\mu^s} Y_3 dV \end{Bmatrix} = \begin{Bmatrix} 0 \\ 0 \\ 0 \end{Bmatrix}. \tag{4.9}$$

Furthermore, the mean normal (see Equation (3.13)) is given by

$$\bar{\boldsymbol{N}} = \frac{1}{A_\mu^{s,b}} \begin{Bmatrix} \int_{\partial\Omega_\mu^{s,b}} N_1 dA \\ \int_{\partial\Omega_\mu^{s,b}} N_2 dA \\ \int_{\partial\Omega_\mu^{s,b}} N_3 dA \end{Bmatrix}, \tag{4.10}$$

while $\bar{\bar{\boldsymbol{X}}}$ (see Equation 3.16) is given by

$$\bar{\bar{\boldsymbol{X}}} = \frac{1}{A_\mu^{s,b}} \begin{bmatrix} \int_{\partial\Omega_\mu^{s,b}} N_1 Y_1 dA & \int_{\partial\Omega_\mu^{s,b}} N_1 Y_2 dA & \int_{\partial\Omega_\mu^{s,b}} N_1 Y_3 dA \\ \int_{\partial\Omega_\mu^{s,b}} N_2 Y_1 dA & \int_{\partial\Omega_\mu^{s,b}} N_2 Y_2 dA & \int_{\partial\Omega_\mu^{s,b}} N_2 Y_3 dA \\ \int_{\partial\Omega_\mu^{s,b}} N_3 Y_1 dA & \int_{\partial\Omega_\mu^{s,b}} N_3 Y_2 dA & \int_{\partial\Omega_\mu^{s,b}} N_3 Y_3 dA \end{bmatrix} - \frac{1}{A_\mu^{s,b}} \boldsymbol{I} V^s. \tag{4.11}$$

In what follows, the description of the discrete micro-scale equilibrium problem is presented in detail for the minimal, periodic and direct constraints.

4.2 Discrete micro-scale equilibrium problem for minimal constraint

4.2.1 Finite element solution of the micro-scale problem

The finite element solution of the discrete equilibrium problem for the minimal constraint is described as follows. The finite element discretisation of Equation (3.43), case of the minimally constrained model, results in

$$\begin{aligned}
&\delta\tilde{\mathbf{u}}^T \int_{\Omega_\mu^s} \left(\mathbf{G}^u\right)^T \mathbf{P}_\mu dV + \delta\boldsymbol{\lambda}_L^T \mathbf{C}_L \tilde{\mathbf{u}}_b + \delta\tilde{\mathbf{u}}^T \mathbf{C}_L^T \boldsymbol{\lambda}_L + \delta\boldsymbol{\lambda}_M^T \mathbf{C}_M \tilde{\mathbf{u}} + \delta\tilde{\mathbf{u}}^T \mathbf{C}_M^T \boldsymbol{\lambda}_M \\
&+ \delta\boldsymbol{\lambda}_V^T \mathbf{C}_V \tilde{\mathbf{u}} + \delta\tilde{\mathbf{u}}^T \mathbf{C}_V^T \boldsymbol{\lambda}_V = 0, \quad \forall \left(\delta\tilde{\mathbf{u}}, \delta\boldsymbol{\lambda}_L, \delta\boldsymbol{\lambda}_M, \delta\boldsymbol{\lambda}_V\right),
\end{aligned} \tag{4.12}$$

where $\mathbf{G}^u$ represents the discrete gradient operator with the derivatives of the shape functions, $\mathbf{P}_\mu$ is the micro-scale Piola-Kirchhoff stress tensor, $\tilde{\mathbf{u}}$ is the nodal displacement fluctuations vector, $\boldsymbol{\lambda}_L$, $\boldsymbol{\lambda}_M$ and $\boldsymbol{\lambda}_V$ indicate the Lagrange multipliers, and $\mathbf{C}_L$, $\mathbf{C}_M$ and $\mathbf{C}_V$ are the corresponding constraint matrices.

Since Equation (4.12) must hold for any $\delta\tilde{\mathbf{u}}$ or $\delta\mathbf{L}$ or $\delta\mathbf{M}$, the following set of discrete equations must be solved

$$\int_{\Omega_\mu^s} \left(\mathbf{G}_i^u\right)^T \mathbf{P}_\mu dV + \mathbf{C}_{V,i}^T \boldsymbol{\lambda}_V = \mathbf{0} \tag{4.13}$$

$$\int_{\Omega_\mu^s} \left(\mathbf{G}_b^u\right)^T \mathbf{P}_\mu dV + \mathbf{C}_L^T \boldsymbol{\lambda}_L + \mathbf{C}_M^T \boldsymbol{\lambda}_M + \mathbf{C}_{V,b}^T \boldsymbol{\lambda}_V = \mathbf{0} \tag{4.14}$$

$$\mathbf{C}_L \tilde{\mathbf{u}}_b = \mathbf{0} \tag{4.15}$$

$$\mathbf{C}_M \tilde{\mathbf{u}}_b = \mathbf{0} \tag{4.16}$$

$$\mathbf{C}_{V,i} \tilde{\mathbf{u}}_i + \mathbf{C}_{V,b} \tilde{\mathbf{u}}_b = \mathbf{0}. \tag{4.17}$$

where the unknowns are the fluctuation displacement and the Lagrange multipliers. Therefore, the residual vector is expressed by

$$\mathbf{r} = \left\{ \begin{array}{c} \mathbf{f}_i + \mathbf{C}_{V,i}^T \boldsymbol{\lambda}_V \\ \\ \mathbf{f}_b + \mathbf{C}_L^T \boldsymbol{\lambda}_L + \mathbf{C}_M^T \boldsymbol{\lambda}_M + \mathbf{C}_{V,b}^T \boldsymbol{\lambda}_V \\ \\ \mathbf{C}_L \tilde{\mathbf{u}}_b \\ \\ \mathbf{C}_M \tilde{\mathbf{u}}_b \\ \\ \mathbf{C}_{V,i} \tilde{\mathbf{u}}_i + \mathbf{C}_{V,b} \tilde{\mathbf{u}}_b \end{array} \right\}, \tag{4.18}$$

where $\mathbf{f}$ indicates the internal nodal force vector.

The linearisation of the problem with $\mathbf{r} = \mathbf{0}$ results in the following iterative linear system of equations to be solved with the Newton-Raphson method

$$\begin{bmatrix} \mathbf{k}_{ii} & \mathbf{k}_{ib} & \mathbf{0} & \mathbf{0} & \mathbf{C}_{V,i}^T \\ \mathbf{k}_{bi} & \mathbf{k}_{bb} & \mathbf{C}_L^T & \mathbf{C}_M^T & \mathbf{C}_{V,b}^T \\ \mathbf{0} & \mathbf{C}_L & \mathbf{0} & \mathbf{0} & \mathbf{0} \\ \mathbf{0} & \mathbf{C}_M & \mathbf{0} & \mathbf{0} & \mathbf{0} \\ \mathbf{C}_{V,i} & \mathbf{C}_{V,b} & \mathbf{0} & \mathbf{0} & \mathbf{0} \end{bmatrix} \begin{Bmatrix} \Delta\tilde{\mathbf{u}}_i \\ \Delta\tilde{\mathbf{u}}_b \\ \Delta\boldsymbol{\lambda}_L \\ \Delta\boldsymbol{\lambda}_M \\ \Delta\boldsymbol{\lambda}_V \end{Bmatrix} = - \begin{Bmatrix} \mathbf{f}_i + \mathbf{C}_{V,i}^T\boldsymbol{\lambda}_V \\ \mathbf{f}_b + \mathbf{C}_L^T\boldsymbol{\lambda}_L + \mathbf{C}_M^T\boldsymbol{\lambda}_M + \mathbf{C}_{V,b}^T\boldsymbol{\lambda}_V \\ \mathbf{C}_L\tilde{\mathbf{u}}_b \\ \mathbf{C}_M\tilde{\mathbf{u}}_b \\ \mathbf{C}_{V,i}\tilde{\mathbf{u}}_i + \mathbf{C}_{V,b}\tilde{\mathbf{u}}_b \end{Bmatrix}. \tag{4.19}$$

A more compact representation of Equation (4.19) is expressed as:

$$\begin{bmatrix} \mathbf{K} & \mathbf{C}^T \\ \mathbf{C} & \mathbf{0} \end{bmatrix} \begin{Bmatrix} \Delta\tilde{\mathbf{u}} \\ \Delta\boldsymbol{\lambda} \end{Bmatrix} = - \begin{Bmatrix} \mathbf{f} + \mathbf{C}^T\boldsymbol{\lambda} \\ \mathbf{C}\tilde{\mathbf{u}} \end{Bmatrix}, \tag{4.20}$$

where $\boldsymbol{\lambda}$ is a vector with the Lagrange multipliers given by

$$\boldsymbol{\lambda} = \begin{Bmatrix} \boldsymbol{\lambda}_L \\ \boldsymbol{\lambda}_M \\ \boldsymbol{\lambda}_V \end{Bmatrix}, \tag{4.21}$$

and $\mathbf{C}$ is the constraint matrix composed of

$$\mathbf{C} = \begin{bmatrix} \mathbf{0} & \mathbf{C}_L \\ \mathbf{0} & \mathbf{C}_M \\ \mathbf{C}_{V,i} & \mathbf{C}_{V,b} \end{bmatrix}. \tag{4.22}$$

4.2.2 Constraint matrices

The constraint matrix $\mathbf{C}_L$ from Equation (4.12) is constructed by

$$\mathbf{C}_L = - \begin{bmatrix} \mathbf{C}_{L,1} & \mathbf{C}_{L,2} & \cdots & \mathbf{C}_{L,n_b} \end{bmatrix}, \tag{4.23}$$

where $\mathbf{C}_{L,k}$, denotes the contribution of each boundary node to the constraint matrix, with k ranging from 1 to the number of boundary nodes, n_b. This matrix is associated with the discrete version of Equation (3.21), which is reproduced here in index notation

$$\left[\int_{\partial\Omega_\mu^{s,b}} \tilde{\boldsymbol{u}} \otimes \left(\boldsymbol{N} - \bar{\boldsymbol{N}}\right) dA\right]_{mn} = \int_{\partial\Omega_\mu^{s,b}} H_p \tilde{u}_{pm} \left(N_n - \bar{N}_n\right) dA. \tag{4.24}$$

Moreover, the contributions $\mathbf{C}_{L,k}$ of Equation (4.23) for each boundary node k are computed by

$$\mathbf{C}_{L,k} = \begin{bmatrix} \left(\int_{\partial\Omega_\mu^{s,b}} H_k \left(N_1 - \bar{N}_1\right) dA\right) \mathbf{I} \\ \left(\int_{\partial\Omega_\mu^{s,b}} H_k \left(N_2 - \bar{N}_2\right) dA\right) \mathbf{I} \\ \left(\int_{\partial\Omega_\mu^{s,b}} H_k \left(N_3 - \bar{N}_3\right) dA\right) \mathbf{I} \end{bmatrix}, \tag{4.25}$$

where N_i indicates the i^{th} component of the outward reference unit vector, H_k represents the shape function associated with the k^{th} node and $\mathbf{I}$ denotes the identity matrix.

Analogously, the constraint matrix $\mathbf{C}_M$ from Equation (4.12) is composed of

$$\mathbf{C}_M = -\begin{bmatrix} \mathbf{C}_{M,1} & \mathbf{C}_{M,2} & \cdots & \mathbf{C}_{M,n_b} \end{bmatrix}, \tag{4.26}$$

where $\mathbf{C}_{M,k}$ is the nodal contribution k, which ranges from 1 to the number of boundary nodes, n_b. It is associated with the discrete version of Equation (3.28), which is expressed in index notation as

$$\left[\int_{\partial\Omega_\mu^{s,b}} \tilde{\boldsymbol{u}} \otimes \left(\boldsymbol{N} \otimes \boldsymbol{Y} - \bar{\bar{\boldsymbol{X}}}\right) dA\right]_{mnq} = \int_{\partial\Omega_\mu^{s,b}} H_l \tilde{u}_{lm} \left(N_n Y_q - \bar{\bar{X}}_{nq}\right) dA. \tag{4.27}$$

Thus, the constraint matrix $\mathbf{C}_M$ is assembled from the nodal contributions $\mathbf{C}_{M,k}$ by

$$\mathbf{C}_{M,k} = \begin{bmatrix} \left(\int_{\partial\Omega_\mu^{s,b}} H_k \left(N_1 Y_1 - \bar{\bar{X}}_{11}\right) dA\right) \mathbf{I} \\ \left(\int_{\partial\Omega_\mu^{s,b}} H_k \left(N_2 Y_1 - \bar{\bar{X}}_{21}\right) dA\right) \mathbf{I} \\ \left(\int_{\partial\Omega_\mu^{s,b}} H_k \left(N_3 Y_1 - \bar{\bar{X}}_{31}\right) dA\right) \mathbf{I} \\ \left(\int_{\partial\Omega_\mu^{s,b}} H_k \left(N_1 Y_2 - \bar{\bar{X}}_{12}\right) dA\right) \mathbf{I} \\ \left(\int_{\partial\Omega_\mu^{s,b}} H_k \left(N_2 Y_2 - \bar{\bar{X}}_{22}\right) dA\right) \mathbf{I} \\ \left(\int_{\partial\Omega_\mu^{s,b}} H_k \left(N_3 Y_2 - \bar{\bar{X}}_{32}\right) dA\right) \mathbf{I} \\ \left(\int_{\partial\Omega_\mu^{s,b}} H_k \left(N_1 Y_3 - \bar{\bar{X}}_{13}\right) dA\right) \mathbf{I} \\ \left(\int_{\partial\Omega_\mu^{s,b}} H_k \left(N_2 Y_3 - \bar{\bar{X}}_{23}\right) dA\right) \mathbf{I} \\ \left(\int_{\partial\Omega_\mu^{s,b}} H_k \left(N_3 Y_3 - \bar{\bar{X}}_{33}\right) dA\right) \mathbf{I} \end{bmatrix}. \tag{4.28}$$

Finally, the constraint matrix $\mathbf{C}_V$ from Equation (4.12) is related to the discretised term that enforces the volume constraint expressed by Equation (3.18). The expression to define $\mathbf{C}_V$ is given by

$$\mathbf{C}_V = -\begin{bmatrix} \mathbf{C}_{V,1} & \mathbf{C}_{V,2} & \cdots & \mathbf{C}_{V,n_n} \end{bmatrix}, \tag{4.29}$$

where n_n denotes the total number of nodes in the finite element model of the RVE. The discretised version to compute $\mathbf{C}_{V,k}$ in index notation can be written as

$$\left[\int_{\Omega_\mu^s} \tilde{\boldsymbol{u}} dV\right]_m = \int_{\Omega_\mu^s} H_l \tilde{u}_{lm} dV. \tag{4.30}$$

Furthermore, the contribution of each node k for $\mathbf{C}_V$ is computed by:

$$\mathbf{C}_{V,k} = \begin{bmatrix} \left(\int_{\Omega_\mu^s} H_k dV\right)\mathbf{I} \\ \left(\int_{\Omega_\mu^s} H_k dV\right)\mathbf{I} \\ \left(\int_{\Omega_\mu^s} H_k dV\right)\mathbf{I} \end{bmatrix}. \tag{4.31}$$

4.2.3 Homogenised first Piola-Kirchhoff stress tensor

The homogenised first Piola-Kirchhoff stress expressed in Equation (3.56) can be obtained by boundary integrals involving the Lagrange multipliers. In the context of computational implementation, the following expression is defined

$$\mathbf{P} = \mathbf{Z}_P \boldsymbol{\lambda} = \begin{bmatrix}\mathbf{Z}_{PL} & \mathbf{Z}_{PM} & \mathbf{0}\end{bmatrix} \begin{Bmatrix} \boldsymbol{\lambda}_L \\ \boldsymbol{\lambda}_M \\ \boldsymbol{\lambda}_V \end{Bmatrix} = \mathbf{Z}_{PL}\boldsymbol{\lambda}_L + \mathbf{Z}_{PM}\boldsymbol{\lambda}_M, \tag{4.32}$$

where $\mathbf{Z}_{PL}$ and $\mathbf{Z}_{PM}$ are homogenisation matrices.

At each node k on the contour of the RVE, $\mathbf{Z}_{PL}$ (matrix with dimensions 9x9) is expressed by

$$\mathbf{Z}_{PL,k} = \frac{1}{V_\mu} \begin{bmatrix} \left(\int_{\partial\Omega_\mu^{s,b}} \left(N_1 - \bar{N}_1\right) Y_1 dA\right)\mathbf{I} & \dots & \left(\int_{\partial\Omega_\mu^{s,b}} \left(N_3 - \bar{N}_3\right) Y_1 dA\right)\mathbf{I} \\ \left(\int_{\partial\Omega_\mu^{s,b}} \left(N_1 - \bar{N}_1\right) Y_2 dA\right)\mathbf{I} & \dots & \left(\int_{\partial\Omega_\mu^{s,b}} \left(N_3 - \bar{N}_3\right) Y_2 dA\right)\mathbf{I} \\ \left(\int_{\partial\Omega_\mu^{s,b}} \left(N_1 - \bar{N}_1\right) Y_3 dA\right)\mathbf{I} & \dots & \left(\int_{\partial\Omega_\mu^{s,b}} \left(N_3 - \bar{N}_3\right) Y_3 dA\right)\mathbf{I} \end{bmatrix}. \tag{4.33}$$

Furthermore, at each node k on the RVE outer contour, $\mathbf{Z}_{PM}$ (matrix with dimensions 9x27) is given by

$$\mathbf{Z}_{PM,k} = \frac{1}{V_\mu} \begin{bmatrix} \left(\int_{\partial\Omega_\mu^{s,b}} \left(N_1 Y_1 - \bar{\bar{X}}_{11}\right) Y_1 dA\right)\mathbf{I} & \dots & \left(\int_{\partial\Omega_\mu^{s,b}} \left(N_3 Y_3 - \bar{\bar{X}}_{33}\right) Y_1 dA\right)\mathbf{I} \\ \left(\int_{\partial\Omega_\mu^{s,b}} \left(N_1 Y_1 - \bar{\bar{X}}_{11}\right) Y_2 dA\right)\mathbf{I} & \dots & \left(\int_{\partial\Omega_\mu^{s,b}} \left(N_3 Y_3 - \bar{\bar{X}}_{33}\right) Y_2 dA\right)\mathbf{I} \\ \left(\int_{\partial\Omega_\mu^{s,b}} \left(N_1 Y_1 - \bar{\bar{X}}_{11}\right) Y_3 dA\right)\mathbf{I} & \dots & \left(\int_{\partial\Omega_\mu^{s,b}} \left(N_3 Y_3 - \bar{\bar{X}}_{33}\right) Y_3 dA\right)\mathbf{I} \end{bmatrix}. \tag{4.34}$$

4.2.4 Homogenised higher-order stress tensor

The homogenised higher-order stress indicated in Equation (3.60) can be obtained from boundary integrals and an additional constant term, both encompassing the Lagrange multipliers. For computational implementation, the following expression is proposed

$$\mathbf{Q} = \mathbf{Z}_Q \boldsymbol{\lambda} = \begin{bmatrix} \mathbf{Z}_{QL} & \mathbf{Z}_{QM} & \mathbf{Z}_{QV} \end{bmatrix} \begin{Bmatrix} \boldsymbol{\lambda}_L \\ \boldsymbol{\lambda}_M \\ \boldsymbol{\lambda}_V \end{Bmatrix} = \mathbf{Z}_{QL}\boldsymbol{\lambda}_L + \mathbf{Z}_{QM}\boldsymbol{\lambda}_M + \mathbf{Z}_{QV}\boldsymbol{\lambda}_V, \tag{4.35}$$

where $\mathbf{Z}_{QL}$, $\mathbf{Z}_{QM}$ and $\mathbf{Z}_{QV}$ are homogenisation matrices.

Thus, at each node k on the RVE outer contour, $\mathbf{Z}_{QL}$ (matrix with dimensions 27x9) is given by:

$$\mathbf{Z}_{QL,k} = \frac{1}{2V_\mu} \begin{bmatrix}
\left(\int_{\partial\Omega_\mu^{s,b}} \left(N_1 - \bar{N}_1\right) Y_1 Y_1 dA\right)\mathbf{I} & \dots & \left(\int_{\partial\Omega_\mu^{s,b}} \left(N_3 - \bar{N}_3\right) Y_1 Y_1 dA\right)\mathbf{I} \\
\left(\int_{\partial\Omega_\mu^{s,b}} \left(N_1 - \bar{N}_1\right) Y_2 Y_1 dA\right)\mathbf{I} & \dots & \left(\int_{\partial\Omega_\mu^{s,b}} \left(N_3 - \bar{N}_3\right) Y_2 Y_1 dA\right)\mathbf{I} \\
\left(\int_{\partial\Omega_\mu^{s,b}} \left(N_1 - \bar{N}_1\right) Y_3 Y_1 dA\right)\mathbf{I} & \dots & \left(\int_{\partial\Omega_\mu^{s,b}} \left(N_3 - \bar{N}_3\right) Y_3 Y_1 dA\right)\mathbf{I} \\
\left(\int_{\partial\Omega_\mu^{s,b}} \left(N_1 - \bar{N}_1\right) Y_1 Y_2 dA\right)\mathbf{I} & \dots & \left(\int_{\partial\Omega_\mu^{s,b}} \left(N_3 - \bar{N}_3\right) Y_1 Y_2 dA\right)\mathbf{I} \\
\left(\int_{\partial\Omega_\mu^{s,b}} \left(N_1 - \bar{N}_1\right) Y_2 Y_2 dA\right)\mathbf{I} & \dots & \left(\int_{\partial\Omega_\mu^{s,b}} \left(N_3 - \bar{N}_3\right) Y_2 Y_2 dA\right)\mathbf{I} \\
\left(\int_{\partial\Omega_\mu^{s,b}} \left(N_1 - \bar{N}_1\right) Y_3 Y_2 dA\right)\mathbf{I} & \dots & \left(\int_{\partial\Omega_\mu^{s,b}} \left(N_3 - \bar{N}_3\right) Y_3 Y_2 dA\right)\mathbf{I} \\
\left(\int_{\partial\Omega_\mu^{s,b}} \left(N_1 - \bar{N}_1\right) Y_1 Y_3 dA\right)\mathbf{I} & \dots & \left(\int_{\partial\Omega_\mu^{s,b}} \left(N_3 - \bar{N}_3\right) Y_1 Y_3 dA\right)\mathbf{I} \\
\left(\int_{\partial\Omega_\mu^{s,b}} \left(N_1 - \bar{N}_1\right) Y_2 Y_3 dA\right)\mathbf{I} & \dots & \left(\int_{\partial\Omega_\mu^{s,b}} \left(N_3 - \bar{N}_3\right) Y_2 Y_3 dA\right)\mathbf{I} \\
\left(\int_{\partial\Omega_\mu^{s,b}} \left(N_1 - \bar{N}_1\right) Y_3 Y_3 dA\right)\mathbf{I} & \dots & \left(\int_{\partial\Omega_\mu^{s,b}} \left(N_3 - \bar{N}_3\right) Y_3 Y_3 dA\right)\mathbf{I}
\end{bmatrix}. \tag{4.36}$$

Moreover, at each node k on the RVE outer boundary, $\mathbf{Z}_{QM}$ (matrix with dimensions 27x27) is given by:

$$\mathbf{Z}_{QM,k} = \frac{1}{2V_\mu} \begin{bmatrix} \left(\int_{\partial\Omega_\mu^{s,b}} \left(N_1Y_1 - \bar{\bar{X}}_{11}\right) Y_1Y_1 dA\right)\mathbf{I} & \dots & \left(\int_{\partial\Omega_\mu^{s,b}} \left(N_3Y_3 - \bar{\bar{X}}_{33}\right) Y_1Y_1 dA\right)\mathbf{I} \\ \left(\int_{\partial\Omega_\mu^{s,b}} \left(N_1Y_1 - \bar{\bar{X}}_{11}\right) Y_2Y_1 dA\right)\mathbf{I} & \dots & \left(\int_{\partial\Omega_\mu^{s,b}} \left(N_3Y_3 - \bar{\bar{X}}_{33}\right) Y_2Y_1 dA\right)\mathbf{I} \\ \left(\int_{\partial\Omega_\mu^{s,b}} \left(N_1Y_1 - \bar{\bar{X}}_{11}\right) Y_3Y_1 dA\right)\mathbf{I} & \dots & \left(\int_{\partial\Omega_\mu^{s,b}} \left(N_3Y_3 - \bar{\bar{X}}_{33}\right) Y_3Y_1 dA\right)\mathbf{I} \\ \left(\int_{\partial\Omega_\mu^{s,b}} \left(N_1Y_1 - \bar{\bar{X}}_{11}\right) Y_1Y_2 dA\right)\mathbf{I} & \dots & \left(\int_{\partial\Omega_\mu^{s,b}} \left(N_3Y_3 - \bar{\bar{X}}_{33}\right) Y_1Y_2 dA\right)\mathbf{I} \\ \left(\int_{\partial\Omega_\mu^{s,b}} \left(N_1Y_1 - \bar{\bar{X}}_{11}\right) Y_2Y_2 dA\right)\mathbf{I} & \dots & \left(\int_{\partial\Omega_\mu^{s,b}} \left(N_3Y_3 - \bar{\bar{X}}_{33}\right) Y_2Y_2 dA\right)\mathbf{I} \\ \left(\int_{\partial\Omega_\mu^{s,b}} \left(N_1Y_1 - \bar{\bar{X}}_{11}\right) Y_3Y_2 dA\right)\mathbf{I} & \dots & \left(\int_{\partial\Omega_\mu^{s,b}} \left(N_3Y_3 - \bar{\bar{X}}_{33}\right) Y_3Y_2 dA\right)\mathbf{I} \\ \left(\int_{\partial\Omega_\mu^{s,b}} \left(N_1Y_1 - \bar{\bar{X}}_{11}\right) Y_1Y_3 dA\right)\mathbf{I} & \dots & \left(\int_{\partial\Omega_\mu^{s,b}} \left(N_3Y_3 - \bar{\bar{X}}_{33}\right) Y_1Y_3 dA\right)\mathbf{I} \\ \left(\int_{\partial\Omega_\mu^{s,b}} \left(N_1Y_1 - \bar{\bar{X}}_{11}\right) Y_2Y_3 dA\right)\mathbf{I} & \dots & \left(\int_{\partial\Omega_\mu^{s,b}} \left(N_3Y_3 - \bar{\bar{X}}_{33}\right) Y_2Y_3 dA\right)\mathbf{I} \\ \left(\int_{\partial\Omega_\mu^{s,b}} \left(N_1Y_1 - \bar{\bar{X}}_{11}\right) Y_3Y_3 dA\right)\mathbf{I} & \dots & \left(\int_{\partial\Omega_\mu^{s,b}} \left(N_3Y_3 - \bar{\bar{X}}_{33}\right) Y_3Y_3 dA\right)\mathbf{I} \end{bmatrix} . \tag{4.37}$$

Finally, the constant term $\mathbf{Z}_{QV}$ is given by:

$$\mathbf{Z}_{QV} = \frac{1}{2}\frac{V_\mu^s}{V_\mu} \begin{bmatrix} (J_{11})\,\mathbf{I} \\ (J_{21})\,\mathbf{I} \\ (J_{31})\,\mathbf{I} \\ (J_{12})\,\mathbf{I} \\ (J_{22})\,\mathbf{I} \\ (J_{32})\,\mathbf{I} \\ (J_{13})\,\mathbf{I} \\ (J_{23})\,\mathbf{I} \\ (J_{33})\,\mathbf{I} \end{bmatrix} . \tag{4.38}$$

It is interesting to note that the homogenisation matrices are constant and can be defined only once during the problem initialisation, which reduces the computational effort.

4.3 Discrete micro-scale equilibrium problem for periodic constraint

4.3.1 Finite element solution of the micro-scale problem

The discrete version of Equation (3.62), which results from the micro-scale weak equilibrium problem for periodic constraint, can be expressed as

$$\begin{aligned} &\delta\tilde{\mathbf{u}}^T \int_{\Omega_\mu^s} \left(\mathbf{G}^u\right)^T \mathbf{P}_\mu dV + \delta\boldsymbol{\lambda}_P^T\mathbf{C}_P\tilde{\mathbf{u}}_b + \delta\tilde{\mathbf{u}}_b^T\mathbf{C}_P^T\boldsymbol{\lambda}_P + \delta\boldsymbol{\lambda}_S^T\mathbf{C}_S\tilde{\mathbf{u}}_b + \delta\tilde{\mathbf{u}}_b^T\mathbf{C}_S^T\boldsymbol{\lambda}_S \\ &+ \delta\boldsymbol{\lambda}_V^T\mathbf{C}_V\tilde{\mathbf{u}} + \delta\tilde{\mathbf{u}}^T\mathbf{C}_V^T\boldsymbol{\lambda}_V = 0, \quad \forall\left(\delta\tilde{\mathbf{u}}, \delta\boldsymbol{\lambda}_P, \delta\boldsymbol{\lambda}_S, \delta\boldsymbol{\lambda}_V\right), \end{aligned} \tag{4.39}$$

where $\boldsymbol{\lambda}_P$, $\boldsymbol{\lambda}_S$ and $\boldsymbol{\lambda}_V$ are the Lagrange multiplier vectors. In addition, the constraint matrices $\mathbf{C}_P$, $\mathbf{C}_S$ and $\mathbf{C}_V$ refer to the constraints given by Equation (3.39).

Equation (4.39) must be valid for any variation of the displacement fluctuation or the Lagrange multipliers according to the variational approach. Including the splitting of the degrees of freedom (see Equation (4.4)):

$$\int_{\Omega_\mu^s} \left(\mathbf{G}_i^u\right)^T \mathbf{P}_\mu dV + \mathbf{C}_{V,i}^T \boldsymbol{\lambda}_{V,i} = \mathbf{0} \tag{4.40}$$

$$\int_{\Omega_\mu^s} \left(\mathbf{G}_b^u\right)^T \mathbf{P}_\mu dV + \mathbf{C}_P^T \boldsymbol{\lambda}_P + \mathbf{C}_S^T \boldsymbol{\lambda}_S + \mathbf{C}_{V,b}^T \boldsymbol{\lambda}_{V,b} = \mathbf{0} \tag{4.41}$$

$$\mathbf{C}_P \tilde{\mathbf{u}}_b = \mathbf{0} \tag{4.42}$$

$$\mathbf{C}_S \tilde{\mathbf{u}}_b = \mathbf{0} \tag{4.43}$$

$$\mathbf{C}_{V,i} \tilde{\mathbf{u}}_i + \mathbf{C}_{V,b} \tilde{\mathbf{u}}_b = \mathbf{0}, \tag{4.44}$$

which consists of the set of equations of the micro-scale equilibrium problem to be solved in finite elements. Therefore, the residual vector is defined as

$$\mathbf{r} = \left\{ \begin{array}{c} \mathbf{f}_i + \mathbf{C}_{V,i}^T \boldsymbol{\lambda}_{V,i} \\ \mathbf{f}_b + \mathbf{C}_P^T \boldsymbol{\lambda}_P + \mathbf{C}_S^T \boldsymbol{\lambda}_S + \mathbf{C}_{V,b}^T \boldsymbol{\lambda}_{V,b} \\ \mathbf{C}_P \tilde{\mathbf{u}}_b \\ \mathbf{C}_S \tilde{\mathbf{u}}_b \\ \mathbf{C}_{V,i} \tilde{\mathbf{u}}_i + \mathbf{C}_{V,b} \tilde{\mathbf{u}}_b \end{array} \right\}. \tag{4.45}$$

The linearisation of the previous expression to $\mathbf{r} = \mathbf{0}$ allows obtaining the following iterative linear system of equations to be solved with the Newton–Raphson scheme:

$$\begin{bmatrix} \mathbf{k}_{ii} & \mathbf{k}_{ib} & \mathbf{0} & \mathbf{0} & \mathbf{C}_{V,i}^T \\ \mathbf{k}_{bi} & \mathbf{k}_{bb} & \mathbf{C}_P^T & \mathbf{C}_S^T & \mathbf{C}_{V,b}^T \\ \mathbf{0} & \mathbf{C}_P & \mathbf{0} & \mathbf{0} & \mathbf{0} \\ \mathbf{0} & \mathbf{C}_S & \mathbf{0} & \mathbf{0} & \mathbf{0} \\ \mathbf{C}_{V,i} & \mathbf{C}_{V,b} & \mathbf{0} & \mathbf{0} & \mathbf{0} \end{bmatrix} \left\{ \begin{array}{c} \Delta\tilde{\mathbf{u}}_i \\ \Delta\tilde{\mathbf{u}}_b \\ \Delta\boldsymbol{\lambda}_P \\ \Delta\boldsymbol{\lambda}_S \\ \Delta\boldsymbol{\lambda}_V \end{array} \right\} = - \left\{ \begin{array}{c} \mathbf{f}_i + \mathbf{C}_{V,i}^T \boldsymbol{\lambda}_{V,i} \\ \mathbf{f}_b + \mathbf{C}_P^T \boldsymbol{\lambda}_P + \mathbf{C}_S^T \boldsymbol{\lambda}_S + \mathbf{C}_{V,b}^T \boldsymbol{\lambda}_{V,b} \\ \mathbf{C}_P \tilde{\mathbf{u}}_b \\ \mathbf{C}_S \tilde{\mathbf{u}}_b \\ \mathbf{C}_{V,i} \tilde{\mathbf{u}}_i + \mathbf{C}_{V,b} \tilde{\mathbf{u}}_b \end{array} \right\}. \tag{4.46}$$

Furthermore, Equation (4.46) can be rewritten in a compact form according to Equation (4.20). In this case, the Lagrange multiplier vector $\boldsymbol{\lambda}$ is organised as follows:

$$\boldsymbol{\lambda} = \left\{ \begin{array}{c} \boldsymbol{\lambda}_P \\ \boldsymbol{\lambda}_S \\ \boldsymbol{\lambda}_V \end{array} \right\}, \tag{4.47}$$

and the constraint matrix $\mathbf{C}$ is composed of:

$$\mathbf{C} = \begin{bmatrix} \mathbf{0} & \mathbf{C}_P \\ \mathbf{0} & \mathbf{C}_S \\ \mathbf{C}_{V,i} & \mathbf{C}_{V,b} \end{bmatrix}, \tag{4.48}$$

where the size of the Lagrange multiplier vector $\boldsymbol{\lambda}_P$ is related to the number of nodes on the positive side of the RVE, the number of components of the vector $\boldsymbol{\lambda}_S$ is six for two-dimensional RVEs and nine for three-dimensional RVEs, and the vector $\boldsymbol{\lambda}_V$ has two components in two-dimensional problems and three for three-dimensional problems.

4.3.2 Constraint matrices

The constraint matrix $\mathbf{C}_P$ is related to the discretised term (see Equation (4.39)) that imposes the periodicity of the fluctuations on the RVE boundary (see Equation (3.34)):

$$-\int_{\partial\Omega_\mu^{s,b+}} \delta\boldsymbol{\lambda}_P \cdot \left(\tilde{\boldsymbol{u}}^+ - \tilde{\boldsymbol{u}}^-\right) \Rightarrow -\delta\boldsymbol{\lambda}_P^T \int_{\partial\Omega_\mu^{s,b+}} \mathbf{H}_+^T \left(\mathbf{H}_+\tilde{\mathbf{u}}_+ - \mathbf{H}_-\tilde{\mathbf{u}}_-\right) = \delta\boldsymbol{\lambda}_P^T\mathbf{C}_P\tilde{\mathbf{u}}_b. \tag{4.49}$$

Conveniently, the RVE contour can be divided into positive ($S+$) and negative faces ($S-$) associated with the respective normal vectors ($N+$ and $N-$). Thus, the boundary degrees of freedom on the RVE ($\tilde{\mathbf{u}}_b$) are split into $\tilde{\mathbf{u}}_+$ and $\tilde{\mathbf{u}}_-$ or in vector format:

$$\tilde{\mathbf{u}}_b = \begin{Bmatrix} \tilde{\mathbf{u}}_+ \\ \tilde{\mathbf{u}}_- \end{Bmatrix}, \tag{4.50}$$

and the discretised constraint is defined as

$$\mathbf{C}_P\tilde{\mathbf{u}}_b = -\begin{bmatrix} \mathbf{C}_+ & -\mathbf{C}_- \end{bmatrix} \begin{Bmatrix} \tilde{\mathbf{u}}_+ \\ \tilde{\mathbf{u}}_- \end{Bmatrix}, \tag{4.51}$$

where the positive constraint matrix is defined by

$$\mathbf{C}_+ = \begin{bmatrix} \mathbf{C}_{11}^+ & \cdots & \mathbf{C}_{1n_+}^+ \\ \vdots & \mathbf{C}_{kl}^+ & \vdots \\ \mathbf{C}_{n_+1}^+ & \cdots & \mathbf{C}_{n_+n_+}^+ \end{bmatrix}, \tag{4.52}$$

and the negative constraint matrix is expressed by

$$\mathbf{C}_- = \begin{bmatrix} \mathbf{C}_{11}^- & \cdots & \mathbf{C}_{1n_-}^- \\ \vdots & \mathbf{C}_{kl}^- & \vdots \\ \mathbf{C}_{n_+1}^- & \cdots & \mathbf{C}_{n_+n_-}^- \end{bmatrix}. \tag{4.53}$$

The sub-matrices $\mathbf{C}_+$ and $\mathbf{C}_-$ are computed by

$$\mathbf{C}_{kl}^{+} = \left(\int_{\partial\Omega^{s,b+}} H_k^+ H_l^+ dA\right)\mathbf{I}, \tag{4.54}$$

$$\mathbf{C}_{kl}^{-} = \left(\int_{\partial\Omega^{s,b+}} H_k^+ H_l^- dA\right)\mathbf{I}, \tag{4.55}$$

respectively. Moreover, k ranges from 1 to the number of nodes on the positive side n_+ and the scalar l ranges from 1 to n_+ for the positive sub-matrices and ranges from 1 to the number of nodes on the negative side n_- for the negative sub-matrices.

The constraint matrix $\mathbf{C}_S$ is related to the discretised term (see Equation (4.39)) that enforces the constraints expressed by Equation (3.38). The representations of $\mathbf{C}_S$ for cubic (three-dimensional) RVEs are:

$$\mathbf{C}_S = -\begin{bmatrix} \mathbf{C}_{S1} & \mathbf{0}_{3\times n_-} \\ \mathbf{C}_{S2} & \mathbf{0}_{3\times n_-} \\ \mathbf{C}_{S3} & \mathbf{0}_{3\times n_-} \end{bmatrix}. \tag{4.56}$$

Regarding Equation (4.56), the sub-matrices $\mathbf{C}_{Ss}$ refer to each one of the positive faces and are obtained through integration of the shape functions on those boundaries, i.e.,

$$\mathbf{C}_{Ss} = \left[\; \left(\int_{\partial\Omega_\mu^{s,b+(i)}} H_1^+ dA\right)\mathbf{I} \;\vdots\; \left(\int_{\partial\Omega_\mu^{s,b+(i)}} H_2^+ dA\right)\mathbf{I} \;\vdots\; \cdots \;\vdots\; \left(\int_{\partial\Omega_\mu^{s,b+(i)}} H_{n_+}^+ dA\right)\mathbf{I} \;\right]. \tag{4.57}$$

Finally, the constraint matrix $\mathbf{C}_V$ from Equation (4.39) is associated with the discretised term that enforces the volume constraint expressed by Equation (3.18). The expression to compute $\mathbf{C}_V$ is presented in Equation (4.29).

4.3.3 Homogenised Piola-Kirchhoff stress tensor

The homogenised first Piola-Kirchhoff stress tensor can be obtained from Equation (3.70), i.e., exclusively through boundary integrals involving the Lagrange multipliers. Therefore, taking into account the concept of homogenisation matrix introduced in Equation (4.32), numerical homogenisation can be performed by

$$\mathbf{P} = \mathbf{Z}_P\boldsymbol{\lambda} = \begin{bmatrix}\mathbf{Z}_{PP} & \mathbf{Z}_{PS} & \mathbf{0}\end{bmatrix}\begin{Bmatrix}\boldsymbol{\lambda}_P \\ \boldsymbol{\lambda}_S \\ \boldsymbol{\lambda}_V\end{Bmatrix} = \mathbf{Z}_{PP}\boldsymbol{\lambda}_P + \mathbf{Z}_{PS}\boldsymbol{\lambda}_S. \tag{4.58}$$

where $\mathbf{Z}_{PP}$ and $\mathbf{Z}_{PS}$ are homogenisation matrices. The contribution of the Lagrange multipliers enforcing periodicity, $\boldsymbol{\lambda}_P$, is introduced through

$$\mathbf{Z}_{PP} = \begin{bmatrix}\mathbf{Z}_{PP,1} & \mathbf{Z}_{PP,2} & \cdots & \mathbf{Z}_{PP,n_+}\end{bmatrix} \tag{4.59}$$

with

$$\mathbf{Z}_{PP,l} = \frac{1}{V_\mu} \begin{bmatrix} \int_{\partial\Omega_\mu^{s,b+}} \left(Y_1^+ - Y_1^-\right) H_l^+ \; dA \; \mathbf{I} \\ \int_{\partial\Omega_\mu^{s,b+}} \left(Y_2^+ - Y_2^-\right) H_l^+ \; dA \; \mathbf{I} \\ \int_{\partial\Omega_\mu^{s,b+}} \left(Y_3^+ - Y_3^-\right) H_l^+ \; dA \; \mathbf{I} \end{bmatrix}. \tag{4.60}$$

The H_l^+ denotes the Lagrange multiplier interpolation function associated with node l on the positive side. The influence of the Lagrange multipliers enforcing the surface constraints is included through the matrix $\mathbf{Z}_{PS}$

$$\mathbf{Z}_{PS} = \begin{bmatrix} \mathbf{Z}_{PS1} & \mathbf{Z}_{PS2} & \mathbf{Z}_{PS3} \end{bmatrix}, \tag{4.61}$$

where

$$\mathbf{Z}_{PSs} = \frac{1}{V_\mu} \begin{bmatrix} \int_{\partial\Omega_\mu}^{s,b+(i)} Y_1 \; dA \; \mathbf{I} \\ \int_{\partial\Omega_\mu}^{s,b+(i)} Y_2 \; dA \; \mathbf{I} \\ \int_{\partial\Omega_\mu}^{s,b+(i)} Y_3 \; dA \; \mathbf{I} \end{bmatrix}. \tag{4.62}$$

4.3.4 Homogenised higher-order stress tensor

The homogenised higher-order stress tensor can be computed exclusively through boundary integrals from Equation (3.71). Taking into account the concept of homogenisation matrix introduced in Equation (4.35), the numerical homogenisation of the higher-order stress tensor can be performed by

$$\mathbf{Q} = \mathbf{Z}_Q \boldsymbol{\lambda} = \begin{bmatrix} \mathbf{Z}_{QP} & \mathbf{Z}_{QS} & \mathbf{Z}_{QV} \end{bmatrix} \begin{Bmatrix} \boldsymbol{\lambda}_P \\ \boldsymbol{\lambda}_S \\ \boldsymbol{\lambda}_V \end{Bmatrix}, \tag{4.63}$$

where $\mathbf{Z}_{QP}$, $\mathbf{Z}_{QS}$ and $\mathbf{Z}_{QV}$ are homogenisation matrices.

In this sense, $\mathbf{Z}_{QP}$ can is defined here by

$$\mathbf{Z}_{QP} = \begin{bmatrix} \mathbf{Z}_{QP,1} & \mathbf{Z}_{QP,2} & \cdots & \mathbf{Z}_{QP,n_+} \end{bmatrix}, \tag{4.64}$$

with

$$\mathbf{Z}_{QP,l} = \frac{1}{2V_\mu}\begin{bmatrix} \left(\int_{\partial\Omega_\mu^{s,b+}} H_l^+ Y_1^+ Y_1^+ \; dA - \int_{\partial\Omega_\mu^{s,b+}} H_l^+ Y_1^- Y_1^- \; dA\right)\mathbf{I} \\ \left(\int_{\partial\Omega_\mu^{s,b+}} H_l^+ Y_2^+ Y_1^+ \; dA - \int_{\partial\Omega_\mu^{s,b+}} H_l^+ Y_2^- Y_1^- \; dA\right)\mathbf{I} \\ \left(\int_{\partial\Omega_\mu^{s,b+}} H_l^+ Y_3^+ Y_1^+ \; dA - \int_{\partial\Omega_\mu^{s,b+}} H_l^+ Y_3^- Y_1^- \; dA\right)\mathbf{I} \\ \left(\int_{\partial\Omega_\mu^{s,b+}} H_l^+ Y_1^+ Y_2^+ \; dA - \int_{\partial\Omega_\mu^{s,b+}} H_l^+ Y_1^- Y_2^- \; dA\right)\mathbf{I} \\ \left(\int_{\partial\Omega_\mu^{s,b+}} H_l^+ Y_2^+ Y_2^+ \; dA - \int_{\partial\Omega_\mu^{s,b+}} H_l^+ Y_2^- Y_2^- \; dA\right)\mathbf{I} \\ \left(\int_{\partial\Omega_\mu^{s,b+}} H_l^+ Y_3^+ Y_2^+ \; dA - \int_{\partial\Omega_\mu^{s,b+}} H_l^+ Y_3^- Y_2^- \; dA\right)\mathbf{I} \\ \left(\int_{\partial\Omega_\mu^{s,b+}} H_l^+ Y_1^+ Y_3^+ \; dA - \int_{\partial\Omega_\mu^{s,b+}} H_l^+ Y_1^- Y_3^- \; dA\right)\mathbf{I} \\ \left(\int_{\partial\Omega_\mu^{s,b+}} H_l^+ Y_2^+ Y_3^+ \; dA - \int_{\partial\Omega_\mu^{s,b+}} H_l^+ Y_2^- Y_3^- \; dA\right)\mathbf{I} \\ \left(\int_{\partial\Omega_\mu^{s,b+}} H_l^+ Y_3^+ Y_3^+ \; dA - \int_{\partial\Omega_\mu^{s,b+}} H_l^+ Y_3^- Y_3^- \; dA\right)\mathbf{I} \end{bmatrix}. \tag{4.65}$$

In turn, $\mathbf{Z}_{QS}$ is assembled as

$$\mathbf{Z}_{QS} = \begin{bmatrix} \mathbf{Z}_{QS1} & \mathbf{Z}_{QS2} & \mathbf{Z}_{QS3} \end{bmatrix}, \tag{4.66}$$

with

$$\mathbf{Z}_{QSs} = \frac{1}{2V_\mu}\begin{bmatrix} \left(\int_{\partial\Omega_\mu^{s,b+(i)}} Y_1 Y_1 \; dA\right)\mathbf{I} \\ \left(\int_{\partial\Omega_\mu^{s,b+(i)}} Y_2 Y_1 \; dA\right)\mathbf{I} \\ \left(\int_{\partial\Omega_\mu^{s,b+(i)}} Y_3 Y_1 \; dA\right)\mathbf{I} \\ \left(\int_{\partial\Omega_\mu^{s,b+(i)}} Y_1 Y_2 \; dA\right)\mathbf{I} \\ \left(\int_{\partial\Omega_\mu^{s,b+(i)}} Y_2 Y_2 \; dA\right)\mathbf{I} \\ \left(\int_{\partial\Omega_\mu^{s,b+(i)}} Y_3 Y_2 \; dA\right)\mathbf{I} \\ \left(\int_{\partial\Omega_\mu^{s,b+(i)}} Y_1 Y_3 \; dA\right)\mathbf{I} \\ \left(\int_{\partial\Omega_\mu^{s,b+(i)}} Y_2 Y_3 \; dA\right)\mathbf{I} \\ \left(\int_{\partial\Omega_\mu^{s,b+(i)}} Y_3 Y_3 \; dA\right)\mathbf{I} \end{bmatrix}. \tag{4.67}$$

Furthermore, the homogenisation matrix $\mathbf{Z}_{QV}$ is determined by Equation (4.38).

4.4 Discrete micro-scale equilibrium problem for direct constraint

4.4.1 Finite element solution of the micro-scale problem

The discretised version of Equation (3.73), which results from the micro-scale weak equilibrium problem of the direct constraint, can be expressed by

$$\begin{aligned} &\delta\tilde{\mathbf{u}}^T \int_{\Omega_\mu^s} \left(\mathbf{G}^u\right)^T \mathbf{P}_\mu dV + \delta\boldsymbol{\lambda}_D^T \mathbf{C}_D \tilde{\mathbf{u}}_b + \delta\tilde{\mathbf{u}}_b^T \mathbf{C}_D^T \boldsymbol{\lambda}_D + \delta\boldsymbol{\lambda}_V^T \mathbf{C}_V \tilde{\mathbf{u}} \\ &+ \delta\tilde{\mathbf{u}}^T \mathbf{C}_V^T \boldsymbol{\lambda}_V = 0, \quad \forall \left(\delta\tilde{\mathbf{u}}, \delta\boldsymbol{\lambda}_D, \delta\boldsymbol{\lambda}_V\right), \end{aligned} \tag{4.68}$$

where $\boldsymbol{\lambda}_D$ and $\boldsymbol{\lambda}_V$ denote the vectors with the Lagrange multipliers, $\mathbf{C}_D$ and $\mathbf{C}_V$ are the corresponding constraint matrices defined by Equation (3.41).

Due to the variational approach, the discretised form of Equation (4.68) can be written as:

$$\int_{\Omega_\mu^s} \left(\mathbf{G}_i^u\right)^T \mathbf{P}_\mu dV + \mathbf{C}_{V,i}^T \boldsymbol{\lambda}_{V,i} = \mathbf{0} \tag{4.69}$$

$$\int_{\Omega_\mu^s} \left(\mathbf{G}_b^u\right)^T \mathbf{P}_\mu dV + \mathbf{C}_D^T \boldsymbol{\lambda}_D + \mathbf{C}_{V,b}^T \boldsymbol{\lambda}_{V,b} = \mathbf{0} \tag{4.70}$$

$$\mathbf{C}_D \tilde{\mathbf{u}}_b = \mathbf{0} \tag{4.71}$$

$$\mathbf{C}_{V,i} \tilde{\mathbf{u}}_i + \mathbf{C}_{V,b} \tilde{\mathbf{u}}_b = \mathbf{0}. \tag{4.72}$$

Therefore, the residual vector is expressed by:

$$\mathbf{r} = \begin{Bmatrix} \mathbf{f}_i + \mathbf{C}_{V,i}^T \boldsymbol{\lambda}_{V,i} \\ \mathbf{f}_b + \mathbf{C}_D^T \boldsymbol{\lambda}_D + \mathbf{C}_{V,b}^T \boldsymbol{\lambda}_{V,b} \\ \mathbf{C}_D \tilde{\mathbf{u}}_b \\ \mathbf{C}_{V,i} \tilde{\mathbf{u}}_i + \mathbf{C}_{V,b} \tilde{\mathbf{u}}_b \end{Bmatrix}. \tag{4.73}$$

The linearisation of Equation (4.73) to be solved with the Newton–Raphson scheme leads to the iterative linear system of equations:

$$\begin{bmatrix} \mathbf{k}_{ii} & \mathbf{k}_{ib} & \mathbf{0} & \mathbf{C}_{V,i}^T \\ \mathbf{k}_{bi} & \mathbf{k}_{bb} & \mathbf{C}_D^T & \mathbf{C}_{V,b}^T \\ \mathbf{0} & \mathbf{C}_D & \mathbf{0} & \mathbf{0} \\ \mathbf{C}_{V,i} & \mathbf{C}_{V,b} & \mathbf{0} & \mathbf{0} \end{bmatrix} \begin{Bmatrix} \Delta\tilde{\mathbf{u}}_i \\ \Delta\tilde{\mathbf{u}}_b \\ \Delta\boldsymbol{\lambda}_D \\ \Delta\boldsymbol{\lambda}_V \end{Bmatrix} = - \begin{Bmatrix} \mathbf{f}_i + \mathbf{C}_{V,i}^T \boldsymbol{\lambda}_{V,i} \\ \mathbf{f}_b + \mathbf{C}_D^T \boldsymbol{\lambda}_D + \mathbf{C}_{V,b}^T \boldsymbol{\lambda}_{V,b} \\ \mathbf{C}_D \tilde{\mathbf{u}}_b \\ \mathbf{C}_{V,i} \tilde{\mathbf{u}}_i + \mathbf{C}_{V,b} \tilde{\mathbf{u}}_b \end{Bmatrix}, \tag{4.74}$$

Equation (4.74) can be expressed more compactly, as shown in Equation (4.20). In this case, the Lagrange multiplier vector $\boldsymbol{\lambda}$ is defined as

$$\boldsymbol{\lambda} = \begin{Bmatrix} \boldsymbol{\lambda}_D \\ \boldsymbol{\lambda}_V \end{Bmatrix}, \tag{4.75}$$

and the constraint matrix $\mathbf{C}$ as

$$\mathbf{C} = \begin{bmatrix} \mathbf{0} & \mathbf{C}_D \\ \mathbf{C}_{V,i} & \mathbf{C}_{V,b} \end{bmatrix}. \tag{4.76}$$

4.4.2 Constraint matrices

The constraint matrix $\mathbf{C}_D$ is defined such that the discretised form of the term

$$-\int_{\partial\Omega_\mu} \delta\boldsymbol{\lambda}_D \cdot \tilde{\mathbf{u}} dA - \int_{\partial\Omega_\mu} \boldsymbol{\lambda}_D \cdot \delta\tilde{\mathbf{u}} dA \tag{4.77}$$

in Equation (3.73) can be expressed by

$$\delta\boldsymbol{\lambda}_D^T \mathbf{C}_D \tilde{\mathbf{u}}_b + \delta\tilde{\mathbf{u}}_b^T \mathbf{C}_D^T \boldsymbol{\lambda}_D. \tag{4.78}$$

It is worth mentioning that the Lagrange multipliers $\boldsymbol{\lambda}_D$ are interpolated with the finite element shape functions ($\mathbf{H}$). Thus, the constraint matrix $\mathbf{C}_D$ can be defined by

$$\mathbf{C}_D = -\int_{\partial\Omega_\mu^{s,b}} \mathbf{H}_b^T \mathbf{H}_b dA, \tag{4.79}$$

where $\mathbf{H}_b$ is the shape function matrix related to the nodes on the RVE boundary

$$\mathbf{H}_b = \begin{bmatrix} H_1\mathbf{I} & H_2\mathbf{I} & \cdots & H_{n_b}\mathbf{I} \end{bmatrix}. \tag{4.80}$$

In addition, an expanded version of $\mathbf{C}_D$ can be written as

$$\mathbf{C}_D = -\begin{bmatrix} \left(\int_{\partial\Omega_\mu^{s,b}} H_1 H_1 dA\right)\mathbf{I} & \left(\int_{\partial\Omega_\mu^{s,b}} H_1 H_2 dA\right)\mathbf{I} & \cdots & \left(\int_{\partial\Omega_\mu^{s,b}} H_1 H_{n_b} dA\right)\mathbf{I} \\ \left(\int_{\partial\Omega_\mu^{s,b}} H_2 H_1 dA\right)\mathbf{I} & \left(\int_{\partial\Omega_\mu^{s,b}} H_2 H_2 dA\right)\mathbf{I} & \cdots & \left(\int_{\partial\Omega_\mu^{s,b}} H_2 H_{n_b} dA\right)\mathbf{I} \\ \vdots & \vdots & \ddots & \vdots \\ \left(\int_{\partial\Omega_\mu^{s,b}} H_{n_b} H_1 dA\right)\mathbf{I} & \left(\int_{\partial\Omega_\mu^{s,b}} H_{n_b} H_2 dA\right)\mathbf{I} & \cdots & \left(\int_{\partial\Omega_\mu^{s,b}} H_{n_b} H_{n_b} dA\right)\mathbf{I} \end{bmatrix}. \tag{4.81}$$

Finally, the constraint matrix $\mathbf{C}_V$ from Equation (4.68) can be computed by Equation (4.29).

4.4.3 Homogenised first Piola-Kirchhoff stress tensor

The homogenised first Piola-Kirchhoff stress tensor can be computed through the discrete form of Equation (3.79) taking into account the following representation

$$\mathbf{P} = \mathbf{Z}_P \boldsymbol{\lambda} = \begin{bmatrix} \mathbf{Z}_{PD} & \mathbf{0} \end{bmatrix} \begin{Bmatrix} \boldsymbol{\lambda}_D \\ \boldsymbol{\lambda}_V \end{Bmatrix}, \tag{4.82}$$

where the homogenisation matrix $\mathbf{Z}_{PD}$ is organised as

$$\mathbf{Z}_{PD} = \begin{bmatrix} \mathbf{Z}_{PD,1} & \mathbf{Z}_{PD,2} & \cdots & \mathbf{Z}_{PD,n_b} \end{bmatrix}, \tag{4.83}$$

with

$$\mathbf{Z}_{PD,l} = \frac{1}{V_\mu} \begin{bmatrix} \left(\int_{\partial\Omega_\mu^{s,b}} Y_1 H_l \, dA\right)\mathbf{I} \\ \left(\int_{\partial\Omega_\mu^{s,b}} Y_2 H_l \, dA\right)\mathbf{I} \\ \left(\int_{\partial\Omega_\mu^{s,b}} Y_3 H_l \, dA\right)\mathbf{I} \end{bmatrix}. \tag{4.84}$$

4.4.4 Homogenised higher-order stress tensor

The discrete form of Equation (3.80) can be explored to compute the homogenised higher-order stress tensor. The discretised version can be expressed as follows

$$\mathbf{Q} = \mathbf{Z}_Q \boldsymbol{\lambda} = \begin{bmatrix} \mathbf{Z}_{QD} & \mathbf{Z}_{QV} \end{bmatrix} \begin{Bmatrix} \boldsymbol{\lambda}_D \\ \boldsymbol{\lambda}_V \end{Bmatrix} = \mathbf{Z}_{QD}\boldsymbol{\lambda}_D + \mathbf{Z}_{QV}\boldsymbol{\lambda}_V, \tag{4.85}$$

where the homogenisation matrix $\mathbf{Z}_{QD}$ can be composed as

$$\mathbf{Z}_{QD} = \begin{bmatrix} \mathbf{Z}_{QD,1} & \mathbf{Z}_{QD,2} & \cdots & \mathbf{Z}_{QD,n_b} \end{bmatrix}, \tag{4.86}$$

and the contribution of each boundary node l is given by

$$\mathbf{Z}_{QD,l} = \frac{1}{2V_\mu} \begin{bmatrix} \left(\int_{\partial\Omega_\mu^{s,b}} H_l Y_1 Y_1 \; dA\right)\mathbf{I} \\ \left(\int_{\partial\Omega_\mu^{s,b}} H_l Y_2 Y_1 \; dA\right)\mathbf{I} \\ \left(\int_{\partial\Omega_\mu^{s,b}} H_l Y_3 Y_1 \; dA\right)\mathbf{I} \\ \left(\int_{\partial\Omega_\mu^{s,b}} H_l Y_1 Y_2 \; dA\right)\mathbf{I} \\ \left(\int_{\partial\Omega_\mu^{s,b}} H_l Y_2 Y_2 \; dA\right)\mathbf{I} \\ \left(\int_{\partial\Omega_\mu^{s,b}} H_l Y_3 Y_2 \; dA\right)\mathbf{I} \\ \left(\int_{\partial\Omega_\mu^{s,b}} H_l Y_1 Y_3 \; dA\right)\mathbf{I} \\ \left(\int_{\partial\Omega_\mu^{s,b}} H_l Y_2 Y_3 \; dA\right)\mathbf{I} \\ \left(\int_{\partial\Omega_\mu^{s,b}} H_l Y_3 Y_3 \; dA\right)\mathbf{I} \end{bmatrix}. \tag{4.87}$$

Finally, $\mathbf{Z}_{QV}$ is computed by Equation (4.38), i.e., this contribution is identical to the respective term presented in the minimal and periodic constraints.

4.5 Consistent macroscopic tangents

In the context of coupled multi-scale analysis, i.e., finite element simulations at the micro-scale and macro-scale, the consistent macroscopic tangents must be computed to solve the non-linear macroscopic equilibrium problem with the Newton–Raphson method. The consistent tangent matrices can be defined by

$$\mathbb{A} = \frac{\partial \mathbf{P}}{\partial \mathbf{F}}, \quad \mathbb{A}_{\mathbf{G}} = \frac{\partial \mathbf{P}}{\partial \mathbf{G}}, \tag{4.88}$$

$$\mathbb{H} = \frac{\partial \mathbf{Q}}{\partial \mathbf{G}}, \quad \mathbb{H}_{\mathbf{F}} = \frac{\partial \mathbf{Q}}{\partial \mathbf{F}}. \tag{4.89}$$

However, as previously discussed, stress tensors can be conveniently written from expressions considering the Lagrange multipliers. Specifically, the first Piola-Kirchhoff stress tensor and the higher-order stress tensor can be obtained by

$$\mathbf{P} = \mathbf{Z}_P \boldsymbol{\lambda}, \tag{4.90}$$

and

$$\mathbf{Q} = \mathbf{Z}_Q \boldsymbol{\lambda}, \tag{4.91}$$

respectively. In addition, $\mathbf{Z}_P$ and $\mathbf{Z}_Q$ are the homogenisation matrices, particularly defined for each micro-constraint.

Equations (4.90) and (4.91) are of particular interest to compute the consistent tangents for coupled multi-scale simulations, since the homogenisation matrices are constant and can be determined only at the beginning of the numerical simulation. Furthermore, the dimensions for the homogenisation matrices are relatively small. In this sense, the consistent tangent matrices can be rewritten as

$$\mathbb{A} = \mathbf{Z}_P \frac{\partial \boldsymbol{\lambda}}{\partial \mathbf{F}}, \quad \mathbb{A}_{\mathbf{G}} = \mathbf{Z}_P \frac{\partial \boldsymbol{\lambda}}{\partial \mathbf{G}}, \tag{4.92}$$

$$\mathbb{H} = \mathbf{Z}_Q \frac{\partial \boldsymbol{\lambda}}{\partial \mathbf{G}}, \quad \mathbb{H}_{\mathbf{F}} = \mathbf{Z}_Q \frac{\partial \boldsymbol{\lambda}}{\partial \mathbf{F}}, \tag{4.93}$$

where the partial derivatives encompassing the Lagrange multipliers can be computed from the solution of a linear system of equations.

The RVE equilibrium is obtained by the stationarity condition of the micro-scale residual vector $\mathbf{r}$. In this context, the equilibrium of the RVE subjected to a given $\boldsymbol{F}$ and $\mathsf{\mathbf{G}}$ can be found with

$$\frac{\partial \mathbf{r}}{\partial \mathbf{F}} = \mathbf{0}, \tag{4.94}$$

and

$$\frac{\partial \mathbf{r}}{\partial \mathbf{G}} = \mathbf{0}, \tag{4.95}$$

where $\mathbf{F}$ and $\mathbf{G}$ indicate the macro-deformation gradient and the macro-second gradient stored in vector format, respectively.

The linearisation of the discrete micro-scale equilibrium problem with $\mathbf{r} = \mathbf{0}$ yields in the general system of equations presented in Equation (4.20), where $\mathbf{C}$ is defined according to the micro-constraint model. Thus, the derivative of the residual with respect to the macro-deformation gradient, i.e., Equation (4.94), can be expressed as

$$\begin{bmatrix} \dfrac{\partial \mathbf{f}}{\partial \mathbf{F}} + \mathbf{C}^T \dfrac{\partial \boldsymbol{\lambda}}{\partial \mathbf{F}} \\ \mathbf{C} \dfrac{\partial \tilde{\mathbf{u}}}{\partial \mathbf{F}} \end{bmatrix} = \mathbf{0}, \tag{4.96}$$

where

$$\frac{\partial \mathbf{f}}{\partial \mathbf{F}} = \frac{\partial \mathbf{f}}{\partial \mathbf{u}} \frac{\partial \mathbf{u}}{\partial \mathbf{F}}. \tag{4.97}$$

In an analogous way, the derivative of the residual with respect to the macro-second gradient, i.e., Eq. (4.95), results in

$$\begin{bmatrix} \dfrac{\partial \mathbf{f}}{\partial \mathbf{G}} + \mathbf{C}^T \dfrac{\partial \boldsymbol{\lambda}}{\partial \mathbf{G}} \\ \mathbf{C} \dfrac{\partial \tilde{\mathbf{u}}}{\partial \mathbf{G}} \end{bmatrix} = \mathbf{0}, \tag{4.98}$$

with

$$\frac{\partial \mathbf{f}}{\partial \mathbf{G}} = \frac{\partial \mathbf{f}}{\partial \mathbf{u}} \frac{\partial \mathbf{u}}{\partial \mathbf{G}}. \tag{4.99}$$

In order to define the partial derivatives of the internal force vector, let us consider the discretised version of Equation (3.5):

$$\mathbf{u} = \mathbf{u}_M + \mathbf{D}^T \left(\mathbf{F} - \{\mathbf{I}\}\right) + \mathbf{V}^T \mathbf{G} + \tilde{\mathbf{u}}, \tag{4.100}$$

where $\{\mathbf{I}\}$ denotes the identity matrix in vector format. Moreover, $\mathbf{D}$ and $\mathbf{V}$ are the nodal coordinate matrices written as

$$\mathbf{D} = \begin{bmatrix} \mathbf{D}_1 & \mathbf{D}_2 & \cdots & \mathbf{D}_{n_n} \end{bmatrix}, \tag{4.101}$$

$$\mathbf{V} = \begin{bmatrix} \mathbf{V}_1 & \mathbf{V}_2 & \cdots & \mathbf{V}_{n_n} \end{bmatrix}, \tag{4.102}$$

where n_n is the number of nodes in the RVE mesh. The nodal sub-matrices are calculated as

$$\mathbf{D}_l = \begin{bmatrix} \bar{Y}_{1l}\mathbf{I} \\ \bar{Y}_{2l}\mathbf{I} \\ \bar{Y}_{3l}\mathbf{I} \end{bmatrix}, \tag{4.103}$$

$$\mathbf{V}_l = \frac{1}{2} \begin{bmatrix} \bar{Y}_{1l}\bar{Y}_{1l}\mathbf{I} \\ \bar{Y}_{2l}\bar{Y}_{1l}\mathbf{I} \\ \bar{Y}_{3l}\bar{Y}_{1l}\mathbf{I} \\ \bar{Y}_{1l}\bar{Y}_{2l}\mathbf{I} \\ \bar{Y}_{2l}\bar{Y}_{2l}\mathbf{I} \\ \bar{Y}_{3l}\bar{Y}_{2l}\mathbf{I} \\ \bar{Y}_{1l}\bar{Y}_{3l}\mathbf{I} \\ \bar{Y}_{2l}\bar{Y}_{3l}\mathbf{I} \\ \bar{Y}_{3l}\bar{Y}_{3l}\mathbf{I} \end{bmatrix}, \tag{4.104}$$

with $\bar{Y}_{il}$ denoting the i^{th} reference coordinate of node l.

Taking into account the definitions of $\mathbf{D}$ and $\mathbf{V}$, Equations (4.97) and (4.99) can be computed by

$$\frac{\partial \mathbf{f}}{\partial \mathbf{F}} = \mathbf{K} \left(\mathbf{D}^T + \frac{\partial \tilde{\mathbf{u}}}{\partial \mathbf{F}} \right) \tag{4.105}$$

and

$$\frac{\partial \mathbf{f}}{\partial \mathbf{G}} = \mathbf{K} \left(\mathbf{V}^T + \frac{\partial \tilde{\mathbf{u}}}{\partial \mathbf{G}} \right), \tag{4.106}$$

respectively. Consequently, Equations (4.96) and (4.98) can be rewritten as

$$\begin{bmatrix} \mathbf{K} & \mathbf{C}^T \\ \mathbf{C} & \mathbf{0} \end{bmatrix} \begin{bmatrix} \frac{\partial \tilde{\mathbf{u}}}{\partial \mathbf{F}} \\ \frac{\partial \boldsymbol{\lambda}}{\partial \mathbf{F}} \end{bmatrix} = - \begin{bmatrix} \mathbf{K}\mathbf{D}^T \\ \mathbf{0} \end{bmatrix} \tag{4.107}$$

and

$$\begin{bmatrix} \mathbf{K} & \mathbf{C}^T \\ \mathbf{C} & \mathbf{0} \end{bmatrix} \begin{bmatrix} \frac{\partial \tilde{\mathbf{u}}}{\partial \mathbf{G}} \\ \frac{\partial \boldsymbol{\lambda}}{\partial \mathbf{G}} \end{bmatrix} = - \begin{bmatrix} \mathbf{K}\mathbf{V}^T \\ \mathbf{0} \end{bmatrix}, \tag{4.108}$$

respectively. Therefore, the solutions of Equations (4.107) and (4.108) allow us to obtain $\partial \boldsymbol{\lambda}/\partial \mathbf{F}$ and $\partial \boldsymbol{\lambda}/\partial \mathbf{G}$.

Furthermore, Equations (4.107) and (4.108) can be combined as

$$\begin{bmatrix} \mathbf{K} & \mathbf{C}^T \\ \mathbf{C} & \mathbf{0} \end{bmatrix} \begin{bmatrix} \frac{\partial \tilde{\mathbf{u}}}{\partial \mathbf{F}} & \frac{\partial \tilde{\mathbf{u}}}{\partial \mathbf{G}} \\ \frac{\partial \boldsymbol{\lambda}}{\partial \mathbf{F}} & \frac{\partial \boldsymbol{\lambda}}{\partial \mathbf{G}} \end{bmatrix} = - \begin{bmatrix} \mathbf{K}\mathbf{D}^T & \mathbf{K}\mathbf{V}^T \\ \mathbf{0} & \mathbf{0} \end{bmatrix}. \tag{4.109}$$

Note that the linear system of equations is composed of a coefficient matrix that has already been determined to solve the micro-scale problem. Thus, the macroscopic consistent tangents can be assembled with low effort. Regarding the efficiency of the strategy, all matrices are stored in COO sparse matrix format to decrease computation time and also memory requirements. Finally, it is worth mentioning that the coordinate matrices $\mathbf{D}$ and $\mathbf{V}$ are computed only once at the problem initialisation.

5 MICRO-SCALE SIMULATIONS ACCOUNTING FOR SECOND-ORDER DEFORMATION MODES

Several numerical examples accounting for the homogenised constitutive behaviour of microstructures with voids are presented in this section. In particular, some numerical exemples were reported in Santos *et al.* (2023). The single-scale numerical experiments address two and three-dimensional RVE models under second-order deformation modes, including applications in architected materials and metamaterials. Particular attention is given to the effect of the boundary conditions, by comparing the results of the three different sets of micro-scale kinematic constraints, i.e., minimal, periodic and direct models. Several loading programs are imposed over the RVEs, encompassing second-order deformation modes. The convergence rates of the Newton-Raphson iterative solution scheme at the micro-scale are also investigated. In all simulations, the matrix material is modelled by a hyperelastic constitutive law, which is based on a linear relationship between the Kirchhoff stress tensor $\boldsymbol{\tau}$ and the logarithmic strain tensor $\boldsymbol{\varepsilon}$, defined through the elastic tensor $\mathbf{D}^e$:

$$\boldsymbol{\tau} = \mathbf{D}^e : \boldsymbol{\varepsilon}, \tag{5.1}$$

$$\boldsymbol{\varepsilon} = \ln\left(\boldsymbol{F}\boldsymbol{F}^T\right). \tag{5.2}$$

The first Piola-Kirchhoff stress tensor is then obtained through:

$$\boldsymbol{P} = \boldsymbol{\tau}\boldsymbol{F}^{-T} = \left(\mathbf{D}^e : \ln\left(\boldsymbol{F}\boldsymbol{F}^T\right)\right) \cdot \boldsymbol{F}^{-T}. \tag{5.3}$$

5.1 Homogenised constitutive behaviour: two-dimensional numerical examples

This subsection discusses examples of porous materials modelled by two-dimensional square RVE models, under the plane strain condition. These numerical simulations focused on deformation modes related to bending and extensional effects.

5.1.1 Two-dimensional micro-scale numerical example 1: RVE with a skew void

The first two-dimensional example is a porous material represented by the RVE (length $l_\mu = 1$ mm) with a skew void and porosity $f = 0.1$ or $f = 10\%$, shown in Figure 10a. The main purpose is to compute the homogenised behaviour of the RVE under three different sets of micro-scale kinematic models derived from the proposed second-order formulation (with volumetric constraint): minimal, periodic and direct constraints. In particular, the periodic model without volumetric constraint is also considered for comparison purposes. Note that the centroid of the solid part of the RVE is not positioned at the centre of the RVE. Thus, the centroid of the RVE must be calculated in order to define the origin of the coordinate system, ensuring the validity of the formulation. Moreover, although simple, the lack of symmetry of the RVE is interesting for clarifying the differences in results. The macroscopic second gradient with $\mathsf{G}_{122} = 0.1$ mm^{-1} (curvature deformation mode associated with bending) was imposed over the RVE. The macroscopic deformation is gradually applied in 5 equally spaced increments. The isoparametric 8-noded quadratic quadrilateral element (Q8) with 9 integration points was adopted for the numerical simulation with finite elements. The corresponding finite element mesh is illustrated in Figure 10b. The elastic properties of the matrix are characterised by the Young modulus $E = 210$ GPa and Poisson ratio $\nu = 0.3$.

Table 1 reports the evolution of the relative residual norm during the last incremental step of the Newton-Raphson iterative solution at the micro-scale for each micro-constraint. Therefore, the consistency of the computational strategy for two-dimensional numerical analyses is confirmed by the quadratic convergence rates.

Figure 10 – Geometry and mesh for the RVE with a skew void ($f = 0.1$).

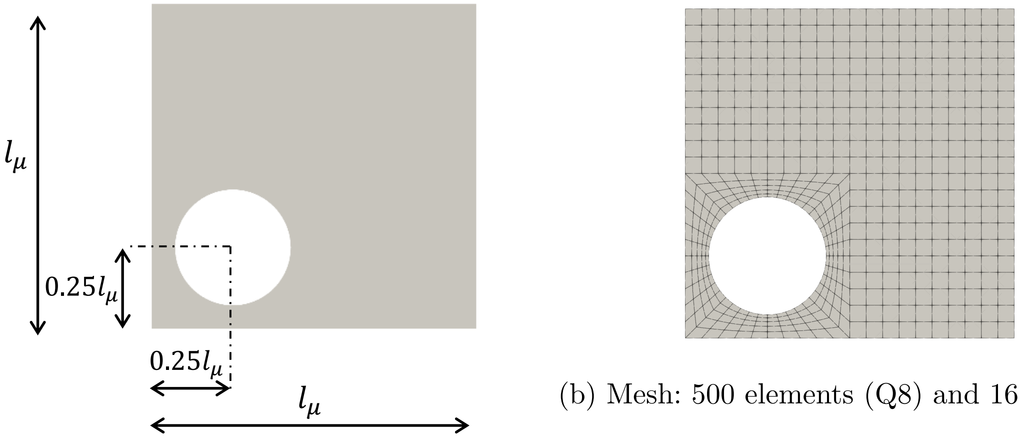

(a) Geometry.

(b) Mesh: 500 elements (Q8) and 1620 nodes.

Source: The author.

Table 1 – Convergence rates at the micro-scale in the last incremental step for the sets of kinematic constraints over the 2D RVE, where the tolerance for the iterative procedure is set to 1.0 x 10^{-6}.

Model	Relative residual norm (%): micro-scale constraint model			
	Iteration 1	Iteration 2	Iteration 3	Iteration 4
Direct	8.9350	0.26290 x 10^{-1}	0.28651 x 10^{-6}	–
Periodic	23.825	0.43388 x 10^{-1}	0.61822 x 10^{-6}	–
Minimal	31.995	0.53851	0.11572 x 10^{-3}	0.16615 x 10^{-10}

Source: The author.

The homogenised values of the stress tensors ($\boldsymbol{P}$ and $\boldsymbol{\mathsf{Q}}$) for different sets of micro-scale kinematic constraints considering the curvature (G_{122}) modes are presented in Table 2. The distributions of the microscopic effective Cauchy stress are shown in Figure 11 for G_{122}

mode. The results of the periodic model without the volumetric constraint on the solid part of the RVE are also compared to the models derived from the new formulation based on MMVP proposed in the present work. It is important to observe that the new formulation accounts for the volumetric constraint of Equation (3.18) for all micro-constraints: minimal, periodic and direct models. In general, the numerical results for the micro-scale kinematic constraints derived from the *Method of the Multi-Scale Virtual Power* are close, especially for the components with higher values. The minimal model is a lower bound, while the direct model is an upper bound. Thus, the periodic model provides an intermediate result for the loading programme under analysis. This conclusion is supported by the following relation between the admissible space for each boundary condition: $\tilde{\mathcal{V}}^{dir} \subset \tilde{\mathcal{V}}^{per} \subset \tilde{\mathcal{V}}$. Note that the RVE deformed configurations are logic for all cases: (i) the direct model has a more restrictive deformation mode on the RVE outer boundary; (ii) the periodic model respects the periodicity on opposite faces, and (iii) the minimal model is less restrictive on the RVE outer boundary. Additionally, problems related to the appearance of spurious effects in the edges were not observed, demonstrating the importance of the volumetric constraint in the second-order computational homogenisation formulation.

Table 2 – Homogenised results for $\boldsymbol{P}$ and Q after imposing $\mathsf{G}_{122} = 0.1$ mm^{-1}.

Component	Micro-scale kinematic constraint model			
	Direct	Periodic	Minimal	Periodic without volumetric constraint
P_{11} (MPa)	-33.4554	-25.9676	-42.6139	-329.0280
P_{22} (MPa)	-27.2810	-24.7001	-36.9473	-136.0271
P_{12} (MPa)	144.0650	200.6139	349.5407	304.3218
P_{21} (MPa)	143.7778	200.9082	349.0771	298.3527
Q_{111} (MPa mm)	-5.1262	-12.5697	-2.4594	-413.6475
Q_{211} (MPa mm)	-93.9658	-110.2824	-155.6519	-65.4166
$\mathsf{Q}_{112} = \mathsf{Q}_{121}$ (MPa mm)	-43.0276	-55.0980	-81.5046	10.8032
$\mathsf{Q}_{212} = \mathsf{Q}_{221}$ (MPa mm)	281.4644	267.5469	235.7000	130.7798
Q_{122} (MPa mm)	566.4371	546.5243	494.0407	444.8555
Q_{222} (MPa mm)	2.8715	-2.9425	4.6359	59.6910

Source: The author.

On the other hand, the numerical results from the present framework based on MMVP have significant differences when compared to the periodic model without the volumetric constraint. For example, the big differences in results for components P_{11} and Q_{111} can be mentioned. The absence of the volume constraint approach requires the imposition of null fluctuations at the corners of the RVE in order to avoid rigid body motion, leading to a non-physical localisation near the RVE corners (see Figure 11d). Some considerations in this sense were discussed by (Lopes; Pires, 2022b) and (Lopes; Pires, 2022d) in the context of composite materials. This kind of issue is not observed in the present formulation for any of the micro-constraints.

Figure 11 – Microscopic effective Cauchy stress (MPa) for deformed RVEs (exaggerated 10 times) under $\mathsf{G}_{122} = 0.1$ mm^{-1}.

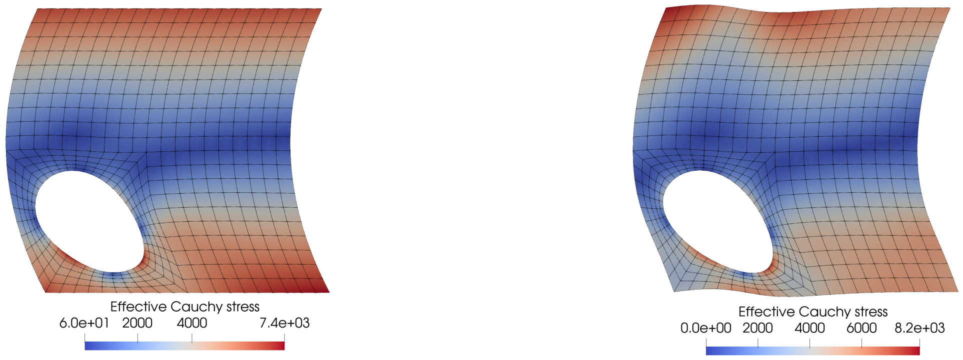

(a) Direct. (b) Periodic.

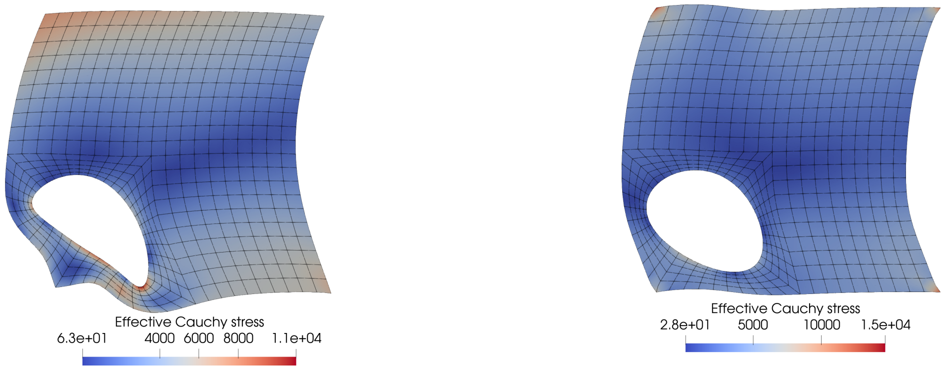

(c) Minimal. (d) Periodic without volumetric constraint.

Source: The author.

5.1.2 Two-dimensional micro-scale numerical example 2: RVE with two skew voids

The RVE (length $l_\mu = 1$ mm) with two skew voids (total porosity $f = 0.06$) shown in Figure 12a is investigated in the second two-dimensional numerical example. In order to further evaluate the role of the models in the effective constitutive behaviour, the micro-scale kinematic constraints derived from *Method of the Multi-Scale Virtual Power* are compared to other second-order deformation modes. In this sense, the loading programme imposed over the RVE consists in $\mathsf{G}_{111} = 0.1$ mm^{-1}, i.e. extensional mode, where the longitudinal transition from a compression to a traction zone is observed. The loading programme is gradually applied in 5 equally spaced increments. Since the RVE has symmetry only with respect to the vertical axis, the effect of the extensional modes is clearly illustrated in the deformed configurations of the RVE. Furthermore, Figure 12b shows the RVE mesh composed by isoparametric 8-node quadrilateral element (Q8) with 9 integration points. The matrix properties are $E = 210$ GPa and $\nu = 0.3$.

Table 3 shows the comparisons of the $\boldsymbol{P}$ and $\boldsymbol{\mathsf{Q}}$ for different micro-scale kinematic constraints models after the RVE subject to $\mathsf{G}_{111} = 0.1$ mm^{-1}. The effect of extensional mode is more clear for the RVE, where the left void is compressed, and the right void is tensioned (see Figure 13). In general, the comparison of homogenised results indicates that the direct model provides an upper bound, the periodic model results in an intermediate limit and the minimal model is a lower bound.

Figure 12 – Geometry and mesh for RVE with two voids ($f = 0.06$).

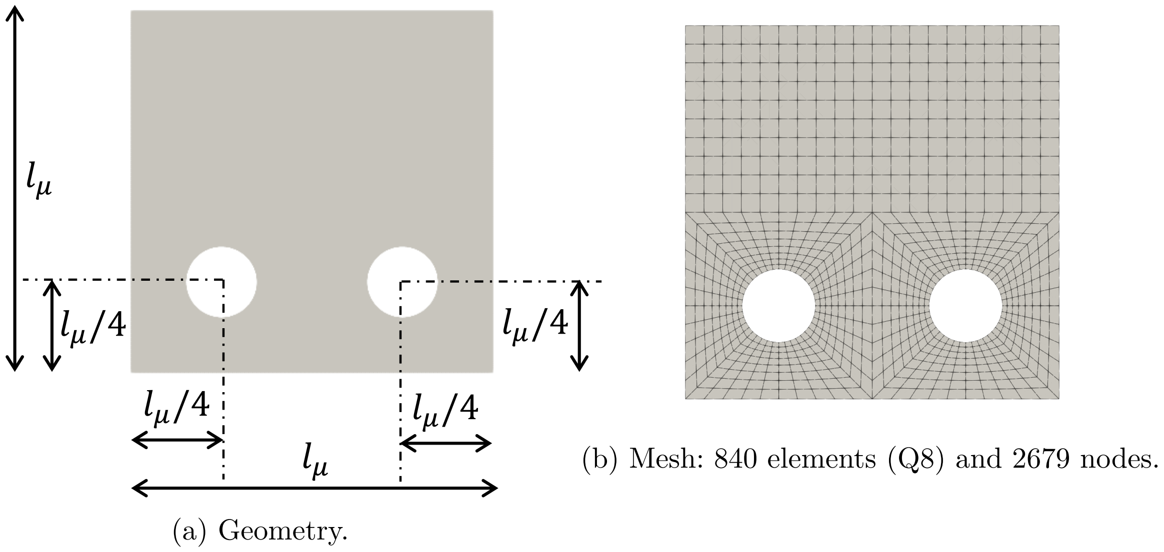

(a) Geometry.

(b) Mesh: 840 elements (Q8) and 2679 nodes.

Source: The author.

Table 3 – Homogenised results for $\boldsymbol{P}$ and Q after impose $\mathsf{G}_{111} = 0.1$ mm^{-1}.

Component	Micro-scale kinematic constraint model		
	Direct	Periodic	Minimal
P_{11} (MPa)	-305.1433	-279.4515	-241.0182
P_{22} (MPa)	-59.4505	-66.8041	-74.1833
P_{12} (MPa)	-3.0946	4.3047	12.9373
P_{21} (MPa)	-3.1168	4.3131	13.0238
Q_{111} (MPa mm)	2050.1935	1989.3619	1943.4949
Q_{211} (MPa mm)	0.2219	-0.0839	-0.8652
$\mathsf{Q}_{112} = \mathsf{Q}_{121}$ (MPa mm)	-1.2227	4.2973	1.7968
$\mathsf{Q}_{212} = \mathsf{Q}_{221}$ (MPa mm)	422.7321	420.2795	413.0163
Q_{122} (MPa mm)	-0.8103	-6.3774	-10.7156
Q_{222} (MPa mm)	3.8426	7.6030	12.8187

Source: The author.

Note that the RVE deformed configurations in Figure 13 make sense for all cases: (i) the direct model has a more restrictive deformation mode on the RVE outer boundary; (ii) the periodic model respect the periodicity on the opposite faces, and (iii) the minimal model is less restrictive on the RVE outer boundary. Moreover, no problems related to the appearance of spurious effects in the edges were observed, corroborating to demonstrate the importance of the volumetric constraint in the second-order computational homogenisation formulation.

Figure 13 – Microscopic effective Cauchy stress (MPa) for deformed RVEs under $\mathsf{G}_{111} = 0.1\ \text{mm}^{-1}$.

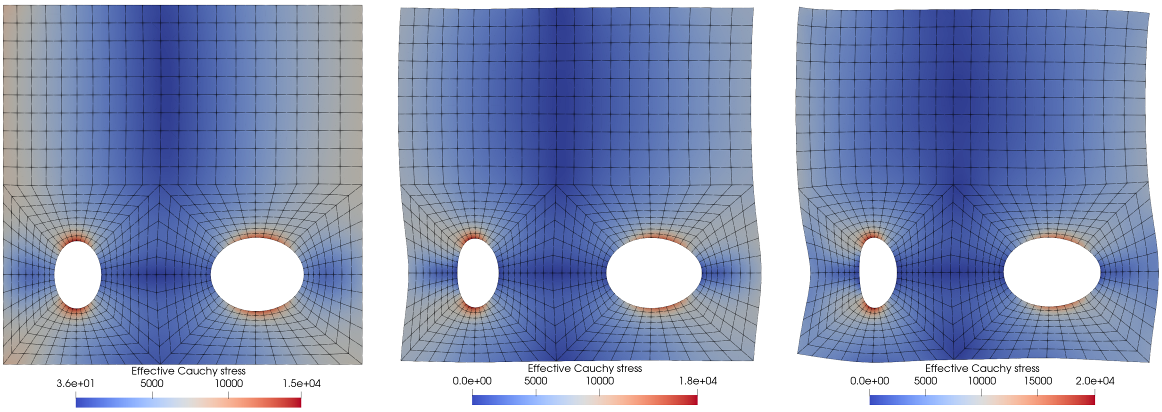

(a) Direct.

(b) Periodic.

(c) Minimal.

Source: The author.

5.1.3 Two-dimensional micro-scale numerical example 3: RVE with a centred void compared to RVE with random voids

The third two-dimensional example evaluates the influence of the void distributions in the RVE of a porous media. Specifically, two distributions of voids were assumed, both with a void volume fraction of $f = 20\%$: (i) RVE with a centred void (see Figure 14a), and (ii) RVE with randomly distributed voids (see Figure 14b).

Figure 14 – Finite element mesh data.

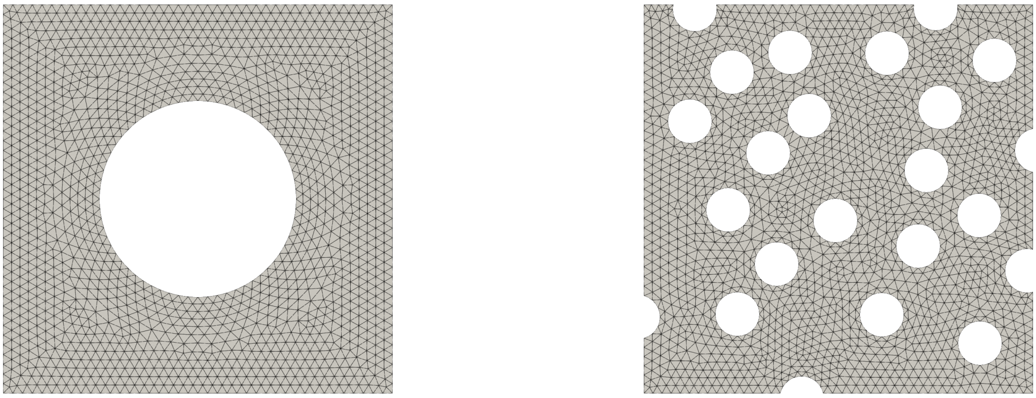

(a) Mesh for the RVE with a centred void ($f = 0.2$): 2792 elements (T6) and 5808 nodes.

(b) Mesh for the RVE with 20 randomly distributed voids ($f = 0.2$): 3242 elements (T6) and 6930 nodes.

Source: The author.

The RVE with random voids is composed of voids inside the RVE and on its outer boundary, exemplifying the robustness and generality of the new second-order computational homogenisation framework proposed for investigating solid porous. In particular, the RVE with randomly distributed voids contains voids on the RVE outer boundary without symmetry in relation to the opposite faces, i.e., non-periodic voids on the RVE outer boundary. Thus, the mean normal computed by Equation (3.13) is not null for the RVE with random voids when analysed with the minimal model and must be accounted for in the numerical simulation. It should be emphasised that the mean normal is null when the minimal model is adopted for RVEs without voids on their outer boundary and RVEs with periodic voids on the opposite faces of their outer boundary. The RVEs are subjected to $\mathsf{G}_{112} = 0.1$ mm^{-1}, i.e., trapezoidal mode associated with bending. The loading programme is gradually applied considering 5 increments. The finite element meshes adopted - all consisting of isoparametric 6-noded quadratic triangle element (T6) with 3 integration points - are presented in Figure 14. The material properties for the solid matrix are $E = 210$ GPa and $\nu = 0.3$.

Table 4 shows the homogenised results of $\boldsymbol{P}$ and $\mathbf{Q}$ for the RVEs subjected to $\mathsf{G}_{112} = 0.1$ mm^{-1}. The periodic model is not compared due to the non-periodic RVE boundary for the second case (see Figure 14b). Therefore, only the direct and minimal models are compared. The distribution of voids has a strong influence on the homogenised macroscopic constitutive behaviour. Some components of $\boldsymbol{P}$ and $\mathbf{Q}$ are null for the RVE with a centred void due to the symmetry of the solid part. Regarding the components more important for the loading programme imposed, the values of the stress tensors for the RVE with a centred void are higher when compared to the RVE with random voids.

Table 4 – Homogenised results for $\boldsymbol{P}$ and $\mathbf{Q}$ after imposing $\mathsf{G}_{112} = 0.1$ mm^{-1}.

Component	Centred void		Random voids	
	Direct	Minimal	Direct	Minimal
P_{11} (MPa)	-317.6065	-296.9127	-589.1455	-614.8182
P_{22} (MPa)	-30.9059	-26.8477	-183.0764	-134.7864
P_{12} (MPa)	0.0000	0.0000	0.9539	2.3533
P_{21} (MPa)	0.0000	0.0000	-2.8373	0.5443
Q_{111} (MPa mm)	0.0000	0.0000	42.9006	-27.2048
Q_{211} (MPa mm)	596.1395	578.3077	445.9014	410.1697
$\mathsf{Q}_{112} = \mathsf{Q}_{121}$ (MPa mm)	1366.0727	1342.4660	938.8182	848.0962
$\mathsf{Q}_{212} = \mathsf{Q}_{221}$ (MPa mm)	0.0000	0.0000	18.9557	9.0452
Q_{122} (MPa mm)	0.0000	0.0000	24.2309	28.5504
Q_{222} (MPa mm)	862.6601	854.0854	553.3661	563.0373

Source: The author.

The distributions of the microscopic effective Cauchy stress can be viewed in Figure 15. The deformed configurations and the microscopic stress distributions at the micro-scale have significant differences with random voids, especially when the minimal constraint model is compared to the direct model. Therefore, the constitutive behaviour of porous materials can be complicated and require more robust strategies to obtain more accurate results.

Figure 15 – Microscopic effective Cauchy stress (MPa) for deformed RVEs (exaggerated 5 times) subjected to $\mathsf{G}_{112} = 0.1$ mm^{-1}.

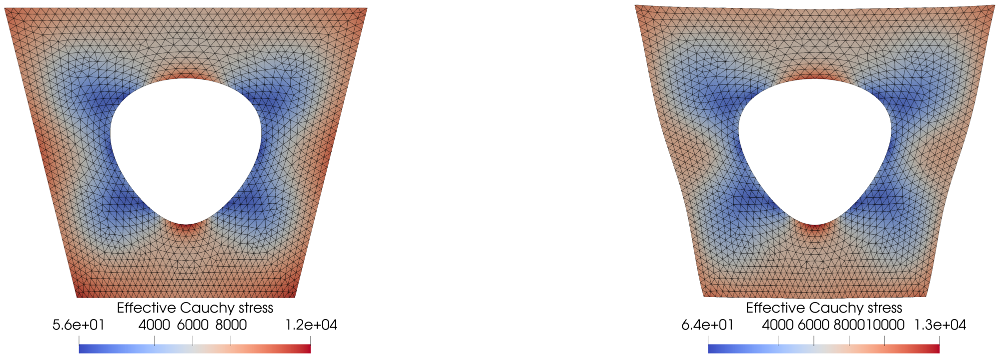

(a) RVE with a centred void: Direct.

(b) RVE with a centred void: Minimal.

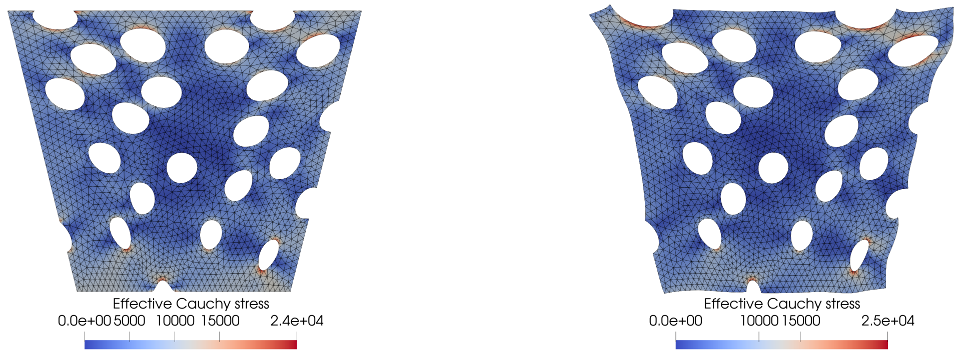

(c) RVE with random voids: Direct.

(d) RVE with random voids: Minimal.

Source: The author.

5.1.4 Two-dimensional micro-scale numerical example 4: comparative study with Kouznetsova, Geers and Brekelmans (2004b)

This subsection addresses the role of the RVE size in the developed second-order computational homogenisation approach. The set of numerical analyses was inspired in a study performed by Kouznetsova, Geers and Brekelmans (2004b), where the hypothesis of a hypoelastic material was adopted for the RVE matrix. However, in this study, a linear elastic constitutive law considering the Eulerian logarithmic strain tensor is assumed in a finite strain framework. The matrix elastic properties are E = 210 GPa and ν = 0.3. The numerical analyses are computed under plane strain condition. RVEs composed by 1, 4, 9 and 16 periodic unit cells are investigated (see Figure 16). Each unit cell has a single circular void, and the cell length is l_μ = 0.001 mm. The void volume fraction of the cell is f = 0.1 or f = 10%. Meshes presented in Figure 17 are composed by isoparametric 8-node quadrilateral element (Q8) with 9 integration points. Note that the same number of finite elements (320 elements) is adopted for each unit cell. Moreover, the meshes are structured, and this characteristic helps to reduce the propagation of errors in different directions. The RVEs have been subjected to a bending-tension deformation path composed by: F_{11} = 1.1, F_{22} = 0.9, G_{211} = -18 mm^{-1}, G_{121} = G_{112} = 12 mm^{-1} and G_{222} = -8 mm^{-1}. The loading programme is prescribed in 100 increments. The main goal of the numerical tests is to compare the homogenised curves that relate: (i) Green-Lagrange strain norm $||\boldsymbol{E}||$ and the first Piola-Kirchhoff stress norm $||\boldsymbol{P}||$, (ii) second-gradient norm $||\mathbf{G}||$ and the higher-order stress norm $||\mathbf{Q}||$.

The norms $||\boldsymbol{E}||$ and $||\boldsymbol{P}||$ are given by:

$$||\boldsymbol{E}|| = \sqrt{E_{ij}E_{ij}}, \quad \text{and} \quad ||\boldsymbol{P}|| = \sqrt{P_{ij}P_{ij}}, \tag{5.4}$$

respectively. In addition, $||\mathbf{G}||$ and $||\mathbf{Q}||$ are calculated by:

$$||\mathbf{G}|| = \sqrt{\mathsf{G}_{ijk}\mathsf{G}_{ijk}}, \quad \text{and} \quad ||\mathbf{Q}|| = \sqrt{\mathsf{Q}_{ijk}\mathsf{Q}_{ijk}}, \tag{5.5}$$

respectively.

Figure 16 – Geometry: (a) RVE - 1 cell: $l_\mu = 0.001$ mm; (b) RVE - 4 cells: $l_\mu = 0.002$ mm; (c) RVE - 9 cells: $l_\mu = 0.003$ mm; (d) RVE - 16 cells: $l_\mu = 0.004$ mm.

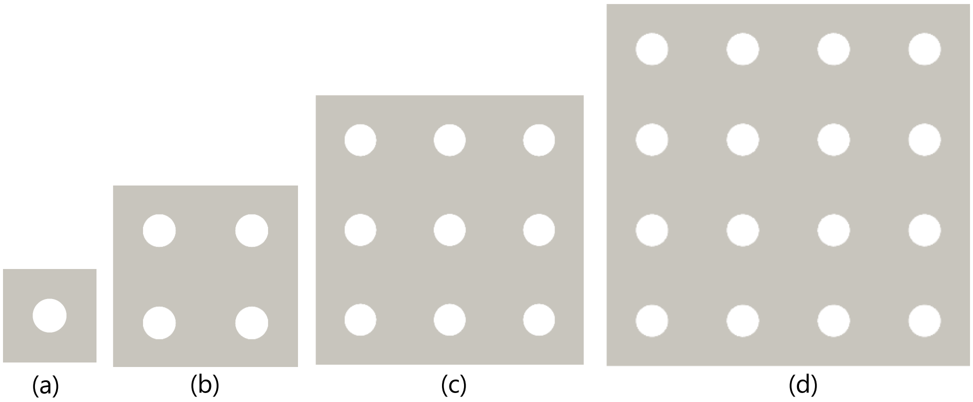

Source: The author.

Figure 17 – Meshes using the isoparametric 8-noded quadratic quadrilateral element (Q8).

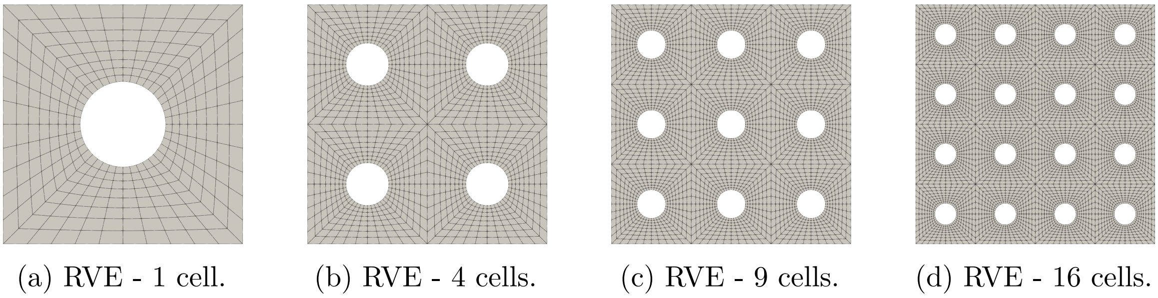

(a) RVE - 1 cell. (b) RVE - 4 cells. (c) RVE - 9 cells. (d) RVE - 16 cells.

Source: The author.

Figure 22 shows the distributions of the microscopic effective Cauchy stress for each RVE. The curves $||\boldsymbol{P}|| - ||\boldsymbol{E}||$ and $||\mathbf{Q}|| - ||\mathbf{G}||$ with the homogenised results for each RVE are shown in Figures 18 and 20, respectively. Note that minimal (M), periodic (P) and direct (D) micro-scale kinematic constraints are compared to the formulation without the volumetric constraint proposed by Kouznetsova (2002) (KP). Comparisons encompassing all RVEs for each micro-scale contraint are presented in Figures 19 and 21, respectively.

Table 5 – Mesh of RVE models.

DNS	**Elements (Q8)**	**Nodes**
Size 1 (1 cell) ($l_\mu = 0.001$ mm)	320	1040
Size 2 (4 cells) ($l_\mu = 0.002$ mm)	1280	4077
Size 3 (9 cells) ($l_\mu = 0.003$ mm)	2880	9112
Size 4 (16 cells) ($l_\mu = 0.004$ mm)	5120	59316

Source: The author.

Regarding the comparison of micro-scale constraints for each RVE (see Figure 18), the curves $||\boldsymbol{P}|| - ||\boldsymbol{E}||$ indicate that the minimal micro-constraint is a lower bound when compared with other micro-constraints based on the MMVP. In particular, the minimal model provides a significant reduction in the homogenised response for the RVE with a unit cell. The periodic and direct models have close results. The model based on Kouznetsova's formulation is close to the periodic and direct micro-constraints for RVE with fewer cells and close to the minimal micro-constraint for RVE with more cells. In general, the differences in the comparative study of the models are more significant for RVEs with fewer cells. This difference in results is strongly associated with the microscopic fields of the RVEs after solving the Micro-scale equilibrium problem. As shown in Figure 22, the deformed configuration of the RVE with a single cell under minimal constraint is clearly different when compared to other models. The RVE size influences the homogenised first Piola-Kirchhoff stress norm, especially in the case of minimal constraint. With regard to the comparison between the number of cells for the same micro-scale constraint (see Figure 19), the increase of the RVE size provides a reduction of $||\boldsymbol{P}||$ for direct, periodic and Kouznetsova models. Nevertheless, the RVE with a single cell under the minimal model results in a more flexible homogenised response.

On the other hand, more significant differences are observed in the comparison of homogenised curves $||\mathbf{Q}|| - ||\mathbf{G}||$ (see Figure 20). Firstly, the micro-contraint effect is more evident in the case of higher-order stress. For RVEs with more cells, the comparison of micro-constraints based on the MMVP indicates that the minimal model results in a lower bound and the direct model provides an upper bound. However, the homogenised results for the RVE with a single cell is different, where the minimal model provides an upper bound. This difference is related to the microscopic fields, including the deformed configuration of the RVE (see Figure 22). In addition, the model based on Kouznetsova's formulation results in the most flexible homogenised response among all models. It is also worth mentioning the problems related to the appearance of spurious effects in the RVE edges (localisation) simulated with the Kouznetsova's formulation (see Figures 22a 22e, 22i, and 22m). Secondly, the RVE size has a strong influence on the homogenised behaviour of the high-order stress norm (see Figure 21). In summary, larger RVEs provide higher values for $||\mathbf{Q}||$.

Figure 18 – $||\boldsymbol{P}|| - ||\boldsymbol{E}||$: different micro-constraint models for each RVE.

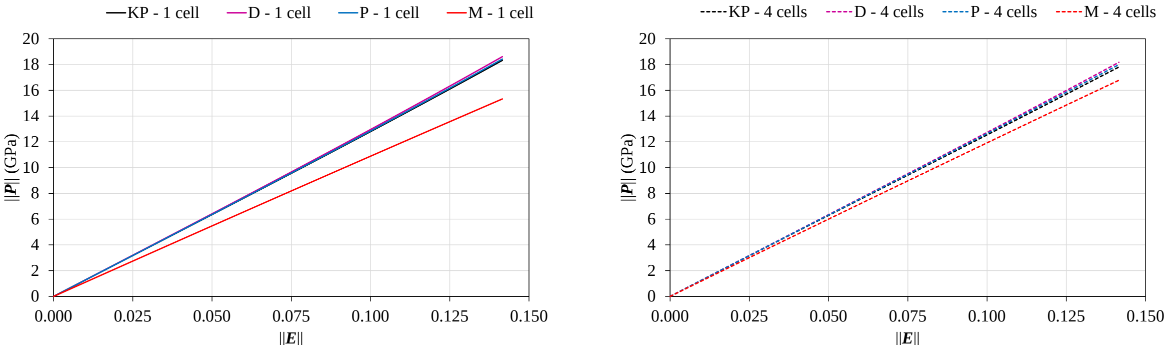

(a) RVE - 1 cell. (b) RVE - 4 cells.

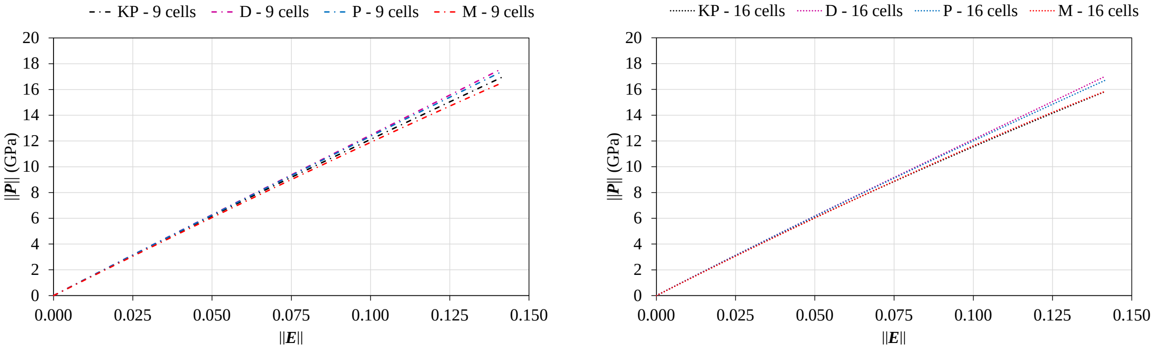

(c) RVE - 9 cells. (d) RVE - 16 cells.

Source: The author.

Figure 19 – $||\boldsymbol{P}|| - ||\boldsymbol{E}||$: different RVE sizes for each micro-constraint model.

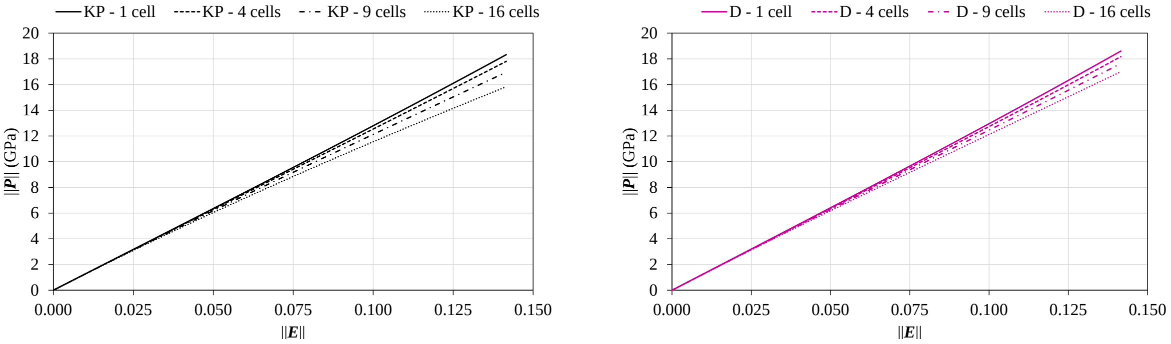

(a) Kouznetsova's model. (b) Direct model.

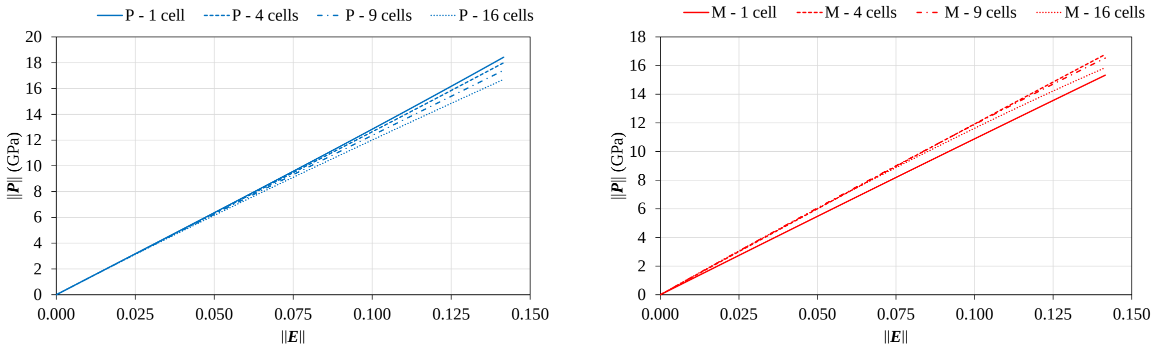

(c) Periodic model. (d) Minimal model.

Source: The author.

Figure 20 – $\|\mathbf{Q}\| - \|\mathbf{G}\|$: different micro-constraint models for each RVE.

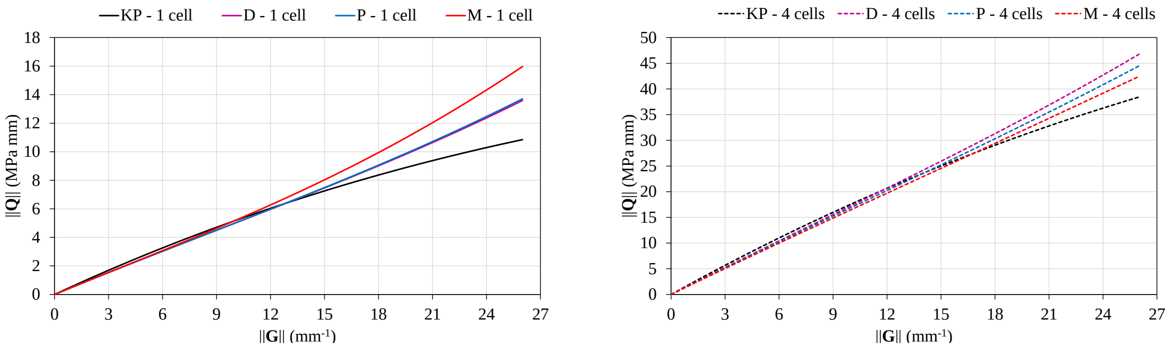

(a) RVE - 1 cell.

(b) RVE - 4 cells.

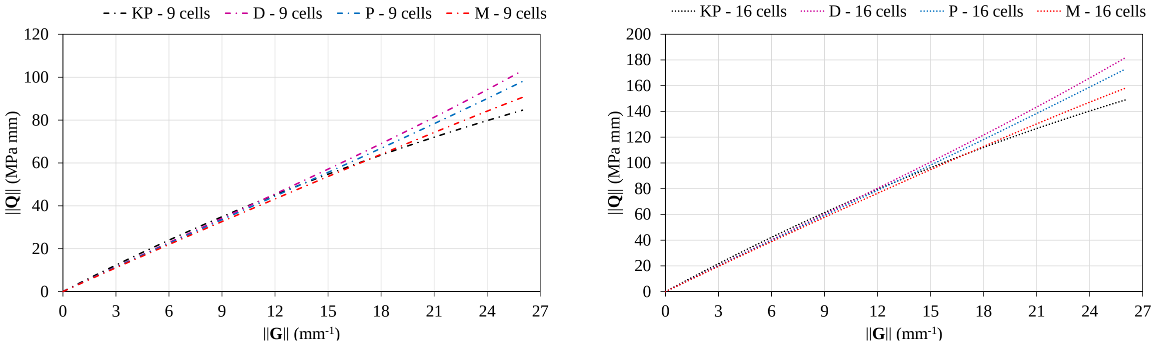

(c) RVE - 9 cells.

(d) RVE - 16 cells.

Source: The author.

Figure 21 – $\|\mathbf{Q}\| - \|\mathbf{G}\|$: different RVE sizes for each micro-constraint model.

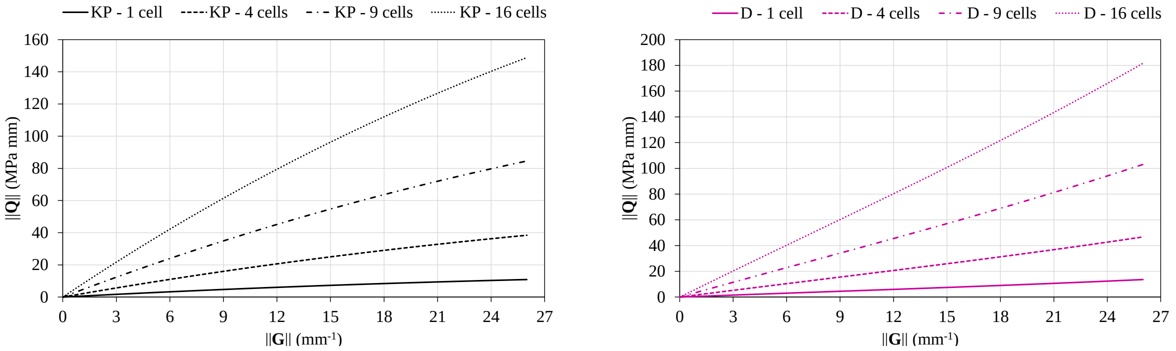

(a) Kouznetsova's model.

(b) Direct model.

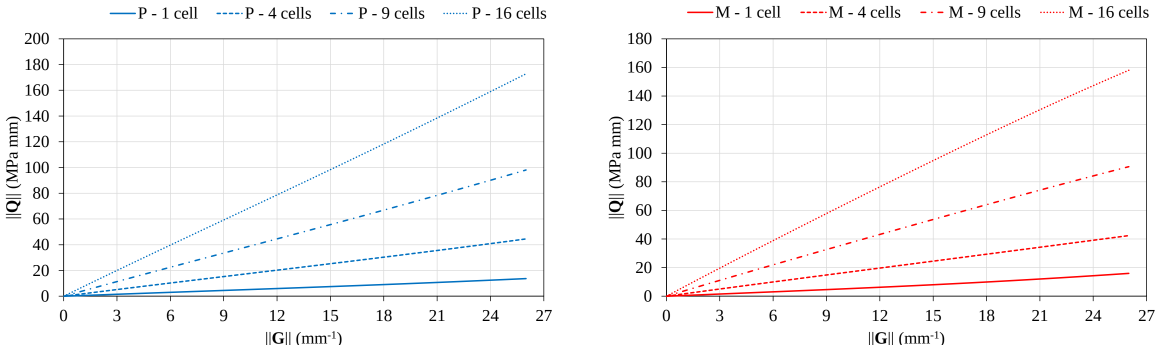

(c) Periodic model.

(d) Minimal model.

Source: The author.

Figure 22 – Microscopic effective Cauchy stress (MPa) for all deformed RVEs.

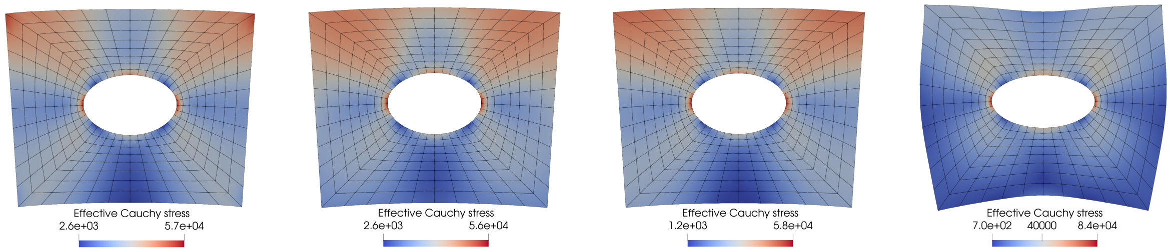

(a) RVE-1: Reference. (b) RVE-1: Direct. (c) RVE-1: Periodic. (d) RVE-1: Minimal.

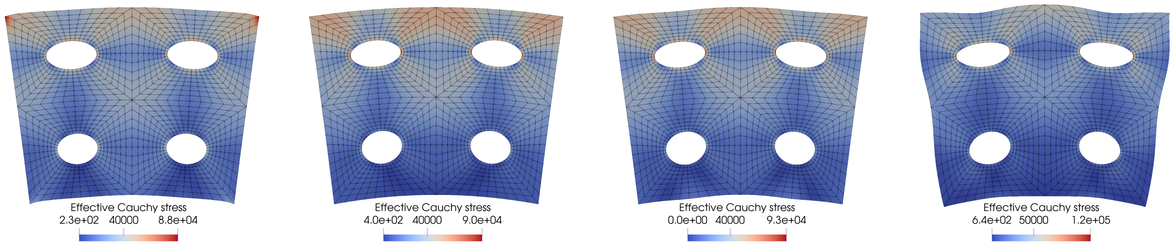

(e) RVE-4: Reference. (f) RVE-4: Direct. (g) RVE-4: Periodic. (h) RVE-4: Minimal.

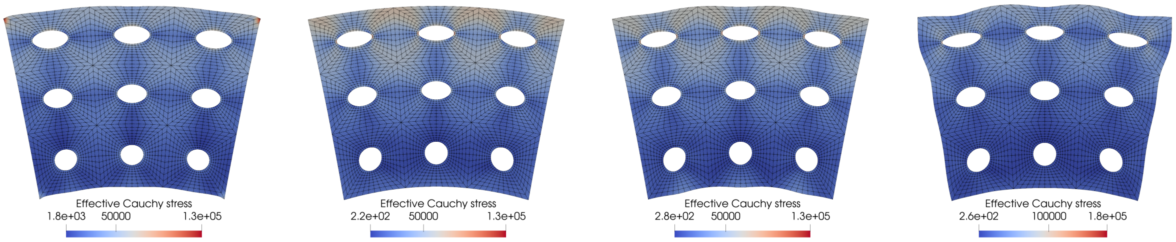

(i) RVE-9: Reference. (j) RVE-9: Direct. (k) RVE-9: Periodic. (l) RVE-9: Minimal.

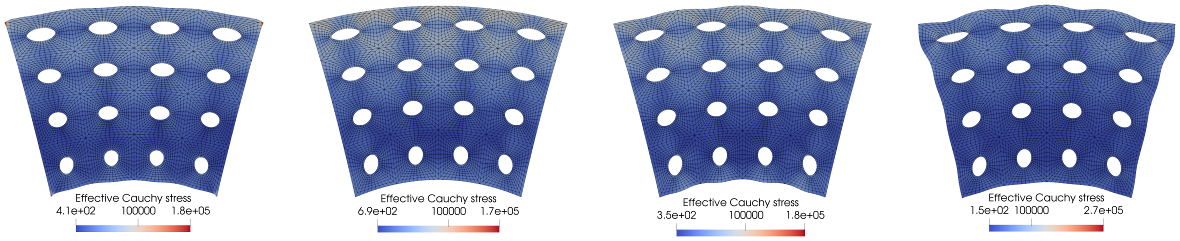

(m) RVE-16: Reference. (n) RVE-16: Direct. (o) RVE-16: Periodic. (p) RVE-16: Minimal.

Source: The author.

5.2 Homogenised constitutive behaviour: three-dimensional numerical examples

Examples of porous materials modelled by three-dimensional cubic RVE models are investigated here. This set of numerical simulations is focused on second-order deformation modes associated with bending and torsion. Different micro-scale kinematic constraints are imposed on the RVEs to understand their influence on the macroscopic homogenised constitutive behaviour.

5.2.1 Three-dimensional micro-scale numerical example 1: RVE of a cubic lattice structure

The first three-dimensional example aims to investigate the constitutive behaviour of a cubic lattice structure, whose geometry is detailed in Figure 23a. The RVE length and the elastic properties of the matrix in this three-dimensional example are the same adopted for the two-dimensional examples. Thus, $l_\mu = 1$ mm and the matrix elastic properties are $E = 210$ GPa and $\nu = 0.3$. A macroscopic second gradient defined by $\mathsf{G}_{122} = 0.1$ mm^{-1}, a component related to bending, is applied to the RVE in 5 equally spaced increments. Isoparametric 20-noded hexahedral elements (H20) with 8 integration points are employed, as illustrated in Figure 23b.

Figure 23 – Geometry and mesh for the RVE of a cubic lattice structure.

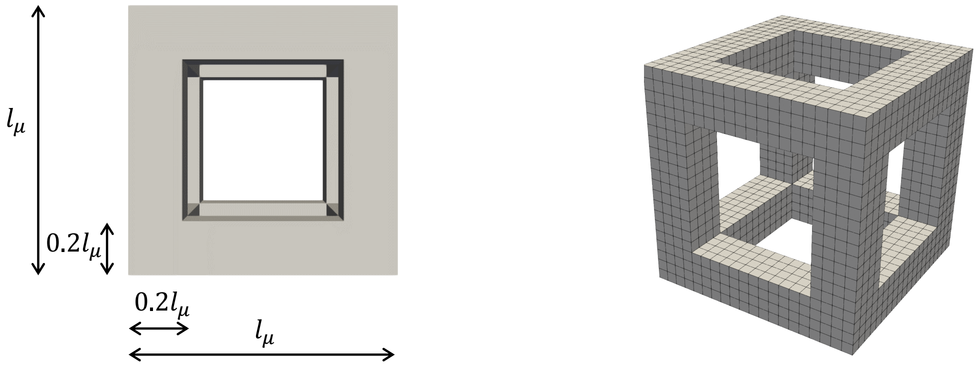

(a) Geometry.

(b) Mesh: 2816 elements (H20) and 15580 nodes.

Source: The author.

The robustness of the three-dimensional computational strategy is demonstrated by the quadratic convergence rate obtained in the micro-scale Newton–Raphson iterative scheme, as presented in Table 6 for the last incremental step of each constraint model.

Table 6 – Convergence rates at the micro-scale in the last incremental step for the sets of micro-scale kinematic constraints over the 3D RVE, where the defined tolerance for the iterative procedure is set to 1.0 x 10^{-6}.

Model	Relative residual norm (%): micro-scale constraint model			
	Iteration 1	Iteration 2	Iteration 3	Iteration 4
Dicrect	25.378	0.07991	0.27683 x 10^{-5}	0.61700 x 10^{-11}
Periodic	28.262	0.14241	0.43332 x 10^{-5}	0.72473 x 10 $^{-11}$
Minimal	33.067	0.32849	0.59438 x 10^{-4}	0.54844 x 10^{-10}

Source: The author.

Table 7 shows the homogenised results of $\boldsymbol{P}$ and $\mathbf{Q}$ for the RVE subjected to G_{122}, considering the different micro-scale kinematic constraints. Figure 24 presents the distributions of the microscopic effective Cauchy stress for all models investigated. The selected kinematic constraint has a strong influence over the values of the homogenised stress tensors. As discussed previously, the minimal model represents a lower bound, the direct model provides an upper bound and the periodic model is an intermediate response. There is a significant reduction of the values for the high-order stress components Q_{122} and $\mathsf{Q}_{212} = \mathsf{Q}_{221}$ in the minimal model when compared to other kinematic constraints (periodic and direct). The deformed configurations presented in Figure 24c show that the minimal model provides an RVE that is more flexible. In addition, stress concentrations are observed on edges and corners, which is typical of problems of this type. However, more refined meshes were simulated and the relative differences in the homogenised results were minimal.

Table 7 – Homogenised results for $\boldsymbol{P}$ and $\boldsymbol{\mathsf{Q}}$ after imposing $\mathsf{G}_{122} = 0.1$ mm^{-1}.

Component	Micro-scale kinematic constraint model		
	Direct	Periodic	Minimal
P_{11} (MPa)	-8.3009	-3.7733	19.6450
P_{22} (MPa)	-7.1382	-0.6186	-7.2831
P_{33} (MPa)	3.3845	3.9701	-0.0318
Q_{111} (MPa mm)	1.6411	15.4585	-22.9042
Q_{122} (MPa mm)	299.0681	251.1346	197.0719
Q_{133} (MPa mm)	-1.5851	33.6097	39.3591
$\mathsf{Q}_{212} = \mathsf{Q}_{221}$ (MPa mm)	130.7025	107.6551	32.6638
$\mathsf{Q}_{313} = \mathsf{Q}_{331}$ (MPa mm)	-8.4999	11.5102	15.8195

Source: The author.

Figure 24 – Microscopic effective Cauchy stress (MPa) for deformed RVEs (exaggerated 10 times) under $\mathsf{G}_{122} = 0.1$ mm^{-1}.

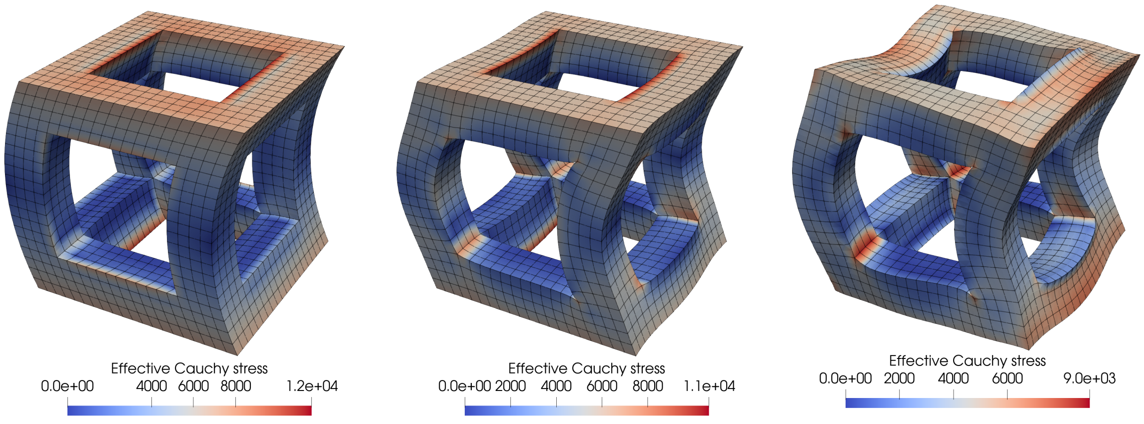

(a) Direct.

(b) Periodic.

(c) Minimal.

Source: The author.

5.2.2 Three-dimensional micro-scale numerical example 2: RVE with unidirectional voids

The second three-dimensional example aims to investigate the constitutive behaviour of a RVE with unidirectional holes of circular cross-section (see Figure 25a). To illustrate the twisting/torsion deformation mode for 3D problems, the component $\mathsf{G}_{123} = 0.1$ mm^{-1} is imposed over the RVE. The loading programme is prescribed over the RVEs considering

5 increments. The three micro-scale kinematic constraints are assessed. For simplicity, the RVE length is $l_\mu = 1$ mm and the matrix elastic properties are $\mathbb{E} = 210$ GPa and $\nu = 0.3$. The total porosity of the RVE is $f = 0.3$ or $f = 30\%$ and the voids have the same diameter (d). The mesh show in Figure 25b is composed by 20-noded hexahedral element (H20) with 8 integration points.

Figure 25 – Geometry and mesh for RVE with unidirectional voids ($f = 0.3$).

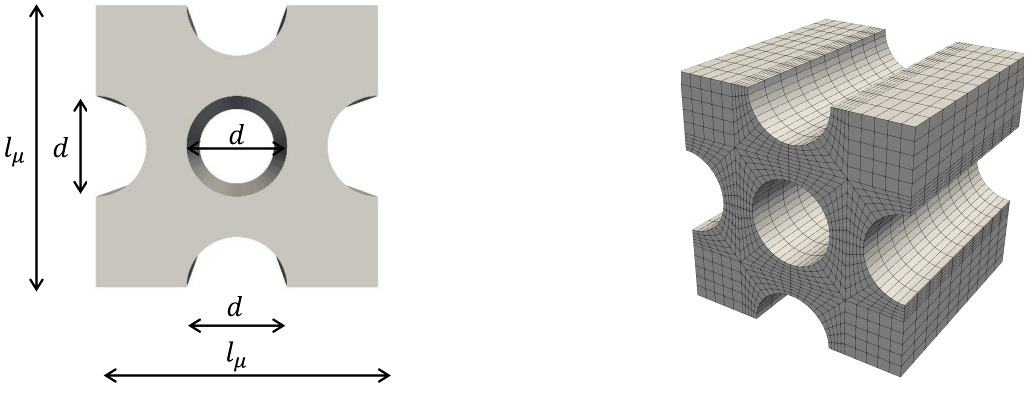

(a) Geometry.

(b) Mesh: 7000 elements (H20) and 33300 nodes.

Source: The author.

The homogenised results of $\boldsymbol{P}$ and $\mathbf{Q}$ for the RVE subjected to $\mathsf{G}_{123} = 0.1$ mm^{-1} are summarised in Table 8. For this loading programme, the homogenised results indicate that the direct and minimal micro-constraints provide the upper and lower bounds, respectively. Consequently, the periodic micro-constraint provide an intermediate effective behaviour. These conclusions match the results and discussions presented in previously examples. Significant differences are observed in the homogenised stress components, specially when the minimal model is compared to direct model. Moreover, Figure 26 illustrates the distributions of the microscopic effective Cauchy stress for the micro-scale kinematic constraints. The deformed configuration for the minimal model is less restrictive when compared to other models under analysis. Note that the torsion effect is evident in the deformed RVEs.

Table 8 – Homogenised results for $\boldsymbol{P}$ and $\mathbf{Q}$ after impose $\mathsf{G}_{123} = 0.1$ mm^{-1}.

Component	Micro-scale kinematic constraint model		
	Direct	Periodic	Minimal
P_{11} (MPa)	-23.7753	-12.4596	15.1123
P_{22} (MPa)	52.5737	2.2422	2.3449
P_{33} (MPa)	-8.3415	-2.6815	11.4657
$\mathsf{Q}_{312} = \mathsf{Q}_{321}$ (MPa mm)	238.4476	231.9060	219.0262
$\mathsf{Q}_{123} = \mathsf{Q}_{132}$ (MPa mm)	406.3870	387.0937	327.2712
$\mathsf{Q}_{213} = \mathsf{Q}_{231}$ (MPa mm)	180.9451	167.7870	132.2344

Source: The author.

Figure 26 – Microscopic effective Cauchy stress (MPa) for deformed RVEs subjected to $\mathsf{G}_{123} = 0.1\ \text{mm}^{-1}$.

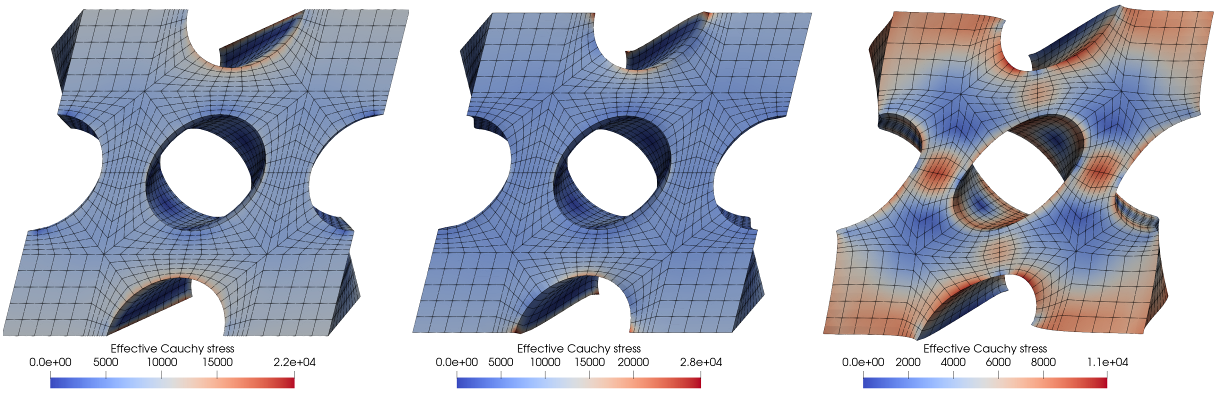

(a) Direct. (b) Periodic. (c) Minimal.

Source: The author.

5.2.3 Three-dimensional micro-scale numerical example 3: RVE of a metamaterial

The primary purpose of the third three-dimensional example is to illustrate the potential applicability of the developed framework for investigating metamaterials. Specifically, the numerical analysis of an RVE with unidirectional voids of circular cross-section is performed in order to capture the change of patterning during the compression. As shown in Figure 27a, a periodic RVE composed of 4 identical unit cells with a unidirectional void of circular cross-section is investigated. The RVE length is $l_\mu = 19.94$ mm, where each unit cell has a length equal to 9.97 mm. The diameter of the circular holes is $d = 8.67$ mm. The total porosity of the RVE is $f = 0.5939$ or $f = 59.39\%$. These specific dimensions for the RVE morphology were extracted from (Mullin, 2007) in order to favor the appearance of the patterning change effect. A soft mechanical metamaterial is considered, where the matrix elastic properties are $E = 9.685$ MPa and $\nu = 0.49$ (i.e., matrix close to incompressibility).

The nonzero components of the prescribed macroscopic kinematic quantities over the RVE are: $F_{11} = F_{22} = 0.9650$, $\mathsf{G}_{111} = 0.0070\ \text{mm}^{-1}$ and $\mathsf{G}_{112} = \mathsf{G}_{121} = 0.0035\ \text{mm}^{-1}$. Regarding the loading programme, the macroscopic deformation gradient and its gradient are applied over the RVE considering 200 increments. The effect of the micro-scale kinematic constraints is also evaluated by comparing the periodic and minimal models. Results for the direct model are not presented, since the mechanism of patterning change is not well captured due to its restrictive conditions on the RVE outer boundary. The mesh composed of 20-noded hexahedral elements (H20) with 8 integration points is presented in Figure 27b. It is worth mentioning that the Line Search method was employed to improve the convergence of the numerical analyses.

Figure 27 – Geometry and mesh for the RVE of a metamaterial.

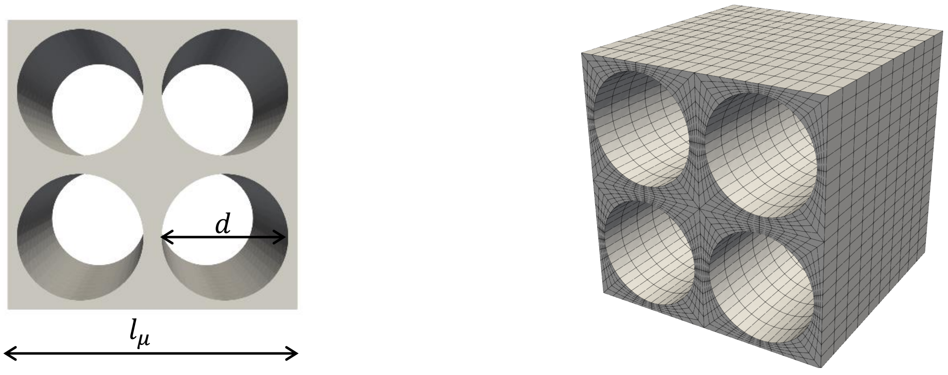

(a) Geometry.

(b) Mesh: 8000 elements (H20) and 38177 nodes.

Source: The author.

Figure 29 compares the evolution of some homogenised stress components for the three micro-scale constraints investigated within the proposed framework. Figure 28 shows the displacement magnitude for the deformed RVEs. Regarding the homogenised behaviour, significant differences are observed for the evolution and values of the homogenised stresses when the micro-constraints are compared, in which the minimal model indicates a lower bound. Strong divergences between P_{11} and P_{22} occur for the minimal constraint model, while close results between P_{11} and P_{22} are observed for the periodic constraint model. The close results for the homogenised stress components in the RVE with the periodic model can be due to the symmetry of RVE geometry and the periodicity of fluctuations required in this constraint model. The change of patterning during the compression is clear for the RVEs under periodic and minimal micro-scale constraints, where the RVE instabilities were captured (see Figure 28). Therefore, although merely illustrative, this example shows the potential applicability of the computational framework for investigating metamaterials.

Figure 28 – Displacement magnitude (mm) for deformed RVEs.

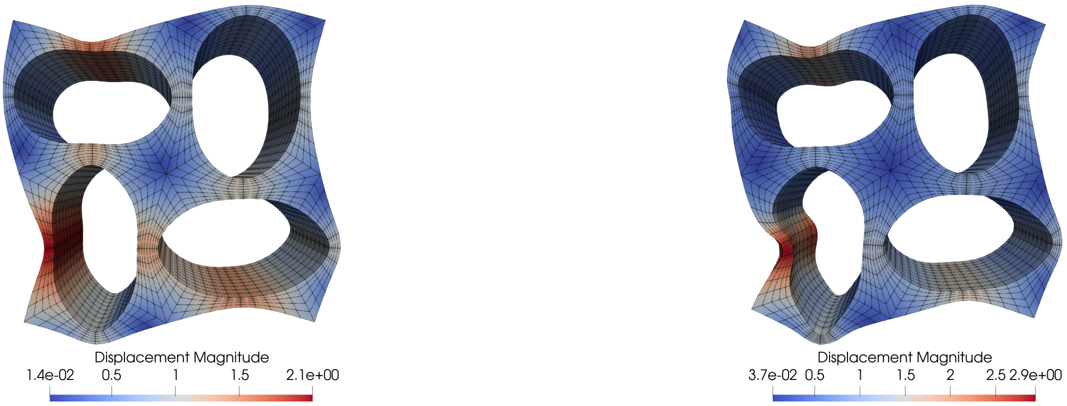

(a) Periodic.

(b) Minimal.

Source: The author.

Figure 29 – Homogenised results for periodic and minimal micro-constraint models.

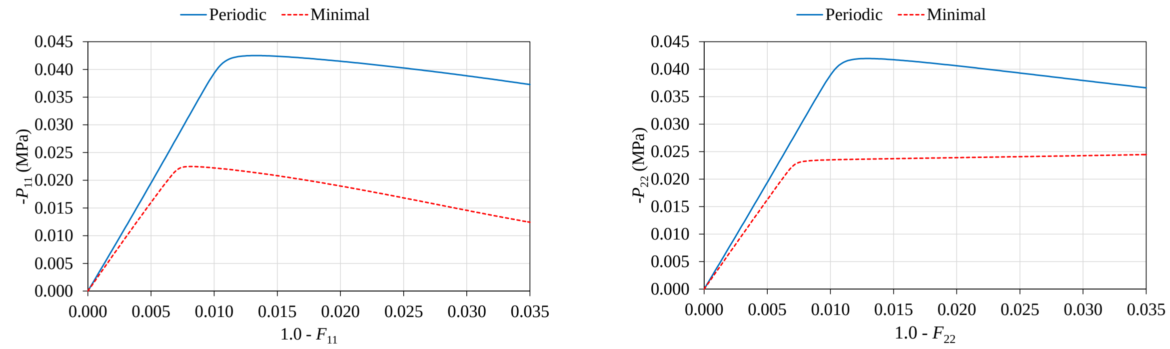

(a) Comparisons for F_{11}.

(b) Comparisons for F_{22}.

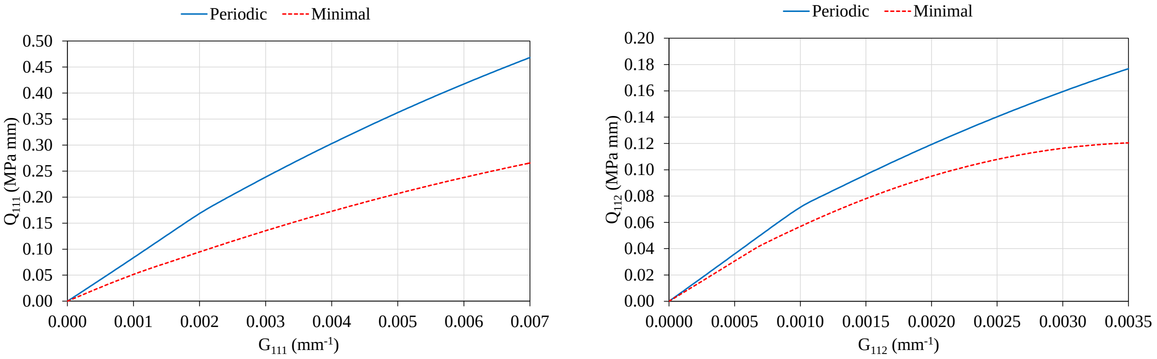

(c) Comparisons for Q_{111}.

(d) Comparisons for Q_{112}.

Source: The author.

5.3 Partial conclusions

The effectiveness of the micro-scale computational strategy was demonstrated by the quadratic convergence observed in numerical simulations at the RVE level using the Newton-Raphson scheme. The generality of the formulation and its numerical implementation allowed the investigation of porous and micro-architected materials with voids inside the RVE and on their outer boundary. Different deformation modes introduced by the second-order gradient were imposed over the RVEs, including bending and twisting modes. The effect of the micro-scale kinematic constraints on the homogenised behaviour was assessed. The minimal constraint provides a lower bound, while the direct constraint defines an upper bound to the homogenised response. The volume constraint naturally incorporated in the micro-scale problem is paramount to achieve physically meaningful results. The strategy of recovering homogenised stress tensors from Lagrange multipliers was validated by comparison with homogenisation expressions based on volume averaging of the microscopic fields over the RVE.

6 COUPLED MULTI-SCALE SIMULATIONS: DEFORMATION MODE COUPLING AND SIZE EFFECTS

In what follows, several coupled multi-scale numerical examples of mechanical metamaterials and architected materials are performed to show the robustness and applicability of the second-order computational framework. Thus, multi-scale simulations are conducted in the context of the FE^2 framework, i.e., finite element analyses at both macro and micro-scales. The numerical results of this section can also be found in Santos *et al.* (2023) and Santos *et al.* (2024). The convergence rates of the Newton-Raphson iterative solution scheme at the macro-scale are also investigated. The developed multi-scale models based on second-order computational homogenisation are confronted with first-order homogenisation to assess their ability to capture bending, deformation mode coupling and size effects. The results of the multi-scale simulations are also compared with Direct Numerical Simulations (DNS), which refer to the geometry of the internal structure explicitly at the macro-scale. To comply with the C^1-continuity requirement, mixed finite elements were employed at the macro-scale (see more details in Lopes and Pires (2022d)).

Different lengths for RVEs (multi-scale simulations) and unit cells (DNS simulations) are defined to assess the impact of the size effect on the global mechanical behaviour of the investigated structures. Mesh convergence studies are conducted in the context of multi-scale simulations to verify the appropriate mesh refinement for modelling each structural problem. Although the results are presented and discussed only for the macro-scale mesh refinement, convergence studies were also carried out for the micro-scale resulting in the meshes selected for the RVE (multi-scale models) and the unit cells (DNS models). In this sense, mesh convergences are obtained both on the macro-scale and on the micro-scale, in which only the macro-scale results are presented. Furthermore, the material is governed by a hyperelastic constitutive law (see Equations (5.2) and (5.3)), assuming an elastic constitutive behaviour.

6.1 Multi-scale numerical example 1: metamaterial with tension-induced bending

The main goal of the numerical example is to show that the second-order computational homogenisation formulation is able to capture the higher-order effects induced by the coarseness and morphology of the internal architecture of the material. In this context, the three second-order multi-scale models (minimal, periodic and direct) are compared to the respective classical first-order multi-scale models (uniform traction, periodic and linear). More details of the first-order models can be found in Reis and Andrade Pires (2013).

A similar study was performed by Yvonnet, Auffray and Monchiet (2020) in the context of composite materials without voids. Here, a structure formed by an architected composite material with voids shown in Figure 30a is adopted. The numerical simulations are conducted under plane strain conditions. The RVE is composed of two materials and the elastic parameters are defined based on Yvonnet, Auffray and Monchiet (2020). Thus, the elastic properties are $E = 1$ MPa, $\nu = 0.3$ for material 1 and $E = 100$ MPa, $\nu = 0.3$ for material 2. The RVE mesh is shown in Figure 30b, in which isoparametric 8-noded quadratic quadrilateral elements (Q8) with 4 integration points were used in the discretisation. In addition, the RVE length is l_μ=1 mm.

The DNS model 1 presented in Figure 31a is simulated in order to provide a reference response. Specifically, the DNS model 1 comprises 40 (10x4) periodic unit cells, where the cell length is l_{cell}=1 mm, i.e., $l_{cell} = l_\mu$. The mesh data for the DNS model 1 is shown in Figure 31b. The macro-scale problem or global structure is illustrated in Figures 31a and 32a, where L_H=10mm and L_V=4mm. Regarding the boundary conditions, the left side of the structure is horizontally and vertically constrained, and the right side is vertically constrained. Furthermore, the right side of the structure is subjected to a prescribed horizontal displacement u_{0x}=0.6 mm enforced in 10 increments.

Figure 30 – Geometry and mesh for RVE and unit cells.

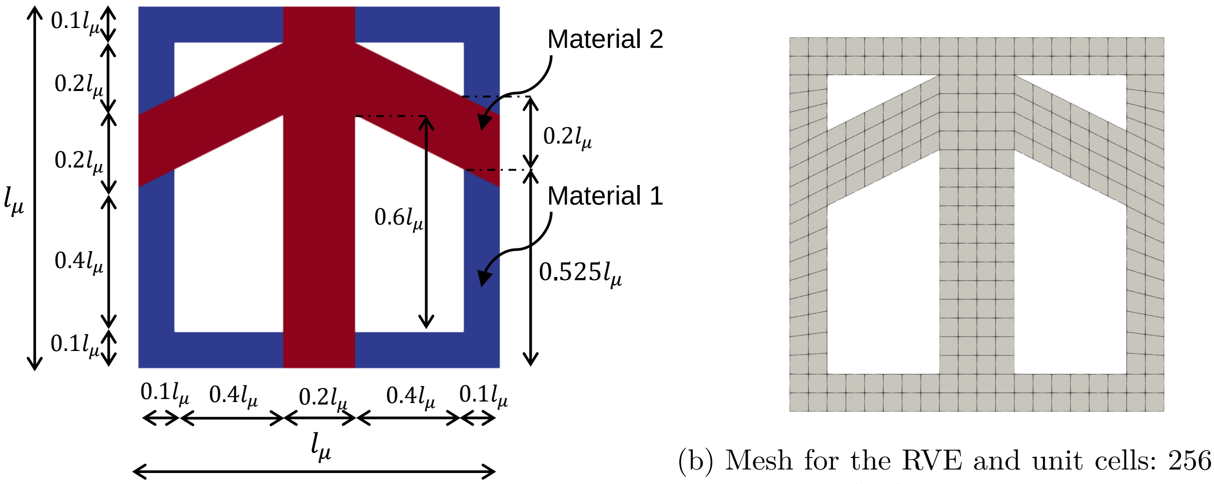

(a) Geometry for RVE and unit cells.

(b) Mesh for the RVE and unit cells: 256 elements (Q8) and 941 nodes.

Source: The author.

Figure 31 – Geometry and mesh for DNS model 1.

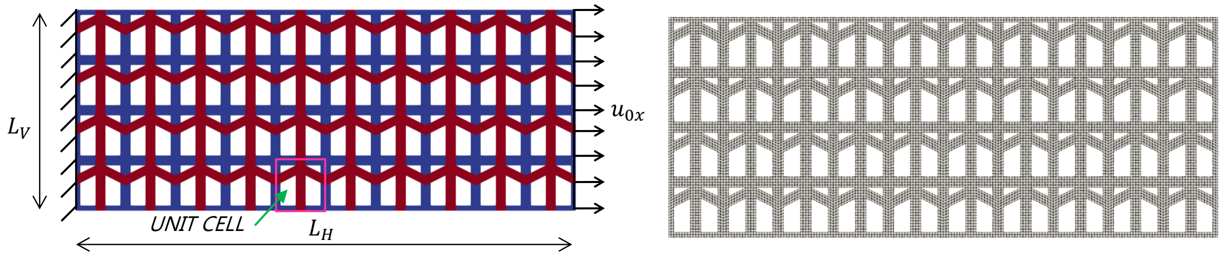

(a) DNS model 1 with 10x4 unit cells.

(b) Mesh: 10240 elements and 34961 nodes.

Source: The author.

For the multi-scale simulations with second-order homogenisation, mixed finite elements (Q8F4L1) with 4 integration points are employed at macro-scale to comply with the C^1-continuity requirement (Lopes, 2019; Lopes; Pires, 2022a). The multi-scale numerical simulations are performed for 3 macro-scale meshes presented in Figures 32b, 32c and 32d. In particular, the macro-scale meshes for the first-order FE^2 simulation sare composed of elements (Q8) with 4 integration points.

Figure 32 – Geometry and meshes for macro-scale.

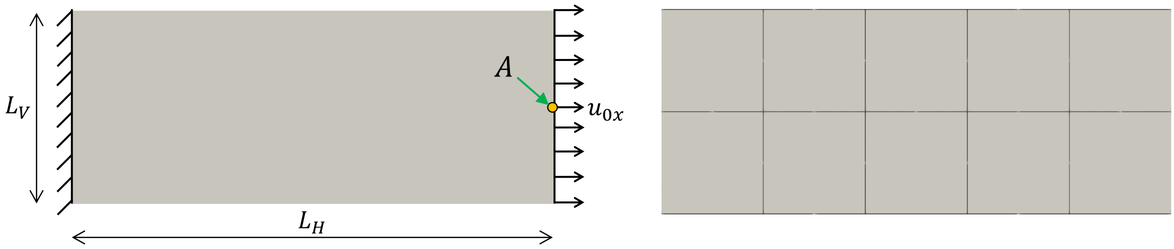

(a) Geometry and imposed boundary conditions. (b) Mesh 1: 10 elements (Q8F4L1) and 45 nodes.

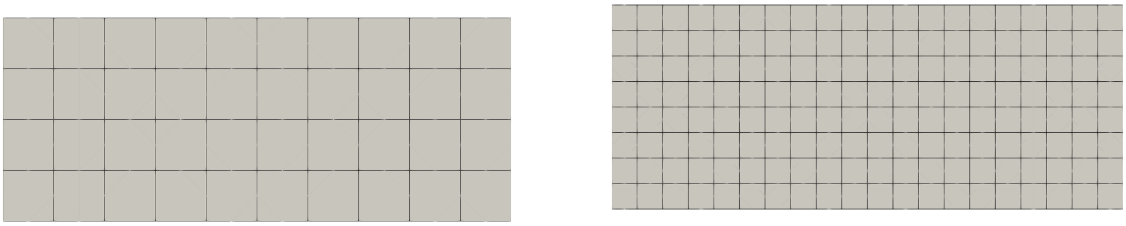

(c) Mesh 2: 40 elements (Q8F4L1) and 149 nodes. (d) Mesh 3: 160 elements (Q8F4L1) and 537 nodes.

Source: The author.

Coupled multi-scale numerical simulations require the solution of macro and micro-scales simultaneously. In this sense, a convergence study is important to evaluate the consistency of the Newton-Raphson iterative solution scheme at the macro-scale. The quadratic convergence observed for all multi-scale models shown in Table 9 illustrates the consistency of the computational strategy, including the implementation of the consistent tangents computed from the Lagrange multipliers.

Table 9 – Convergence rates at the macro-scale mesh 2 in the last incremental step for the sets of multi-scale models, where the adopted tolerance for the iterative procedure is set to 1.0 x 10^{-8}.

Model	Relative residual norm (%): macro-scale mesh 2 (two-dimensional)		
	Iteration 1	Iteration 2	Iteration 3
Direct	0.43599 x 10^{-1}	0.41677 x 10^{-5}	0.21054 x 10^{-11}
Periodic	0.28059 x 10^{-1}	0.20563 x 10^{-5}	0.23360 x 10^{-11}
Minimal	0.43991 x 10^{-1}	0.26085 x 10^{-6}	0.90282 x 10^{-11}

Source: The author.

The results of the vertical displacements for the DNS model 1 are shown in Figure 33. Although the boundary conditions imposed at the macro-scale indicate internal forces associated with a tensile stress state, the geometry and micro-scale properties result in macroscopic behaviour with the presence of bending. The bending of the DNS model 1 is evidenced by the more pronounced vertical displacement at the bottom boundary compared to the top boundary. It is worth mentioning that the non-uniformity of the reaction forces was observed for the left and right sides of the structure.

Figure 33 – Vertical displacements (mm) for the DNS model 1 (exaggerated 10 times).

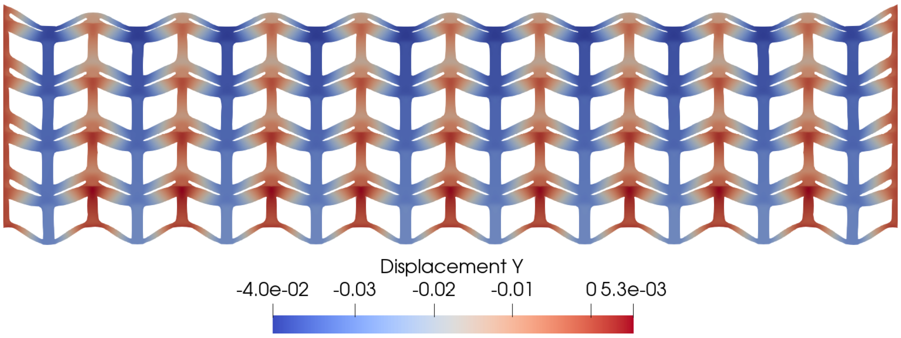

Source: The author.

The high-order effects favour the appearance of reaction bending moments at the left and right sides of the structure. The results of the DNS model 1 are compared with the coupled multi-scale simulations through a graph relating the reaction moment (M) and prescribed displacement (u_{0x}), i.e., M and u_{0x}. The reaction moment is calculated from the reaction forces on the right side of the structure, taking as reference the point A indicated in Figures 32a and 31a. In this context, the results for M and u_{0x} for first- and second-order multi-scale models are compared to DNS model 1 in Figure 34, encompassing the 3 macro-scale meshes.

The first-order multi-scale models (Figures 34b, 34d and 34f) do not adequately capture the reaction moment at the macro-scale. Despite the different results when comparing the first-order models, the deformed configurations of the macro-scale indicate symmetry in relation to the vertical displacements at the top and bottom of the macro-scale. Thus, the reaction forces on the right side of the structure are uniform, leading to the absence of results with no reaction moment. Similar conclusions were also reported by Yvonnet, Auffray and Monchiet (2020), where the first-order models did not adequately capture the higher-order effects in a composite with arrow-shaped inclusions.

On the other hand, the second-order multi-scale models (Figures 34a, 34c and 34e) captured the moment reaction, evidencing the predictive capability of the proposed computational framework. The deformed configurations indicate more pronounced vertical displacements at the bottom boundary of the structures. Moreover, the reaction moment in second-order multi-scale models results from non-uniform reaction forces on the structure boundary. In particular, the second-order periodic model derived from the developed second-order formulation (see Figure 34c) provided a response in close agreement with DNS model 1. The minimal and direct models (see Figures 34a and 34e) also captured the bending moment, in which the direct condition provides an upper bound and the minimal model provides a lower bound. Therefore, the proposed second-order computational homogenisation formulation is an attractive alternative for investigating structures composed of porous materials with more complex behaviour subject to higher-order effects. Finally, the discussed example also illustrated the applicability of the second-order multi-scale approach for investigating non-homogeneous structures composed of different materials and voids.

Figure 34 – Reaction moment (M) at point A (see Figure 32a) for different macro-scale meshes: first- and second-order multi-scale models compared to DNS model 1.

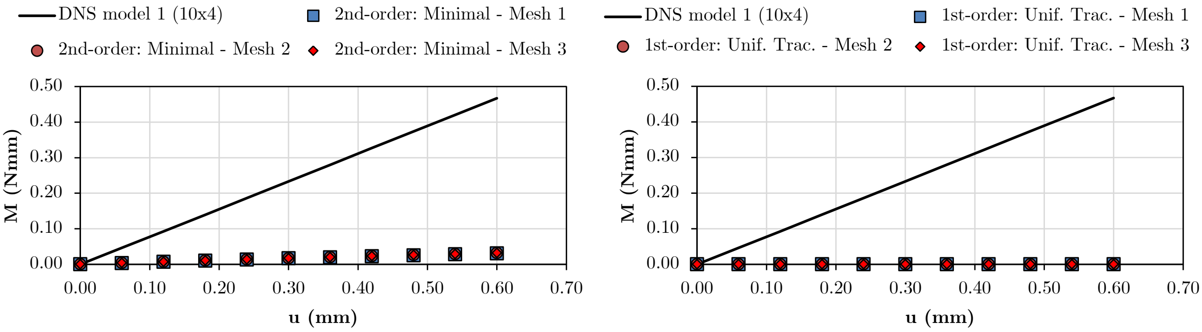

(a) Second-order: Minimal.

(b) First-order: Uniform traction.

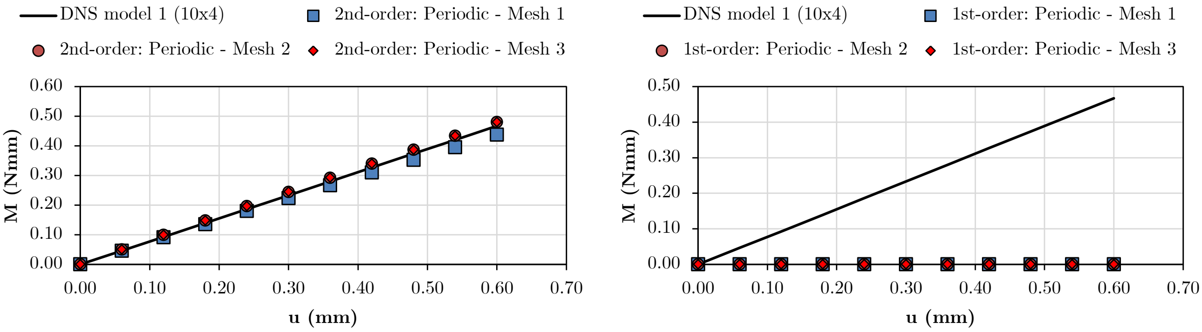

(c) Second-order: Periodic.

(d) First-order: Periodic.

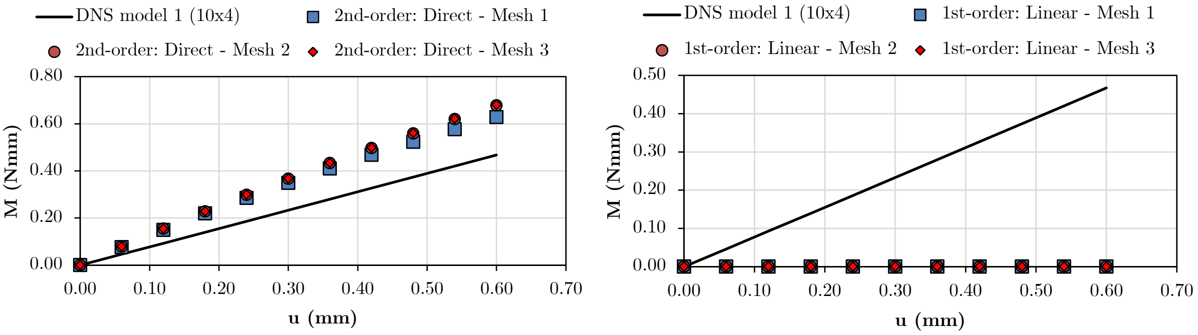

(e) Second-order: Direct.

(f) First-order: Linear.

Source: The author.

The vertical displacements of the deformed macro-scale meshes 2 and 3 for the first- and second-order multi-scale models are presented in Figures 35 and 36. Regarding the macro-scale meshes, the results are similar in general for all cases studied. More sensitive differences occur for the second-order multi-scale models, where the results for periodic and direct models with mesh 1 diverge from meshes 2 and 3. On the other hand, a convergence of the mesh is observed through the proximity of the results for meshes 2 and 3.

Figure 35 – Vertical displacements (mm) for the deformed structure (exaggerated 10 times) with the macro-scale mesh 2: first- and second-order multi-scale models.

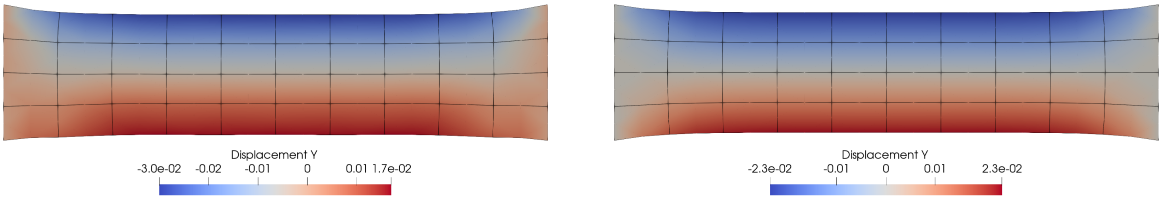

(a) Second-order: Minimal.

(b) First-order: Uniform traction.

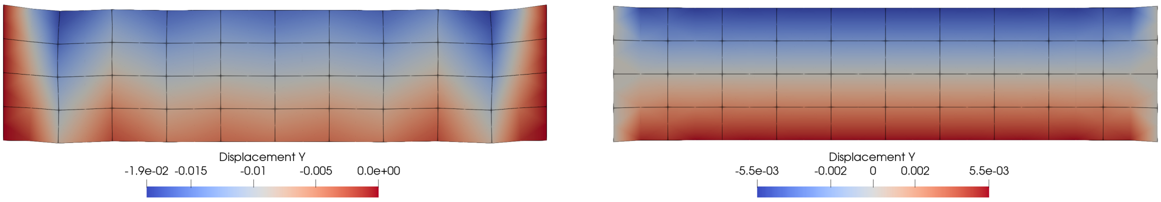

(c) Second-order: Periodic.

(d) First-order: Periodic.

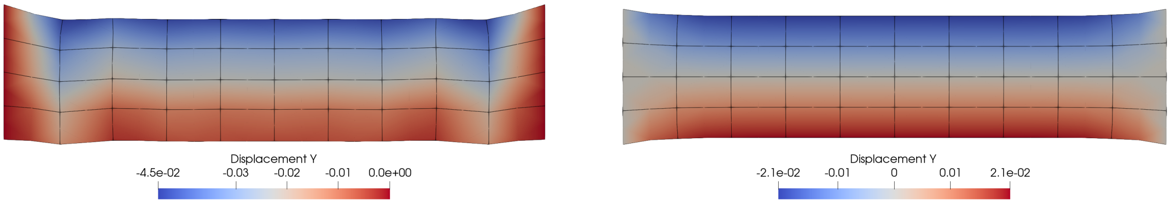

(e) Second-order: Direct.

(f) First-order: Linear.

Source: The author.

Figure 36 – Vertical displacements (mm) for the deformed structure (exaggerated 10 times) with the macro-scale mesh 3: first- and second-order multi-scale models.

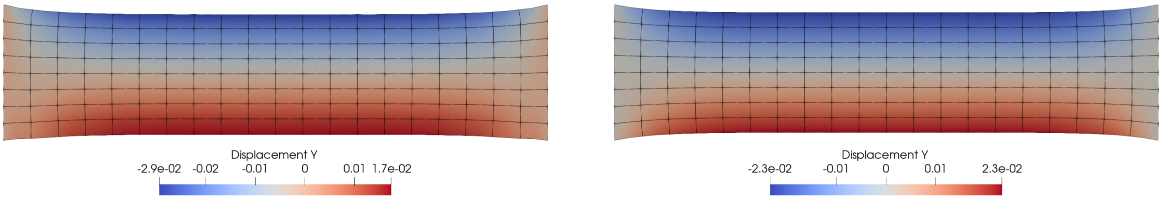

(a) Second-order: Minimal.

(b) First-order: Uniform traction.

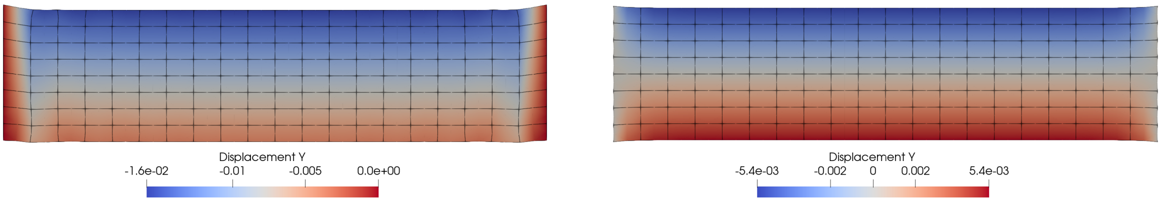

(c) Second-order: Periodic.

(d) First-order: Periodic.

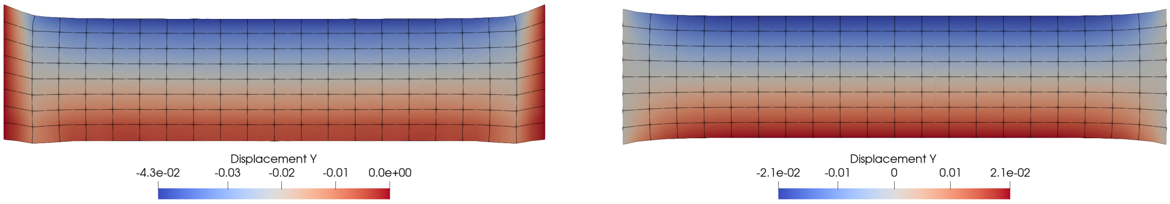

(e) Second-order: Direct.

(f) First-order: Linear.

Source: The author.

6.1.1 Influence of the RVE length

The effect of the RVE length is assessed in the context of coupled multi-scale simulations. The problem at the macro-scale (geometry, dimensions and imposed boundary conditions) has already been described in Subsection 6.1 (see Figure 32a). In this case, FE^2 simulations with the second-order multi-scale models are explored to investigate three RVE lengths: (i) l_μ=1 mm, (ii) l_μ=1/2 mm, and (iii) l_μ=1/3 mm. A mesh convergence study was also carried out considering the three macro-scale meshes shown in Figure 32. As revealed in Subsection 6.1, the results were very close for macro-scale meshes 2 and 3. Thus, macro-scale mesh 2 (see Figure 32c) was adopted to study the influence of the RVE length. In order to compare the results for the same macro-scale mesh, three DNS models shown in Figure 37 were also investigated. The DNS model 1 (10x4) is the same as presented in Subsection 6.1. In turn, the DNS model 2 (20x8) is constructed by 160 unit periodic cells, where each unit cell has l_{cell}=1/2 mm. Finally, the DNS model 3 (30x12) is formed by 360 unit periodic cells of l_{cell}=1/3 mm. It is worth mentioning that the lengths for RVEs and unit cells are the same ($l_\mu = l_{cell}$) for the respectively compared models, i.e., multi-scale and DNS. The number of elements and nodes for the DNS models is reported in Table 10. The mesh of each RVE and unit cell follows the arrangement of Figure 30b.

Figure 37 – DNS models.

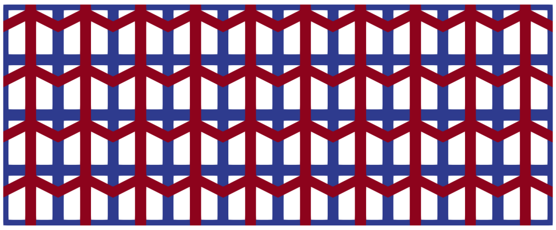

(a) DNS model 1 with 10x4 unit cells (l_{RVE}=1 mm).

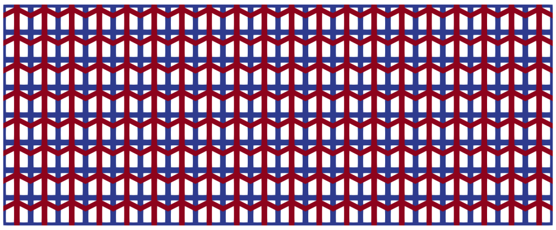

(b) DNS model 2 with 20x8 unit cells (l_{RVE}=1/2 mm).

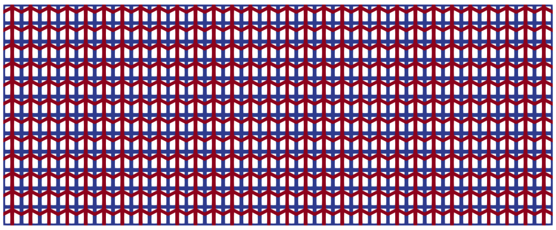

(c) DNS model 3 with 30x12 unit cells (l_{RVE}=1/3 mm).

Source: The author.

Table 10 – Mesh of DNS models.

DNS	**Elements (Q8)**	**Nodes**
Model 1 - Size 1 ($l_\mu = 1.00$ mm)	10240	34961
Model 2 - Size 2 ($l_\mu = 0.50$ mm)	40960	138721
Model 3 - Size 3 ($l_\mu = 0.33$ mm)	92160	311281

Source: The author.

Figure 38 presents the relation between the reaction bending moment (M) and the RVE length (l_μ). Note that the DNS models exhibit a linear behaviour between M and l_μ, where the decrease in the RVE length reduces the bending moment of the structure. Regarding the multi-scale models, numerical tests were conducted for first- and second-order homogenisation strategies. The first-order multi-scale models do not capture the bending of the structure. On the other hand, the second-order multi-scale models capture the reduction of the bending moment at the macro-scale with the decrease in the RVE length. Still concerning the second-order multi-scale models: (i) the periodic condition accurately captures the bending moment compared to the DNS model, (ii) the minimal condition represents a lower bound, where the results have significant differences compared to the DNS model, and (iii) the direct condition represents an upper bound, where the results are closer to the DNS model when compared to the minimal condition.

Figure 38 – Reaction moment (M) at point A (see Figure 32a) for different macro-scale for different RVE lengths.

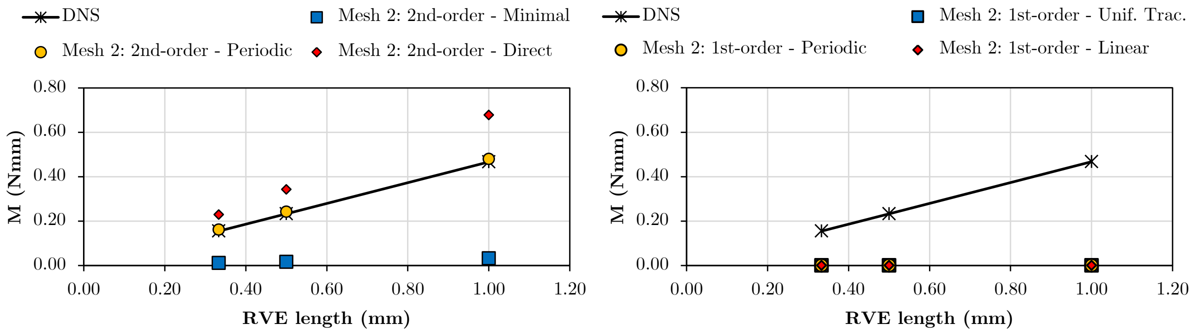

(a) Mesh 2: Multi-scale second-order models. (b) Mesh 2: Multi-scale first-order models.

Source: The author.

The results for the vertical displacements help to explain the reduction in the bending moment of the structure with the decrease in the RVE length. Regarding the results for the DNS models (Figures 33, 39a and 40a), smaller lengths of unit cells reduce the maximum vertical displacements at the bottom of the structure. The second-order multi-scale models (Figures 35, 39 and 40) also capture the reduction of the maximum vertical displacements at the bottom of the macro-scale, evidencing the consistency of the strategy proposed in this work. In particular, the deformed configurations are qualitatively well reproduced by the second-order multi-scale model periodic compared to DNS models.

Figure 39 – Vertical displacements (mm) for the deformed structure (exaggerated 10 times): DNS model 2 and second-order multi-scale models for macro-scale mesh 2.

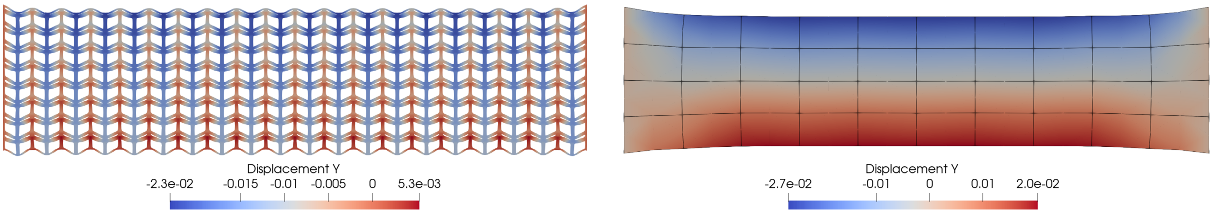

(a) DNS model 2. (b) Macro-scale mesh 2: Second-order - Minimal.

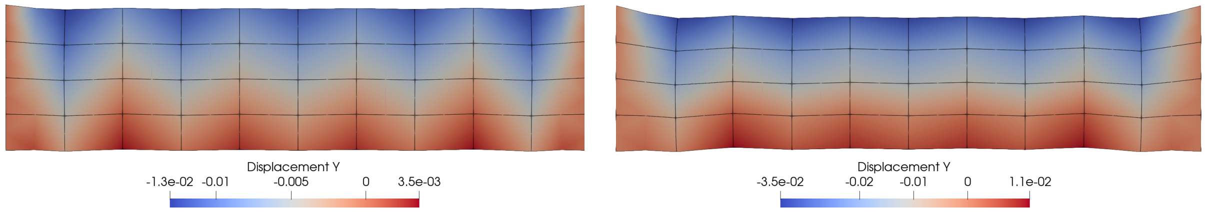

(c) Macro-scale mesh 2: Second-order - Periodic. (d) Macro-scale mesh 2: Second-order - Direct.

Source: The author.

Figure 40 – Vertical displacements (mm) for the deformed structure (exaggerated 10 times): DNS model 3 and second-order multi-scale models for macro-scale mesh 2.

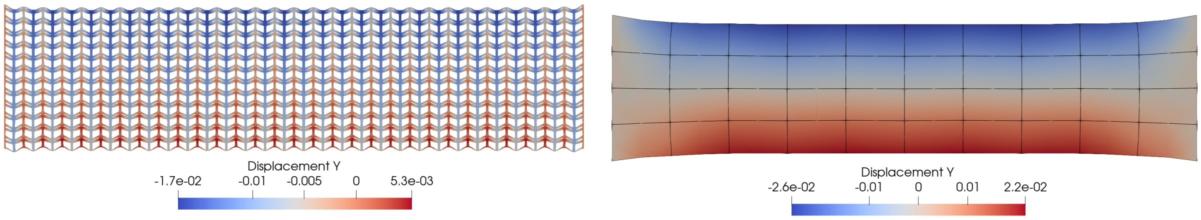

(a) DNS model 3. (b) Macro-scale mesh 2: Second-order - Minimal.

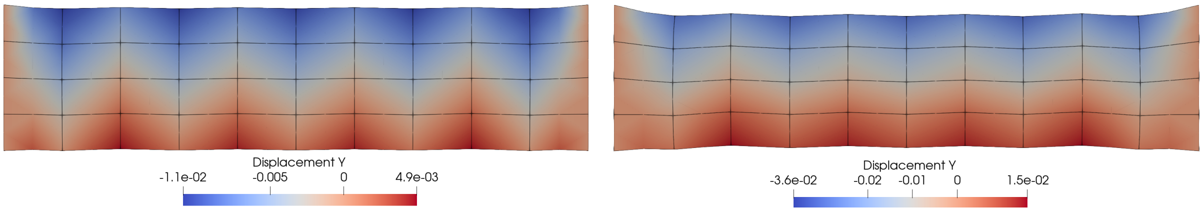

(c) Macro-scale mesh 2: Second-order - Periodic. (d) Macro-scale mesh 2: Second-order - Direct.

Source: The author.

6.1.2 Computational cost: DNS models versus second-order multi-scale models

Simulation time and memory requirements were estimated to compare the computational cost between DNS models and second-order multi-scale models. In this context, Table 11 shows the computational cost for DNS model 1 (10x4) and second-order multi-scale models with l_μ=1 mm. The results for DNS model 2 (20x8) and second-order multi-scale models with l_μ=0.5 mm are presented in Table 12. Furthermore, Table 13 indicates the results of DNS model 3 (30x12) compared to second-order multi-scale models with l_μ=0.33 mm. Numerical simulations were computed with the Intel Processor Core i7-6800K CPU 3.4GHz (6 cores and 12 threads). Furthermore, it is worth mentioning that a parallel computing strategy was explored in the simulations to reduce the computational cost of the numerical analyses.

Table 11 – Computational cost: time and memory requirements for DNS model 1 (10x4) compared to the second-order multi-scale models (l_μ=1 mm) with mesh 2.

Model	Time (s)	Memory requirements (MB)
DNS 1 (10x4)	65	≈ 323
Direct (l_μ=1 mm) - Mesh 2	41	≈ 241
Periodic (l_μ=1 mm) - Mesh 2	48	≈ 241
Minimal (l_μ=1 mm) - Mesh 2	43	≈ 240

Source: The author.

Table 12 – Computational cost: time and memory requirements for DNS model 2 (20x8) compared to the second-order multi-scale models (l_μ=1/2 mm) with mesh 2.

Model	Time (s)	Memory requirements (MB)
DNS 2 (20x8)	310	≈ 1178
Direct (l_μ=1/2 mm) - Mesh 2	41	≈ 241
Periodic (l_μ=1/2 mm) - Mesh 2	48	≈ 241
Minimal (l_μ=1/2 mm) - Mesh 2	44	≈ 240

Source: The author.

Table 13 – Computational cost: time and memory requirements for DNS model 3 (30x12) compared to the second-order multi-scale models (l_μ=1/3 mm) with mesh 2.

Model	Time (s)	Memory requirements (MB)
DNS 3 (30x12)	801	≈ 2613
Direct (l_μ=1/3 mm) - Mesh 2	42	≈ 241
Periodic (l_μ=1/3 mm) - Mesh 2	49	≈ 241
Minimal (l_μ=1/3 mm) - Mesh 2	44	≈ 240

Source: The author.

The results show that the second-order multi-scale approach presents significantly lower times than the DNS models, particularly for more refined DNS models. For example, the periodic model is 6 times faster compared to the DNS model 2 (20x8) model. This difference is more pronounced in the case of the DNS model 3 (30x12), where the periodic model is 16 times faster. Regarding memory requirements, second-order multi-scale approaches are also more advantageous when compared with DNS models. The multi-scale models require approximately 5 times less memory than the DNS model 2 and 11 times less memory than the DNS model 3.

Therefore, a disadvantage of DNS models is the significant increase in computational cost for simulating more refined models, i.e., DNS models with many unit cells. On the other hand, the second-order multi-scale strategy allows us to simulate different RVE lengths with similar computational costs. Thus, the second-order multi-scale framework presented in this work can reduce the computational time and memory requirements when compared to DNS models.

6.2 Multi-scale numerical example 2: metamaterial with tension/compression-induced undulation

The second numerical example aims at investigating a new design for a mechanical metamaterial which displays transverse undulation when subjected to a tensile or compressive loading. In the authors' best knowledge, this is the first time a metamaterial of this type is analysed. This new microstructure can be explored for shape-shifting applications in architected robotic metamaterials, for instance. The mechanical behaviour of this architected material is illustrated by two-dimensional finite element models, considering plane strain conditions. Regarding the elastic properties, a Young's modulus of $E = 210$ GPa and Poisson's ratio of $\nu = 0.3$ are assumed.

6.2.1 DNS models

Figure 41 shows the unit cell geometry for the new metamaterial, along with the mesh that is composed of isoparametric 8-noded quadratic quadrilateral elements (Q8).

Figure 41 – Unit cell and RVE.

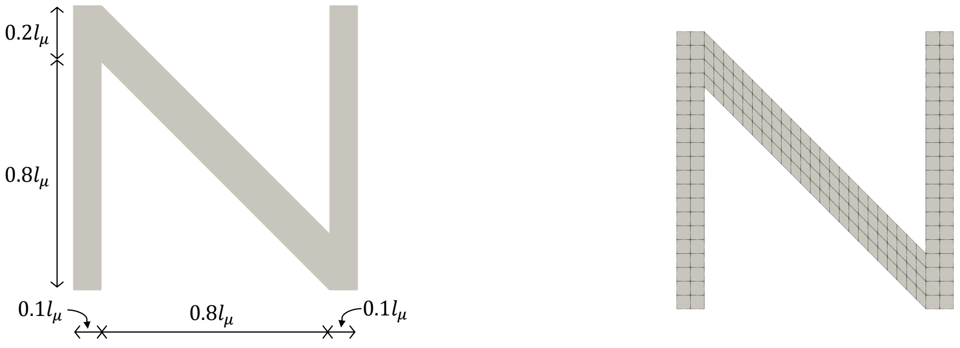

(a) Geometry.

(b) Mesh: 172 elements (Q8) and 643 nodes.

Source: The author.

DNS models are formed by periodic arrays based on the unit cell of Figure 41. In this context, Figure 42 presents three DNS models proposed to simulate the new metamaterial: (i) DNS model 1 (20x8 unit cells), (ii) DNS model 2 (30x12 unit cells) and (iii) DNS model 3 (40x16 unit cells). It is worth mentioning that the macroscopic dimensions of the DNS models are the same. Thus, the unit cell size (l_μ) is different for each DNS model: (I) DNS model 1: $l_\mu = 1.00$ mm, (II) DNS model 2: $l_\mu = 0.50$ mm, and (iii) DNS model 3: $l_\mu = 0.25$ mm. Moreover, mesh data for the DNS models are presented in Table 14. Regarding the boundary conditions of the DNS model, zero displacements are prescribed on the left side of the structure ($u_{0x} = u_{0y} = 0$). On the right side of the structure, zero displacements are vertically prescribed ($u_{0y} = 0$) and non-zero displacements are horizontally imposed ($u_{0x} \neq 0$) considering: (i) $u_{0x} = 0.5$ mm (loading programme associated with tension), and (ii) u_{0x} = -0.5 mm (loading programme associated with compression). The prescribed displacements are imposed in 10 equally-spaced increments.

Table 14 – Mesh of DNS models.

DNS	Elements (Q8)	Nodes
Model 1 - Size 1 ($l_\mu = 0.50$ mm)	27520	95381
Model 2 - Size 2 ($l_\mu = 0.33$ mm)	61920	214231
Model 3 - Size 3 ($l_\mu = 0.25$ mm)	110080	380521

Source: The author.

Figure 42 – Geometry of the DNS models ($L_x = 10$ mm and $L_y = 4$ mm).

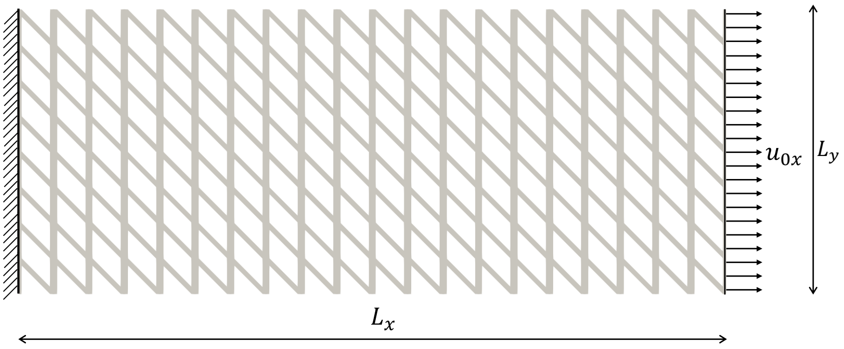

(a) DNS model 1 (20x8 unit cells): Size 1.

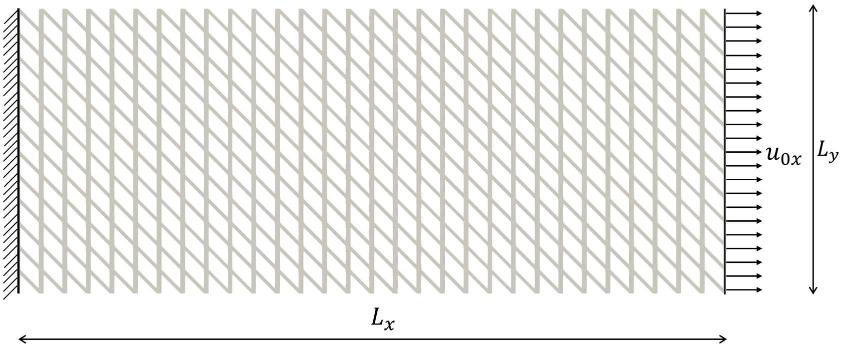

(b) DNS model 2 (30x12 unit cells): Size 2.

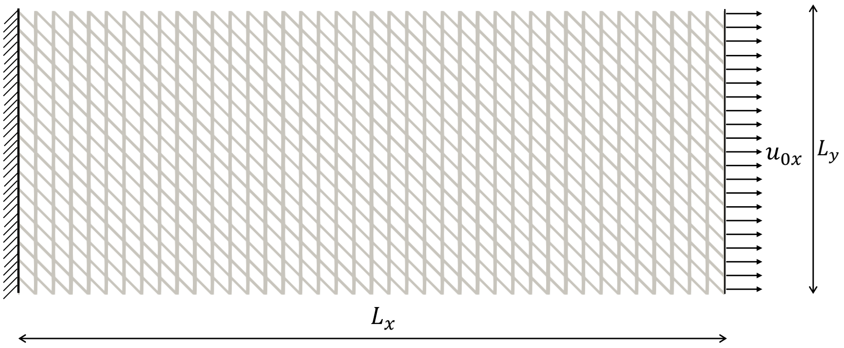

(c) DNS model 3 (40x16 unit cells): Size 3.
Source: The author.

The deformed configuration of the DNS models for the compressive and tensile loadings is shown in Figures 43 and 44, respectively. Note that the new material has a tension/compression-induced undulation behaviour, which is a different response than expected for a natural material. Moreover, the shape of the induced vertical waves inverts, when comparing deformation induced by tension and compression. The size of the unit cell size has no significant influence on the maximum vertical displacements of the deformed structure. Therefore, this new metamaterial does not display significant size effects, concerning the microstructural size. Note that the loading programme associated with compression results in higher values for the maximum vertical displacement compared to the loading programme associated with tension.

Figure 43 – Vertical displacements in mm (scale factor = 4) for DNS models under compression.

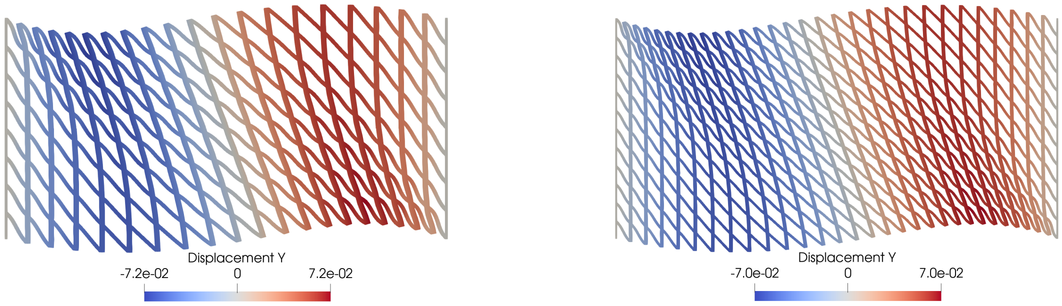

(a) DNS model 1 (20x8 unit cells).

(b) DNS model 2 (30x12 unit cells).

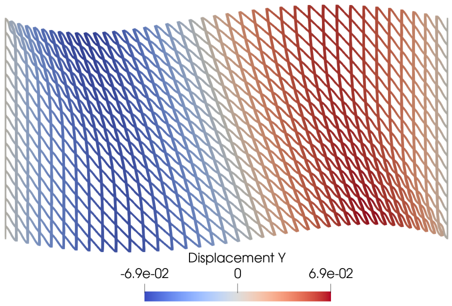

(c) DNS model 3 (40x16 unit cells).

Source: The author.

Figure 44 – Vertical displacements in mm (scale factor = 4) for DNS models under tension.

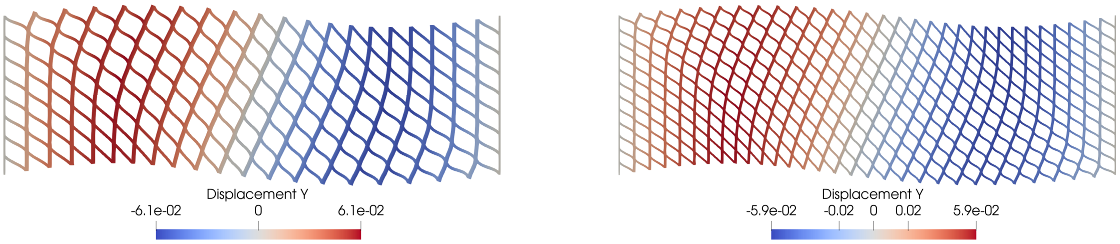

(a) DNS model 1 (20x8 unit cells).

(b) DNS model 2 (30x12 unit cells).

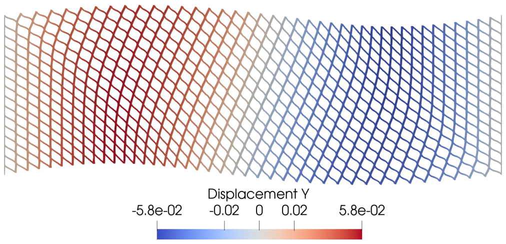

(c) DNS model 3 (40x16 unit cells).

Source: The author.

6.2.2 Multi-scale simulations

The three boundary conditions derived from the second-order multi-scale formulation, introduced in Section 3.2, are imposed to investigate the new metamaterial: (I) second-order minimal constraint (2nd-order - Minimal) or lower bound, (II) second-order periodic constraint (2nd-order - Periodic), and (III) second-order direct constraint (2nd-order - Direct) or upper bound. For comparison purposes, three boundary conditions derived from the classical first-order multi-scale formulation (see Reis and Andrade Pires (2013)) were also investigated: (i) first-order uniform traction boundary condition (1st-order - Traction) or lower bound, (ii) first-order periodic boundary condition (1st-order - Periodic), and (iii) first-order linear boundary condition (1st-order Linear) or upper bound.

In the context of coupled multi-scale analyses, modelling aspects of the macro-scale and the micro-scale must be defined. As shown in Figure 45, the geometry and boundary conditions of the structure at the macro-scale are consistent with the DNS model. For the simulations with second-order homogenisation, mixed quadrilateral finite elements (Q8F4L1) were employed at macro-scale. For first-order homogenisation, standard isoparametric elements with 8 nodes (Q8) and 4 integration points were used. This type of element was also employed at the RVE level, for both cases. The micro-scale is modelled by the RVE shown in Figure 41. The geometry, boundary conditions and mesh of the RVE are the same as those defined for the unit cells of the DNS models. Hence, the loading programmes associated with tension ($u_{0x} = 0.5$ mm) and compression ($u_{0x} = -0.5$ mm) were imposed at the macro-scale to perform the multi-scale simulations.

Figure 45 – Geometry and boundary conditions ($L_x = 10$ mm and $L_y = 4$ mm).

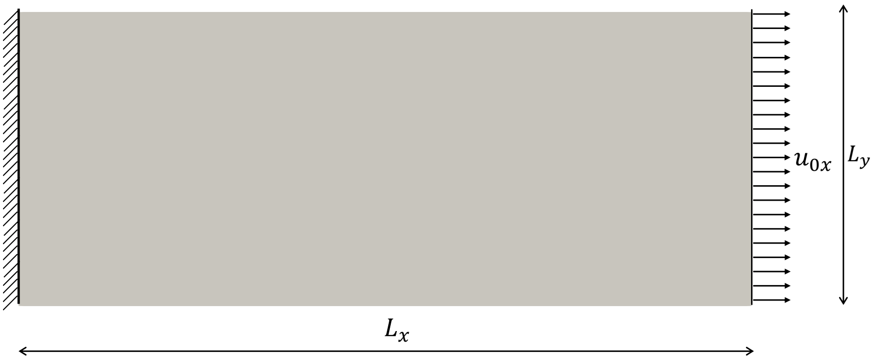

Source: The author.

In the first place, three macro-scale meshes were investigated in order to verify the convergence of results for multi-scale analyses. The RVE discretisation is kept consistent with the meshes employed in the DNS. The mesh data, including the number of elements and nodes, is presented in Figure 46. The mesh refinement studies, performed for $l_\mu = 0.500$ mm and based on the horizontal reaction force (F_x), are presented in Tables 15 and 16 for tension and compression loading programmes, respectively (see also Figure 47). To be more precise, F_x is determined by the sum of nodal horizontal reaction forces on the right side of the structure, where the displacement is imposed. Since the relative differences are small, there is no influence of the macroscopic discretisation in the obtained results. Therefore, mesh 1 is sufficient to perform the multi-scale analyses.

Figure 46 – Macro-scale meshes.

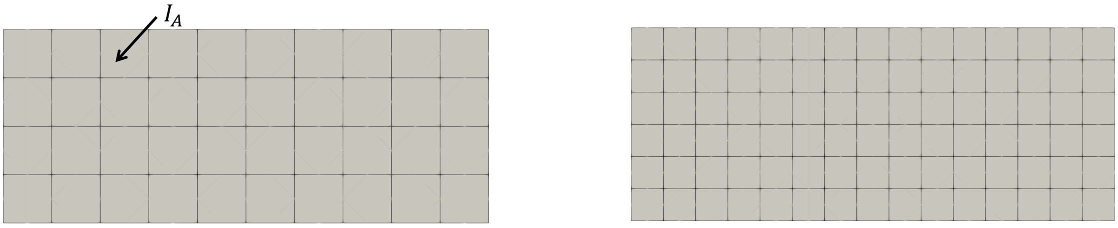

(a) Mesh 1: 40 elements (Q8F4L1) and 149 nodes.

(b) Mesh 2: 90 elements (Q8F4L1) and 313 nodes.

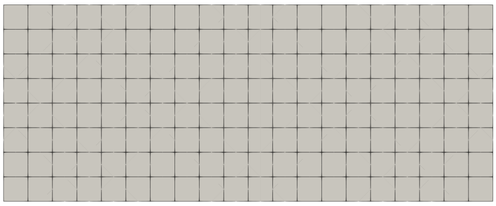

(c) Mesh 3: 160 elements (Q8F4L1) and 537 nodes.

Source: The author.

Figure 47 – Mesh study for multi-scale analysis with RVE size 1 ($l_\mu = 0.5$ mm): mesh x reaction force (F_x).

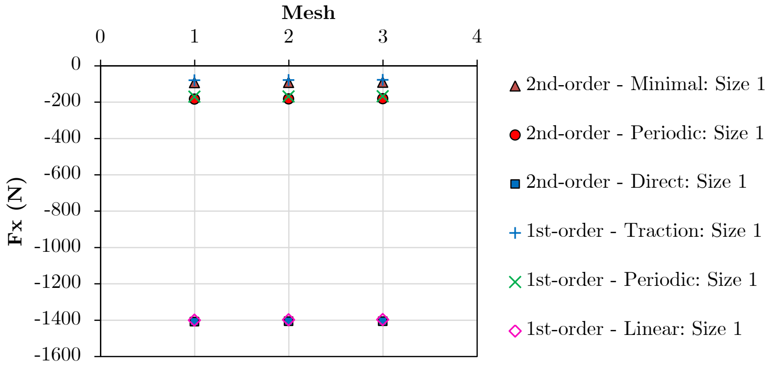

(a) Loading programme associated with compression.

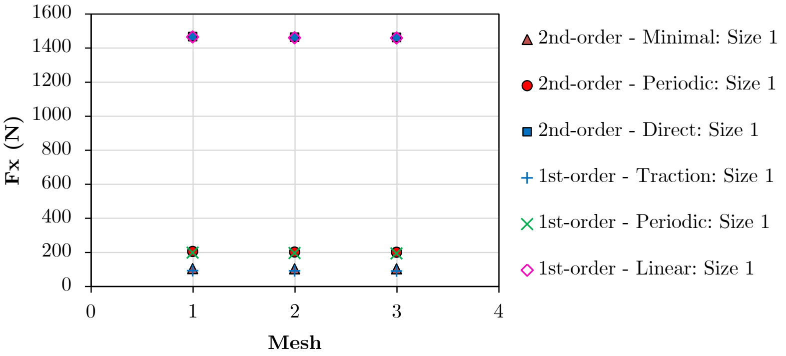

(b) Loading programme associated with tension.

Source: The author.

Table 15 – Mesh study for multi-scale analysis with RVE length 1 ($l_\mu = 0.500$ mm) - loading programme associated with tension: mesh x reaction force (F_x).

	Reaction force F_x (N)				
	Mesh 1	**Mesh 2**	**Mesh 3**	**Differences in module**	
Multi-scale models	**(1)**	**(2)**	**(3)**	**(2) to (1)**	**(3) to (2)**
2nd-order: Minimal	102.58	101.82	101.67	0.75%	0.14%
2nd-order: Periodic	209.95	207.31	206.29	1.26%	0.49%
2nd-order: Direct	1469.22	1466.08	1464.92	0.21%	0.08%
1st-order: Uniform Traction	91.57	89.90	89.14	1.82%	0.85%
1st-order: Periodic	196.69	193.91	192.59	1.42%	0.68%
1st-order: Linear	1462.73	1458.62	1456.75	0.28%	0.13%

Source: The author.

Table 16 – Mesh study for multi-scale analysis with RVE length 1 ($l_\mu = 0.500$ mm) - loading programme associated with compression: mesh x reaction force (F_x).

	Reaction force F_x (N)				
	Mesh 1	**Mesh 2**	**Mesh 3**	**Differences in module**	
Multi-scale models	**(1)**	**(2)**	**(3)**	**(2) to (1)**	**(3) to (2)**
2nd-order: Minimal	-94.08	-93.07	-92.71	1.07%	0.39%
2nd-order: Periodic	-185.06	-183.25	-182.57	0.98%	0.37%
2nd-order: Direct	-1409.28	-1407.64	-1407.08	0.12%	0.04%
1st-order: Uniform Traction	-81.22	-79.98	-79.43	1.52%	0.69%
1st-order: Periodic	-172.00	-170.24	-169.44	1.02%	0.48%
1st-order: Linear	-1401.71	-1399.46	-1398.46	0.16%	0.07%

Source: The author.

In the second place, three RVE lengths were investigated, corresponding to the unit cell sizes considered in the DNS simulations: $l_\mu = 0.500$ mm, $l_\mu = 0.333$ mm and $l_\mu = 0.250$ mm. Figures 48b and 48a show the comparison of the horizontal reactive force obtained with the multi-scale simulations (first- and second-order homogenisation) and the DNS models, considering axial tension and axial compression, respectively. For quantitative comparison purposes, Tables 17, 18, 19 and 20 show the relative differences (in modulus) of the multi-scale models compared to the respective DNS models. In order to contribute to the discussion of results, the deformed macroscopic meshes for the multi-scale models with $l_\mu = 0.50$ mm are shown in Figures 50 and 49.

The multi-scale simulations also capture both the tension and compression-induced undulation for the novel metamaterial. Regarding simulations with second-order multi-scale models: (i) the periodic constraint provides results in close agreement with the DNS model, (ii) the minimum constraint represents a lower bound, but keeping close to the model response DNS, (iii) the direct constraint results in an upper bound, i.e. the stiffest solution (most kinematically constrained), whose response has a significant difference when compared to DNS model. Furthermore, the previously described conclusions are analogous for first-order multi-scale simulations under the respective assumptions of: (I) periodic boundary condition, (II) uniform traction boundary condition, and (III) linear boundary condition. These observations are consistent with the maximum vertical displacement values obtained.

The first- and second-order multi-scale models lead to similar values of the macroscopic reaction force, but the deformed macroscopic model is slightly affected by the selected formulation. Nonetheless, the periodic boundary conditions are the ones that result in maximum vertical displacements closer to the values obtained with the DNS.

Figure 48 – Size effect study considering the macro-scale mesh 1: RVE length x reaction force (F_x).

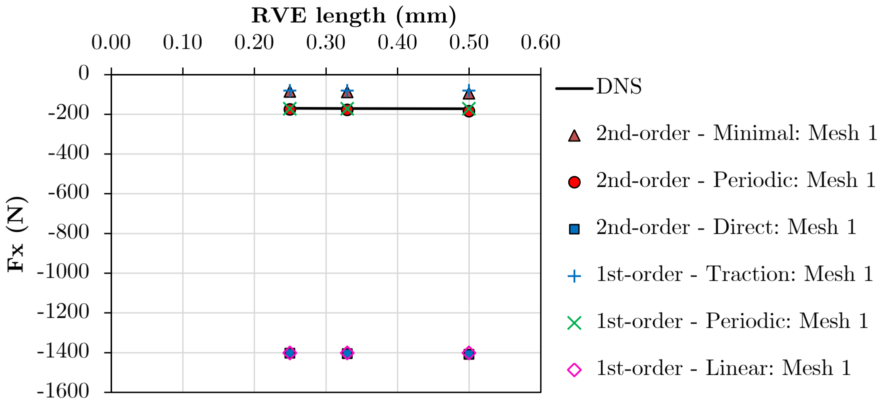

(a) Loading programme associated with compression.

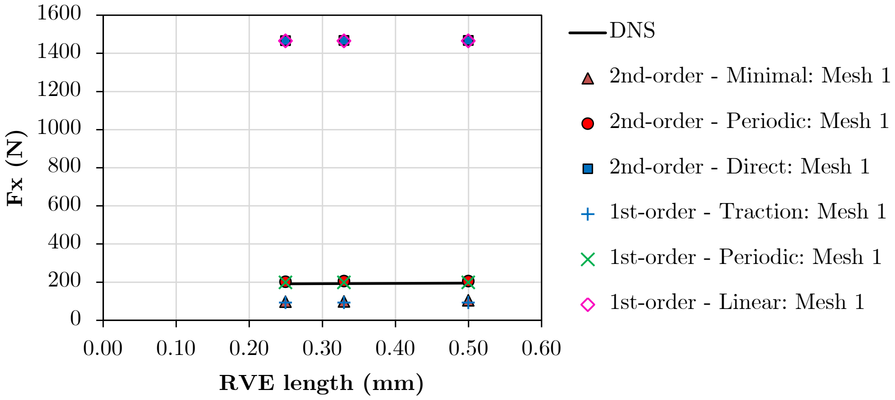

(b) Loading programme associated with tension.

Source: The author.

Table 17 – Size effect study considering the macro-scale mesh 1 for loading programme associated with tension: differences in reaction forces (F_x) for second-order multi-scale models compared to DNS models.

RVE length (mm)	**F_x (N) and difference compared to DNS model**						
	DNS	**Minimal**		**Periodic**		**Direct**	
$l_\mu = 0.500$ mm	194.89	102.58	47.36%	209.95	7.73%	1469.22	653.88%
$l_\mu = 0.333$ mm	192.88	97.30	49.55%	203.35	5.43%	1465.75	659.94%
$l_\mu = 0.250$ mm	191.89	95.10	50.44%	200.77	4.63%	1464.47	663.19%

Source: The author.

Table 18 – Size effect study considering the macro-scale mesh 1 for loading programme associated with tension: differences in reaction forces (F_x) for first-order multi-scale models compared to DNS models.

RVE length (mm)	**F_x (N) and difference compared to DNS model**						
	DNS	**Uniform traction**		**Periodic**		**Linear**	
$l_\mu = 0.500$ mm	194.89	91.57	53.02%	196.69	0.93%	1462.73	650.55%
$l_\mu = 0.333$ mm	192.88	91.57	52.53%	196.69	1.98%	1462.73	658.38%
$l_\mu = 0.250$ mm	191.89	91.57	52.28%	196.69	2.50%	1462.73	662.29%

Source: The author.

Table 19 – Size effect study considering the macro-scale mesh 1 for loading programme associated with compression: differences in reaction forces (F_x) for second-order multi-scale models compared to DNS models.

RVE length (mm)	**F_x (N) and difference compared to DNS model**						
	DNS	**Minimal**		**Periodic**		**Direct**	
$l_\mu = 0.500$ mm	-171.81	-94.08	45.24%	-185.06	7.71%	-1409.28	720.27%
$l_\mu = 0.333$ mm	-170.31	-87.94	48.36%	-178.30	4.69%	-1405.22	725.09%
$l_\mu = 0.250$ mm	-169.56	-85.32	49.68%	-175.72	3.63%	-1403.73	727.85%

Source: The author.

Table 20 – Size effect study considering the macro-scale mesh 1 for loading programme associated with compression: differences in reaction forces (F_x) for first-order multi-scale models compared to DNS models.

RVE length (mm)	**F_x (N) and difference compared to DNS model**						
	DNS	**Uniform traction**		**Periodic**		**Linear**	
$l_\mu = 0.500$ mm	-171.81	-81.22	52.73%	-172.00	0.11%	-1401.71	715.86%
$l_\mu = 0.333$ mm	-170.31	-81.22	52.31%	-172.00	0.99%	-1401.71	723.03%
$l_\mu = 0.250$ mm	-169.56	-81.22	52.10%	-172.00	1.44%	-1401.71	726.66%

Source: The author.

Figure 49 – Vertical displacements in mm (scale factor = 4) for first- and second-order models considering the RVE (length 1, i.e., $l_\mu = 0.50$ mm) under compression.

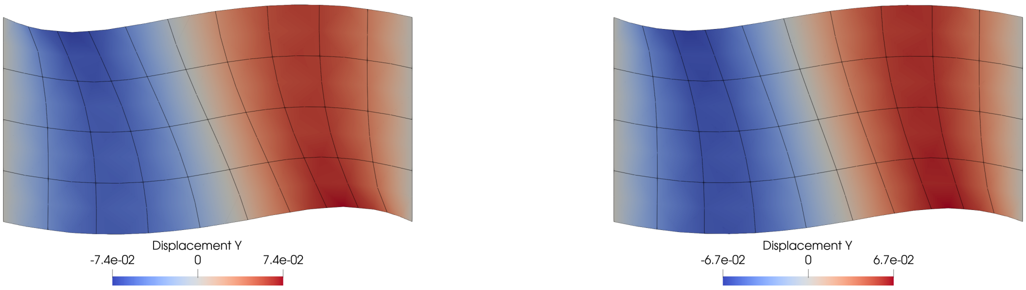

(a) Second-order: Minimal.

(b) Second-order: Periodic.

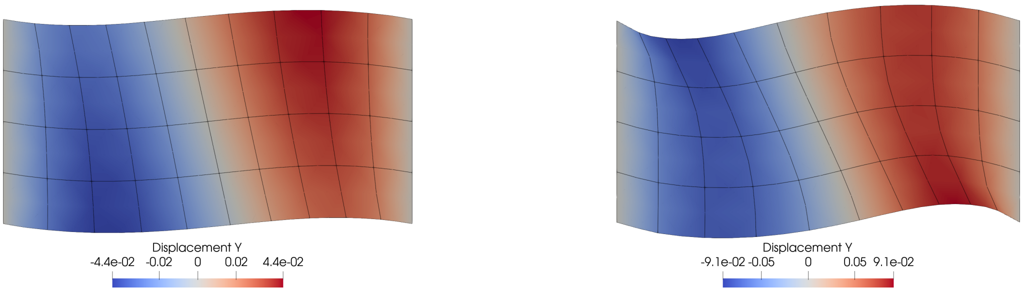

(c) Second-order: Direct.

(d) First-order: Uniform traction.

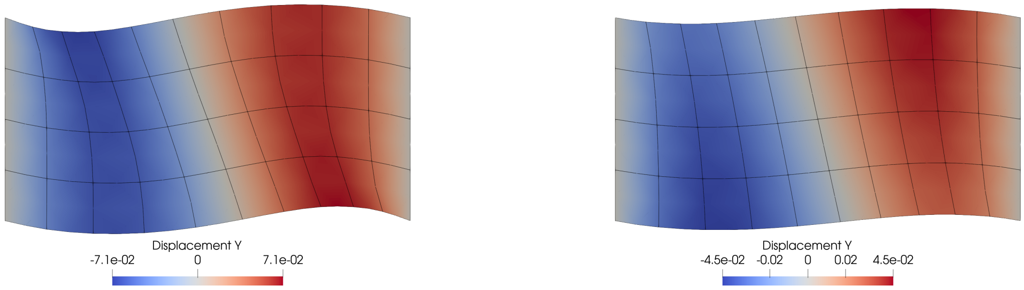

(e) First-order: Periodic.

(f) First-order: Linear.

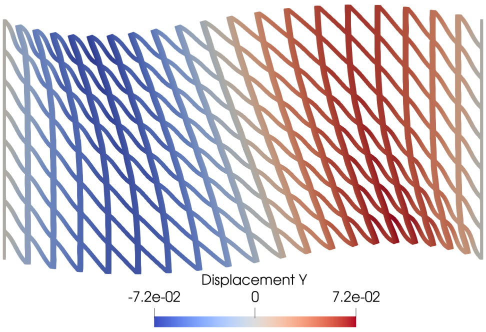

(g) DNS model 1.

Source: The author.

Figure 50 – Vertical displacements in mm (scale factor = 4) for first- and second-order models considering the RVE (length 1, i.e., $l_\mu = 0.50$ mm) under tension.

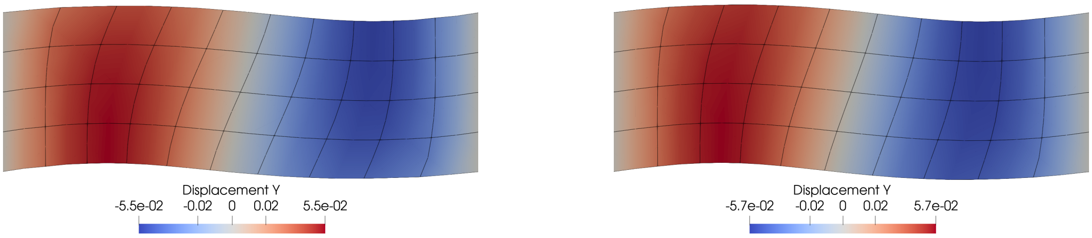

(a) Second-order: minimal. (b) Second-order: periodic.

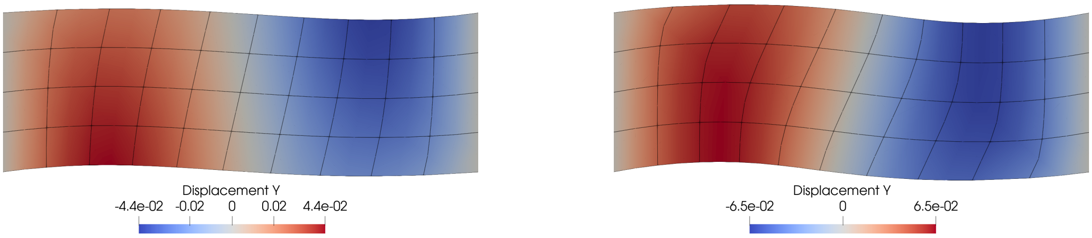

(c) Second-order: direct. (d) First-order: uniform traction.

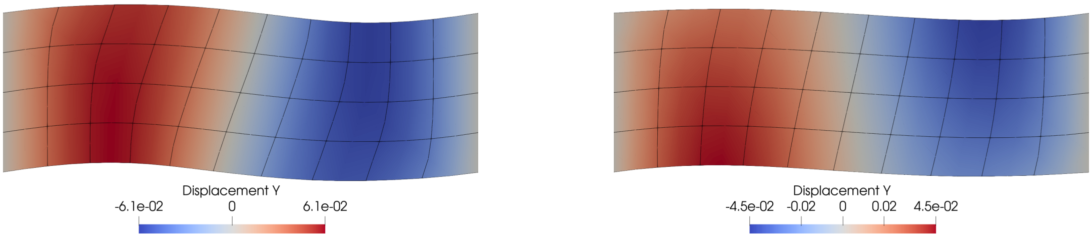

(e) First-order: periodic. (f) First-order: linear.

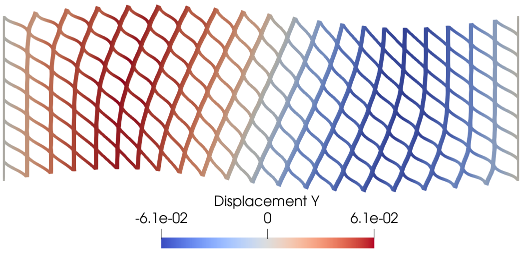

(g) DNS model 1.

Source: The author.

6.2.3 Analysis of the homogenised properties

The initial consistent tangents are interesting to better understand the axial tension/compression-induced undulation for the new metamaterial. The coupling-tangents $\mathbf{A}_\mathbf{G}$ and $\mathbf{H}_{\boldsymbol{F}}$, which couple first and second-order deformation modes, have null values for all components in this numerical example. Therefore, the observed mechanical behaviour is not a consequence of that kind of coupling, and that is the reason why first-order homogenisation is able to capture the undulation. Alternatively, the consistent tangent $\mathbf{A}$, which associates $\boldsymbol{P}$ with $\boldsymbol{F}$, is assessed to better understand the coupling mechanism that characterises this metamaterial.

For two-dimensional problems, the classical constitutive law for a homogeneous isotropic material can be written in simplified form as:

$$\begin{bmatrix} P_{11} \\ P_{21} \\ P_{12} \\ P_{22} \end{bmatrix} = \begin{bmatrix} \lambda+2\mu & 0 & 0 & \lambda \\ 0 & \mu & \mu & 0 \\ 0 & \mu & \mu & 0 \\ \lambda & 0 & 0 & \lambda+2\mu \end{bmatrix} \begin{bmatrix} F_{11}-1 \\ F_{21} \\ F_{12} \\ F_{22}-1 \end{bmatrix}, \tag{6.1}$$

where μ and λ are the Lamé parameters.

For multi-scale analysis, the initial version for the consistent tangent A is equivalent to the homogenised elastic constitutive tensor indicated in Equation (6.1), i.e.,

$$\begin{bmatrix} P_{11} \\ P_{21} \\ P_{12} \\ P_{22} \end{bmatrix} = \begin{bmatrix} A_{1111} & A_{1121} & A_{1112} & A_{1122} \\ A_{2111} & A_{2121} & A_{2112} & A_{2122} \\ A_{1211} & A_{1221} & A_{1212} & A_{1222} \\ A_{2211} & A_{2221} & A_{2212} & A_{2222} \end{bmatrix} \begin{bmatrix} F_{11}-1 \\ F_{21} \\ F_{12} \\ F_{22}-1 \end{bmatrix}. \tag{6.2}$$

In this context, the initial results of A for multi-scale models are presented in matrix representation ($\boldsymbol{A}$) as follows:

1. linear boundary condition (first-order) and direct constraint (second-order):

$$\boldsymbol{A}^{linear}_{1st-order} \approx \boldsymbol{A}^{direct}_{2nd-order} = \begin{bmatrix} 16045.84 & -11492.74 & -11492.74 & 11722.31 \\ -11492.74 & 14105.26 & 14105.26 & -9740.49 \\ -11492.74 & 14105.26 & 14105.26 & -9740.49 \\ 11722.31 & -9740.49 & -9740.49 & 58206.23 \end{bmatrix} \text{MPa},$$

2. periodic boundary condition (first-order) and periodic constraint (second-order):

$$\boldsymbol{A}^{periodic}_{1st-order} \approx \boldsymbol{A}^{periodic}_{2nd-order} = \begin{bmatrix} 12418.76 & -11928.96 & -11928.96 & 10715.56 \\ -11928.96 & 12158.33 & 12158.33 & -10949.70 \\ -11928.96 & 12158.33 & 12158.33 & -10949.70 \\ 10715.56 & -10949.70 & -10949.70 & 57206.25 \end{bmatrix} \text{MPa},$$

3. uniform traction boundary condition (first-order) and minimum constraint (second-order):

$$\boldsymbol{A}^{traction}_{1st-order} \approx \boldsymbol{A}^{minimal}_{2nd-order} = \begin{bmatrix} 3555.25 & -2693.13 & -2693.13 & 2500.95 \\ -2693.13 & 2225.52 & 2225.52 & -2010.42 \\ -2693.13 & 2225.52 & 2225.52 & -2010.42 \\ 2500.95 & -2010.42 & -2010.42 & 48814.20 \end{bmatrix} \text{MPa},$$

where the responses are similar for all RVE lengths. It is also worth mentioning that the initial values for $\boldsymbol{A}$ are the same in tension and compression, and that they are not dependent on the type of multi-scale formulation (first or second-order).

It is noteworthy that all components of $\mathbf{A}$ have non-null values, unlike the idealisation of Equation (6.1). Specifically, negative values arise for components of $\mathbf{A}$ (see values highlighted in pink and light gray) compared to Equation (6.1). Such components of $\mathbf{A}$ with negative values are associated with coupling mechanisms relating axial tension/compression and shear. Furthermore, the differences between the pink and light gray components occur due to the geometry of the RVE, since the homogenised material is not isotropic and the stiffness depends on the direction. Therefore, the effect of tension/compression-induced undulation is related to the coupling between tension/compression and shear, quantified by the shaded values in the initial consistent tangent $\mathbf{A}$, which is promoted by the geometry of the new micro-architected material. Moreover, the maximum vertical displacements are superior for the loading associated with compression when compared to the loading programme associated with tension, except for the linear boundary condition (first-order model) and the direct constraint (second-order model) which result in similar responses.

In order to explain this difference, Figure 51 shows the evolution of $\mathbf{A}$ for multi-scale models based on second-order computational homogenisation considering the integration point I_A at macro-scale mesh 1 (see Figure 46a). In addition, Figure 52 displays the particular case of A_{2111} component that relates P_{21} with F_{11}, i.e., the coupling effect between shear and tension/compression.

Figure 51 – Norm of $\mathbf{A}$ required for multi-scale modelling based on second-order homogenisation: comparison between compression and tension loading programmes.

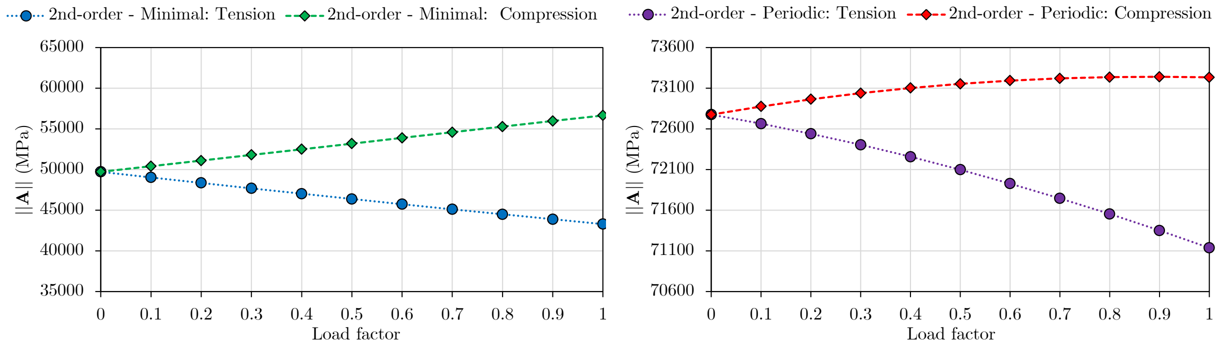

(a) Second-order: Minimal.

(b) Second-order: Periodic.

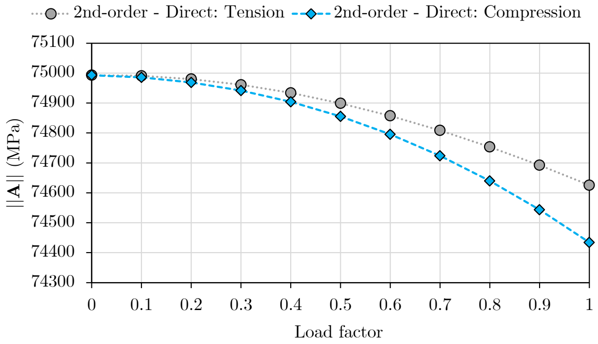

(c) Second-order: Direct.

Source: The author.

Figure 52 – Results for A_{2111} component (coupling between P_{21} and F_{11}) for second-order homogenisation: compression and tension loading programmes.

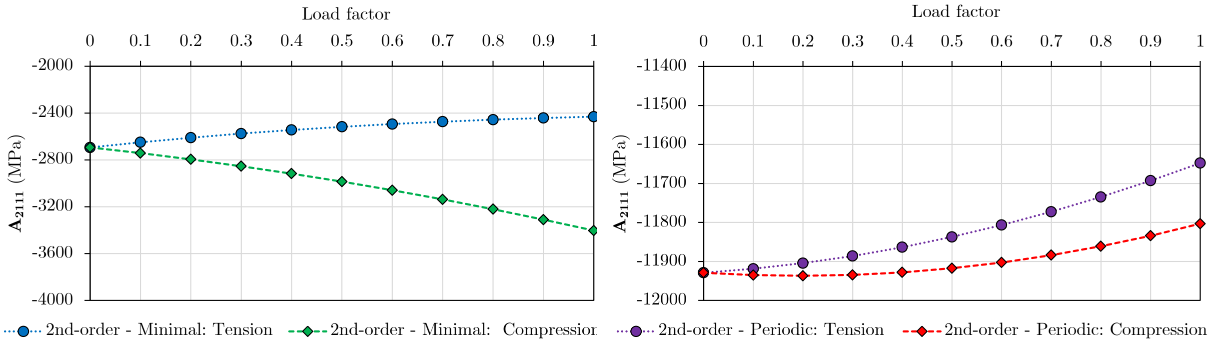

(a) Second-order: Minimal.

(b) Second-order: Periodic.

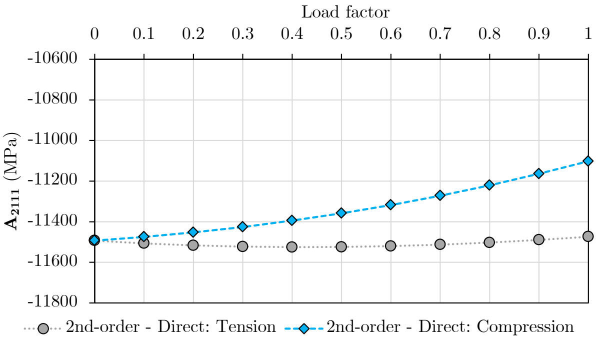

(c) Second-order: Direct.

Source: The author.

It is possible to observe that the evolution of the responses is different for tension and compression, which contributes to the difference in the maximum vertical macroscopic displacements. In particular, the differences in the evolution of $\mathbf{A}$, considering compression and tension, are more pronounced for periodic and minimal constraint, in which a stronger coupling occurs for compression loading programme. Such observations justify the differences in the maximum displacements observed in periodic and minimal constraint models when comparing tension and compression. Such difference is not observed for the direct constraint since it is the most restrictive boundary condition. Finally, the conclusions are analogous to multi-scale models based on first-order homogenisation.

6.2.3.1 Symmetry class of the homogenised material properties

It is also relevant to explore the symmetry class related to the material properties of the new mechanical metamaterial with tension/compression-induced undulation. In this case, three-dimensional simulations are employed to verify more components of the homogenised elastic constitutive tensor associated, unraveling other possible couplings. In this context, an analogous three-dimensional unit cell (see Figure 53) was simulated to obtain the initial consistent tangent $\mathbf{A}$ that is equivalent to the homogenised elastic constitutive tensor.

Figure 53 – Three-dimensional unit cell or RVE.

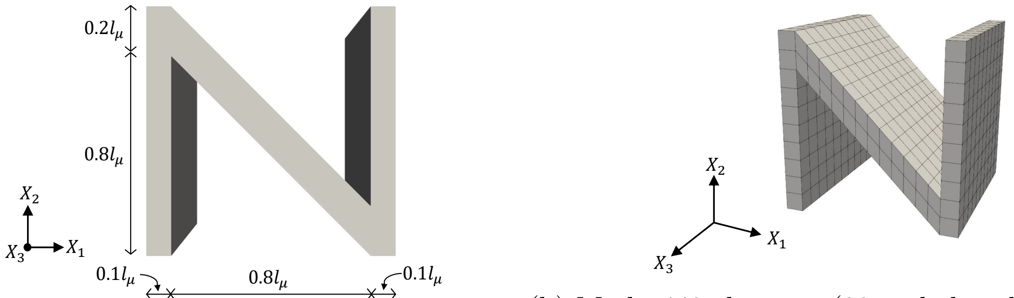

(a) Geometry.

(b) Mesh: 440 elements (20-node hexahedron or H20) and 2937 nodes.

Source: The author.

For three-dimensional analysis, the constitutive relationship between $\boldsymbol{P}$ and $\boldsymbol{F}$, taking into account $\mathsf{\mathbf{A}}$, can be expressed in matrix form as follows

$$\begin{bmatrix} P_{11} \\ P_{21} \\ P_{31} \\ P_{12} \\ P_{22} \\ P_{32} \\ P_{13} \\ P_{23} \\ P_{33} \end{bmatrix} = \begin{bmatrix} A_{1111} & A_{1121} & A_{1131} & A_{1112} & A_{1122} & A_{1132} & A_{1113} & A_{1123} & A_{1133} \\ A_{2111} & A_{2121} & A_{2131} & A_{2112} & A_{2122} & A_{2132} & A_{2113} & A_{2123} & A_{2133} \\ A_{3111} & A_{3121} & A_{3131} & A_{3112} & A_{3122} & A_{3132} & A_{3113} & A_{3123} & A_{3133} \\ A_{1211} & A_{1221} & A_{1231} & A_{1212} & A_{1222} & A_{1232} & A_{1213} & A_{1223} & A_{1233} \\ A_{2211} & A_{2221} & A_{2231} & A_{2212} & A_{2222} & A_{2232} & A_{2213} & A_{2223} & A_{2233} \\ A_{3211} & A_{3221} & A_{3231} & A_{3212} & A_{3222} & A_{3232} & A_{3213} & A_{3223} & A_{3233} \\ A_{1311} & A_{1321} & A_{1331} & A_{1312} & A_{1322} & A_{1332} & A_{1313} & A_{1323} & A_{1333} \\ A_{2311} & A_{2321} & A_{2331} & A_{2312} & A_{2322} & A_{2332} & A_{2313} & A_{2323} & A_{2333} \\ A_{3311} & A_{3321} & A_{3331} & A_{3312} & A_{3322} & A_{3332} & A_{3313} & A_{3323} & A_{3333} \end{bmatrix} \begin{bmatrix} F_{11}-1 \\ F_{21} \\ F_{31} \\ F_{12} \\ F_{22}-1 \\ F_{32} \\ F_{13} \\ F_{23} \\ F_{33}-1 \end{bmatrix}. \tag{6.3}$$

Due to the conditions of major and minor symmetries at the undeformed configuration, an anisotropic material exhibits 21 independent elastic constants. Thus, $\mathsf{\mathbf{A}}$ can be rewritten in simplified matrix form as

$$\boldsymbol{A} = \begin{bmatrix} A_{1111} & A_{1122} & A_{1133} & A_{1123} & A_{1131} & A_{1112} \\ A_{2211} & A_{2222} & A_{2233} & A_{2223} & A_{2231} & A_{2212} \\ A_{3311} & A_{3322} & A_{3333} & A_{3323} & A_{3331} & A_{3312} \\ A_{2311} & A_{2322} & A_{2333} & A_{2323} & A_{2331} & A_{1312} \\ A_{3111} & A_{3122} & A_{3133} & A_{3123} & A_{3131} & A_{3112} \\ A_{1211} & A_{1222} & A_{1233} & A_{1223} & A_{1231} & A_{1212} \end{bmatrix}, \tag{6.4}$$

where the 6x6 matrix is symmetric due to major symmetry.

For example, considering Equation (6.3), the initial consistent tangent for first-and second-order periodic multi-scale models ($\boldsymbol{A}_{per.}$) is given by

$$\boldsymbol{A}_{per.} = \begin{bmatrix} 12473.61 & 10763.24 & 6971.06 & 0.00 & 0.00 & -11957.20 \\ 10763.24 & 57342.19 & 20431.63 & 0.00 & 0.00 & -10976.77 \\ 6971.06 & 20431.63 & 83820.80 & 0.00 & 0.00 & -6880.19 \\ 0.00 & 0.00 & 0.00 & 22287.91 & -6891.89 & 0.00 \\ 0.00 & 0.00 & 0.00 & -6891.89 & 9241.15 & 0.00 \\ -11957.20 & -10976.77 & -6880.19 & 0.00 & 0.00 & 12186.84 \end{bmatrix} \text{MPa},$$

where negative components with shear-normal coupling (pink box) and shear-shear coupling (light gray box) can be observed.

It is worth mentioning that material symmetry refers to how constitutive properties vary with respect to direction in a fixed material point. In particular, the new metamaterial is called monoclinic with one plane of material symmetry (in this case, X_3 direction). Therefore, the metamaterial has 13 independent elastic constants.

6.3 Multi-scale numerical example 3: two-dimensional architected material under bending with size effects

The main goal of this numerical experiment is to show the capacity of second-order homogenisation to deal with size effects of architected materials under bending with size effects through two-dimensional numerical simulations. The elastic properties for the architected material are E = 100 MPa and ν = 0.3. Moreover, the assumption of plane strain is adopted for the two-dimensional structure.

6.3.1 DNS Models

The geometry for the periodic unit cells of the architected material is indicated in Figure 54. Information about all DNS models and the discretisation is provided in Table 21. It is important to note that the material volume fraction remains invariant across all DNS models. The DNS models are created as a periodic array from the unit cell, where different cell sizes are defined. For illustration purposes, Figure 55 shows three coarser DNS models. Regarding the Dirichlet boundary conditions, the left side of the structure is fixed, i.e., $u_{0x} = u_{0y} = 0.0$. Concerning the Neumann boundary conditions, a uniformly distributed vertical load t_{0y} is applied on the top side of the structure. Specifically, the loading programme t_{0y} = -5.0 x 10^{-5} N/mm is imposed in 10 equally spaced increments. Moreover, the distribution of the applied load provides a linear shear force and a quadratic bending moment along the length (L_x) of the structure.

Figure 54 – Unit cell and RVE.

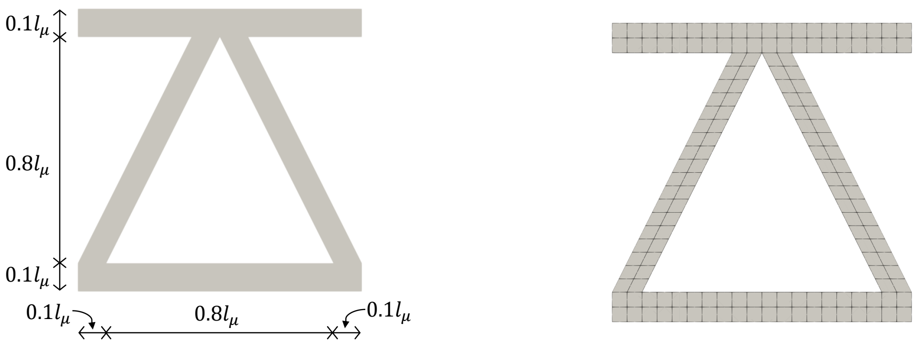

(a) Geometry.

(b) Mesh: 152 elements (Q8) and 608 nodes.

Source: The author.

Figure 55 – Geometry of the DNS models ($L_x = 25$ mm and $L_y = 1$ mm).

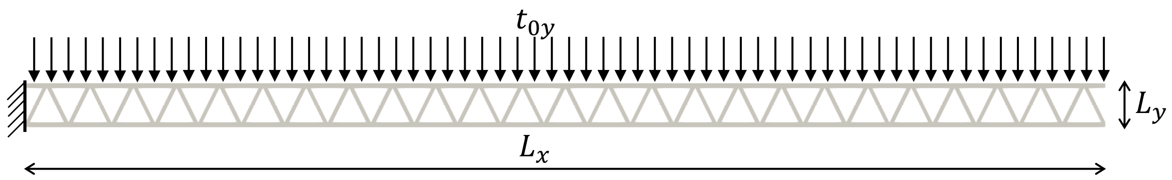

(a) DNS model 1 (25x1 unit cells) - Size 1.

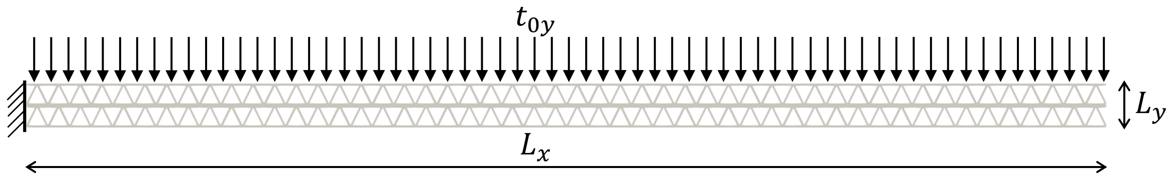

(b) DNS model 2 (50x2 unit cells) - Size 2.

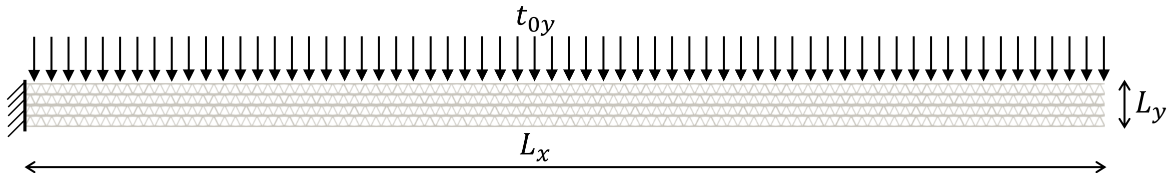

(c) DNS model 3 (100x4 unit cells) - Size 3.

Source: The author.

A comparison of the vertical displacements for the DNS models is shown in Figure 56. It is clear that the length of the unit cell plays an important role in the deformable behaviour of the structure. In summary, decreasing the unit cell size increases the maximum displacements of DNS models, i.e., the structure becomes more flexible. Consequently, DNS model 1 is the stiffest and DNS model 3 is the most flexible. Furthermore, the deformed configuration of DNS model 2 is closer to the response observed for DNS model 3. Thus, the size effects cannot be neglected in the structure and higher-order continuum theories can be important for modelling this type of architected material.

Table 21 – Mesh of DNS models.

DNS	**Elements (Q8)**	**Nodes**
Model 1 - Size 1 ($l_\mu = 1.000$ mm)	3800	14960
Model 2 - Size 2 ($l_\mu = 0.500$ mm)	15200	57819
Model 3 - Size 3 ($l_\mu = 0.250$ mm)	60800	227237
Model 4 - Size 4 ($l_\mu = 0.167$ mm)	136800	508255
Model 5 - Size 5 ($l_\mu = 0.125$ mm)	243200	900873
Model 6 - Size 6 ($l_\mu = 0.100$ mm)	380000	1405091

Source: The author.

Figure 56 – DNS models (scale factor = 4).

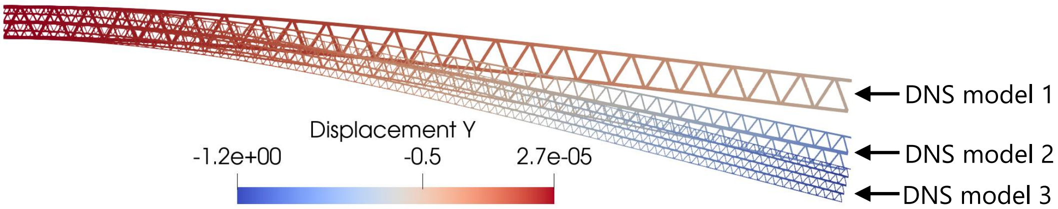

Source: The author.

6.3.2 Multi-scale simulations

This bending problem is solved using multi-scale FE^2 models, with both first and second-order homogenisation approaches. Different classes of boundary conditions are also considered, similar to the analysis performed in Section 6.2.2. The RVE geometry and mesh were previously presented in Figure 54. Regarding the macro-scale, the geometry and boundary conditions are illustrated in Figure 57.

Figure 57 – Geometry and boundary conditions.

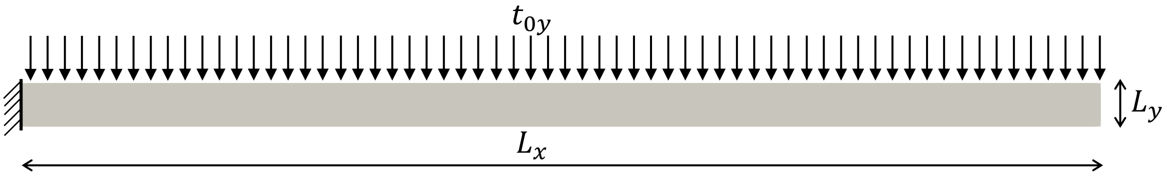

Source: The author.

Moreover, mixed quadrilateral finite elements (Q8F4L1) (Lopes; Pires, 2022d) with 4 integration points are defined for macro-scale for second-order homogenisation. The first-order multi-scale simulations were performed using Q8 elements. To perform a numerical convergence analysis, three meshes (see Figure 58) were employed to discretise the macro-scale domain, and the simulations have been performed with an RVE length l_μ = 1.00 mm. The obtained maximum vertical displacements are presented in Figure 59, where it is observed that the maximum values are similar for all meshes. Consequently, mesh 1 is adopted for investigating the architected material, from a multi-scale perspective.

Figure 58 – Macro-scale meshes.

(a) Mesh1: 100 elements (Q8F4L1) and 405 nodes.

(b) Mesh 2: 400 elements (Q8F4L1) and 1409 nodes.

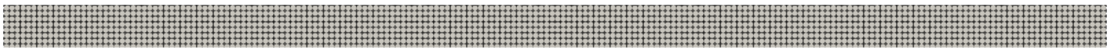

(c) Mesh 3: 1600 elements (Q8F4L1) and 5217 nodes.

Source: The author.

Figure 59 – Mesh study considering the maximum vertical displacement U_y (mm) on the right side of the structure for RVE size 1 ($l_\mu = 1.00$ mm).

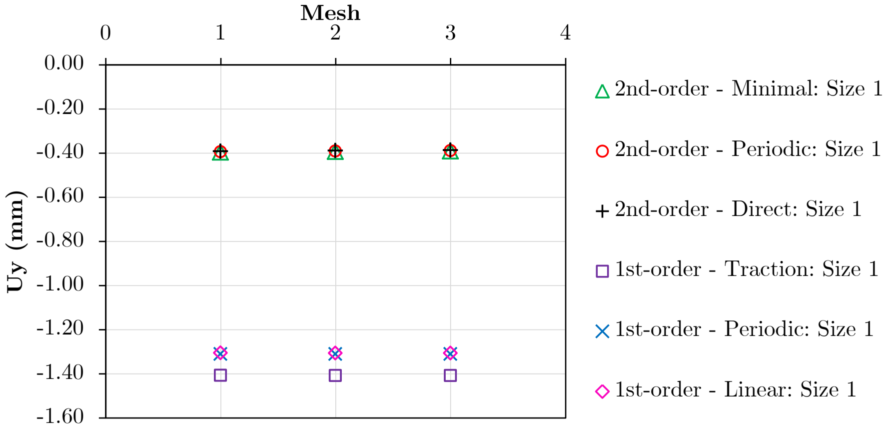

Source: The author.

In order to investigate the microstructural size effect, six values were considered for the RVE length: $l_\mu = 1.000$ mm (size 1), $l_\mu = 0.500$ mm (size 2), $l_\mu = 0.250$ mm (size 3), $l_\mu = 0.167$ mm (size 4), $l_\mu = 0.125$ mm (size 5) and $l_\mu = 0.100$ mm (size 6). The results for the maximum vertical displacement associated with each characteristic length are shown in Figure 60, where the values obtained with the multi-scale models, both first- and second-order homogenisation, are represented along with the corresponding DNS results. Tables 22 and 23 show the differences (in module) of multi-scale models compared to DNS models. In addition, Figures 61 and 62 show the results of the vertical displacements of the deformed structures ($l_\mu = 1.000$ mm) for the first- and second-order homogenisation strategies, respectively.

In general, second-order multi-scale models (minimal, periodic and direct constraints) have similar results. An analogous conclusion is observed for first-order multi-scale models (uniform traction, periodic and linear boundary conditions). Moreover, since the size effect is significant in this structure, the first-order (so-called classical) multi-scale computational homogenisation scheme looses accuracy. It must be highlighted that the response obtained with first-order homogenisation is independent of the RVE length, and significant differences are observed for larger RVEs. On the other hand, second-order multi-scale computational homogenisation models capture the trend observed in the DNS models, with an increase of the maximum displacements for a reduction in the RVE size. It is worth noting that the responses are close for smaller characteristic lengths of RVE. Therefore, second-order homogenisation is needed to better predict the macroscopic behaviour of the architected material, in particular to capture the underlying size effects.

Figure 60 – RVE length x maximum vertical displacement U_y (mm) on the right side of the structure for macro-mesh 1.

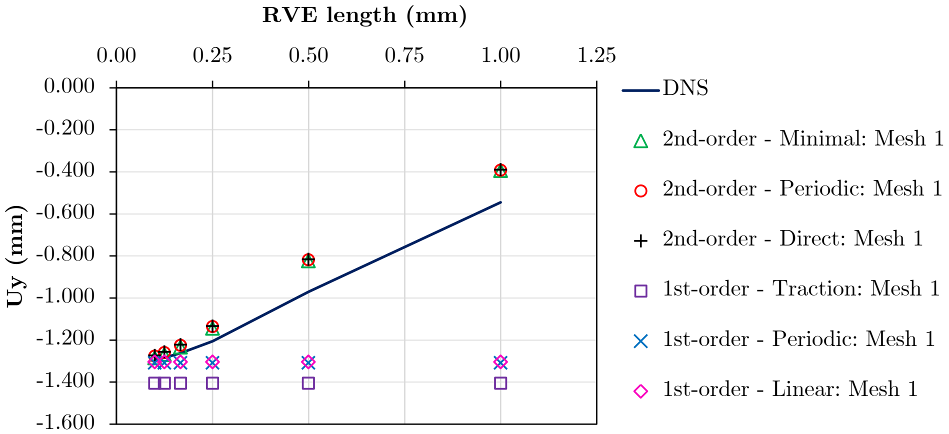

Source: The author.

Table 22 – Maximum vertical displacement on the right side of the structure (U_y) for all second-order multi-scale models, including differences in comparison with DNS models.

RVE length (mm)	**U_y (mm) and differences compared to DNS model**						
	DNS	**Minimal**		**Periodic**		**Direct**	
$l_\mu = 1.000$	-0.545	-0.396	27.46%	-0.393	27.92%	-0.391	28.29%
$l_\mu = 0.500$	-0.970	-0.825	14.92%	-0.820	15.46%	-0.817	15.72%
$l_\mu = 0.250$	-1.206	-1.146	4.98%	-1.138	5.64%	-1.135	5.87%
$l_\mu = 0.167$	-1.262	-1.235	2.16%	-1.226	2.86%	-1.223	3.08%
$l_\mu = 0.125$	-1.284	-1.270	1.06%	-1.261	1.77%	-1.258	1.99%
$l_\mu = 0.100$	-1.294	-1.287	0.52%	-1.277	1.24%	-1.275	1.47%

Source: The author.

Table 23 – Maximum vertical displacement on the right side of the structure (U_y) for all first-order multi-scale models, including differences compared to DNS models.

RVE length (mm)	**U_y (mm) and differences compared to DNS model**						
	DNS	**Uniform Traction**		**Periodic**		**Linear**	
$l_\mu = 1.000$	-0.545	-1.406	157.84%	-1.310	140.15%	-1.305	139.30%
$l_\mu = 0.500$	-0.970	-1.406	45.02%	-1.310	35.07%	-1.305	34.59%
$l_\mu = 0.250$	-1.206	-1.406	16.65%	-1.310	8.65%	-1.305	8.27%
$l_\mu = 0.167$	-1.262	-1.406	11.40%	-1.310	3.76%	-1.305	3.39%
$l_\mu = 0.125$	-1.284	-1.406	9.57%	-1.310	2.05%	-1.305	1.69%
$l_\mu = 0.100$	-1.294	-1.406	8.72%	-1.310	1.26%	-1.305	0.90%

Source: The author.

Figure 61 – Vertical displacements (mm) for first-order multi-scale models: Size 1, 2 and 3 (scale factor = 4).

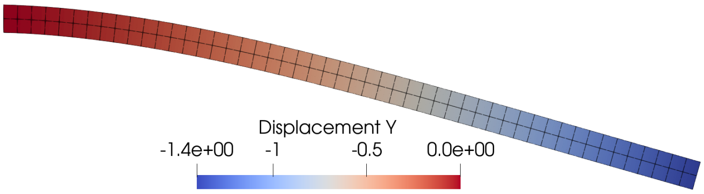

(a) First-order: Uniform traction.

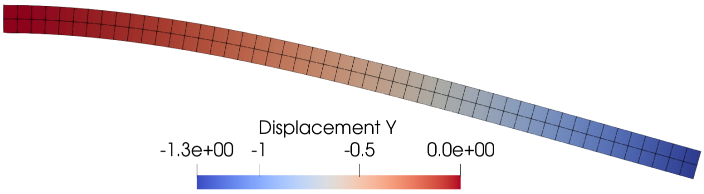

(b) First-order: Periodic.

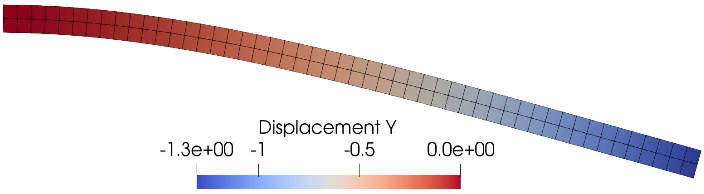

(c) First-order: Linear.

Source: The author.

Figure 62 – Vertical displacements (mm) for second-order multi-scale models: Size 1, 2 and 3 (scale factor = 4).

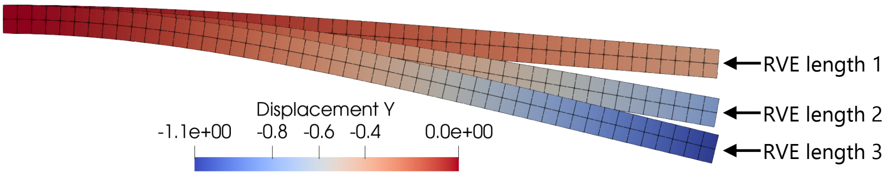

(a) Second-order: Minimal.

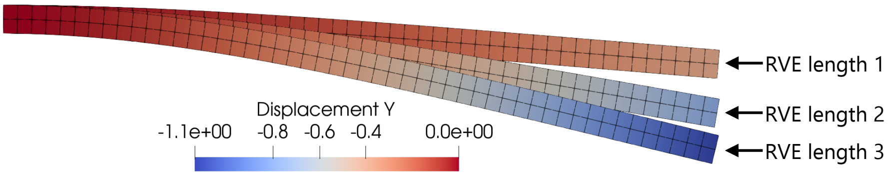

(b) Second-order: Periodic.

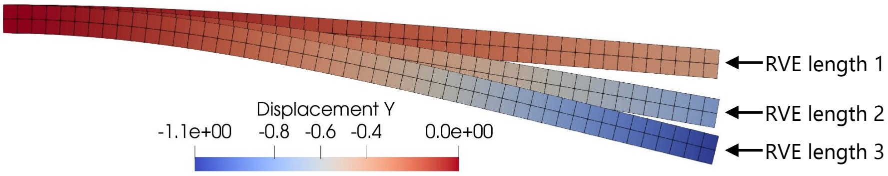

(c) Second-order: Direct.

Source: The author.

6.4 Multi-scale numerical example 4: three-dimensional architected material under bending exhibiting size effects

The objective of this numerical experiment is to demonstrate the effectiveness of second-order homogenisation in addressing size effects in three-dimensional architected materials under bending exhibiting size effects. This is achieved through three-dimensional numerical simulations. The elastic properties are $E = 100$ MPa and $\nu = 0.3$.]

6.4.1 DNS models

Regarding DNS models, the three-dimensional architected material is formed by a micro-architected arrangement of unit cells with a triangle-shaped cross-section (see Figure 63). Three DNS models were explored in the numerical analyses (see Figure 64), taking into account $l_\mu = 1.00$ mm, $l_\mu = 0.50$ mm, and $l_\mu = 0.33$ mm.

Figure 63 – Unit cell and RVE.

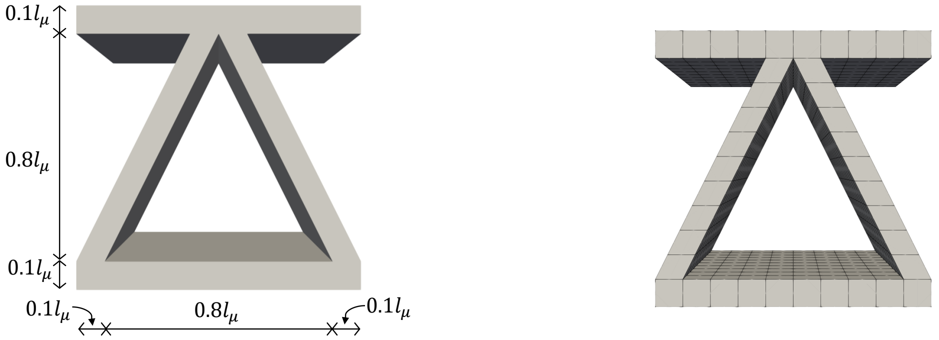

(a) Geometry. (b) Mesh: 152 elements (Q8) and 608 nodes.

Source: The author.

Figure 64 – Geometry of the DNS models ($L_x = 25$ mm and $L_y = 1$ mm).

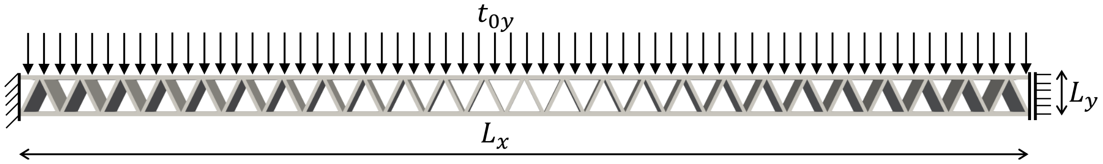

(a) DNS model 1 (25x1 unit cells) - Size 1.

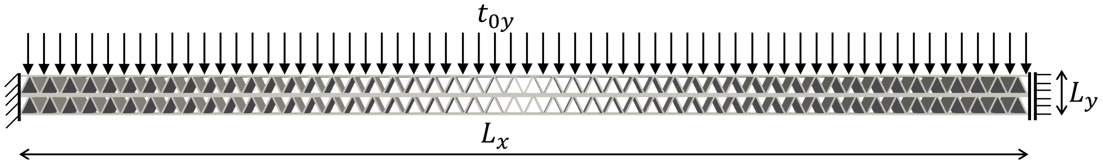

(b) DNS model 2 (50x2 unit cells) - Size 2.

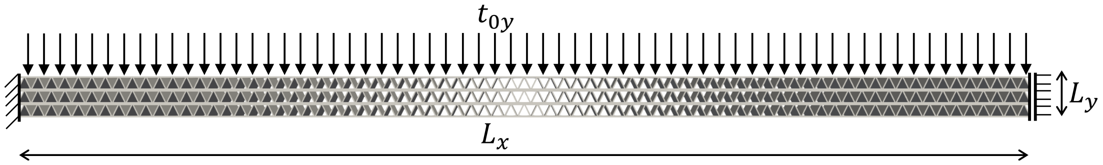

(c) DNS model 3 (100x4 unit cells) - Size 3.

Source: The author.

The available memory requirements of the computer used in the numerical simulations limited more refined DNS models. This limitation regarding memory requirements highlights a drawback of more refined DNS models, whose simulation may become impractical. As shown in Figure 64, the left side of the structures is fixed (i.e., $u_{0x} = u_{0y} = u_{0z} = 0$), whereas the right side is constrained only in the x- and z-directions (i.e., $u_{0x} = u_{0z} = 0$). The loading programme is defined by a uniformly distributed load t_{0y} = -2.0 x 10^{-4} N/mm^2 on the upper surface of the structure, considering 15 increments. Mesh details for the DNS models are provided in Table 24, where the H20 element were defined to discretise the structures.

Table 24 – Mesh of DNS models.

DNS	**Elements (H20)**	**Nodes**
Model 1 - Size 1 (l_μ = 1.00 mm)	9500	68706
Model 2 - Size 2 (l_μ = 0.50 mm)	76000	499771
Model 3 - Size 3 (l_μ = 0.33 mm)	256500	1632196

Source: The author.

Figure 65 shows the maximum vertical displacements obtained from the DNS finite element models. In summary, the architected structure displays the size effect, where DNS Model 1 is stiffer and DNS Model 3 is more flexible. Although DNS Model 2 exhibits an intermediate response, its results are close to those of DNS Model 3.

Figure 65 – Vertical displacements (mm) for DNS models 1, 2, and 3 (scale factor = 5).

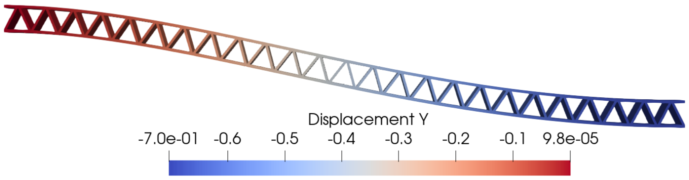

(a) DNS model 1.

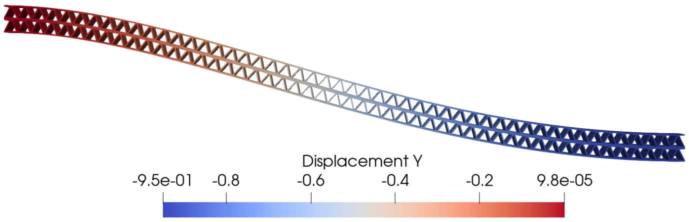

(b) DNS model 2.

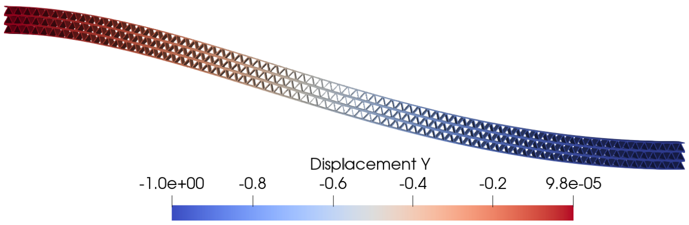

(c) DNS model 3.
Source: The author.

6.4.2 Multi-scale simulations

’ Regarding the coupled multi-scale simulations, geometry and mesh parameters must be defined for the macro and micro-scales. Figure 76 illustrates the geometry and boundary conditions for macro-scale (analogous to DNS models). The features of the RVE are shown in Figure 63, including its morphology and mesh (composed of H20 elements). In this case, seven RVE sizes were simulated: $l_\mu = 1.000$ mm, $l_\mu = 0.500$ mm, $l_\mu = 0.333$ mm, $l_\mu = 0.250$ mm, $l_\mu = 0.125$ mm, and $l_\mu = 0.100$ mm. Note that multi-scale simulations allow us to consider smaller RVE lengths with similar computational cost and memory requirements, which is an advantage compared to DNS models that were unfeasible due to the limited memory requirements of the processing computer. Coupled numerical simulations are conducted for all first- and second-order multi-scale models. Mixed hexahedral elements with 20 nodes (H20F8L1) and 8 integration points are employed to discretise the macro-scale to comply with the C^1-continuity requirement in second-order multi-scale simulations (Lopes, 2019; Lopes; Pires, 2022a). The first-order multi-scale simulations were performed using H20 elements. To conduct a refinement study, two meshes were investigated at the macro-scale for $l_\mu = 1.000$ mm (see Figure 67).

Figure 66 – Data for macro-scale simulations ($L_x = 25$ mm and $L_y = L_z = 1$ mm).

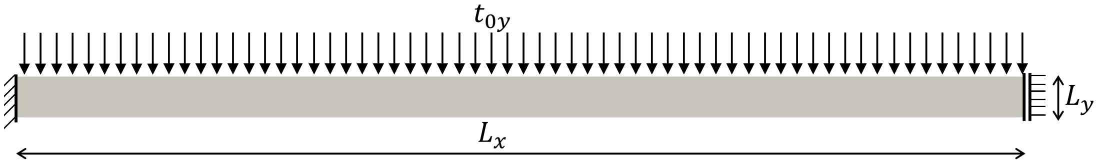

Source: The author.

Figure 67 – Macro-scale meshes.

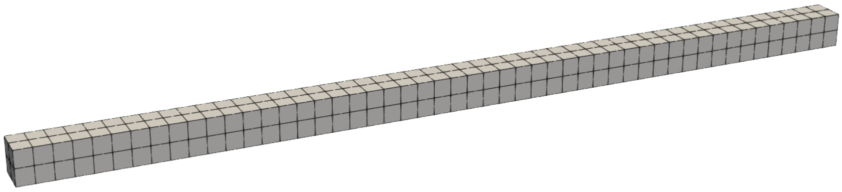

(a) Mesh 1: 200 elements (H20F8L1) and 1521 nodes.

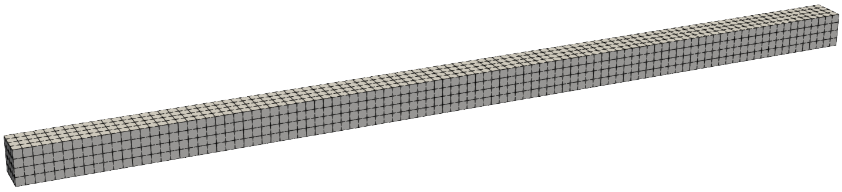

(b) Mesh 2: 1600 elements (H20F8L1) and 9065 nodes.
Source: The author.

The mesh refinement study was carried out taking into account the maximum vertical displacement of the structures. As shown in Figure 77, the responses are very close for both meshes defined at the macro-scale. In particular, the first-order approach with the uniform traction boundary condition did not show convergence in the numerical analysis. Since mesh 1 is in close agreement with the result of mesh 2, it is more computationally efficient to select mesh 1 for performing the remaining numerical simulations.

Figure 68 – Mesh study considering the maximum vertical displacement U_y (mm) on the right side of the structure for RVE size 1 ($l_\mu = 1.00$ mm).

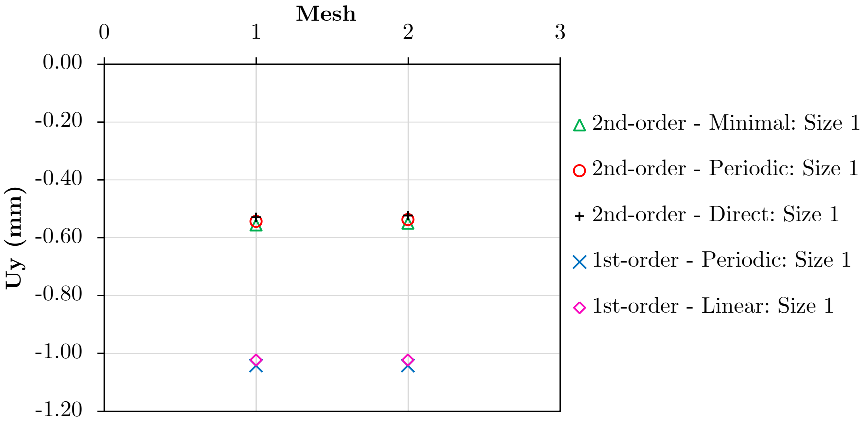

Source: The author.

Figure 69 depicts the numerical results of the size effect on architected structures under bending, where the first- and second-order multi-scale simulations are compared with DNS models. For example, Figures 70 and 71 display colour maps of the vertical displacements of the deformed structures simulated by the first- and second-order periodic multi-scale models, respectively. Second-order models yield similar results, and the same conclusion applies to first-order models. The second-order multi-scale simulations show better agreement with the DNS models, capturing the scale effect of the architected structures. Moreover, the second-order models (periodic and minimum constraint) converge to their respective first-order models (periodic and linear boundary conditions).

Figure 69 – RVE length x maximum vertical displacement U_y (mm) on the right side of the structure for macro-mesh 1.

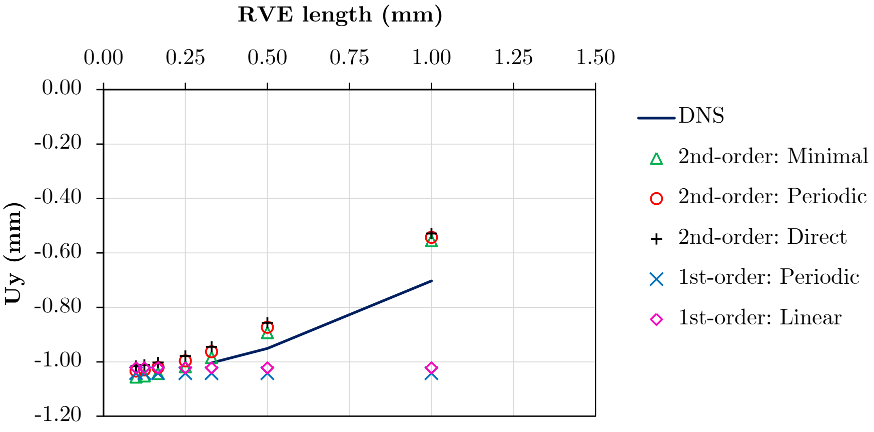

Source: The author.

Figure 70 – Vertical displacements (mm) for first-order periodic multi-scale model: All sizes (scale factor = 5).

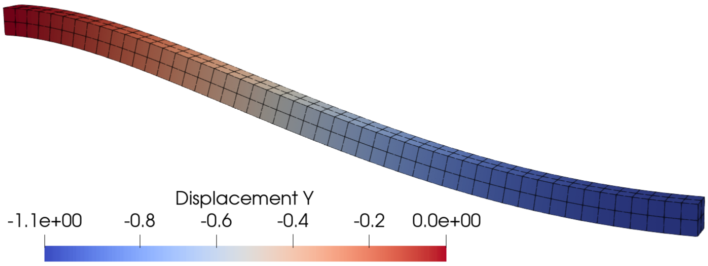

Source: The author.

Figure 71 – Vertical displacements (mm) for second-order periodic multi-scale model: Size 1, 2 and 3 (scale factor = 5).

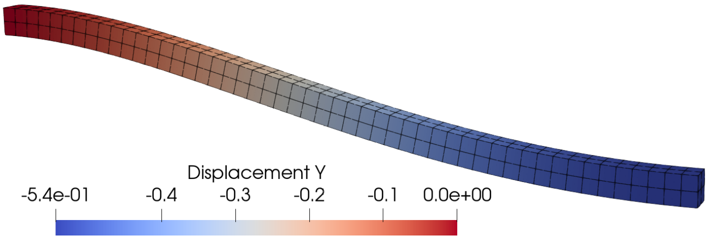

(a) Size 1.

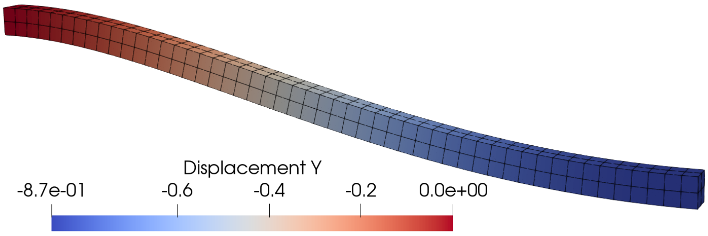

(b) Size 2.

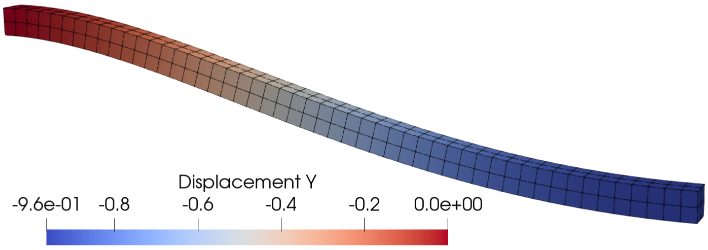

(c) Size 3.

Source: The author.

6.5 Multi-scale numerical example 5: three-dimensional architected material under bending displaying size effects

This example aims to investigate an architected material under bending displaying size effects through three-dimensional numerical simulations. The material properties of the matrix are $E = 100$ MPa and $\nu = 0.3$.

6.5.1 DNS models

In this case, the architected material under study consist of periodic cellular materials formed by the unit cell shown in Figure 73. Figure 72 presents the DNS models that represent the architected structures, incluindo including cases formed by unit cells with $l_\mu = 1.00$ mm, $l_\mu = 0.50$ mm, and $l_\mu = 0.33$ mm.

Figure 72 – Geometry of the DNS models ($L_x = 25$ mm and $L_y = L_z = 1$ mm).

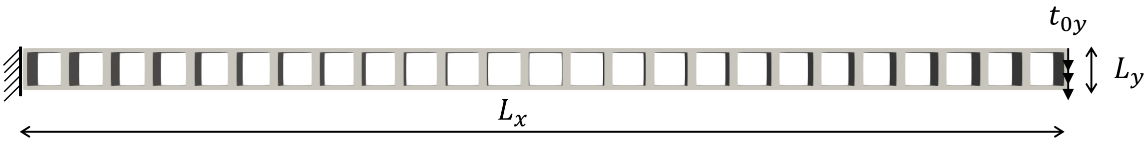

(a) DNS model 1 (25x1x1 unit cells): Size 1.

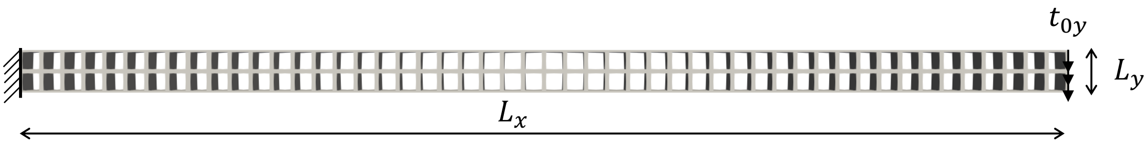

(b) DNS model 2 (50x2x2 unit cells): Size 2.

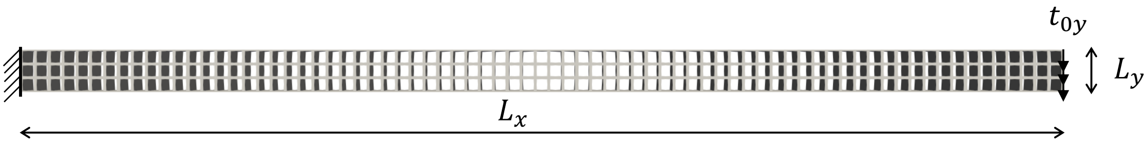

(c) DNS model 3 (75x3x3 unit cells): Size 3.

Source: The author.

Figure 73 – Unit cell and RVE.

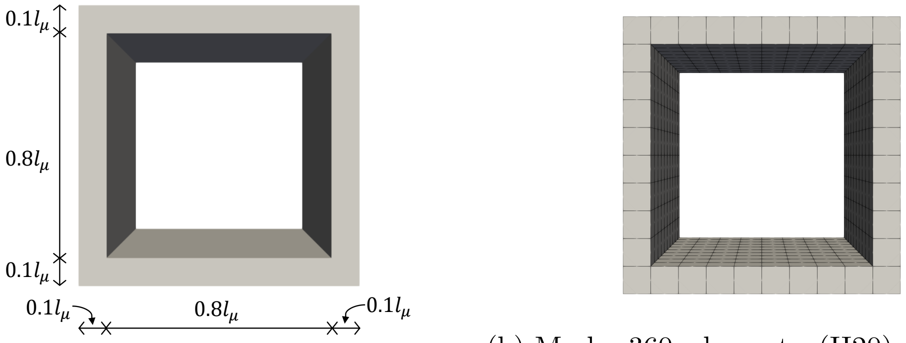

(a) Geometry.

(b) Mesh: 360 elements (H20) and 2700 nodes.

Source: The author.

The left side of the structures is fixed, i.e. the following Dirichlet boundary conditions are prescribed: $u_{0x} = u_{0y} = u_{0z} = 0$. The loading programme consists of a vertical tangential distributed load t_{0y} = -1.0 x 10^{-3} N/mm^2 imposed on the right side of the structure considering 10 increments (see detail in Figure 74). With respect to internal forces, the distribution of the applied load indicates a constant shear force and a linear bending moment along the length (L_x) of the structure. Meshes data for the DNS models are shown in Table 25, where the H20 elements with 8 integration points were defined to create the structured meshes. Since a large number of unit cells results in a significant increase in finite elements and degrees of freedom, more refined DNS models were limited by the available memory requirements of the computer used in the numerical simulations.

Figure 74 – Distributed vertical loading (t_{oy}) applied on the right side of DNS models.

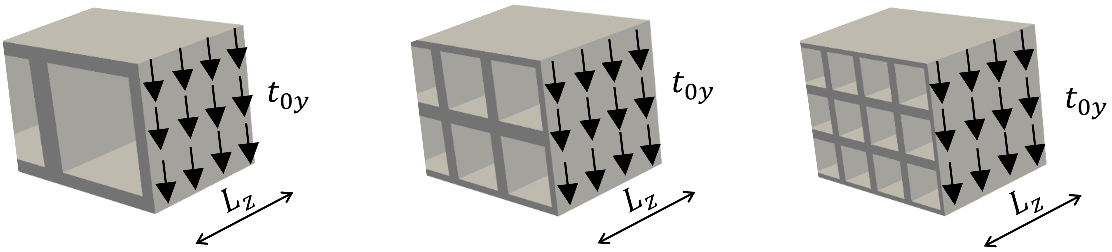

(a) DNS model 1. (b) DNS model 2. (c) DNS model 3.

Source: The author.

Table 25 – Mesh of DNS models.

DNS	Elements (H20)	Nodes
Model 1 - Size 1 ($l_\mu = 1.00$ mm)	9000	59316
Model 2 - Size 2 ($l_\mu = 0.50$ mm)	72000	426181
Model 3 - Size 3 ($l_\mu = 0.33$ mm)	243000	1385596

Source: The author.

Figure 75 presents a comparison of the vertical displacements for the DNS models. DNS model 1 is the structure with the most stiffness, while DNS model 3 is the most flexible. The DNS 2 model presents an intermediate response, being closer to the DNS 3 model. In this manner, the architected structure has the so-called size dependence related to material microstructure. Therefore, the generalised continuum mechanics can be more suitable for modelling this numerical example.

Figure 75 – Vertical displacements (mm) for DNS models (scale factor = 3).

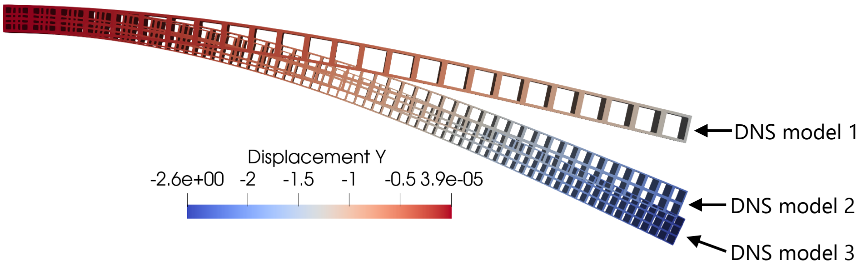

Source: The author.

6.5.2 Multi-scale simulations

Regarding the coupled multi-scale simulations, geometry and mesh parameters must be defined for the macro and micro-scales. The RVE data are shown in Figure 73, including the mesh modelled with hexahedral elements (H20) and 8 integration points. Seven RVE lengths were considered for the multi-scale simulations: $l_\mu = 1.000$ mm (size 1), $l_\mu = 0.500$ mm (size 2), $l_\mu = 0.333$ mm (size 3), $l_\mu = 0.250$ mm (size 4), $l_\mu = 0.167$ mm (size 5), $l_\mu = 0.125$ mm (size 6) and $l_\mu = 0.100$ mm (size 7). Figure 76 illustrates the geometry and boundary conditions for macro-scale. In the second-order multi-scale simulations, H20F8L1 elements are employed to discretise the macro-scale. The first-order multi-scale simulations were performed using H20 elements. Multi-scale numerical simulations based on first and second-order computational homogenisation are shown only for periodic boundary conditions due to the better results when compared with the DNS models. Multi-scale analyses based on first-order homogenisation (periodic and uniform traction) and second-order homogenisation (periodic and minimal constraints) were explored in the numerical simulations. It is worth mentioning the convergence difficulties observed for the lower-bound multi-scale models, with the following observations: (i) the minimum constraint model (second-order strategy) achieved convergence only for larger RVE sizes, suggesting that the structure became too flexible for smaller RVE lengths, and (ii) the uniform traction model (first-order strategy) did not converge due to the excessive flexibility. In this context, the numerical results are shown only for periodic boundary conditions due to the better results when compared with the DNS models.

Figure 76 – Data for macro-scale simulations ($L_x = 25$ mm and $L_y = L_z = 1$ mm).

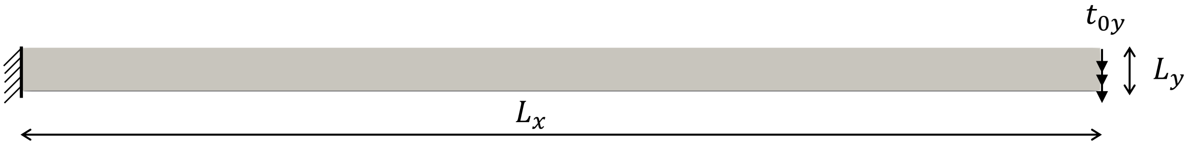

(a) Geometry and boundary conditions for macro-scale.

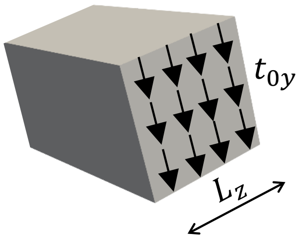

(b) Detail of distributed vertical loading (t_{oy}) applied on the right side of the macro-scale.

Source: The author.

A mesh refinement study was performed for the macro-scale, in which two meshes were investigated (see Figure 67) for $l_\mu = 1.0$ mm. As shown in Figure 77, the mesh convergence study was carried out taking into account the maximum vertical displacements of the structure. The responses are very close for both meshes defined at the macro-scale, i.e., the result of mesh 1 is in close agreement with the result of mesh 2. Thus, mesh 1 is sufficient to compute the numerical simulations.

Figure 77 – Mesh study for RVE size 1 ($l_\mu = 1.00$ mm) taking into account the maximum vertical displacement U_y (mm) on the right side of the structure.

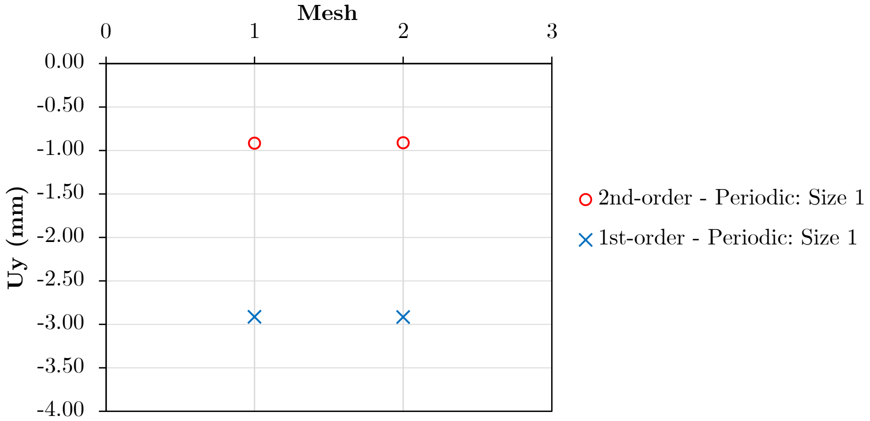

Source: The author.

Figure 78 shows the numerical results of the size effects study for the architected structures, where multi-scale simulations based on first- and second-order computational homogenisation with the periodic constraint are confronted with DNS models. The vertical displacements for first- and second-order multi-scale periodic boundary conditions are presented in Figures 79 and 80, respectively. The second-order homogenisation captures the increase in the maximum vertical displacement with the reduction of the RVE length. As observed in the DNS models, the periodic second-order multi-scale model associated with RVE size 2 (i.e., $l_\mu = 0.50$ mm) provides a deformed response close to the RVE size 3 (i.e., $l_\mu = 0.33$ mm). Therefore, the qualitative results of the second-order approach adhere to the DNS models. The quantitative differences between second-order approach and DNS models can be associated with higher-order terms not covered in the second-order strategy. Furthermore, second-order effects were not adequately captured by first-order homogenisation, where strong differences are observed in comparison to DNS models.

Figure 78 – RVE length x maximum vertical displacement U_y (mm) on the right side of the structure for macro-scale mesh 1.

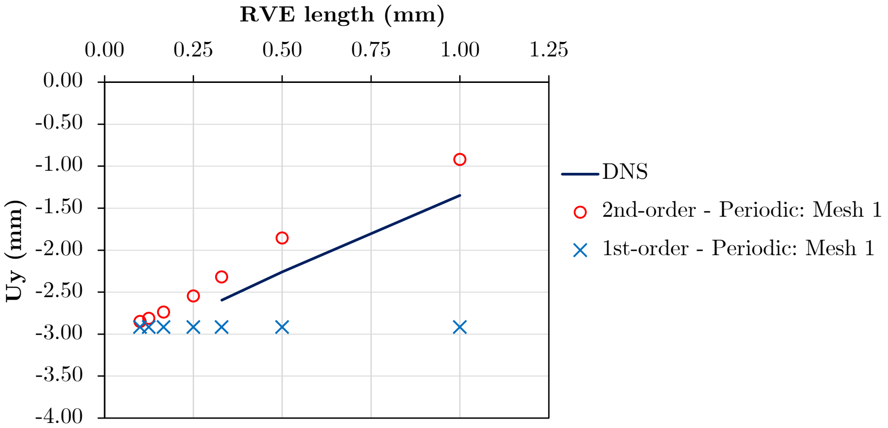

Source: The author.

Figure 79 – Vertical displacements (mm) for first-order multi-scale periodic boundary condition: Size 1, 2 and 3 (scale factor = 3).

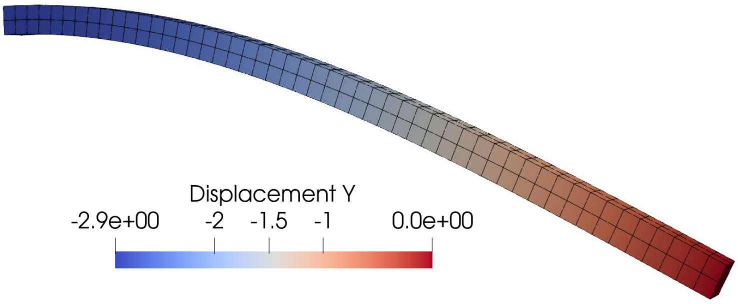

Source: The author.

Figure 80 – Vertical displacements (mm) for second-order multi-scale periodic constraint: Size 1, 2 and 3 (scale factor = 3).

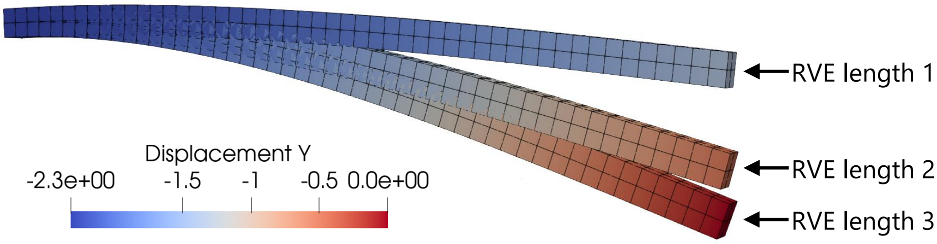

Source: The author.

6.6 Multi-scale numerical example 6: three-dimensional metamaterial with compression-induced-twisting

The purpose of this example is to simulate three-dimensional metamaterials with twisting behaviour when subjected to compression loading, i.e., compression-induced-twisting. For instance, this type of metamaterial has potential applications in sensors and actuators (Li; Yang; Lu, 2019). Concerning the elastic properties for the matrix, the metamaterial is modelled with $E = 210$ GPa and $\nu = 0.3$.

6.6.1 DNS Models

The geometry for the unit cells of the DNS models is shown in Figure 82. The numerical simulations are performed considering the 8-node hexahedron solid element (H8) with 8 integration points. The unit cell mesh is composed of 1216 elements (H8) and 2700 nodes. In order to assess the size effect, three DNS models were simulated (see Figure 82). The bottom side of the structure has the nodes fixed in the 3 directions, i.e., $u_{0x} = u_{0y} = u_{0z} = 0.0$. With respect to the top side of the structure, a compressive displacement of u_{0y} = -0.5 mm is prescribed in the vertical direction, considering 20 increments. Table 26 indicates the mesh data for each DNS model. Furthermore, more refined DNS models were not added due to the limitation of available memory requirements of the computer used for the numerical simulations.

Figure 81 – Unit cell and RVE.

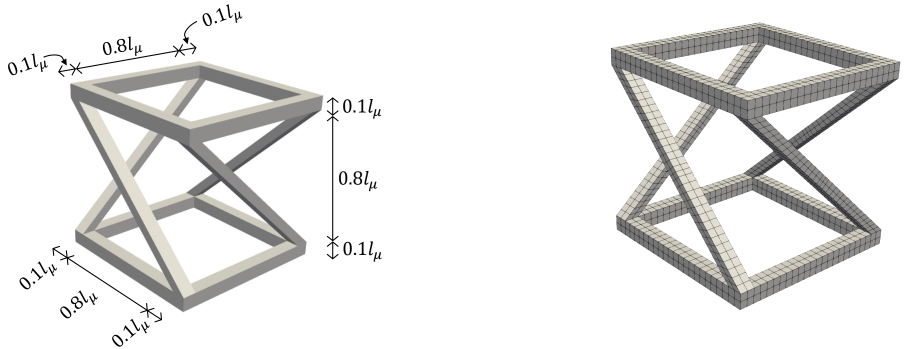

(a) Geometry.

(b) Mesh: 1216 elements (H8) and 2700 nodes.

Source: The author.

Figure 82 – Geometry (3D view) and boundary conditions for DNS models ($L_x = L_z = 1$ mm and $L_y = 3$ mm).

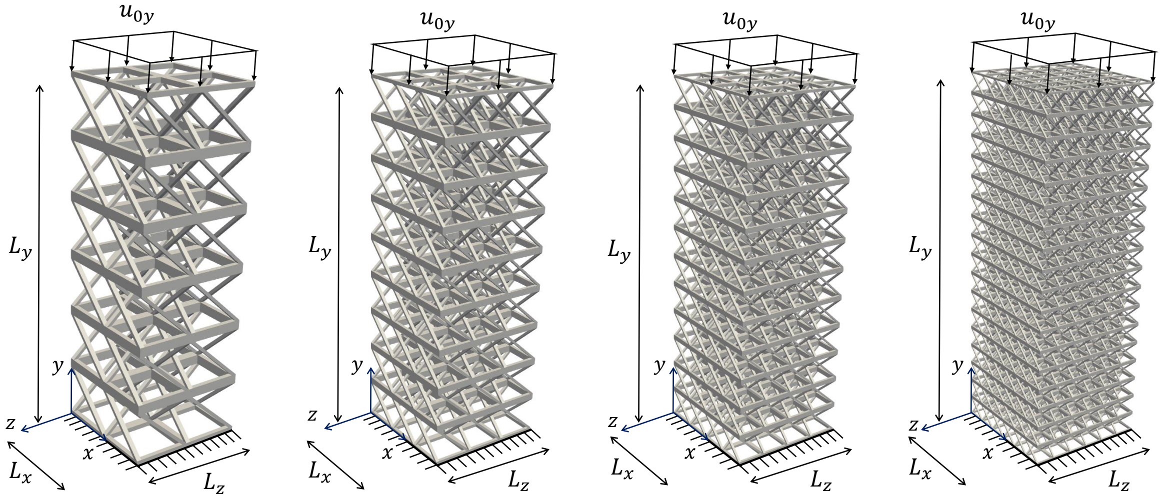

(a) DNS model 1 (2x6x2 unit cells): Size 1.

(b) DNS model 2 (4x12x4 unit cells): Size 2.

(c) DNS model 3 (4x12x4 unit cells): Size 3.

(d) DNS model 4 (6x18x6 unit cells): Size 4.

Source: The author.

Table 26 – Mesh of DNS models.

DNS	**Elements (H8)**	**Nodes**
Model 1 - Size 1 ($l_\mu = 0.50$ mm)	29184	56235
Model 2 - Size 2 ($l_\mu = 0.33$ mm)	98496	185104
Model 3 - Size 3 ($l_\mu = 0.25$ mm)	233472	433293
Model 4 - Size 4 ($l_\mu = 0.17$ mm)	787968	1444087

Source: The author.

Figure 83 presents the front view of the deformed DNS models after imposing the load program. Thus, the deformed structures show the conversion of axial compression into torsion, i.e., a behaviour with compression-induced-twisting. Furthermore, the size effect is also clear in the metamaterial, where the reduction of the rotation angle due to the decrease in the unit cell length is observed for DNS models. Figure 84 with the top view of the deformed DNS models also helps to visualize the reduction in rotation due to the decrease in the RVE length.

Figure 83 – Modulus of the displacement vector field for DNS models in a front view (scale factor = 4).

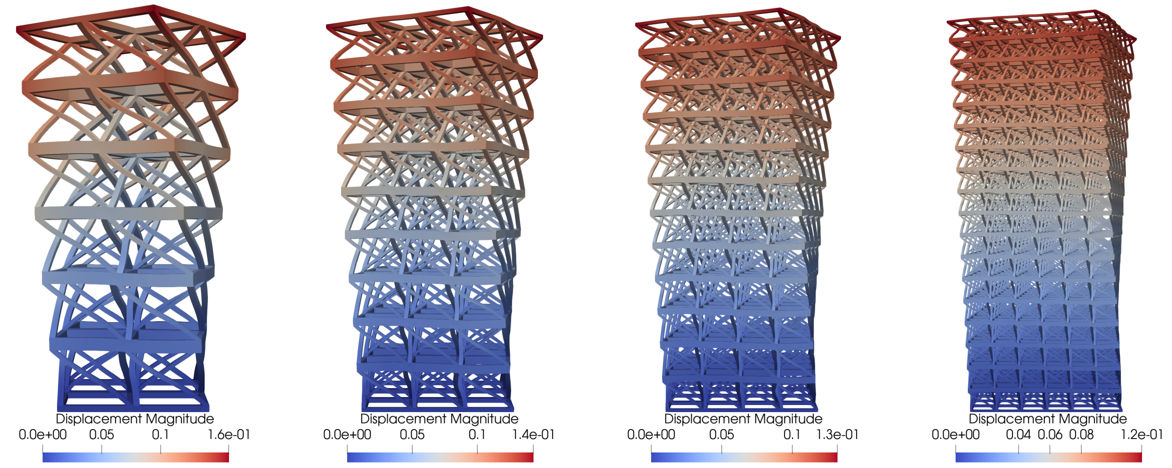

(a) DNS model 1. (b) DNS model 2. (c) DNS model 3. (d) DNS model 4.

Source: The author.

Figure 84 – Modulus of the displacement vector field for DNS models in a top view (scale factor = 4).

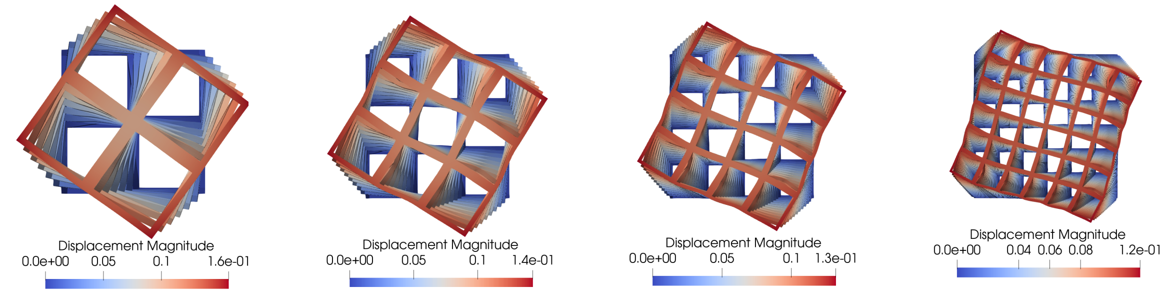

(a) DNS model 1. (b) DNS model 2. (c) DNS model 3. (d) DNS model 4.

Source: The author.

6.6.2 Multi-scale simulations

Regarding the multi-scale simulations based on second-order homogenisation, only the minimal constraint was considered to discuss the results. Note that the periodic constraint is not applicable due to the geometry of the RVE. Moreover, the direct constraint did not adequately capture the compression-induced-twisting because of the significantly stiffer homogenised behaviour. For comparison purposes, the classical uniform traction boundary condition derived from first-order homogenisation was also investigated.

The geometry and mesh of the RVE are shown in Figure 81. Concerning the macro-scale problem, the geometry and boundary conditions are depicted in Figure 85. For second-order multi-scale simulations, mixed hexahedral elements with 20 nodes (H20F8L1) are employed in the finite element discretisation at the macro-scale . On the other hand, the first-order multi-scale simulations at the macro-scale were conducted using H20 elements. Three macro-scale meshes shown in Figure 86 were adopted to evaluate mesh convergence. Figure 88 presents the results of the mesh refinement study for $l_\mu = 0.50$ mm accounting for the rotation angle (θ) of the deformed structure (see Figure 87). In summary, the results are close for all meshes investigated, indicating mesh convergence.

Figure 85 – Geometry (3D view) and boundary conditions ($L_x = L_z = 1$ mm and $L_y = 3$ mm).

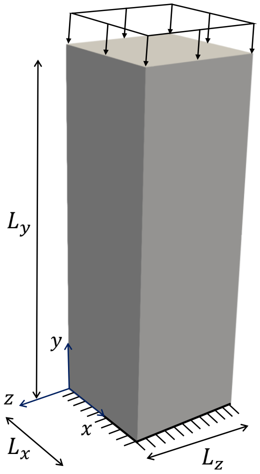

Source: The author.

Figure 86 – Macro-scale meshes.

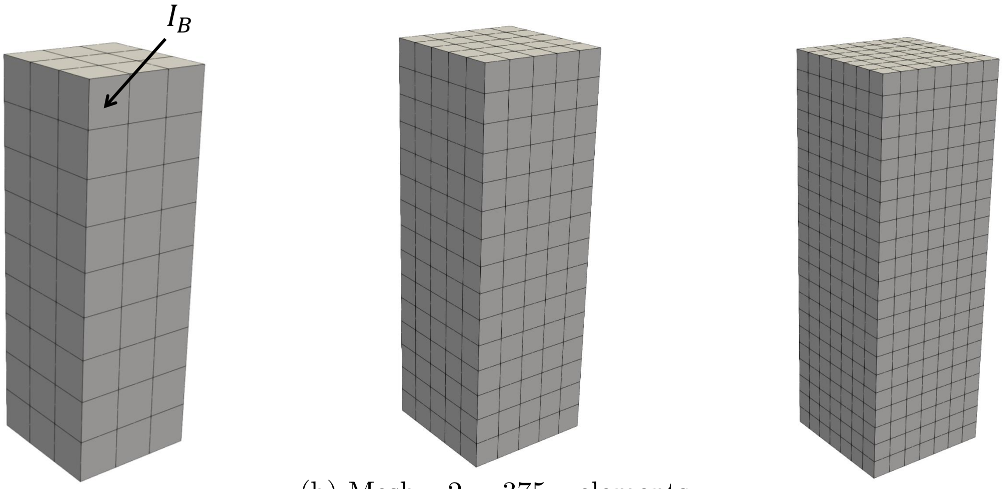

(a) Mesh 1: 81 elements (H20F8L1) and 544 nodes.

(b) Mesh 2: 375 elements (H20F8L1) and 2076 nodes.

(c) Mesh 3: 1029 elements (H20F8L1) and 5216 nodes.

Source: The author.

Figure 87 – Rotation angle (θ) for a top view of the structure.

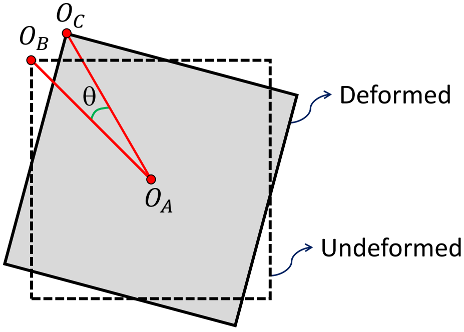

Source: The author.

Figure 88 – Mesh study for RVE size 1 ($l_\mu = 0.50$ mm) accounting for the rotation angle (θ): second-order minimal constraint (2nd-order - Minimal: Size 1) and first-order uniform traction boundary condition (1st-order - Traction: Size 1).

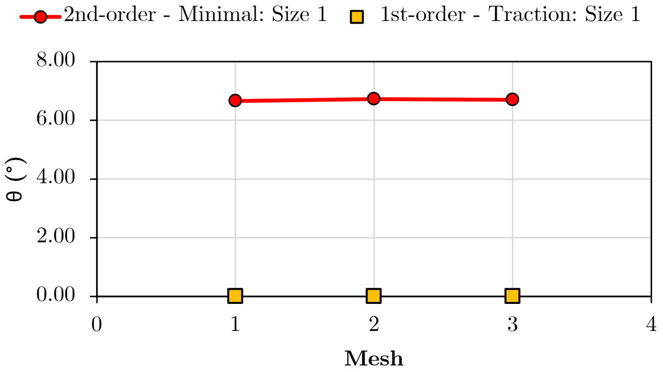

Source: The author.

Towards multi-scale analyses, seven RVE lengths were investigated: $l_\mu = 0.500$ mm (size 1), $l_\mu = 0.333$ mm (size 2), $l_\mu = 0.250$ mm (size 3), $l_\mu = 0.167$ mm (size 4) , $l_\mu = 0.125$ mm (size 5), $l_\mu = 0.100$ mm (size 6) and $l_\mu = 0.083$ mm (size 7). The results associated with the rotation angle (θ) of the deformed structure (see Figure 87) for all RVE lengths are presented in Figure 89. The deformed macro-scale structures are shown in Figure 90 (front view) and Figure 91 (top view) to compare results with DNS models. In addition, Figure 92 shows the distribution of the effective Cauchy stress (MPa) for the deformed RVE ($l_\mu = 0.50$mm) associated with the integration point I_B at macro-scale mesh 1 (see approximate region indicated in Figure 86a). The first-order multi-scale analyses performed with the uniform traction boundary condition did not capture the rotation of the structure. Despite quantitative differences compared to DNS models, the second-order multi-scale minimal constraint based on second-order homogenisation captures the compression-induced-torsion at macro-scale. It is worth highlighting the deformed RVE in Figure 92, where the effect of torsion is clear at the micro-scale. Following the discussion for DNS models, the reduction of the rotation angle for smaller RVE lengths was also captured in the coupled second-order multi-scale simulations with the minimal constraint. Thus, the computational approach via second-order homogenisation captures the size effect of the metamaterial with compression-torsion coupling. Furthermore, a non-linear behaviour is observed in the curves relating θ and the RVE length.

Figure 89 – RVE length x rotation angle: second-order minimal constraint with macro-scale mesh 1 (2nd-order - Minimal: Mesh 1) and first-order uniform traction boundary condition with macro-scale mesh 1 (1st-order - Traction: Mesh 1).

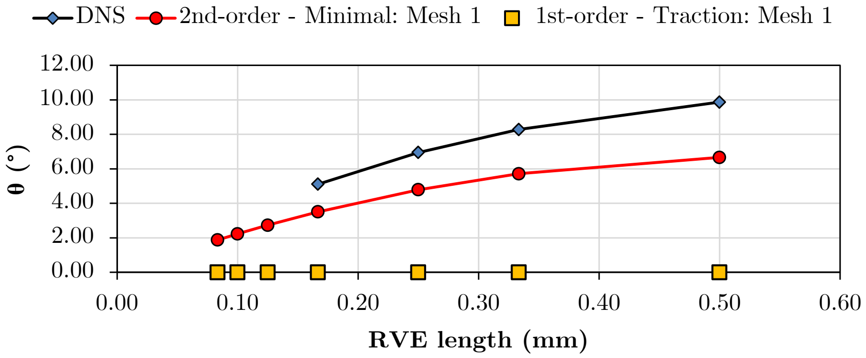

Source: The author.

Figure 90 – Modulus of the displacement vector field in mm for macro-scale structures (front view): Second-order - Minimal (scale factor = 4).

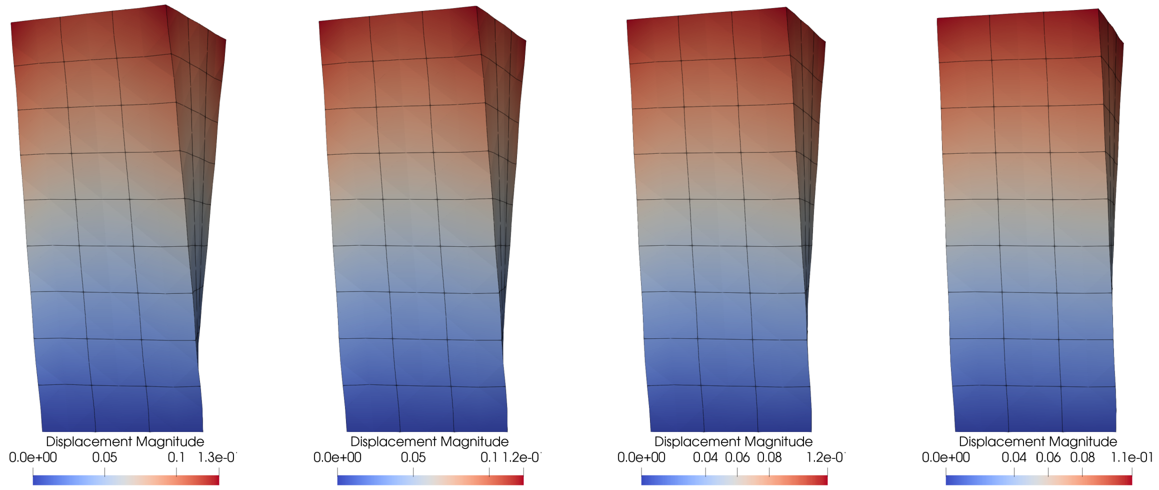

(a) Size 1: $l_\mu = 0.50$ mm. (b) Size 2: $l_\mu = 0.33$ mm. (c) Size 3: $l_\mu = 0.25$ mm. (d) Size 4: $l_\mu = 0.17$ mm.

Source: The author.

Figure 91 – Modulus of the displacement vector field in mm for macro-scale structures (top view): Second-order - Minimal (scale factor = 4).

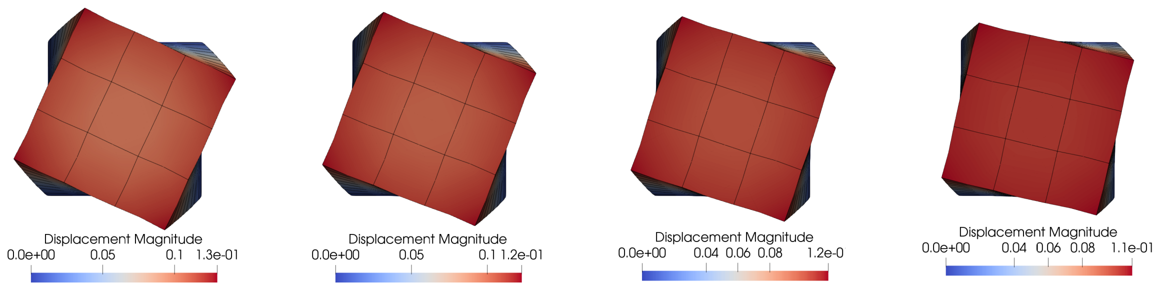

(a) Size 1: $l_\mu = 0.50$ mm. (b) Size 2: $l_\mu = 0.33$ mm. (c) Size 3: $l_\mu = 0.25$ mm. (d) Size 4: $l_\mu = 0.17$ mm.

Source: The author.

Figure 92 – Effective Cauchy stress (MPa) for the deformed RVE ($l_\mu = 0.50$ mm) associated with the integration point I_B at macro-scale mesh 1 (see approximate region indicated in Figure 86a) for the multi-scale analysis via second-order computational homogenisation under the minimal constraint assumption (scale factor = 4).

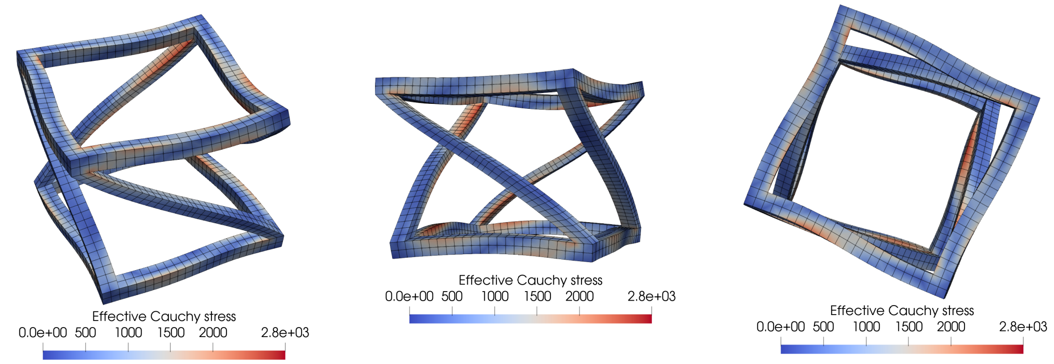

(a) Three-dimensional view.
(b) Front view.
(c) Top view.

Source: The author.

6.6.3 Analysis of the homogenised properties

The consistent tangents required to solve the coupled multi-scale problem are important for understanding the compression-induced-torsion observed for the metamaterial. In particular, the so-called coupling tangents are more relevant to explain the coupling deformation mechanism of torsion (second-order deformation mode) associated with compression (first-order deformation mode). Concerning the cross-relations established by these consistent tangents, $\mathbf{A_G}$ (A_{Gijklm}) associates $\boldsymbol{P}$ (P_{ij}) and $\mathbf{G}$ (G_{klm}):

$$A_{Gijklm} = \frac{\partial P_{ij}}{\partial G_{klm}}, \tag{6.5}$$

and $\mathbf{H}_{\boldsymbol{F}}$ (H_{Fijklm}) relates $\mathbf{Q}$ (Q_{ijk}) and $\boldsymbol{F}$ (F_{lm}):

$$H_{Fijklm} = \frac{\partial Q_{ijk}}{\partial F_{lm}}. \tag{6.6}$$

In this context, Figure 93 shows the norms of the initial consistent tangents $|\mathbf{A_G}|$ and $|\mathbf{H}_{\boldsymbol{F}}|$ of RVEs required for the FE^2 framework with the minimal constraint related to second-order homogenisation. The non-null values for the consistent tangents indicate their contribution to the solution of the multi-scale problem based on second-order homogenisation. It is worth mentioning that there is a linear relationship between the norm of consistent tangents and the RVE length. On the other hand, these particular tangents are not considered in the solution for the uniform traction boundary condition related to the multi-scale strategy based on first-order homogenisation, where the compression-torsion coupling was not captured. Therefore, $|\mathbf{A_G}|$ and $|\mathbf{H}_{\boldsymbol{F}}|$ were important for the second-order multi-scale approach to capture the effect of compression-induced-torsion. For an in-depth discussion of the effect of compression-induced-twisting, Figure 94 presents the A_{G22312}

component with coupling between normal stresses P_{22} and the torsion deformation mode G_{312}. Hence, the A_{G22312} component indicates the coupling between normal and torsional effects for the metamaterial.

Figure 93 – Norm of consistent tangents required for the second-order multi-scale modelling with the minimal constraint.

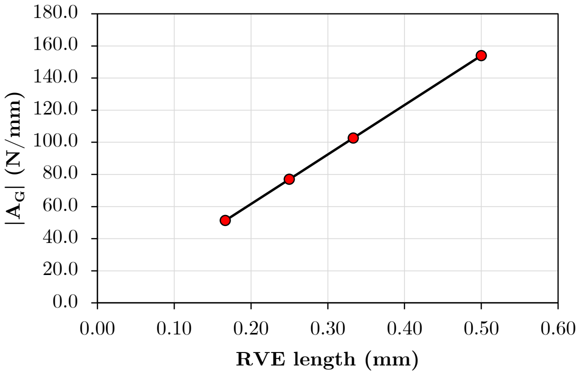

(a) Results for $|\mathbf{A_G}|$. (b) Results for $|\mathbf{H}_{\boldsymbol{F}}|$.

Source: The author.

Figure 94 – Results for A_{G22312} component with coupling between normal stresses P_{22} and the torsion deformation mode G_{312}.

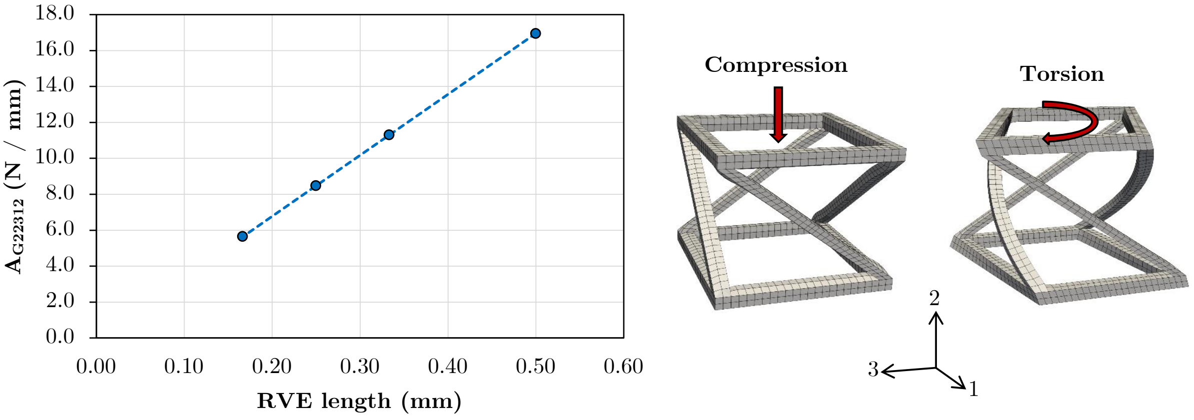

Source: The author.

6.7 Multi-scale numerical example 7: 3D-printed lattice beams under bending

This numerical example examines the size effects on 3D-printed lattice beams under bending, where experimental data obtained by Molavitabrizi *et al.* (2023) are compared with the coupled multi-scale simulations.

6.7.1 Experimental results

Recently, Molavitabrizi *et al.* (2023) presented experimental results of lattice structures fabricated by additive manufacturing, highlighting the size effect after three-point bending tests. Specifically, the lattice structures were 3D-printed with the base material polyamide PA-12 (semi-crystalline polymer) using the HP MFJ 580 machine and multi jet fusion technology. Figure 95 shows the 3D-printed structures with size 1 (1 layer and l_{cell} =20 mm), size 2 (2 layers and l_{cell} =10 mm), size 3 (4 layers and l_{cell} =5 mm), and size 4 (8 layers and l_{cell} =2.5 mm)

Figure 95 – Additively manufactured lattice beam structures (Size1, 2, 3 and 4) made of PA-12.

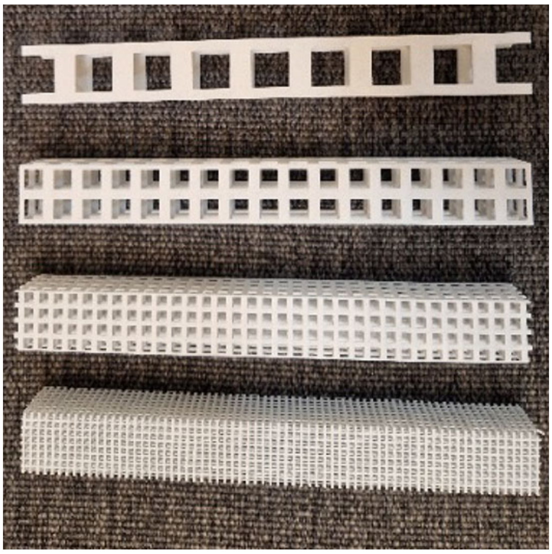

Source: Molavitabrizi *et al.* (2023).

The architected structures are formed from the arrangement of unit cells whith the morphology indicated in Figure 96. For example, Figure 97 shows the lattice structure with unit cell size 1 positioned for the three-point bending tests, including the global dimensions of the lattice structures (L_x = 170 mm and L_y = L_z = 20 mm) as well as the distance between the lower supports (L_s = 140 mm). Note that the global dimensions of the beam and the distance between the supports in the bending test are also shown in Figure 97.

Figure 96 – Unit cell.

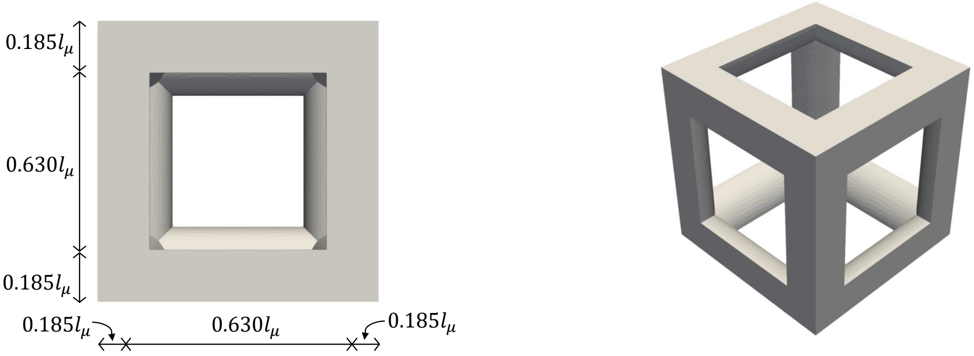

(a) Geometry: front view.

(b) Geometry: 3D view.

Source: The author.

Figure 97 – DNS model 1 (Size 1) with L_x = 170 mm, $L_y = L_Z$ = 20 mm and L_S = 140 mm composed of seven complete unit cells.

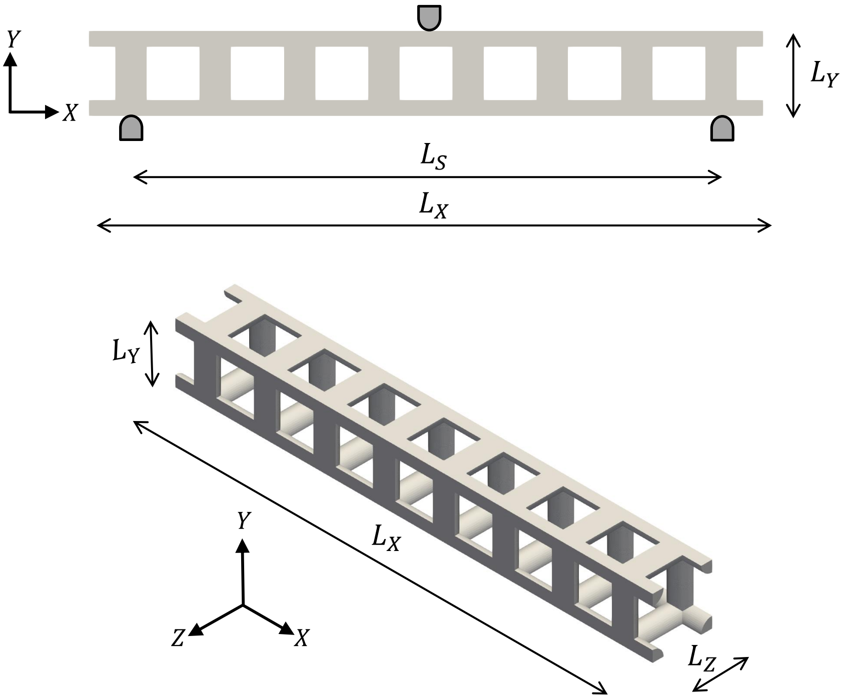

Source: The author.

Figure 98 presents the results of the reactive forces vs. prescribed displacement for the lattice structures in the 3-point bending tests, where # indicates the repetition number for each case size (1, 2, 3 and 4). It is important to note that each lattice structures was tested in two repetitions. Table 27 presents the average results for each lattice structure with different unit cell sizes. In particular, the responses are compared for u_0 =1 mm and u_0 =2.5 mm.

Figure 98 – Prescribed displacement vs reaction force in the middle of lattice beam structures under 3-point bending.

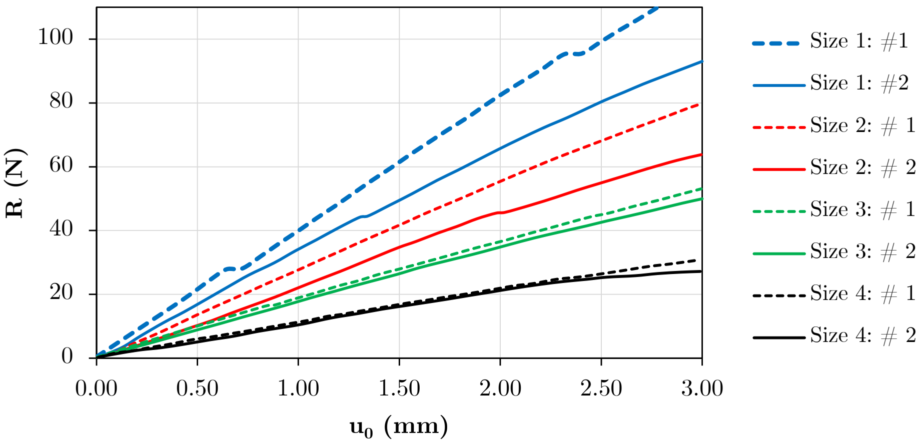

Source: Molavitabrizi *et al.* (2023).

Table 27 – Average results for reaction force (R) from the experimental investigation on scale effects carried out by Molavitabrizi *et al.* (2023).

Unit cell size	**Average results for R (N)**	
	$u_0 = 1.00$ mm	$u_0 = 2.50$ mm
Size 1 ($l_\mu = 20$ mm)	36.90	89.69
Size 2 ($l_\mu = 10$ mm)	24.71	61.45
Size 3 ($l_\mu = 5.0$ mm)	18.16	43.82
Size 4 ($l_\mu = 2.5$ mm)	10.72	25.85

Source: The author.

6.7.2 Multi-scale simulations

In the multi-scale bending beam problem, the macro-scale is defined as illustrated in Figure 99. The two mesh configurations shown in Figure 100 were investigated to assess the macro-scale discretisation in the numerical results. In the first-order multi-scale simulations (with periodic and uniform traction boundary conditions), H20 elements were employed in the discretisation of the structure. In the second-order multi-scale analyses (with periodic and minimal constraints), H20F8L1 elements were defined for the structure. Upper-bound multi-scale models were not considered to reduce the cost of numerical simulations. The quasi-static elastic numerical simulations were conducted with $u_0 = 3$ mm applied at the centre of the beams in 12 equally spaced increments.

Figure 99 – Macro-scale with $L_x = 170$ mm, $L_y = L_Z = 20$ mm and $L_S = 140$ mm.

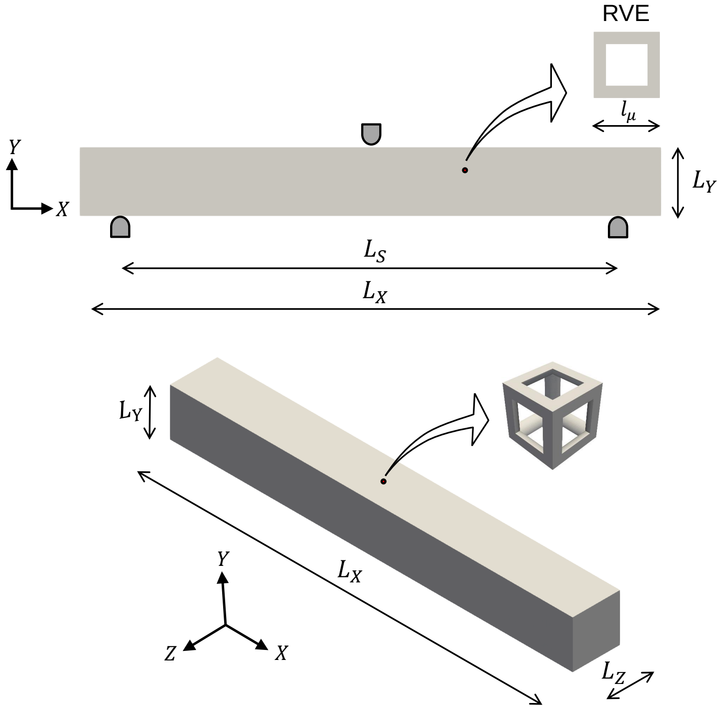

Source: The author.

The RVE morphology follows the unit cell geometry (see Figure 96) used in the composition of the 3D-printed lattice arrangement. As shown in Figure 101, the

RVE mesh is composed of 10-node tetrahedral elements (T10) with 4 integration points. The constitutive elastic parameters were defined according to the experimental material characterisation data reported by Molavitabrizi *et al.* (2023), where the following elastic properties were obtained: $E = 1.58$ GPa and $\nu = 0.4$.

Figure 100 – Macro-scale meshes.

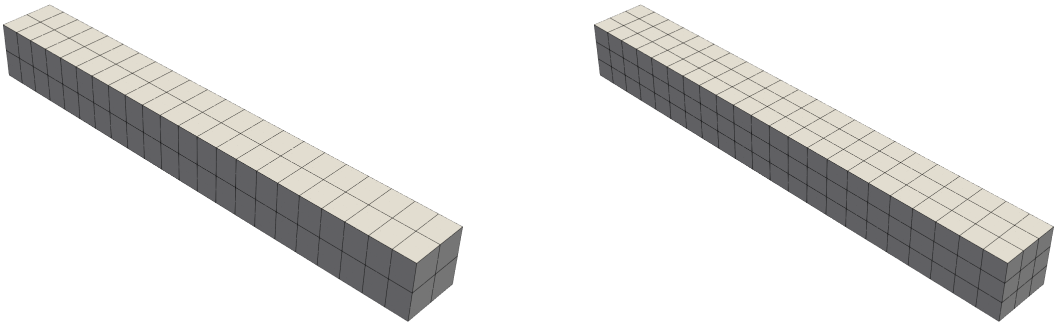

(a) Mesh 1: 88 elements (H20 and H20F8L1) and 681 nodes.
(b) Mesh 2: 198 elements (H20 and H20F8L1) and 1272 nodes.

Source: The author.

Figure 101 – RVE: mesh composed of 6920 elements (T10) and 11940 nodes.

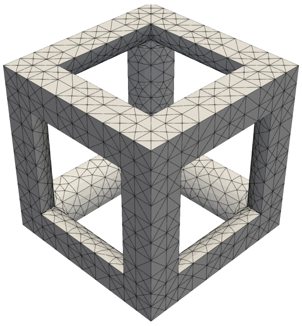

Source: The author.

Tables 28 and 29 show the mesh comparison study at the macro-scale for the multi-scale models of uniform traction boundary condition (first-order) and minimal constraint (second-order). Note that the relative differences (in modulus) are also indicated in the comparison. In summary, the numerical results are similar for the meshes. Thus, mesh 1 was chosen to perform the remaining coupled multi-scale simulations.

Table 28 – Mesh refinement study assessing R for lattice beams with $u_0 = 1.0$ mm.

	R (N)		
Multi-scale model	**Mesh 1**	**Mesh 2**	**Differences**
Second-order: Minimal - Size 2	18.01	17.73	1.54%
First-order: Uniform traction - All sizes	8.41	8.37	0.55%

Source: The author.

Table 29 – Mesh refinement study assessing R for lattice beams with $u_0 = 2.5$ mm.

	R (N)		
Multi-scale model	**Mesh 1**	**Mesh 2**	**Differences**
Second-order: Minimal - Size 2	44.63	43.94	1.54%
First-order: Uniform traction - All sizes	20.86	20.74	0.57%

Source: The author.

Regarding the size effects study for lattice beams under bending, Figure 102 shows the comparison of the numerical results from multi-scale simulations with the experimental data. In particular, the minimal constraint multi-scale model (second-order) provided results in better agreement with the laboratory experiments. The periodic models (first-order and second-order) were excessively stiff, particularly for smaller RVE sizes. On the other hand, the uniform tension multi-scale model (first-order) was excessively flexible, particularly for larger RVE lengths. Finally, it is worth mentioning that the second-order models capture the size effect and converge to the respective first-order models in cases with smaller RVE sizes.

Figure 102 – Reaction force versus RVE length in the centre of the lattice beam structures under 3-point bending.

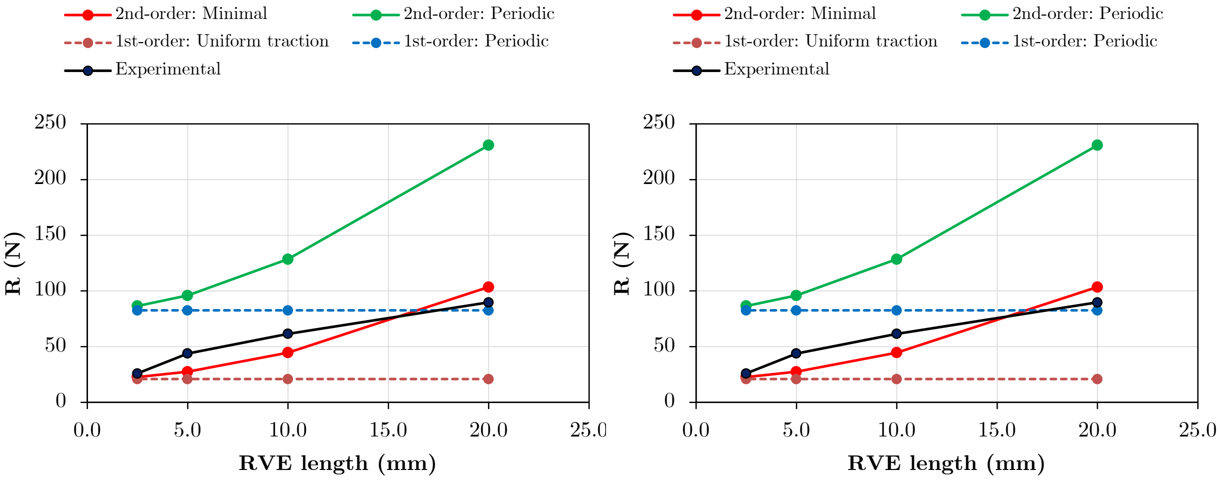

(a) Results up to $u_0 = 1$ mm. (b) Results up to $u_0 = 2.5$ mm.

Source: The author.

6.8 Partial conclusions

The consistency of the FE^2 multi-scale strategy was demonstrated by the quadratic convergence rates observed in the Newton-Raphson scheme at micro- and macro-scales. Two and three-dimensional numerical simulations highlighted some significant advantages of second-order strategies when compared to first-order theories for investigating the mechanical behaviour of architected structures with thin-walled elements under bending exhibiting size effects. In general, the multi-scale second-order strategy presented responses in close agreement with the results from DNS models, mainly for the periodic constraint. Conversely, the first-order approach presented significant differences when compared to DNS models. The size effects due to the RVE length were captured in the numerical results from the multi-scale approach based on second-order homogenisation. Thus, the second-order approach has proven to be important in the numerical modelling of architected structures under bending with size effects.

Mechanical metamaterials with coupled deformation modes were also investigated in this work. In this context, architected metamaterials with tension-induced bending and compression-induced torsion were explored through two- and three-dimensional numerical simulations, respectively. A computational cost study showed that the multi-scale second-order computational homogenisation framework could have significant advantages in terms of memory requirements and even processing time, compared to DNS models. It has been shown that multi-scale models based on second-order homogenisation can capture these complicated couplig deformation mechanisms, involving both first- and second-order deformation modes. DNS finite elements models composed of different unit cell sizes revealed a size effect in these metamaterials. First-order homogenisation was not able to capture such deformation mode couplings and size effects. At the same time, multi-scale models based on second-order homogenisation can predict tension-induced bending and compression-induced torsion, as well as the associated size effect.

Still in the context of coupling deformation modes, a novel exotic metamaterial with tension/compression-induced undulation has been analysed through two-dimensional elastic numerical simulations. When subjected to tension or compression, its mechanical response was not influenced by size effect associated with the length of the unit cell, as revealed in the numerical simulations with DNS models. Consequently, the multi-scale approaches based on first- and second-order computational homogenisation presented similar results for the mechanical behaviour of the metamaterial, capturing the tension/compression-induced undulation. Regarding the accuracy of the multi-scale models, periodic boundary conditions provided results in close agreement with the DNS models, resulting in better predictions compared to other classes of constraints. Moreover, the new exotic behaviour, which can be employed in shape-shifting applications associated with soft robotics and/or programmable materials, resulted from a non-conventional coupling between tension/compression and shear that was quantified in the material tangent modulus. This coupling was not associated with second-order deformation modes and, consequently, was accurately predicted by first-order homogenisation.

7 ADDITIVE MANUFACTURING OF ARCHITECTED SOLIDS

7.1 Additive manufacturing technology

Additive manufacturing (AM), originally referred to as rapid prototyping and popularly known as 3D printing, is a relatively newer process for fabricating objects directly from 3D digital models, usually by adding material layer by layer (Gibson; Rosen; Stucker, 2014; Kanishka; Acherjee, 2023). One of the key advantages of AM technology is its ability to produce optimised and/or personalised objects, revolutionising various industries by enabling the creation of complex designs and shapes (Iftekar *et al.*, 2023). It is worth noting that economically efficient structures with optimal shapes have been designed by combining topology optimisation strategies with additive manufacturing (Plocher; Panesar, 2019; Nazir *et al.*, 2019; Pan; Han; Lu, 2020; Kladovasilakis; Tsongas; Tzetzis, 2023). In this context, 3D printing has been employed to fabricate desired products for applications in aerospace, automotive, mechanical, civil, and biomedical fields (Wu *et al.*, 2023a). Kanishka and Acherjee (2023) present Figure 103 with the distribution of research documents on AM across subject areas derived from the Scopus database spanning from 1972 to 2022. Note that engineering and materials science are the dominant fields, demonstrating their relevance in terms of research and application. For a more detailed study of additive manufacturing, including an overview, advancements, limitations and challenges, readers are encouraged to consult Gibson, Rosen and Stucker (2014), Iftekar *et al.* (2023), Kanishka and Acherjee (2023) and Zhou *et al.* (2024).

Figure 103 – Distribution of research documents on AM across subject areas.

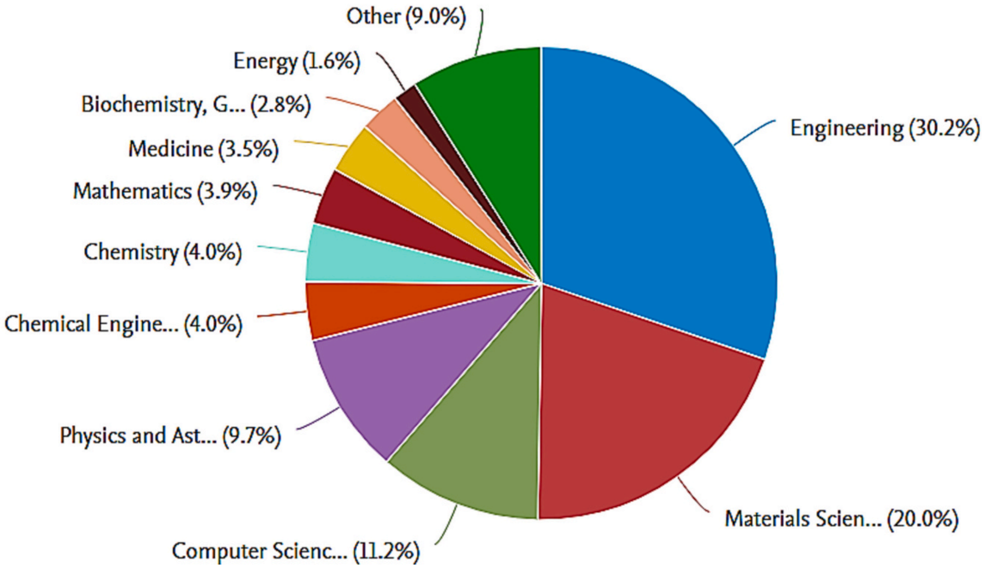

Source: Kanishka and Acherjee (2023).

In particular, a brief overview of additive manufacturing is provided in the following subsections, with a focus on the FDM 3D printing process for fabricating polymer architected materials. Furthermore, key information regarding architected materials are available in Askari *et al.* (2020), Benedetti *et al.* (2021), Uribe-Lam Cecilia D. Treviño-Quintanilla and Olvera-Silva (2021), Kladovasilakis *et al.* (2022), and Wu *et al.* (2023a).

7.2 Fundamental principles and main steps of the AM process

Kanishka and Acherjee (2023) define the following fundamental principles and key features of the AM: (i) Layer-by-layer fabrication: objects are built by adding successive layers of material, enabling the fabrication of intricate and challenging shapes; (ii) Digital design: digital models are prepared using Computer-Aided Design (CAD) software and later converted into machine-readable code with instructions/directives to conduct the 3D printing process; (iii) Material versatility: different materials can be used as feedstock (plastics, metals, ceramics, and composites); (iv) Reduced waste: AM reduces waste by depositing material only in the areas where it is needed, resulting in cost savings and a reduced environmental impact; (v) Customisation and personalisation: customised and personalised objects can be built for specific applications; (vi) Rapid prototyping: AM speeds up the design and development process, allowing for the fast production of prototypes for testing; (vii) Post-processing requirements: depending on the printing technique and the intended use, post-processing steps may be required (e.g., sanding, polishing, machining or even heat treatment); and (viii) Equipment and process optimisation: AM requires knowledge of the technology and specialised equipment to function effectively.

In summary, the generic 3D printing encompasses digital, manufacturing and post-processing stages. Kanishka and Acherjee (2023) divide the AM process into eight key steps, as shown in Figure 104. Important considerations are also reported in the comprehensive review presented by Zhou *et al.* (2024). In this context, the bridge between digital design and physical realisation is associated with (see Figure 104):

1. CAD-Model: The first step involves modelling the geometry of the component using three-dimensional CAD models. It is worth noting that CAD software currently available allows the design of intricate and sophisticated geometries. Thus, the final output of this stage is the digital model of the desired object (3D solid or surface representation). This digital model can also be created using reverse engineering tools, such as laser and optical scanning technologies (Gibson; Rosen; Stucker, 2014).

2. STL file: The next step is to convert the CAD model into the Standard Triangle Language (STL format), also referred to as Standard Tessellation Language. This process consists of converting a 3D design into a format that 3D printers can interpret

(Zhou *et al.*, 2024). This file format is embedded in almost all CAD systems and is accepted by almost all available slicers associated with 3D printers.

3. Data preparation: In this step, the STL file is transferred to the software that will define the directives of the AM machine. The file is conveniently manipulated to position the components optimally, including determining the best position and orientation for 3D printing. If necessary, support structures must be added to ensure proper construction of the components. The printing technology and feedstock must be taken into account when defining these aspects.

4. Machine setup: This step consists of defining the AM machine settings, usually performed by means of slicing softwares. The output of the slicing process is the generation of G-code, a universally recognised programming language for Computer Numerical Control (CNC) machinery (Zhou *et al.*, 2024). G-code contains detailed and precise instructions for 3D printers. In this context, print parameters such as layer thickness, infill pattern, infill density, raster angle, temperatures (nozzle and print bed), and printing speed must be properly configured before 3D printing. Thus, an optimised G-code file containing all print parameters is ready to be sent to the 3D printer.

5. Built: This stage involves the manufacturing process using the selected feedstock. In particular, leveling the print bed is important to guarantee the adhesion of the first layer. The building process is mostly automated, requiring minimal supervision. Monitoring remains necessary to check for issues such as running out of feedstock, power outages, or improper material accumulation caused by incorrect configurations, for instance.

6. Remove: Once the 3D printing process is complete, the components must be removed from the 3D printer, ensuring the necessary cooling time before moving the objects. The removal process must be done carefully to avoid damaging the 3D-printed objects.

7. Post-processing: Then, the components can be cleaned, and any supporting structures carefully removed. The post-processing steps depend on the printing technology employed and the end-use of the object (Zhou *et al.*, 2024). This step often requires time and careful, as well as experienced manual manipulation. If necessary, objects may require additional treatment to make them suitable for their intended use, including techniques for improving surface finish (e.g., texture refinement and polishing), as well as possible painting.

8. Application: Finally, the components can be used in the desired applications.

Figure 104 – Main steps of the AM process.

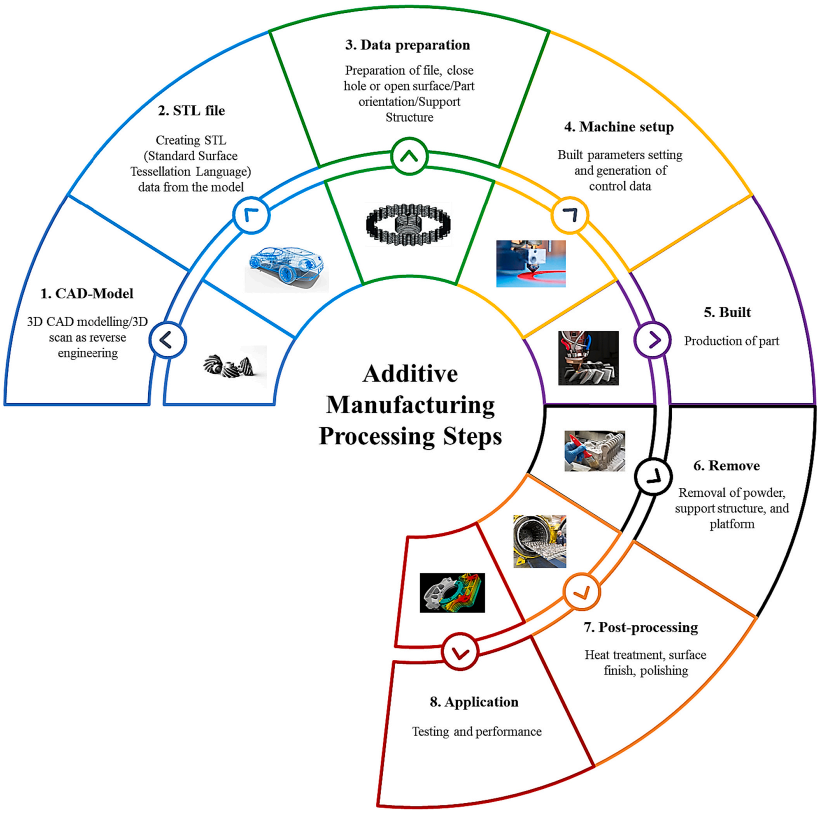

Source: Kanishka and Acherjee (2023).

7.3 Materials and AM processes

The selection of additive manufacturing technology depends on the feedstock, the intended application, and the available resources (knowledge and equipment). For example, factors such as mechanical stiffness/strength, ductility, manufacturing cost, and/or print quality/resolution can influence the choice of 3D printing technique. Regarding feedstock, polymers (thermoplastics and thermosets), metals, ceramics, and composites (polymer composites, metal composites, and ceramic matrix composites) are commonly used in AM (see more details in Bourell *et al.* (2017)).

A detailed analysis of the various AM processes is provided in Kanishka and Acherjee (2023). For instance, some 3D printing technologies and their features include:

- Material extrusion: A solid thermoplastic material is melted and extruded through a heated nozzle to build a physical object, layer by layer. FDM (Fused Deposition Modeling), often referred to as FFF (Fused Filament Fabrication), is an extrusion-based 3D printing technology. Some advantages include low cost, speed efficiency, and ease of printing. On the other hand, challenges are observed when manufacturing certain geometries, including the need for excessive material supports.

- Vat photopolymerisation: A liquid photopolymer resin contained within a reservoir is cured and solidified layer by layer using light, often the ultraviolet (UV). Common 3D printing techniques in this context are SLA (Stereo Lithography) and DLP (Digital Light Processing). The main advantage lies in the ability to create objects with an excellent level of geometric fine detail (high resolution). However, some disadvantages include limited build volume and warping, as well as toxicity and environmental concerns (Zhou *et al.*, 2024).

- Material jetting: Droplets of a photosensitive material (e.g., photopolymer and waxy polymers) are jetted and solidified under UV light to build a component, layer by layer. In this case, Zhou *et al.* (2024) indicate the following: (i) advantages - exceptional resolution and detail, multi-material and full-color capabilities, and a wide array of materials; and (ii) disadvantages - high costs, restricted build volume, and low printing speed.

- Binder jetting: The process consists of spreading a thin layer of powder over the build platform. Next, the printhead selectively deposits binder droplets into the powder bed. This process occurs layer by layer until the object construction is completed. Therefore, this 3D printing process uses a binder material to bond powder particles layer by layer. The feedstock versatility is an advantage, including the possibility of using plastics, ceramics, metals, and composites. Zhou *et al.* (2024) mention as disadvantages the low-density parts, labor-intensive and complex post-processing.

- Powder bed fusion: This 3D printing process employs a heat source, such as a laser or electron beam, to selectively melt fuse layers of powdered material, constructing a component layer by layer. For example, SLS (Selective Laser Sintering) is commonly employed for plastics, composites, and ceramics. SLM (Selective Laser Melting) and DMLS (Direct Metal Laser Sintering) are applied in the context of metals and alloys. Zhou *et al.* (2024) outline the following advantages and disadvantages of each 3D printing technique: (i) SLS offers advantages such as support-free, isotropic final products, and complex geometries, whereas its limitations include porosity, shrinkage, impurities, poor surface quality, and post-processing to achieve the final appearance; (ii) SLM provides positive characteristics such as binder-free, often faster than SLS, and high powder recyclability, whereas its limitations include high costs, less material flexibility and support structures; and (iii) DMLS offers benefits such as applicability to various metal alloy materials, and high powder recyclability, whereas its disadvantages include high costs, high porosity, and limited build volume.

- Direct energy deposition: The feedstock, often metal wire or powder, is melted by a concentrated energy source such as a laser, electron beam, or electric arc. The melted material is then deposited directly onto the building platform or a previously printed layer. Although material limitations and specific use cases are some disadvantages, this technology offers advantages such as minimizing waste, enabling part repair and modification, and providing efficiency for larger components (Zhou *et al.*, 2024).

7.4 FDM process for polymer architected materials

Although mechanical metamaterials exhibit superior performance due to the improved effective material properties derived from their internal micro-architecture, designing engineered microstructures to achieve advanced physical and mechanical properties remains both critical and challenging (Jiao; Alavi, 2021). The advancement of 3D printing technology enables more feasible tailored structures with multi-functional properties provided by the precise control of the micro-architecture (Benedetti *et al.*, 2021; Yang *et al.*, 2024; Bhat *et al.*, 2024). Wu *et al.* (2023a) highlight that 3D printing techniques provide greater flexibility to design innovative lightweight materials and structures in an efficient way, allowing the manufacturing of more environmentally friendly and sustainable products (less material and lower energy consumption).

A wide variety of materials, encompassing metals, polymers, ceramics, and polymer-composite materials, have been employed to fabricate architected structures through additive manufacturing (Benedetti *et al.*, 2021). In particular, thermoplastic polymers are widely used in the 3D printing of architected materials due to their favorable characteristics, including a range of properties, lightweight, ease of use. Furthermore, amorphous thermoplastics are commonly employed in material extrusion, while semicrystalline polymers are frequently used in powder bed fusion (Bourell *et al.*, 2017).

In this context, FDM 3D printing technology using polymers provides benefits such as availability, affordable acquisition cost, low maintenance, and easy-to-use equipment. In this case, various polymeric materials such as polyethylene terephthalate glycol (PETG), polylactic acid (PLA), acrylonitrile butadiene styrene (ABS), and thermoplastic polyurethane (TPU) can be used as feedstock, for instance. However, this material extrusion-based technique can present challenges in printing certain geometries, such as: (i) architected structures that require support material with complex removal, and (ii) thin-walled elements due to limitations in nozzle diameter.

Furthermore, as shown in Figure 105, the extruder mechanisms for FDM printing are classified as follows: (a) direct drive, where the extruder motor is mounted directly on the printhead (hotend o heater), pushing the filament directly into the hotend; and (b) Bowden, where the extruder motor is mounted on the frame of the 3D printer, feeding the filament through a long tube (Bowden tube) to the hotend. Direct drive extruders provide better filament control at the printhead, a lower risk of clogging, and ease of filament changes. Bowden extruders offer a lower weight on the printhead, greater stability, and faster print speeds compared to direct drive mechanisms.

Figure 105 – Schematic illustration showing the differences between: (a) a direct-drive extruder and (b) a Bowden extruder.

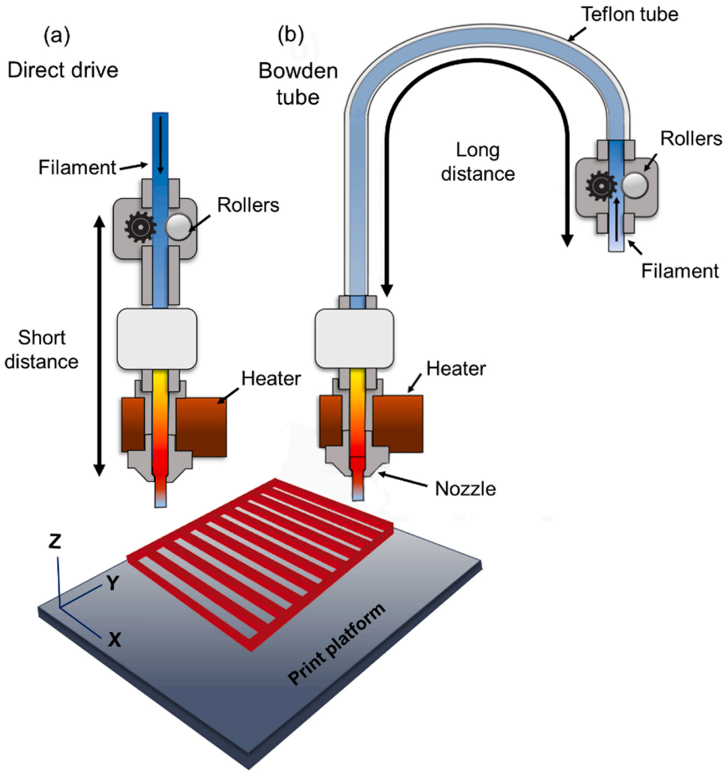

Source: Moetazedian *et al.* (2021).

8 A NOVEL 3D-PRINTED POLYMER MECHANICAL METAMATERIAL DISPLAYING TENSION-INDUCED UNDULATION

The methodology and results associated with this Chapter are reported in Santos *et al.* (2025a). In this context, the present contribution integrates additive manufacturing technology and finite element numerical simulations to investigate a novel metamaterial exhibiting tension-induced undulation mechanical behaviour, as reported in Subsection 6.2 through two-dimensional elastic numerical simulations. Using the material extrusion additive manufacturing technique known as FDM, test specimens and architected structures are 3D-printed from a commercially available PETG. Aspects of the 3D printing manufacturing process and material characterisation are addressed in detail. A comprehensive analysis of the experimental mechanical behaviour of the novel 3D-printed metamaterial is herein presented based on uniaxial tensile experiments conducted in the laboratory. The experimental investigation focuses on capturing tension-induced undulation, failure mechanisms, the influence of prescribed displacement rates, and plastic behaviour via cyclic testing. To compare with the experimental results, we perform quasi-static three-dimensional elasto-plastic finite element analysis employing two computational modelling options: (i) full-scale models referred to as DNS models, where the structure is composed of an array of unit cells, and (ii) FE^2 multi-scale analyses based on first-order computational homogenisation with periodic model. The comparison between experimental data and numerical results allows the assessment of the advantages and challenges of integrating 3D printing and modelling options to enhance the design and fabrication processes of architected metamaterials.

Remark 7. *Since the novel metamaterial did not exhibit pronounced size effects and demonstrated coupled first-order deformation modes (i.e., tension-shear), the two-dimensional elastic simulations reported in Subsection 6.2 indicated that the first-order and second-order multi-scale approaches yield similar mechanical behaviour of the architected structure with tension-induced undulation. In this context, only first-order multi-scale analyses were explored for this numerical/experimental study involving the novel 3D-printed polymer mechanical metamaterial, reducing the computational cost of numerical simulations.*

8.1 Experimental investigation of the architected polymeric metamaterial

This section outlines the preparation for the experimental investigation of the mechanical behaviour of the 3D-printed polymer metamaterial exhibiting tension-induced undulation, resulting from a coupling deformation mechanism reported in Subsection 6.2 via two-dimensional elastic numerical simulations. The experimental study involves the design and manufacturing of the architected structure, material characterisation, and procedures for uniaxial tensile tests of the metamaterial.

8.1.1 FDM-based additive manufacturing process for the fabrication of architected structures

Regarding material selection, the PETG filament with a diameter of 1.75 mm and uniform opaque color was chosen for 3D printing of the architected structures. Some properties of the PETG provided by the manufacturer (3D LAB, 2025) are presented in Table 30. PETG is an amorphous polymer commonly used in additive manufacturing. This thermoplastic material offers several beneficial properties, including: (i) ease of fabrication, (ii) suitability for 3D printing and the ability to be molded into complex shapes, (iii) good cost-performance efficiency, (iv) a balanced combination of strength, flexibility, and toughness, and (v) chemical resistance, among others. Given its beneficial properties, PETG is well-suited for structural applications, including mechanical parts, printer parts, and protective components (Iftekar *et al.*, 2023).

Table 30 – Typical material properties of the filament (feedstock) provided by the manufacturer.

Material properties for filament (feedstock)	**Value**	**Method**
Density	1.27 g/cm^3	ASTM D792
Fusion temperature	240°C - 260°C	ASTM D3418
Glass transition temperature or Tg	70°C	ASTM D1525
Modulus of elasticity	2100 MPa	ASTM D790
Tensile stress at yield	50 MPa	ASTM D638
Flexural strength	70 MPa	ASTM D790
IZOD impact strength	101 J/m	ASTM D256

Source: 3D LAB (2025).

The additive manufacturing technology based on the FDM technique was defined for 3D printing the polymeric architected structures due to its versatility, cost-effectiveness, and ease of use, which enable the fabrication of intricate designs and geometries. The FDM 3D printing technique is a widely used additive manufacturing process for polymers, in which a thermoplastic filament is melted and extruded through a nozzle, layer by layer, to build a 3D object. We employed the Sethi3D AiP A3 printer (SETHI3D, 2025) equipped with a direct drive extruder and a 0.4 mm diameter brass nozzle (see Figure 106). It is worth mentioning that this printer has a low purchase cost, which facilitates access to the 3D printing process. The 3D slicer named Simplify3D was used to convert the 3D model into instructions interpretable by the 3D printer. Initially, printing parameters were calibrated to ensure the construction of high-quality architected structures. In this context, the main print settings have been set as follows: (i) nozzle temperature of 250°, (ii) heatbed temperature of 75°, (iii) print speed of 50 mm/s, (iv) layer height of 0.2 mm, (v) extrusion factor of 0.96, (vi) infill 100% rectilinear 0/90 (xy plane), and (vii) three perimeters defined on the outer contour of the structure.

Figure 106 – Sethi3D AiP A3 printer.

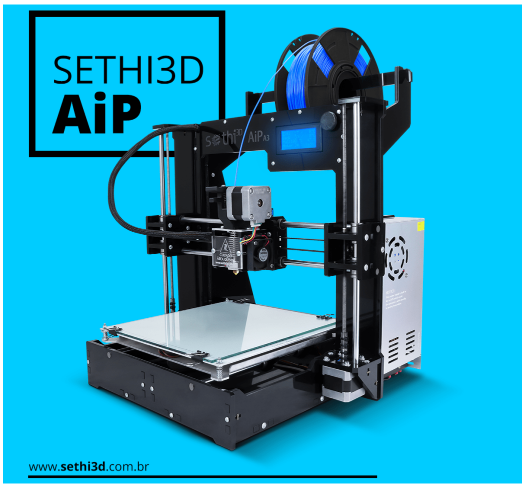

Source: SETHI3D (2025).

8.1.2 Material characterisation through tensile testing

The mechanical properties of the printed polymer depend on the printing process. The material characterisation was conducted in accordance with ASTM D638-14 (American Society for Testing and Materials, 2014). As shown in Figure 107, the uniaxial tensile tests were carried out using five dumbbell-shaped specimens of Type I with a length overall LO = 165 mm, width overall WO = 19 mm, and thickness T = 3 mm (see details in ASTM D638-14). It is worth noting that T = 3 mm was adopted because the architected structures are composed of elements with small thickness. The Type I specimens were tested at a speed of 5 mm/min using an Instron 5969 Dual Column Testing System equipped with a 5 kN static load cell. Using this testing setup, the characterisation was carried out to determine the modulus of elasticity (E), maximum tensile stress (σ_{max}), tensile strength at failure (σ_b), and elongation at failure (ε_b).

Figure 107 – Specimens of Type I for uniaxial tensile testing.

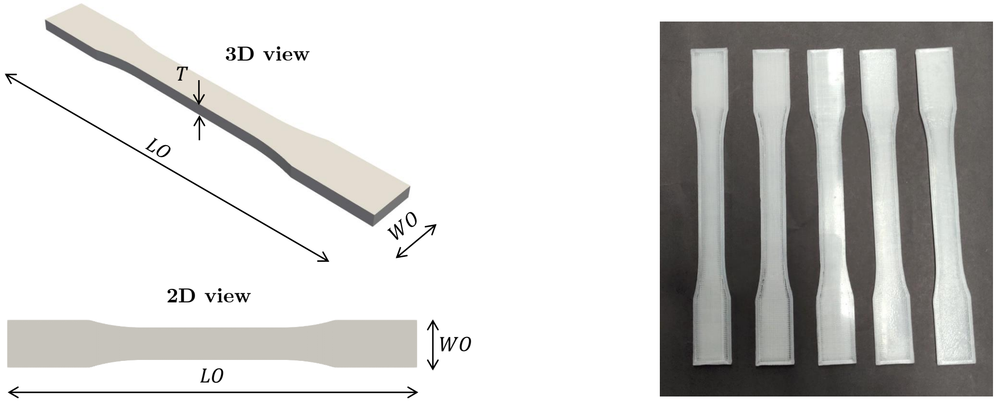

(a) Specimen of Type I with length overall LO = 165 mm, width overall WO = 19 mm, and thickness T = 3 mm.

(b) Five 3D-printed specimens of Type I for material characterisation.

Source: The author.

Figure 108a shows the setup for the uniaxial tensile test, where a mechanical extensometer was used to measure the longitudinal strain in the specimen. The five broken Type I specimens after testing are shown in Figure 108b. The constitutive stress-strain behaviour (σ_t-ε_t) for each tested specimen is shown in Figure 109. Furthermore, the results for the material properties (E, σ_{max}, σ_b, and ε_b) are reported in Table 31.

Figure 108 – Uniaxial tensile testing for material characterisation.

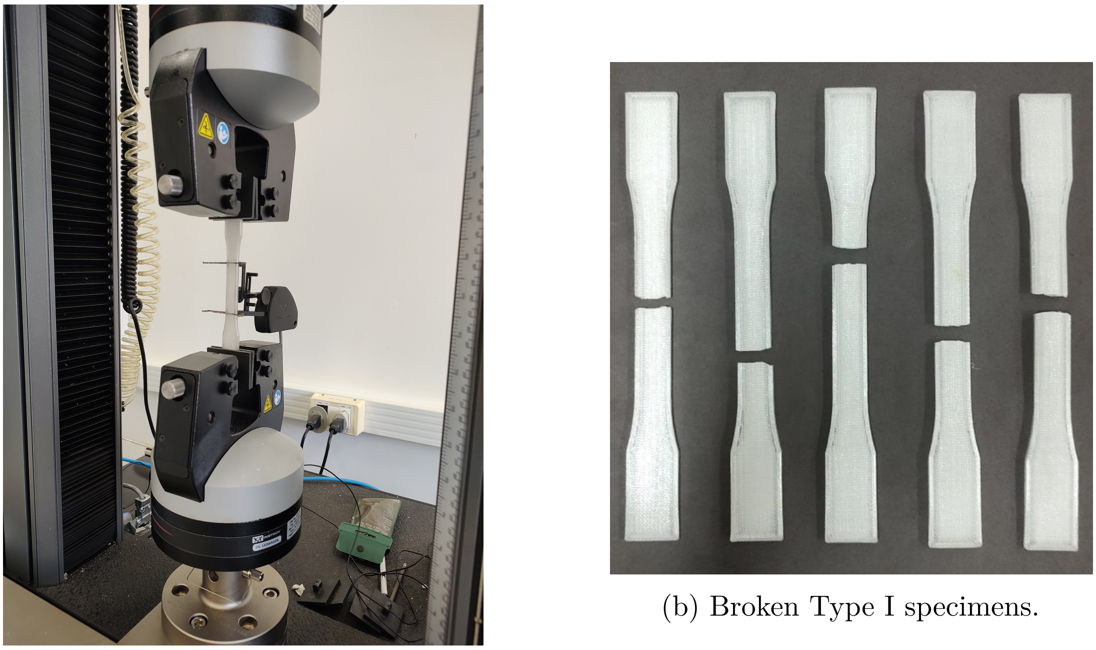

(a) Uniaxial tensile testing of a Type I specimen.

(b) Broken Type I specimens.

Source: The author.

Figure 109 – Tensile stress associated with tensile strain (σ_t - ε_t) for uniaxial tensile test, considering five Type I specimens (# 1, # 2, # 3, # 4 and # 5).

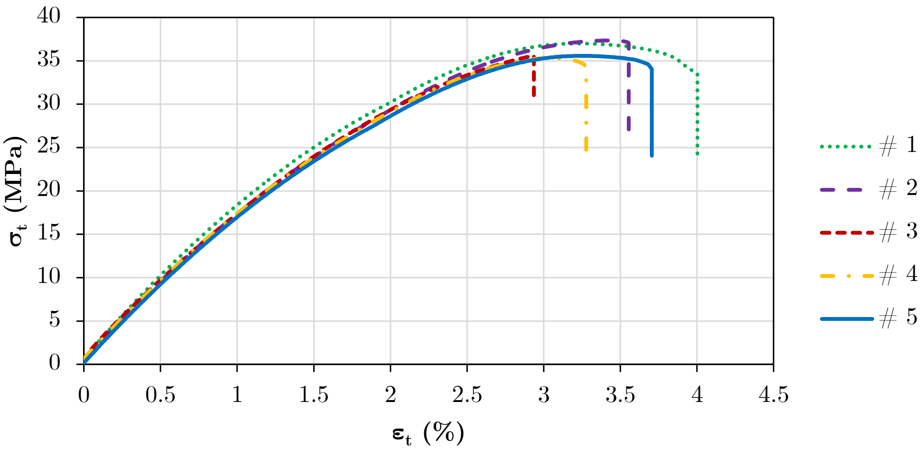

Source: The author.

Table 31 – Mechanical properties obtained from tensile tests of five Type I specimens (T = 3 mm).

Specimen	$E^{\#}$ (MPa)	$\sigma_{max}^{\#}$ (MPa)	$\sigma_b^{\#}$ (MPa)	$\varepsilon_b^{\#}$ (%)
# 1	2057	36.99	33.52	4.00 %
# 2	1926	37.34	36.99	3.56 %
# 3	1948	35.62	35.62	2.94 %
# 4	1943	35.34	34.21	3.28 %
# 5	1844	35.58	34.05	3.71 %

Source: The author.

In particular, an optical extensometer-based approach was employed to obtain the transverse and longitudinal strains required to determine the Poisson's ratio (ν). In this case, five Type I specimens were printed with a thickness of $T = 7$ mm to facilitate the visualisation of the transverse strain. The uniaxial tensile tests were performed using an Instron 5969 Dual Column Testing System equipped with a 5 kN load cell. The tensile tests were conducted at a speed of 1 mm/min to more effectively monitor the evolution of longitudinal and transverse strains using the optical extensometer. Table 32 summarises the experimental values of ν for each tested specimen.

Table 32 – Poisson's ratio from tensile tests of five Type I specimens ($T = 7$ mm).

Specimen	$\nu^{\#}$
# 1	0.40
# 2	0.42
# 3	0.23
# 4	0.27
# 5	0.33

Source: The author.

The results of PETG material characterisation through 3D printing are presented in Table 39. The average results for each material parameter are presented in Table 39, including the standard deviation (SD) and the coefficient of variation (CV).

Table 33 – Mechanical properties from tensile tests of 3D-printed Type I specimens manufactured using PETG.

Mechanical properties	**Value**	*SD*	*CV*
E	1944 MPa	76.01 MPa	3.91%
ν	0.33	0.08	24.71%
σ_{max}	36.17 MPa	0.92 MPa	2.54%
σ_b	34.88 MPa	1.41 MPa	4.05%
ε_b	3.50%	0.41%	11.61%

Source: The author.

8.1.3 Design and preparation of the architected metamaterial for laboratory testing

Next, the design and additive manufacturing of a 3D-architected polymer metamaterial are addressed in detail. The experimental test for the metamaterial exhibiting tension-induced undulation is conducted using the 3D architected structure depicted in Figures 110 and 111. The geometry follows a 2D numerical example developed by Santos *et al.* (2024), where the main difference is the addition of dense material blocks at the longitudinal ends of the specimen to provide fixation for the claws used in the uniaxial tensile test. An example of the printed architected structure is shown in Figure 112. To reduce printing time, higher speeds (e.g., 80 mm/s, resulting in a printing time of ≈ 8. hours) were tested during the 3D printing process of the architected metamaterial. This led to reproducibility issues due to significant material accumulation in the nozzle. Therefore, a speed of 50 mm/s was chosen to produce architected structures without the accumulation of unwanted material. The time required to print each specimen was ≈ 11 hours (print speed of 50mm/s).

Figure 110 – Front view of the architected structure: $L_x = 150$ mm, $L_y = 60$ mm, and $L_z = 15$ mm.

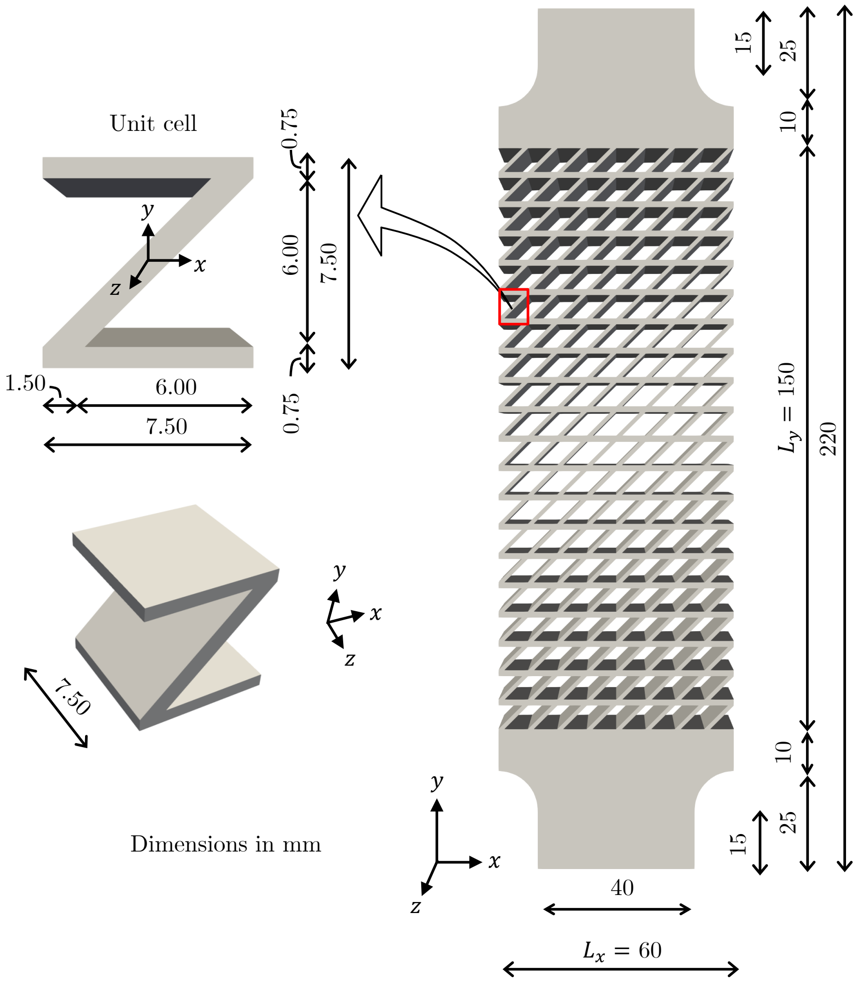

Source: The author.

Figure 111 – 3D view of the architected structure: $L_x = 150$ mm, $L_y = 60$ mm, and $L_z = 15$ mm.

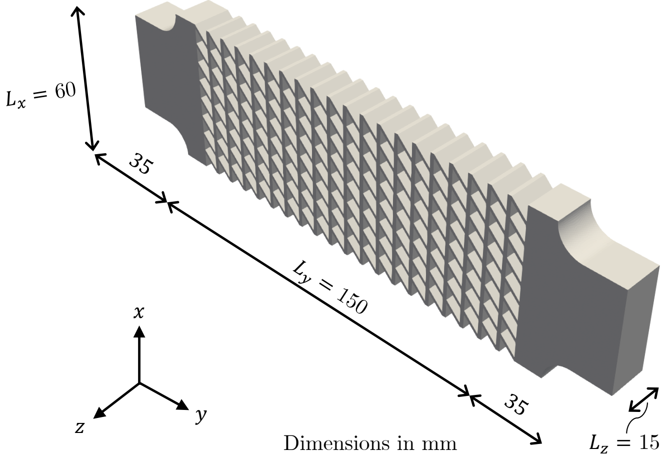

Source: The author.

Figure 112 – 3D-printed architected structure for uniaxial tensile testing.

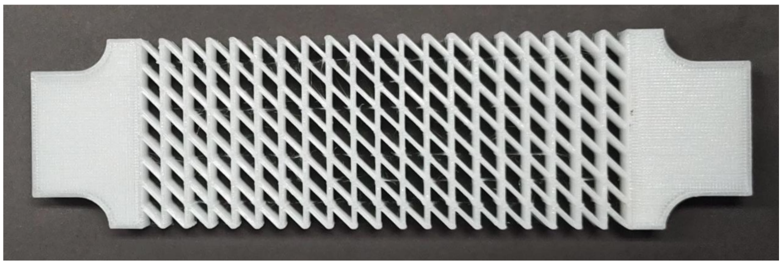

Source: The author.

The uniaxial tensile tests were conducted for the architected structures using a universal testing machine (Instron 5969 Dual Column Testing System) with a 5 kN static load cell. To evaluate the influence of the prescribed displacement rate, laboratory experiments were conducted at constant displacement rates of 1 mm/min, 5 mm/min, and 10 mm/min. To assess the representativeness of the results, three structures were experimentally tested for each prescribed displacement rate. As shown in Figure 113, the jaws of the uniaxial tensile testing equipment are positioned on the dense regions of the longitudinal ends of the structure. The experiments allow for the determination of the reaction force associated with prescribed displacement curves (R - u_0) for the three structures tested in the laboratory. In this case, the determination of displacements is also interesting for quantifying the coupling effect that provides tension-induced undulation. In this context, the experimental tests were recorded using an 8K ultra-high definition (UHD) camera positioned to capture the undulation in the xy plane (see Figure 113b). After conducting the experiments, the undulation was accounted for by image processing the video of the uniaxial tensile test using ImageJ software. It is worth mentioning that we attempted to perform a uniaxial compression test on the same structure, but the instability/buckling outside the xy plane did not allow us to obtain the compression-induced undulation.

Figure 113 – Architected structure for uniaxial tensile testing.

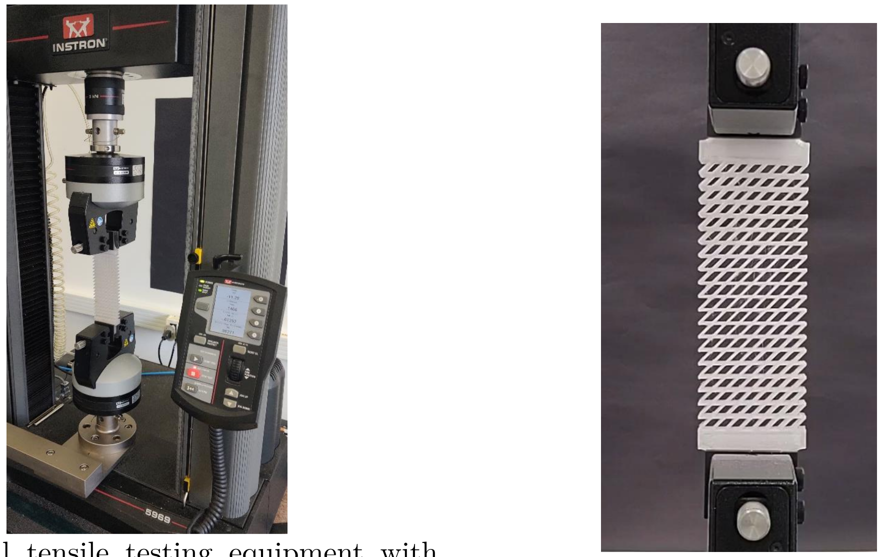

(a) Uniaxial tensile testing equipment with claws to fix the longitudinal ends of the structure.

(b) Architected structure positioned for the test (front view).

Source: The author.

8.2 Numerical simulations

This subsection presents the main aspects of three-dimensional numerical modelling of the architected mechanical metamaterial. Quasi-static finite element simulations were conducted within a finite strain framework to compare the numerical results with the experimental data. It is worth highlighting that finite strain theory, due to its ability to account for large displacements and rotations, offers significant advantages for accurately simulating and predicting material behaviour under complex loading and deformation conditions. More specifically, the numerical modelling is conducted using two approaches: (i) DNS models, where the structure is explicitly simulated at the macro-scale through the arrangement of unit cells, and (ii) Multi-scale periodic model based on first-order computational homogenisation. Therefore, the two-dimensional elastic numerical simulations (assuming the plane strain hypothesis) of the metamaterial conducted by Santos *et al.* (2024) are extended to three-dimensional analyses, using the constitutive parameters identified experimentally through the characterisation tests reported in Section 8.1.2.

In all simulations, the matrix material is modelled using a hyperelastic constitutive law driven by the Eulerian logarithmic strain tensor (see Equations (5.2) and (5.3)). First, the numerical analyses are conducted assuming linear elastic constitutive behaviour with E = 1944 MPa and $\nu = 0.33$, corresponding to the elastic parameters derived from material characterisation tests. Simulations with elastic constitutive behaviour are interesting for evaluating the the effects of geometric nonlinearity in the architected metamaterial. Afterwards, numerical simulations are performed with the von Mises elasto-plastic constitutive model following the hardening curve defined in Figure 114. In this context, following the uniaxial characterisation tests: (i) the hardening curve is defined with plastic strains initiated at the yield stress of $\sigma_p \approx 25$ MPa, (ii) hardening is non-linear up to the maximum mean uniaxial tensile stress ($\sigma_p^{max} = \sigma_{max} \approx 36.17$ MPa). Still referring to Figure 114, after the maximum mean stress observed in the experimental tests, a perfect elasto-plastic behaviour (no hardening) is assumed for the final stage of the hardening law. Despite the simplified constitutive model, exploring DNS models and coupled three-dimensional multi-scale simulations remains challenging in the computational modelling of architected structures across multiple scales due to the high computational cost.

Figure 114 – Hardening curve, encompassing the relationship between plastic stress and plastic strain (σ_p - ε_p) for the von Mises elasto-plastic constitutive model.

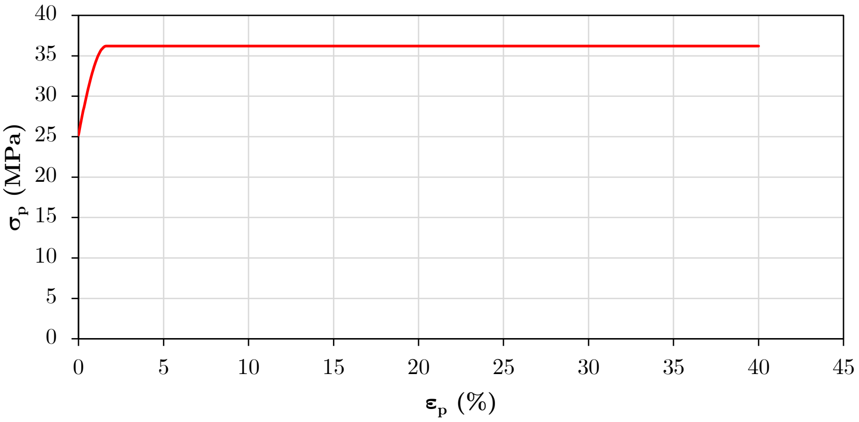

Source: The author.

8.2.1 Direct Numerical Simulations (DNS)

Preliminary numerical simulations of the structure with dense blocks at the longitudinal ends (see Figure 110) were performed within the context of elastic constitutive behaviour. Despite the significant increase in computational cost (particularly memory requirements), the architected structure with dense blocks also exhibited mechanical behaviour similar to the architected geometry shown in Figure 115. Therefore, the dense blocks added to the experimental specimen are not required in the DNS model, as boundary conditions can be easily applied in numerical simulations. In this context, the DNS model for the metamaterial is shown in Figure 115, including details of the geometry, dimensions, and boundary conditions. Note that the DNS model consists of a periodic arrangement of $8 \times 20 \times 2$ unit cells, with the dimensions of each cell being $7.5 \times 7.5 \times 7.5$ mm^3. The three-dimensional numerical simulation of the DNS model was performed using the Finite Element Method, where the mesh is composed of H20 elements with 8 integration points (see details in Figure 116). The prescribed displacement $u_0 = 60$ mm was applied in: (i) 20 increments for elastic simulations, and (ii) 100 increments for elasto-plastic simulations.

Figure 115 – Architected material: $L_x = 150$ mm, $L_y = 60$ mm and $L_z = 15$ mm.

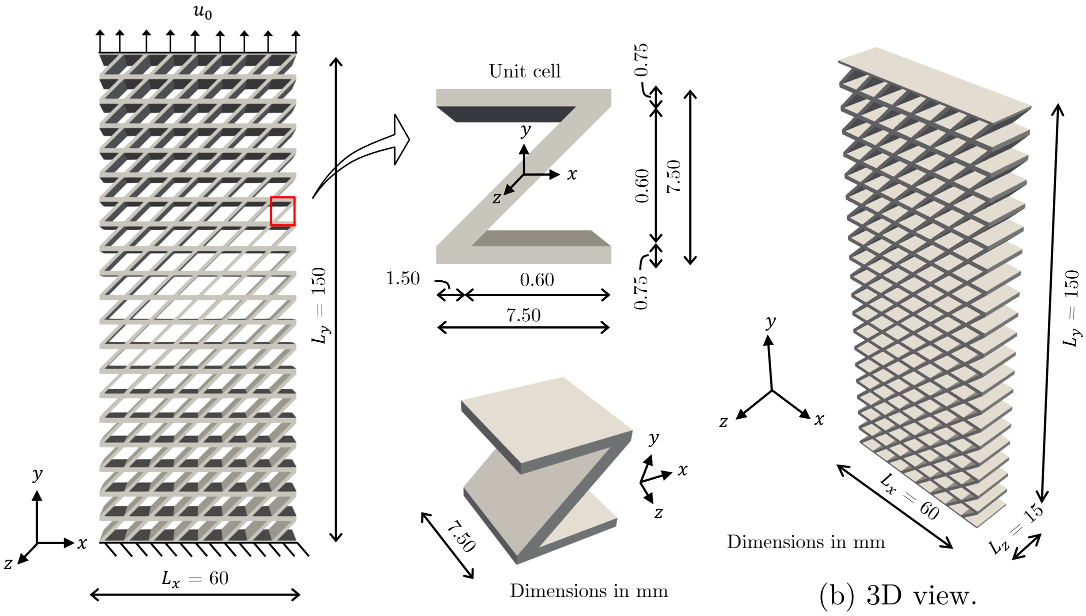

(a) Front view.

(b) 3D view.

Source: The author.

Figure 116 – Mesh for DNS model composed of 140800 elements and 784461 nodes.

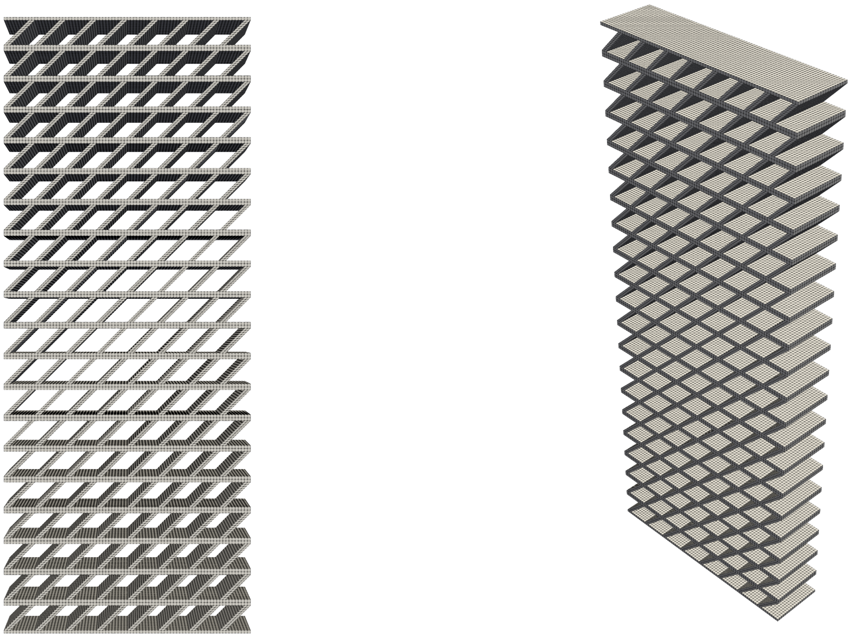

(a) Front view.

(b) 3D view.

Source: The author.

8.2.2 FE^2 multi-scale simulations

Quasi-static FE^2 multi-scale numerical analyses based on first-order computational homogenisation are carried out to model the architected metamaterial. The macro-scale problem is presented in Figure 117a, which includes the global dimensions of the three-dimensional structure and its boundary conditions. The macro-scale dimensions ($L_x = 150$

mm, $L_y = 60$ mm and $L_z = 15$ mm) are identical to those defined for the DNS model (see Figure 115). The boundary conditions are also similar to those of the DNS model, where the prescribed displacement corresponds to $u_0 = 60$ mm applied into: (i) 20 increments for the elastic analysis and (ii) 100 increments for the elasto-plastic analysis. The geometry and dimensions of the RVE employed to model the architected metamaterial are shown in Figure 117b, where the RVE length (l_μ) corresponds to the unit cell size of the DNS model.

Figure 117 – Multi-scale problem comprising the macro-scale and RVE.

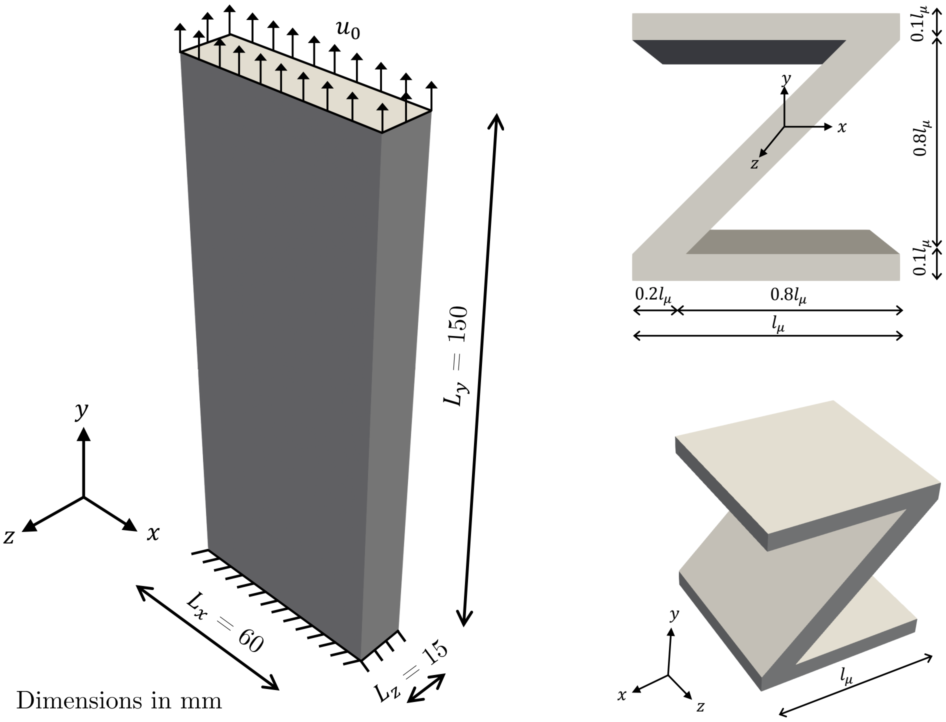

(a) Geometry and boundary conditions at the macro-scale.

(b) Geometry and dimensions of the RVE model ($l_\mu = 7.5$ mm).

Source: The author.

Finite element analyses are performed for both the macro-scale and the micro-scale, with the numerical solution obtained through an iterative Newton–Raphson scheme. The H20 element with 8 integration points (reduced integration) was employed in the numerical simulations. The meshes shown in Figure 118 were simulated to assess mesh convergence at the macro-scale. Details of the micro-scale mesh are shown in Figure 119. It is important to note that each integration point of the macro-scale mesh corresponds to an RVE in the FE^2 multi-scale analysis. As mentioned in Subsection 8.2.1, the metamaterial is composed of a periodic architecture at the microstructural level, consisting of an arrangement of unit cells. Therefore, periodic boundary conditions were imposed at the RVE level to conduct the coupled multi-scale simulations.

Figure 118 – Meshes employed at the macro-scale.

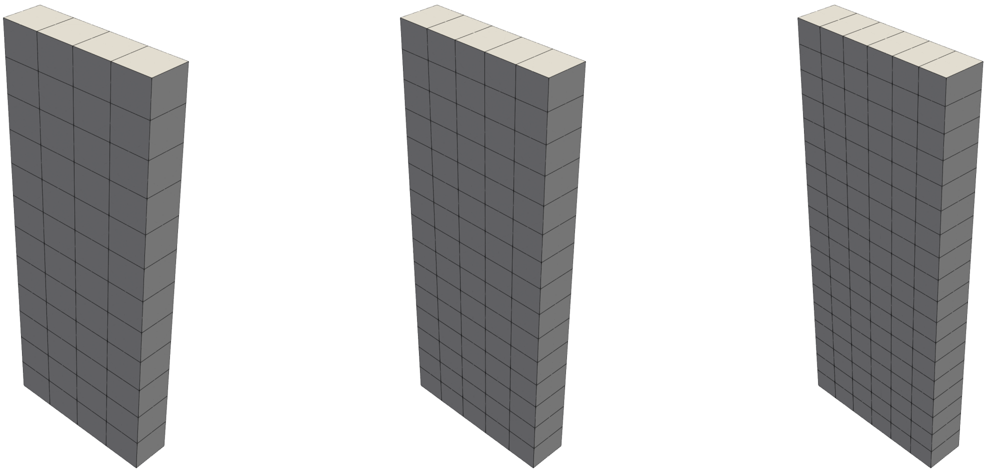

(a) 48 elements and 419 nodes. (b) 75 elements and 628 nodes. (c) 108 elements and 879 nodes.

Source: The author.

Figure 119 – RVE mesh composed of 440 elements (H20) and 2937 nodes.

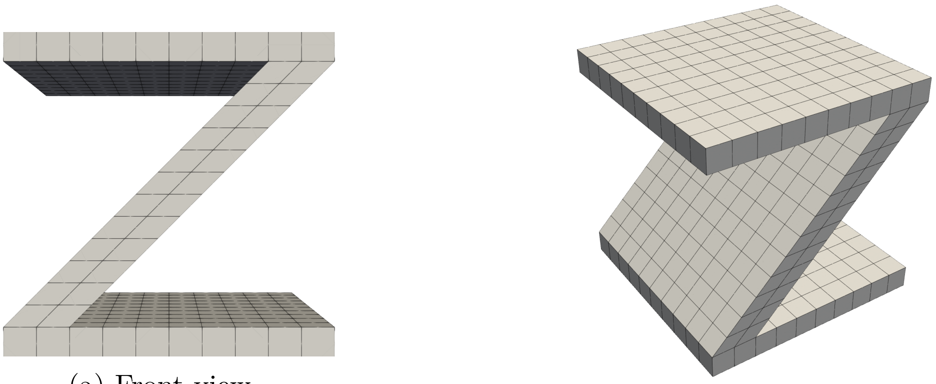

(a) Front view.

(b) 3D view.

Source: The author.

8.3 Results and discussion

In the following, the experimental observations of the exotic mechanical behaviour of the architected metamaterial are presented and discussed, including comparisons with the numerical predictions obtained through DNS and multi-scale numerical simulations.

8.3.1 Experimental mechanical behaviour of tension-induced undulation and failure modes

Figure 120 presents the reaction force results associated with the prescribed displacement (R - u_0) for the experimental test of the metamaterial at a prescribed displacement rate of 1 mm/min. A more detailed view of the deformed structures (specimens #1, #2 and #3) at different stages of the prescribed displacement is shown in Figure 121, including the failure modes at the end of the experimental process.

Figure 120 – Experimental reaction force versus imposed displacement (R - u_0) curves for structures tested at 1 mm/min (# indicates test specimen).

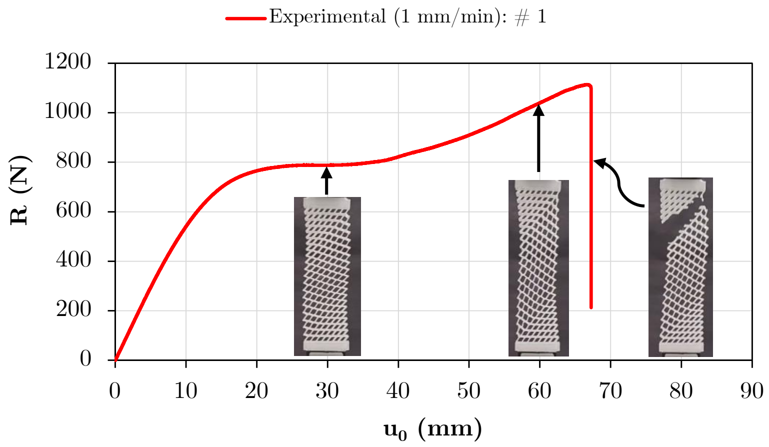

(a) R - u_0 for #1.

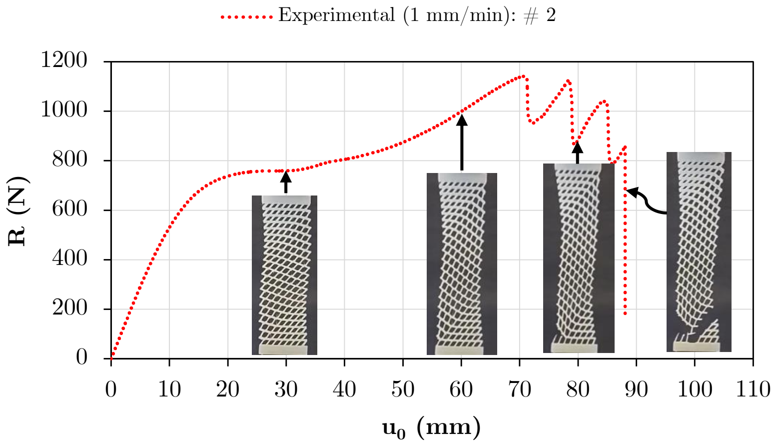

(b) R - u_0 for #2.

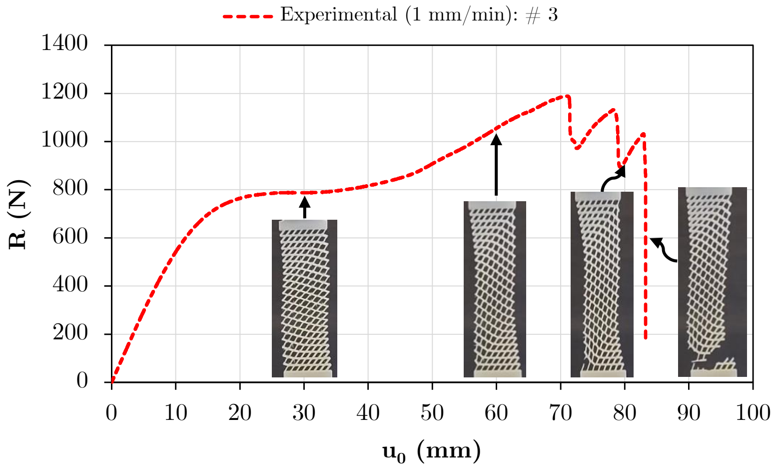

(c) R - u_0 for #3.

Source: The author.

Figure 121 – Deformed structures during the uniaxial tensile test for each prescribed displacement level u_0 for specimens tested at a speed of 1 mm/min.

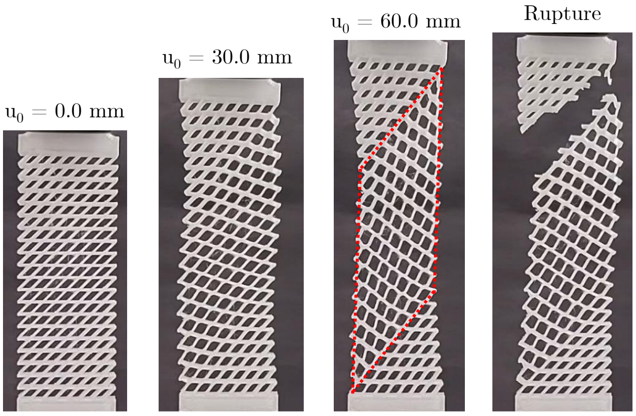

(a) Experimental: # 1.

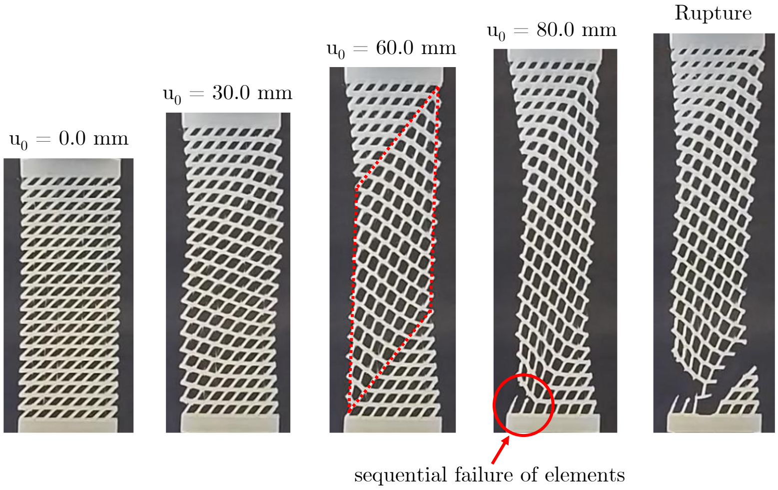

(b) Experimental: # 2.

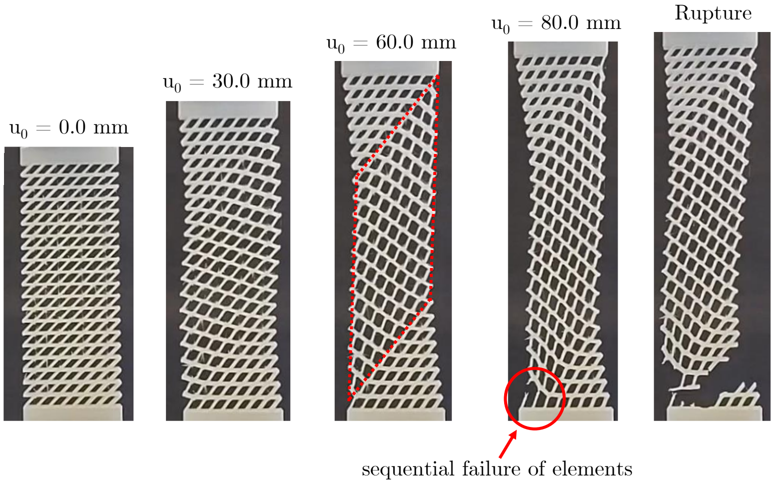

(c) Experimental: # 3.

Source: The author.

The tension-induced undulation effect is clear at $u_0 = 30$ mm, demonstrating the tension-shear deformation mode coupling analysed by Santos *et al.* (2024) exclusively from two-dimensional elastic numerical simulations is observed experimentally, and highlighting the potential of simulation-assisted metamaterial design. Table 120 presents the undulation for each structure accounted for by video image processing of the uniaxial tensile test using ImageJ software. In this case, the undulation is defined as the maximum displacement in the horizontal direction or x-direction (u_x^{max}) along the outer contour of the structures. The average undulation values, including the corresponding standard deviations and coefficients of variation, are also provided in Table 120. At the $u_0 = 60$ mm stage, the formation of strain localisation bands with a direction of approximately 45° is observed for the architected structures, which indicates association with shear throughout the progressive deformation process. The discontinuities observed in test specimens #2 and #3 for $u_0 > 70$ mm are attributed to the sequential failure of structural elements near the lower support (see the red-highlighted region in Figure 121b), which consequently contribute to the global failure of the overall structure at a more advanced stage of the loading program.

Table 34 – Undulation of the structure (u_x^{max}) in the experimental investigation at $u_0 = 30$ mm, including the standard deviation (SD) and coefficient of variation (CV).

Sample	$u_{x\#}^{max}$ **(mm)**	u_x^{max} **(mm)**	**SD**	**CV**
# 1	3.04			
# 2	3.11	3.03	0.0854	2.82%
# 3	2.94			

Source: The author.

8.3.2 Mechanical behaviour of the architected metamaterial at different displacement rates

In the experimental context, uniaxial tensile tests were also conducted for different displacement rates applied to the metamaterial. Displacement rates of 1 mm/min, 5 mm/min, and 10 mm/min were imposed on the architected structures. The mechanical behaviour results for different displacement rates are shown in Figure 122. Tables 35 and 36 present the average reaction force values for the structure at $u_0 = 30$ mm and $u_0 = 60$ mm, respectively. Moreover, Table 37 shows the comparison of experimental reaction forces for structures tested at different prescribed displacement rates, along with the relative differences in modulus ($|Dif|$). The analysis of the experimental results indicates that the prescribed displacement rate had no significant effect on the mechanical behaviour of the metamaterial up to $u_0 = 60$ mm.

Regarding material failure, differences were observed among the three structures tested under the same prescribed displacement rate. At a rate of 1 mm/min, specimen #1 exhibited an earlier failure compared to specimens #2 and #3, which displayed a more ductile behaviour with successive element fractures prior to complete failure. In general, structures tested at 1 mm/min exhibited a more ductile behaviour compared to 5 mm/min and 10 mm/min. This increased ductility may be attributed to the metamaterial's enhanced ability to accommodate strain at lower displacement rates. On the other hand, the structures tested at 10 mm/min did not exhibit successive element fractures prior to the complete failure of the metamaterial, leading to a more abrupt rupture of the structures.

Figure 122 – Experimental reaction force associated with imposed displacement (R - u_0).

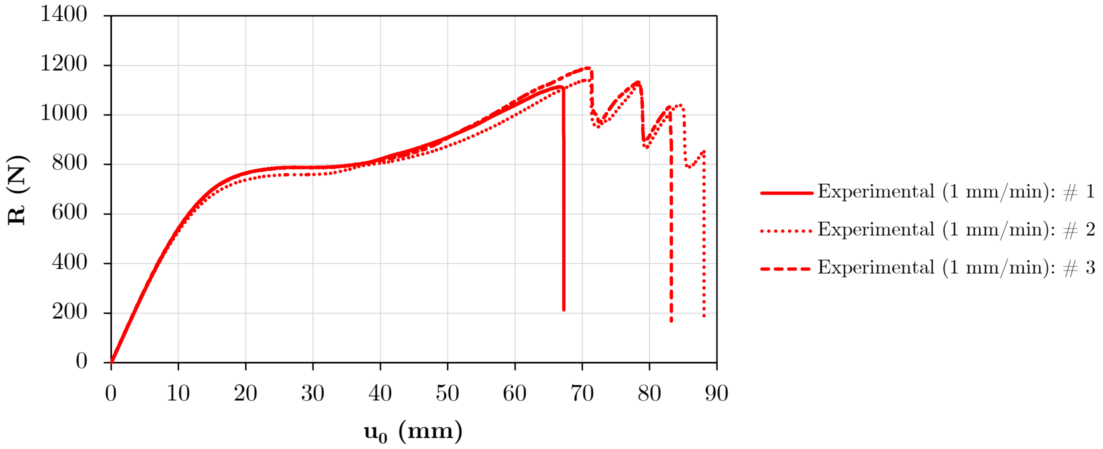

(a) Results for displacement rate of 1 mm/min.

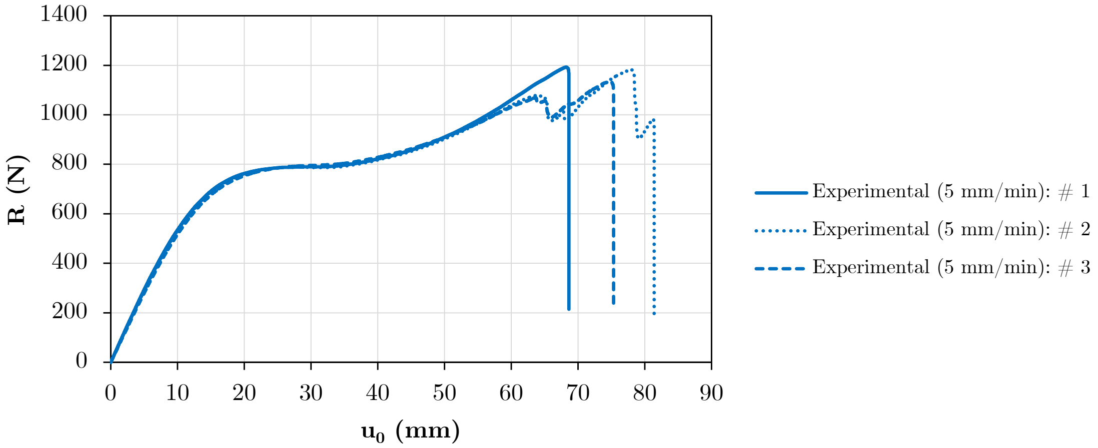

(b) Results for displacement rate of 5 mm/min.

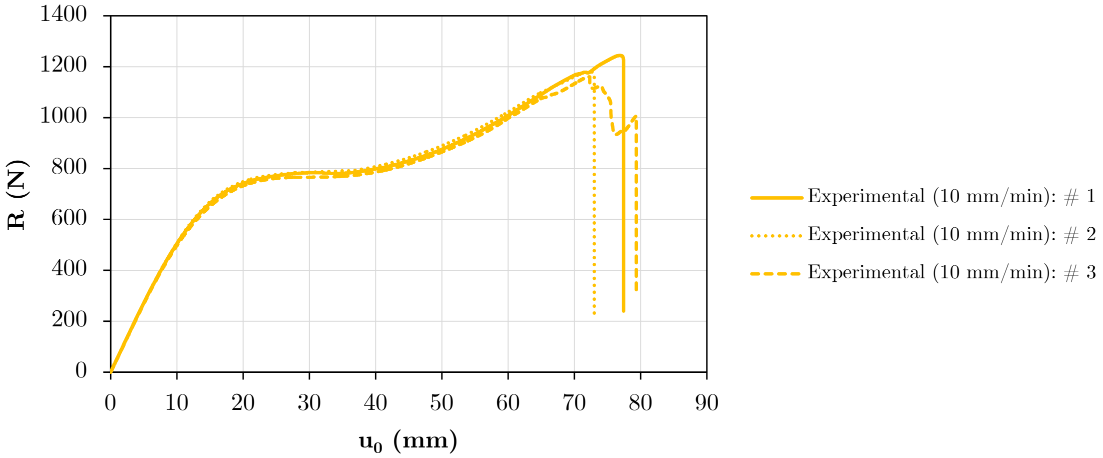

(c) Results for displacement rate of 10 mm/min.

Source: The author.

Figure 123 – Experimental reaction force versus imposed displacement (R - u_0): comparison across all displacement rates.

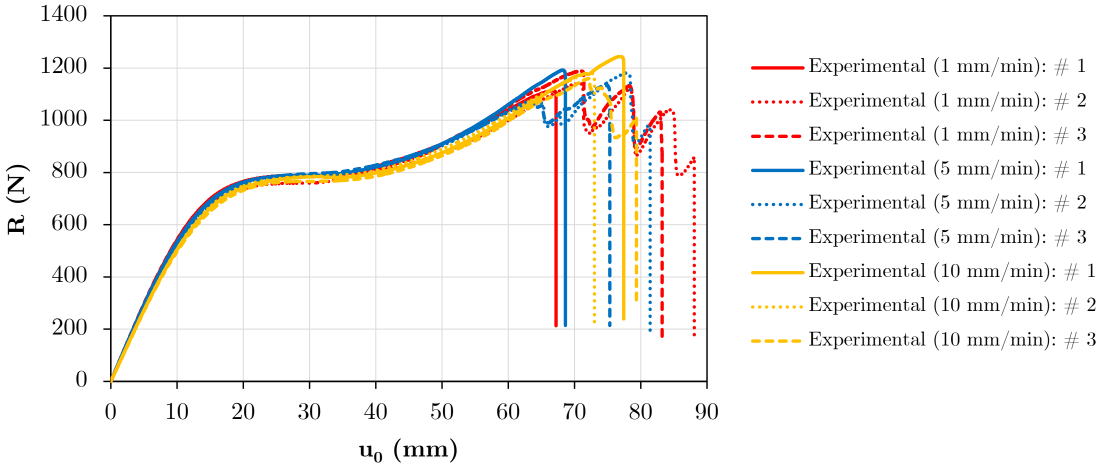

Source: The author.

Table 35 – Experimental reaction forces (R) for u_0 = 30 mm.

Speed test	**Sample**	$R_{\#}$ (N)	R (N)	SD (N)	CV (%)
1 mm/min	# 1	787.89	778.36	16.19	2.08
	# 2	759.67			
	# 3	787.53			
5 mm/min	# 1	789.53	790.76	4.10	0.52
	# 2	787.41			
	# 3	795.33			
10 mm/min	# 1	783.39	778.42	10.83	1.39
	# 2	785.88			
	# 3	766.00			

Source: The author.

Table 36 – Experimental reaction forces (R) for u_0 = 60 mm.

Speed test	**Sample**	$R_{\#}$ (N)	R (N)	SD (N)	CV (%)
1 mm/min	# 1	1039.84	1031.30	29.05	2.82
	# 2	998.94			
	# 3	1055.13			
5 mm/min	# 1	1059.66	1042.90	14.88	1.43
	# 2	1037.81			
	# 3	1031.23			
10 mm/min	# 1	1008.31	1009.37	12.18	1.21
	# 2	1022.05			
	# 3	997.76			

Source: The author.

Table 37 – Average experimental reaction forces (R) for $u_0 = 30$ mm, along with the relative differences in modulus ($|Dif|$).

	R (N)			$\lvert Dif \rvert$	
u_0	**1 mm/min** (1)	**5 mm/min** (2)	**10 mm/min** (3)	(2) to (1)	(3) to (1)
30 mm	778.36	790.76	778.42	1.59 %	0.01 %
60 mm	1031.30	1042.90	1009.37	1.12 %	2.13 %

Source: The author.

8.3.3 Metamaterial subjected to experimental cyclic testing

Experimental cyclic tests were conducted to evaluate the mechanical behaviour of the architected structures after unloading, enabling the assessment of residual displacements associated with permanent plastic strain in the polymeric material. In this context, three architected structures were tested at a prescribed displacement rate of 5 mm/min, with unloading levels set at 750 N, 850 N, 1000 N, and 1200 N. The experimental results of the mechanical behaviour for all specimens are compared in Figure 125. Moreover, the experimental results of each specimen are shown in Figure 125. The experimental data reveal that the structure exhibits significant residual displacement, characterised by mechanical behaviour with approximately parallel loading and unloading paths, with a slope similar to the initial one. Thus, the metamaterial exhibits an elasto-plastic constitutive behaviour, characterised by significant permanent strains, a typical property of polymeric materials such as PETG. In the context of computational modelling of the metamaterial via numerical simulations, the observations of cyclic tests also contribute to justifying the use of an elasto-plastic constitutive model to predict the mechanical behaviour of the polymeric architected structure.

Figure 124 – Experimental reaction force associated with imposed displacement (R - u_0) for all test specimens after cyclic experimental testing.

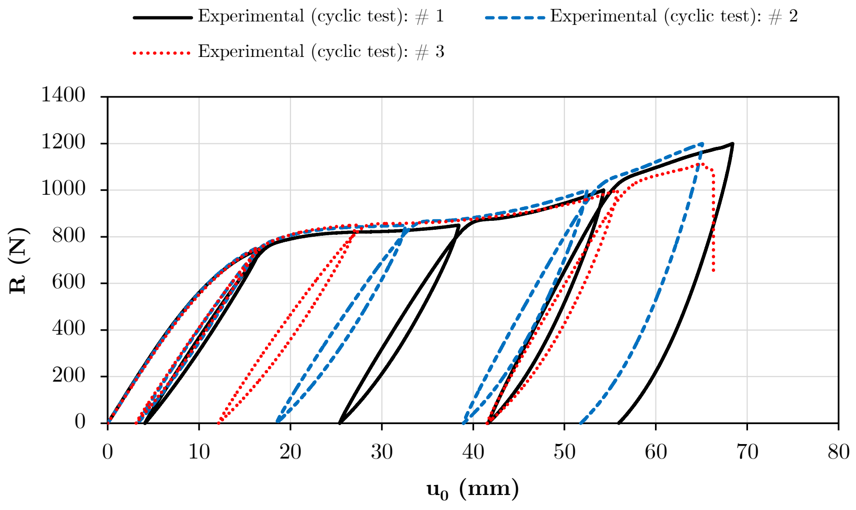

Source: The author.

Figure 125 – Experimental reaction force associated with imposed displacement (R - u_0) for each specimen after cyclic experimental testing.

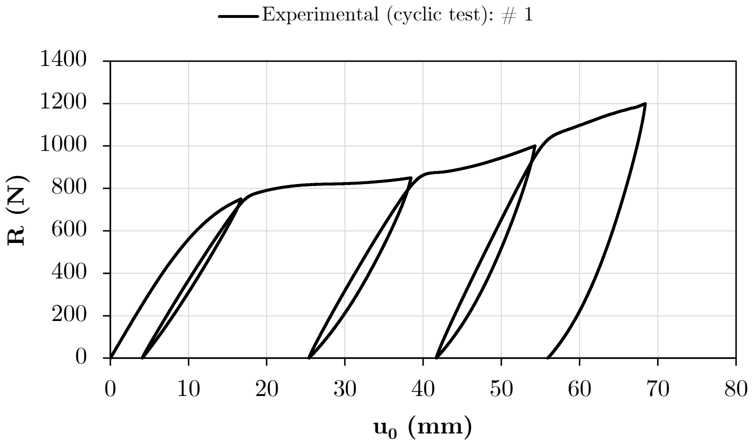

(a) Reaction force - imposed displacement for #1.

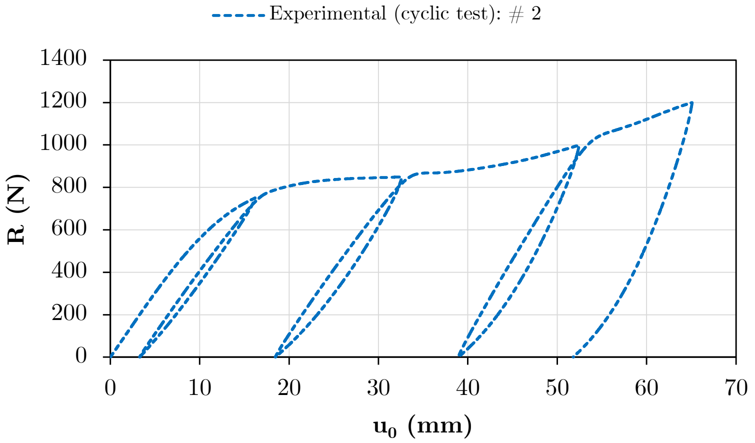

(b) R - u_0 for #2.

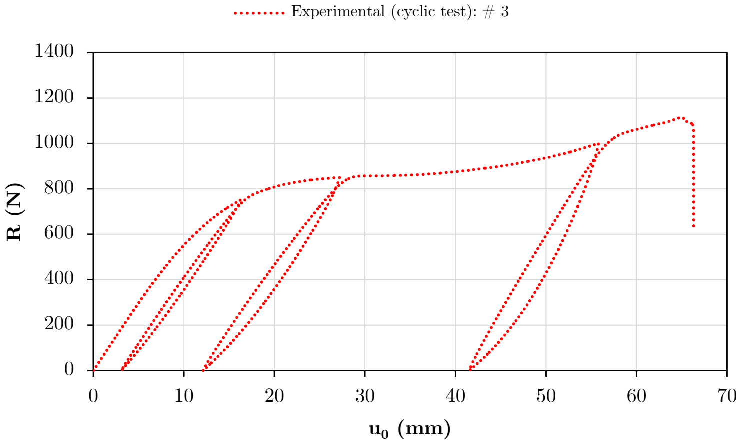

(c) R - u_0 for #3.

Source: The author.

8.3.4 Quasi-static numerical simulations compared with laboratory experiments

Figure 126 presents the results of the mesh refinement study for the periodic multi-scale model with an elastic constitutive response. The mechanical behaviour of the architected metamaterial exhibits similar results for all cases, indicating mesh convergence. Within the elastic regime, Figure 127 compares the multi-scale periodic model (mesh 3) with the DNS model. In this case, the multi-scale model is in close agreement with the DNS model. Furthermore, the elastic numerical simulations indicate that the mechanical response of the metamaterial is nonlinear, confirming the presence of geometric nonlinearity effects in the architected structure.

Figure 126 – Mesh convergence study for multi-scale coupled analyses with elastic constitutive behaviour.

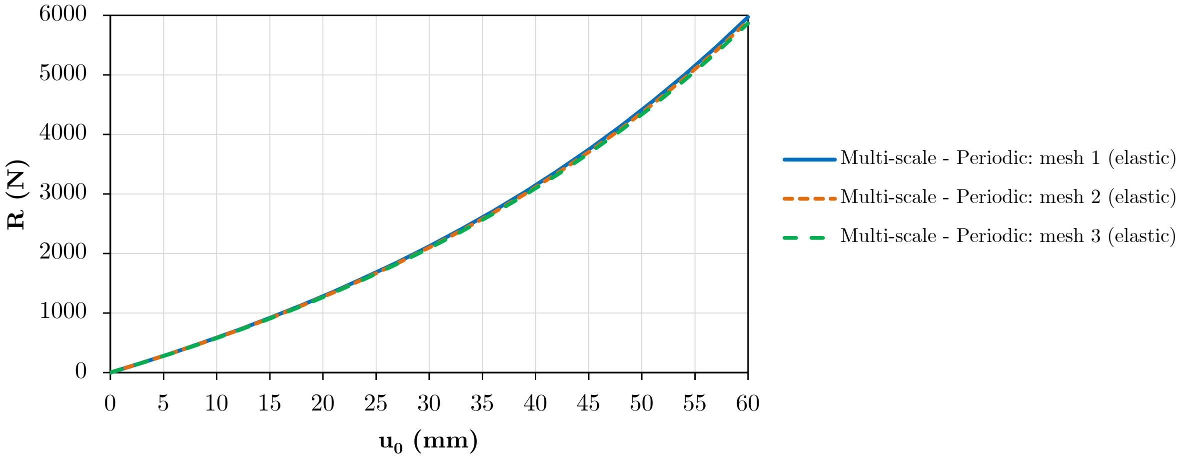

Source: The author.

Figure 127 – Comparison of mechanical behaviour (R - u_0) between multi-scale periodic model (mesh 3) and DNS model, assuming elastic constitutive behaviour.

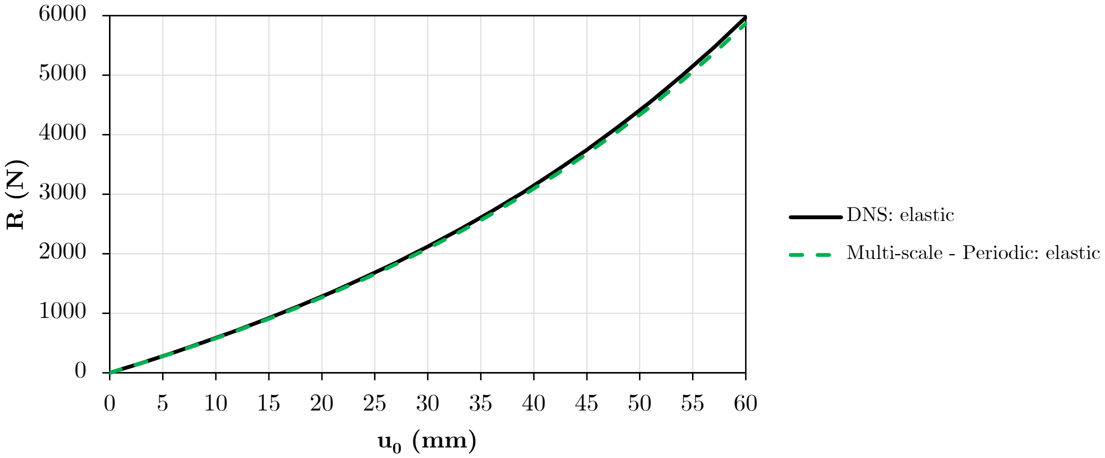

Source: The author.

Figure 128 presents the results of the elastic mechanical behaviour obtained from numerical simulations of the DNS model and multi-scale models, compared with experimental data. Since the loading rate did not significantly affect the mechanical behaviour, the comparison of responses is based on the set of tests conducted at a prescribed displacement rate of 1 mm/min. Overall, the numerical and experimental results show good agreement within the elastic regime (i.e., the initial portion of the R - u_0 curve).

Figure 128 – Comparison of mechanical behaviour (R - u_0) between experimental data and numerical predictions, assuming an elastic constitutive response.

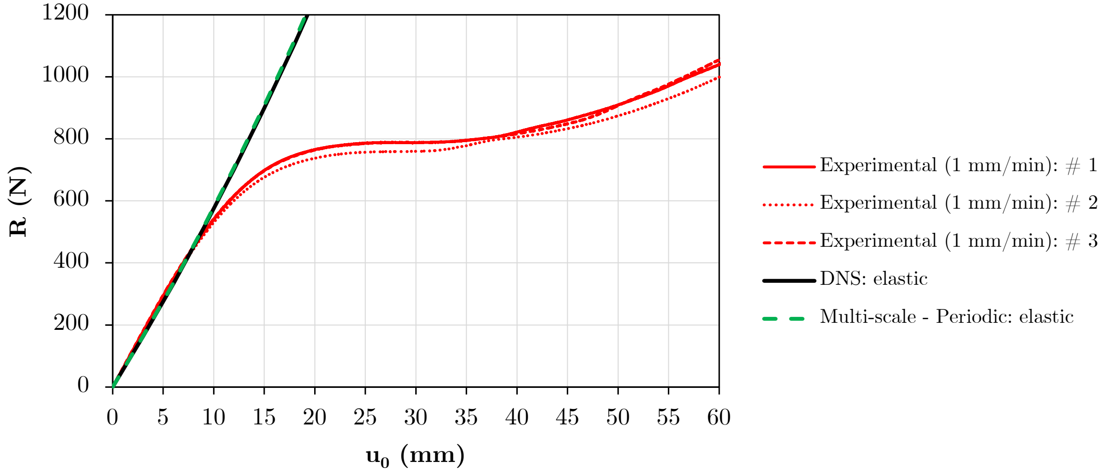

Source: The author.

Figure 129 depicts the mesh refinement study for the periodic multi-scale model, assuming an elasto-plastic constitutive behaviour. The mechanical response is similar for meshes 2 and 3 (i.e., the more refined meshes), indicating mesh convergence. Therefore, mesh 3 is sufficient to represent the architected material accurately in the context of the FE^2 multi-scale simulations with the periodic model.

Figure 129 – Mesh convergence study for multi-scale coupled analyses with elasto-plastic constitutive behaviour.

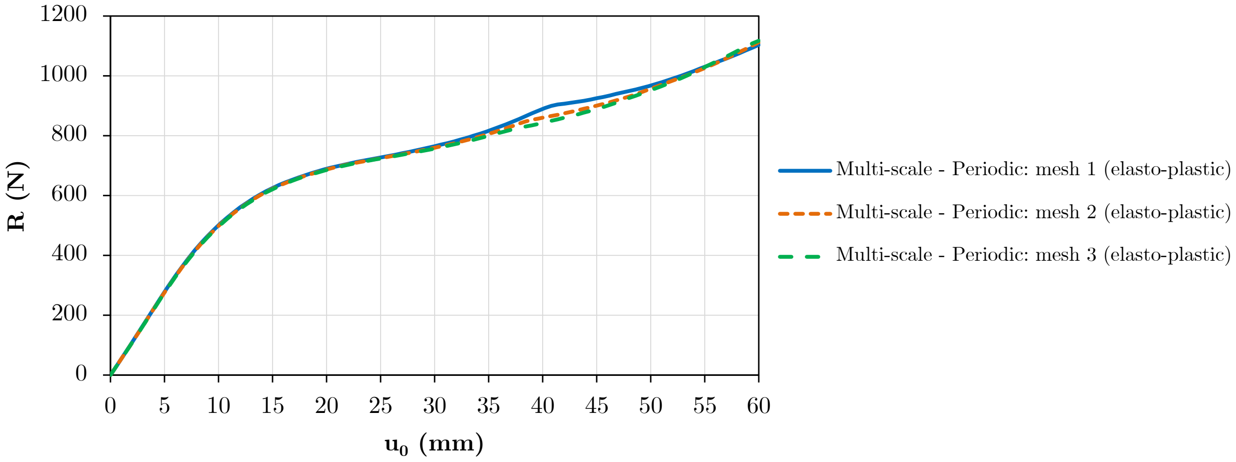

Source: The author.

Regarding the mechanical behaviour (R - u_0) of the architected metamaterial, Figure 130 compares the quasi-static elasto-plastic numerical simulations and laboratory experiments. Within the context of numerical simulations, the DNS results show good agreement with the multi-scale periodic response obtained using mesh 3. Comparisons of the deformed structures obtained through different investigation approaches (experimental, DNS model, and multi-scale periodic model), considering $u_0 = 30$ mm and $u_0 = 60$ mm, are shown in Figures 131 and 132, respectively. As shown in Figure 131, the effect of tension-induced undulation was captured by both the DNS model and the multi-scale models, indicating the predictive capability of homogenisation-based approaches. Figure 132 shows that the numerical models also captured the deformed behaviour of the metamaterial under the advanced imposed displacement stage, where the undulation disappears due to significant plastic strains. Note that the displacement values in the x-direction are close for all approaches. The numerical simulations also indicate the onset of strain localisation at $u_0 = 60$ mm (see Figure 132). Moreover, it is worth noting that the discontinuity in the R - u_0 curve for the DNS model is linked to the mentioned strain localisation.

Figure 130 – Comparison of mechanical behaviour (R - u_0) between experimental data and numerical predictions (DNS model and periodic model with mesh 3) assuming an elasto-plastic constitutive response.

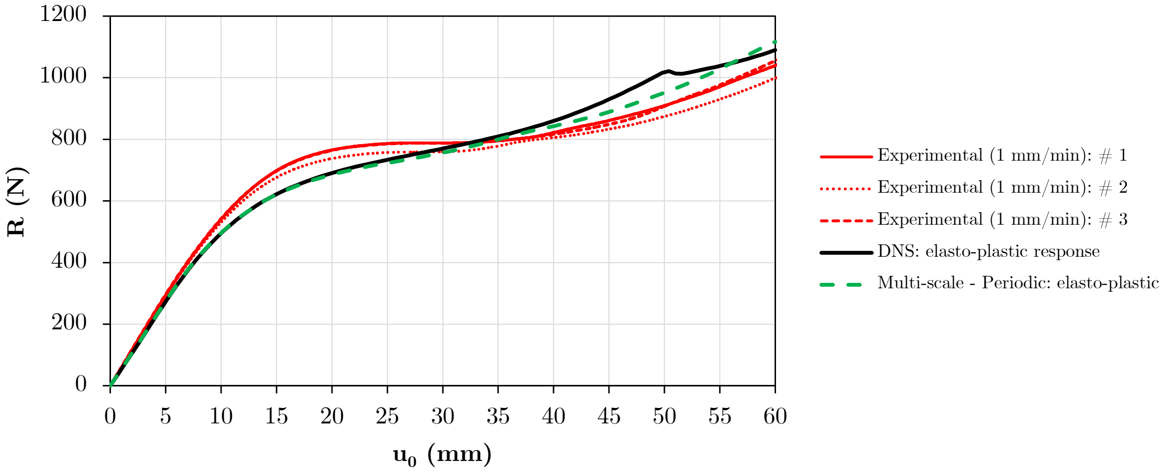

Source: The author.

Figure 131 – Comparison of results up to $u_0 = 30$ mm: experimental versus DNS model versus multi-scale periodic model.

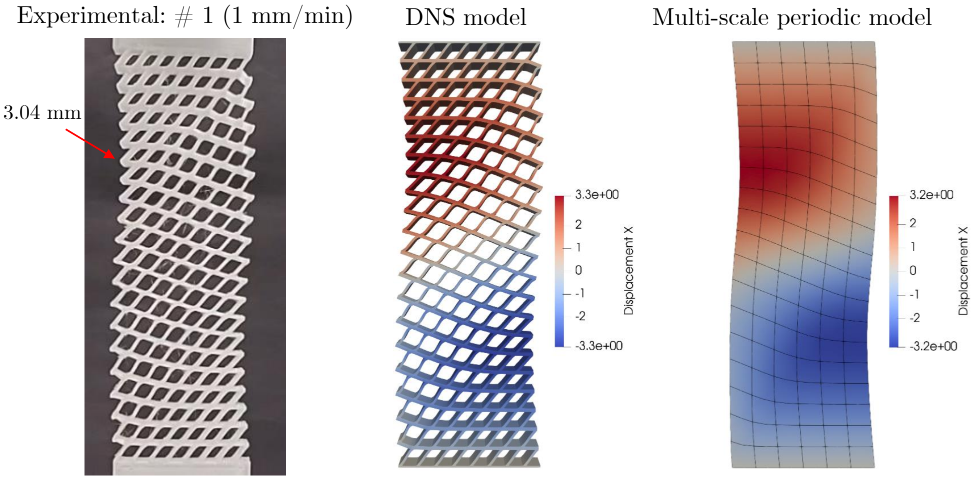

Source: The author.

Figure 132 – Comparison of results up to $u_0 = 60$ mm: experimental versus DNS model versus multi-scale periodic model.

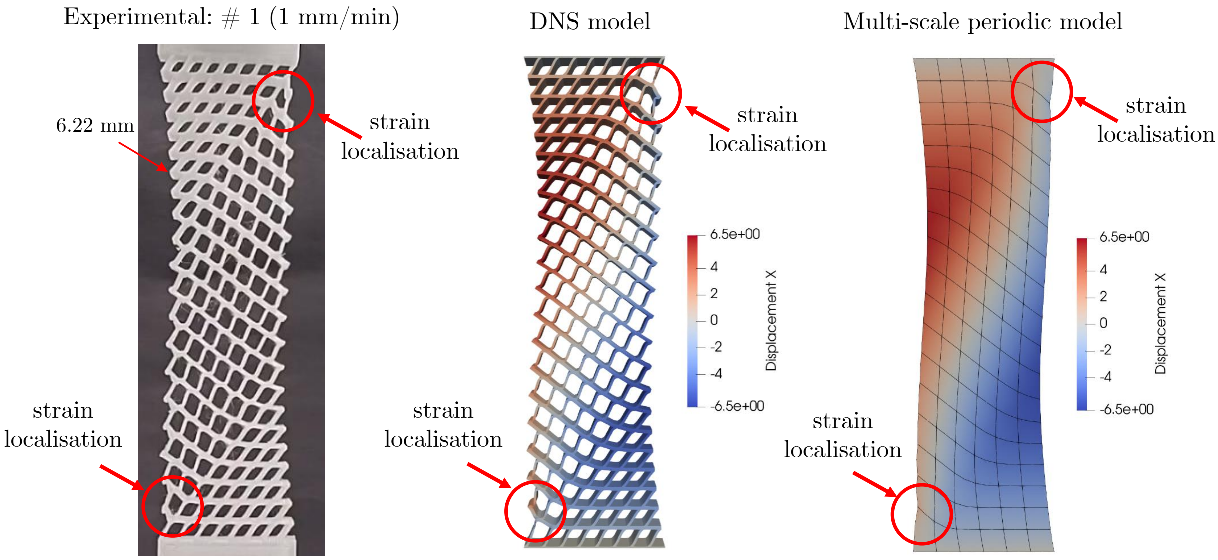

Source: The author.

In summary, the differences between the experimental data and the numerical results are mainly observed in the inelastic regime of the material behaviour, likely due to the anisotropy introduced by the FDM-based 3D printing process. Although these differences are relatively minor and do not significantly impact the conclusions of this study, a more detailed investigation is warranted to improve the accuracy of numerical modelling in future work. This should include exploring advanced material characterisation and incorporating coupled three-dimensional multi-scale simulations to better capture the observed behaviour.

8.4 Partial conclusions

A mechanical metamaterial displaying tension-induced undulation was explored through experimental and computational modelling approaches. Within the experimental context, the architected metamaterial was designed and fabricated via additive manufacturing for uniaxial tensile testing. The manufacturing process of the architected structure using FDM-3D printing with PETG (polymeric material) was reported in detail. Experimental characterisation tests were conducted on PETG specimens to obtain parameters for the material's constitutive modelling.

The phenomenon of tension-induced undulation, resulting from the coupling of tensile and shear deformations, was observed in the experimental tests. The experimental mechanical behaviour indicated that the metamaterial exhibits a favorable strength-to-weight ratio. Moreover, the progressive loading process of the structures resulted in ductile behaviour, characterised by significant strain prior to failure. Strain localisation mechanisms and failure modes were identified experimentally for the architected material. In general, the different displacement rates applied in the experimental tests did not significantly affect the mechanical behaviour. However, it is worth mentioning a tendency towards more ductile behaviour before failure at lower prescribed displacement rates. The cyclic tests indicate that the metamaterial exhibits elasto-plastic behaviour, characterised by significant residual displacements and permanent strains.

Regarding the computational modelling of the architected metamaterial, this work explored numerical strategies based on three-dimensional elasto-plastic finite element simulations, including DNS models and FE^2 multi-scale analyses. In summary, the numerical results showed good agreement across the different approaches, demonstrating the predictive capability of the multi-scale modelling in comparison to the classical DNS approach. The numerical results for the mechanical behaviour showed a good correlation with the experimental data within the elastic regime. However, differences were observed in the material's nonlinear regime, highlighting the limitations of the constitutive model defined to represent the polymeric material. Nevertheless, valuable qualitative insights were captured in the metamaterial modelling, including tension-induced undulation and strain localisation mechanisms observed in the inelastic mechanical behaviour regime.

Integrating 3D printing and numerical simulations provides a powerful framework for advancing the development of architected metamaterials with intricate geometries tailored for specific applications. This approach enables precise control over material properties, unlocking superior mechanical performance and functionality.

9 MECHANICAL BEHAVIOUR OF 3D-PRINTED POLYMER LATTICE MATERIALS UNDER BENDING WITH SIZE EFFECTS

The methodology and results associated with this Chapter are presented in Santos *et al.* (2025b). This contribution investigates size effects in additively manufactured architected structures through a combination of experimental and numerical approaches. Towards a more affordable additive manufacturing approach, polymeric structures were 3D-printed based on the FDM-based additive manufacturing method with PETG filament. Afterwards, mechanical experiments associated with three-point bending tests were conducted in the laboratory for lattice beams composed of micro-architected arrangements of unit cells with different morphologies, revealing the presence of size effects in the experimental data. For comparison with experimental results, single-scale numerical simulations, referred to as DNS models, are employed to model the lattice structures using three-dimensional finite element analysis. Furthermore, coupled multi-scale numerical simulations based on first- and second-order computational homogenisation are also performed to predict the effective mechanical behaviour of the architected structures. Thus, numerical results from different computational approaches are compared with experimental data, allowing for the examination of the advantages and limitations of each modelling option.

9.1 Experimental investigation: manufacturing, material characterisation and mechanical testing

This section outlines the procedures for the experimental investigation of additively manufactured architected structures under bending. Specifically, the study investigates the size effects in lattice beams composed of periodic arrangements of unit cells with different morphologies. The experimental investigation encompasses the fabrication, material characterisation, and mechanical testing of the architected structures.

The FDM-based additive manufacturing method was chosen to 3D print the architected structures and standard test specimens (material characterisation) using the PETG filament supplied by the manufacturer 3D LAB (2025). In this context, 3D printer details, print settings and feedstock porperties were reported in Subsection 8.1.1.

9.1.1 Characterisation of the mechanical properties of the printed polymer

Even though the PETG filament's mechanical properties are provided, the mechanical properties of the printed polymer depend on the printing conditions. Therefore, characterisation tests are conducted on standardised specimens, following ASTM D638 (American Society for Testing and Materials, 2014), produced with the same printing conditions employed to manufacture the lattice structures to obtain realistic properties of the base material that can be used in the numerical models. The uniaxial tensile tests were carried out using type I specimens with length overall $LO = 165$ mm, width overall

$WO = 19$ mm, and thickness $T = 7$ mm (see Figure 133). The set of tensile tests aimed to determine the modulus of elasticity (E), tensile stress at yield (σ_0), tensile strength at failure (σ_b), and elongation at failure (ε_b). The tests were conducted at a speed of 5 mm/min using an Instron 5969 Dual Column Testing System equipped with a 5 kN load cell. As shown in Figure 133a, a mechanical strain gauge was employed to measure the longitudinal deformations. Figure 133b shows the broken test specimens after the uniaxial tensile tests. The results depicting the constitutive behaviour in terms of tensile stress versus tensile strain (σ_t versus ε_t) are presented in Figure 135. The results of material characterisation of five Type I specimens manufactured with PETG by 3D printing are shown in Table 38.

Figure 133 – Type I specimens for uniaxial tensile test.

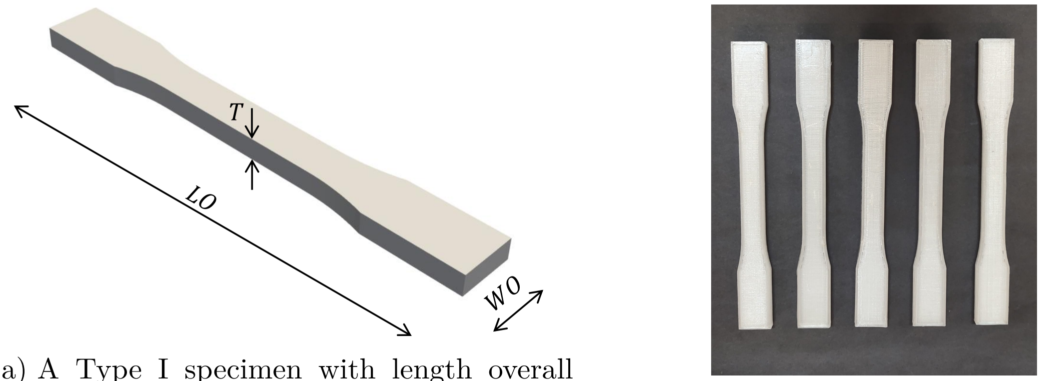

(a) A Type I specimen with length overall $LO = 165$ mm, width overall $WO = 19$ mm, and thickness $T = 7$ mm.

(b) Five 3D-printed specimens of type I for material characterisation.

Source: The author.

Figure 134 – Uniaxial tensile tests for five Type I specimens.

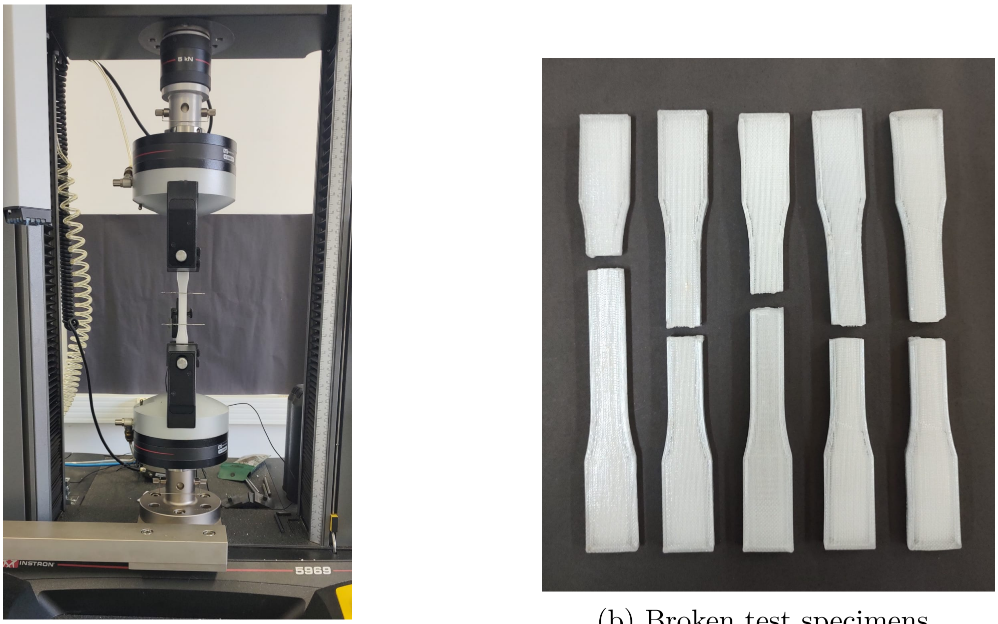

(a) 3D-printed specimen under uniaxial tensile test.

(b) Broken test specimens.

Source: The author.

Figure 135 – Tension stress versus tensile strain (σ_t versus ε_t) for uniaxial tensile test considering five test specimens (# 1, # 2, # 3, # 4 and # 5).

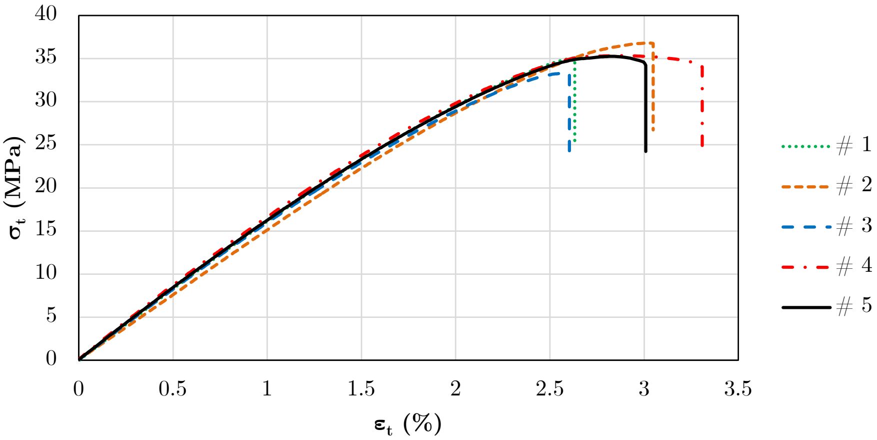

Source: The author.

Table 38 – Mechanical properties from tensile tests of five 3D-printed Type I specimens manufactured with PETG.

Specimen	$E^{\#}$ (MPa)	$\sigma^{\#}_{max}$ (MPa)	$\sigma^{\#}_{b}$ (MPa)	$\varepsilon^{\#}_{b}$
# 1	1654	35.07	34.97	2.63 %
# 2	1519	36.80	36.74	3.05 %
# 3	1652	33.28	33.05	2.60 %
# 4	1747	35.33	34.05	3.31 %
# 5	1690	35.26	34.22	3.01 %

Source: The author.

The average results for each material parameter are presented in Table 39, including the standard deviation (SD) and the coefficient of variation (CV). In particular, the experimental data associated with the Poisson's ratio (ν) were obtained in Subsection 8.1.2, where an optical extensometer-based method was employed to measure the transverse and longitudinal deformations of Type I test specimens fabricated with PETG from the same manufacturer (3D LAB, 2025). It is important to note that the elastic parameters E and ν are essential for performing elastic finite element numerical simulations of architected structures manufactured via FDM-based 3D printing.

Table 39 – Mechanical properties from tensile tests of 3D-printed Type I specimens manufactured with PETG.

Mechanical properties	**Value**	**SD**	**CV**
E	1652 MPa	83.61 MPa	5.06%
ν^*	0.33	0.08	24.71%
σ_{max}	35.15 MPa	1.25 MPa	3.56%
σ_b	34.61 MPa	1.36 MPa	3.97%
ε_b	2.92 %	0.30 %	10.33%

*Value reported in Subsection 8.1.2

Source: The author.

9.1.2 Specimens and experimental apparatus for three-point bending tests

Three-point bending experimental mechanical tests were conducted for two sets of architected structures: (i) lattice beams composed of unit cells with a triangle-shaped cross-section (triangular lattice, see Figures 136 and 137), and (ii) lattice beams composed of unit cells with a square-shaped cross-section (square lattice, see Figures 138 and 139). The beams have equal overall dimensions, with a longitudinal length of $L_x = 240$ mm and a cross-section of $L_y = 20$ mm by $L_z = 20$ mm. Regarding the setup for the three-point bending test, a distance of $L_s = 200$ mm is set between the two supports at the bottom of the lattice beams. To assess the size effect on the architected structures, three specimen configurations were designed for each type of lattice, considering different unit cell (UC) sizes, denoted by l_μ. The specimen configurations are characterised by: (I) UC size 1 ($l_\mu = 20.00$ mm), composed of 12 unit cells (12x1x1), (II) UC size 2 ($l_\mu = 10.00$ mm), composed of 96 unit cells (24x2x2), and (III) UC size 3 ($l_\mu = 6.67$ mm), composed of 324 unit cells (36x3x3). Cellular beam specimens with more unit cells (i.e., more refined micro-architected arrangements) were discarded due to poor 3D print quality, which highlighted the limitations of the equipment and technique used in the fabrication process.

Figures 140 and 141 present photos of the 3D-printed architected specimens, illustrating the different configurations manufactured for both triangular and square lattice beams, respectively. Three test specimens were printed for each beam configuration to assess the representativeness of the mechanical results. Three-point quasi-static bending tests were performed on a universal testing machine (Instron 5969 Dual Column Testing System) at a speed of 2 mm/min, using a 5 kN static load cell. The load cell was positioned in the centre of the lattice beams. The purpose of the experimental tests is to obtain the mechanical behaviour associated with reaction force versus prescribed displacement curves (R - u_0). Finally, Figures 142 and 143 show the lattice beam models positioned for the three-point bending tests.

Figure 136 – Triangular cross-section unit cell: geometry and dimensions.

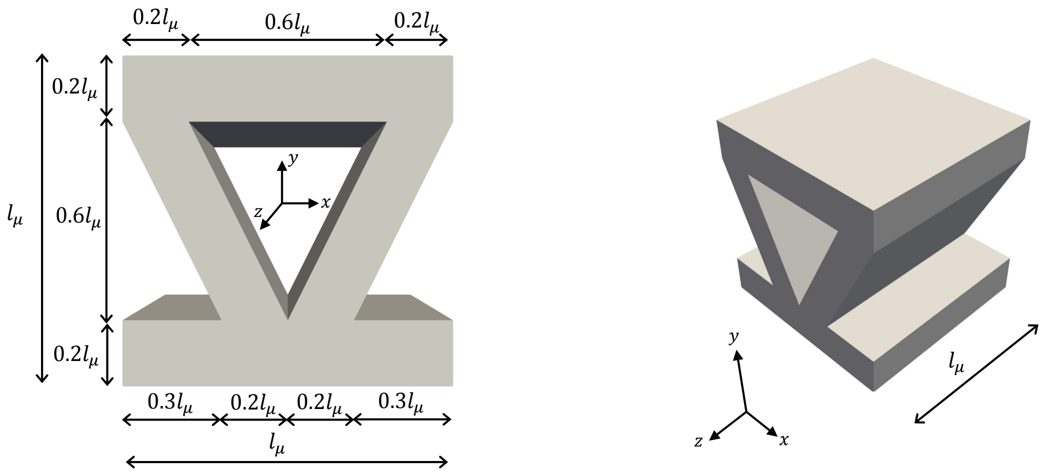

Source: The author.

Figure 137 – Dimensions ($L_x = 240$ mm, $L_s = 200$ mm, and $L_y = L_z = 20$ mm) and boundary conditions for structures with triangular cross-section unit cells.

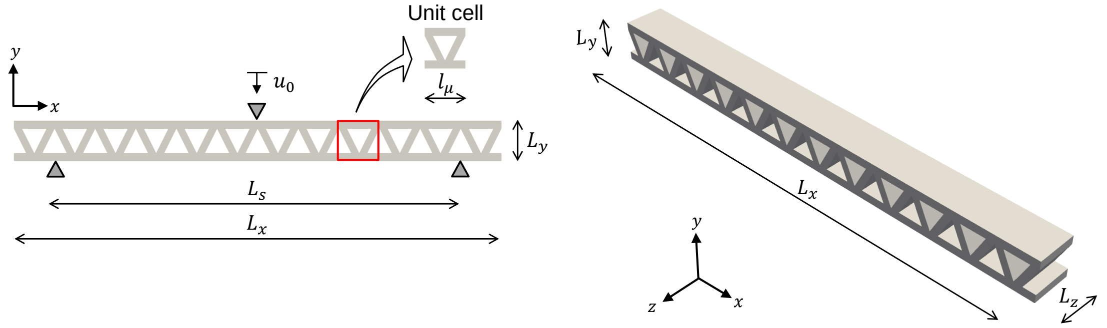

(a) UC Size 1 ($l_\mu = 20.00$ mm).

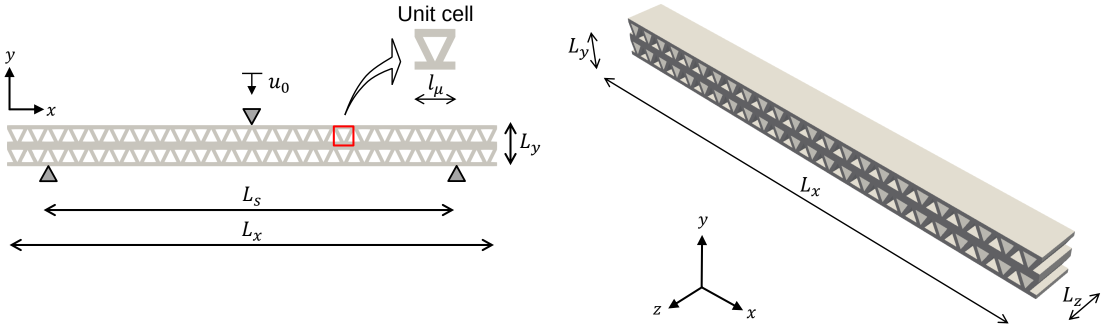

(b) UC Size 2 ($l_\mu = 10.00$ mm).

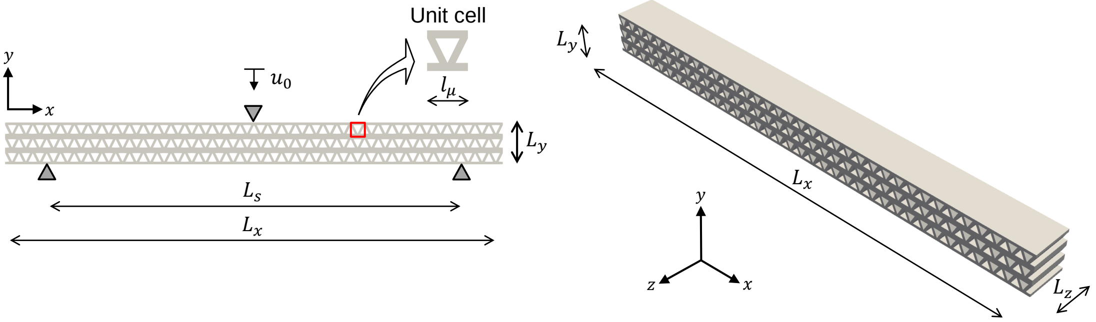

(c) UC Size 3 ($l_\mu = 6.67$ mm).

Source: The author.

Figure 138 – Square cross-section unit cell: geometry and dimensions

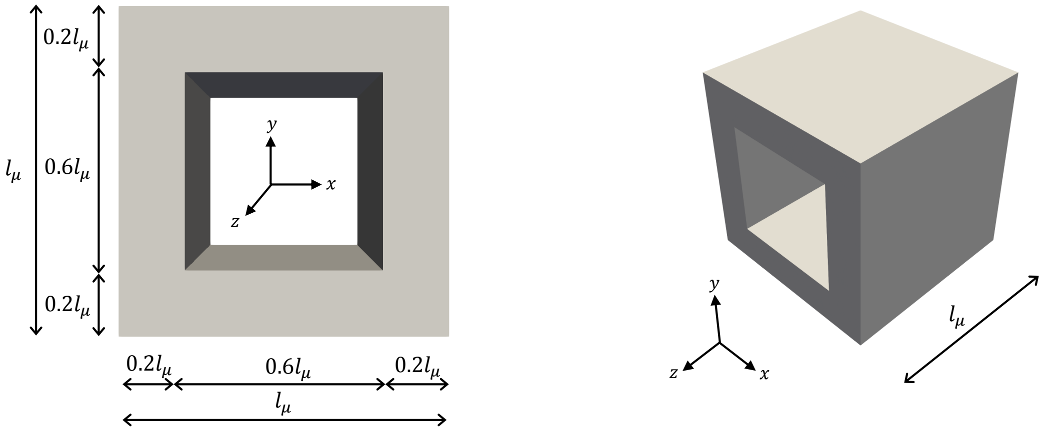

Source: The author.

Figure 139 – Dimensions (L_x = 240 mm, L_s = 200 mm, and $L_y = L_z$ = 20 mm) and boundary conditions for structures with square cross-section unit cells.

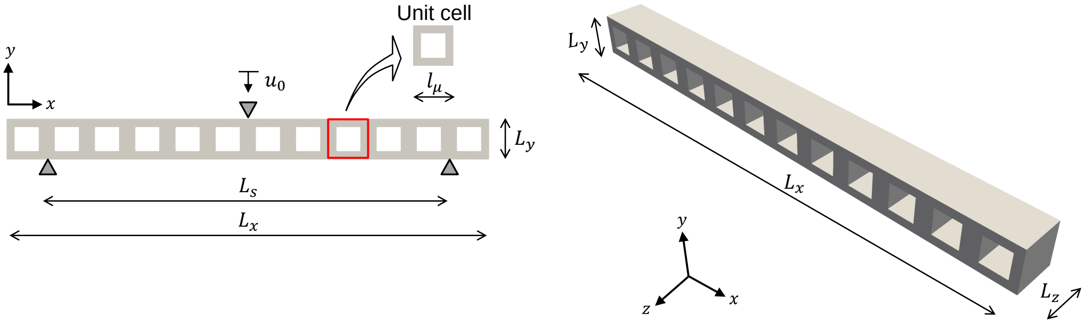

(a) UC Size 1 (l_μ = 20.00 mm).

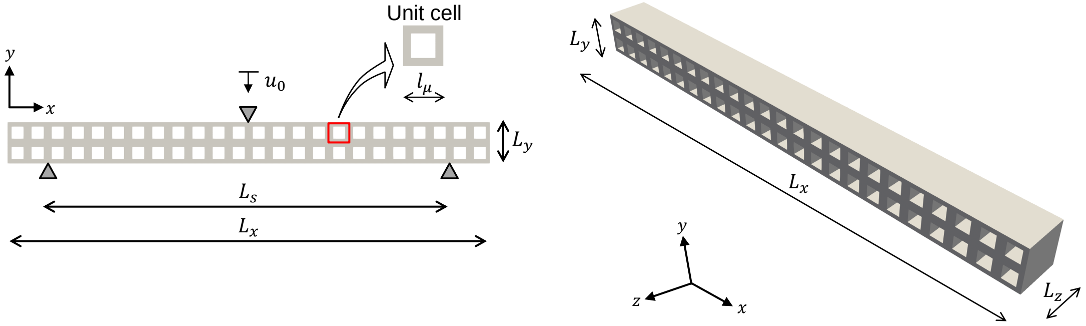

(b) UC Size 2 (l_μ = 10.00 mm).

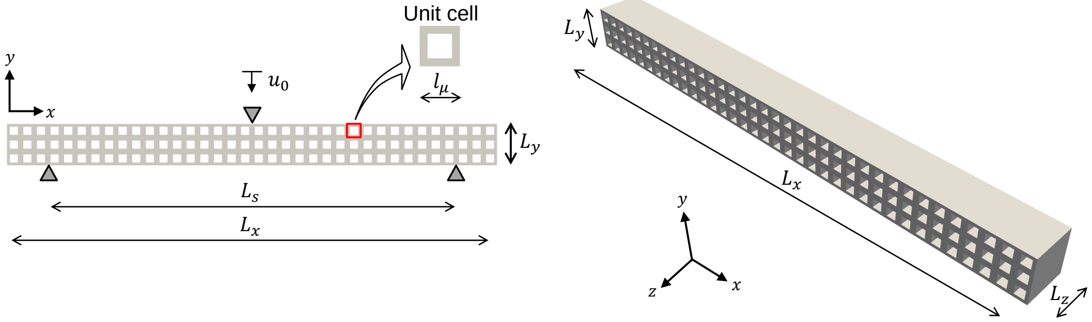

(c) UC Size 3 (l_μ = 6.67 mm).

Source: The author.

Figure 140 – 3D-printed triangular lattice beams produced for three-point bending tests.

(a) UC Size 1 (l_μ = 20.00 mm).

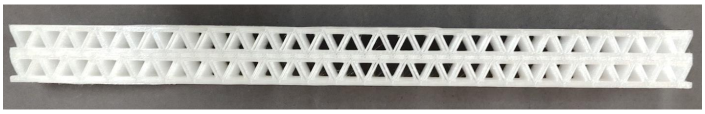

(b) UC Size 2 (l_μ = 10.00 mm).

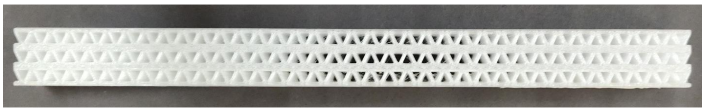

(c) UC Size 3 (l_μ = 6.67 mm).

Source: The author.

Figure 141 – 3D-printed square lattice beams produced for three-point bending tests.

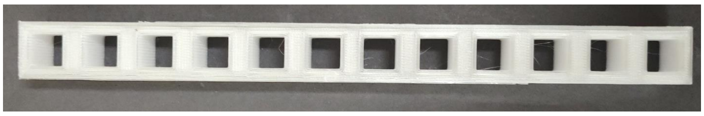

(a) UC Size 1 ($l_\mu = 20.00$ mm).

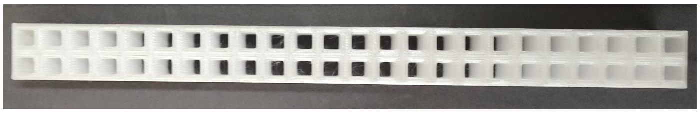

(b) UC Size 2 ($l_\mu = 10.00$ mm).

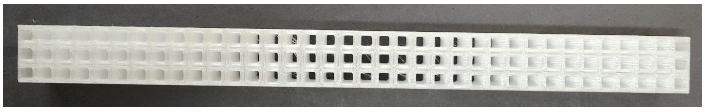

(c) UC Size 3 ($l_\mu = 6.67$ mm).

Source: The author.

Figure 142 – Experimental apparatus for three-point bending tests on triangular lattice beams.

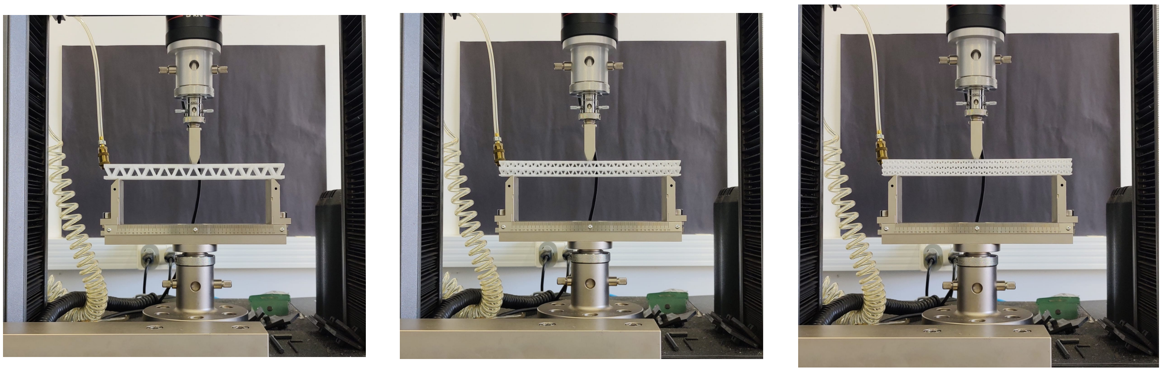

(a) UC Size 1.
(b) UC Size 2.
(c) UC Size 3.

Source: The author.

Figure 143 – Experimental apparatus for three-point bending tests on square lattice beams.

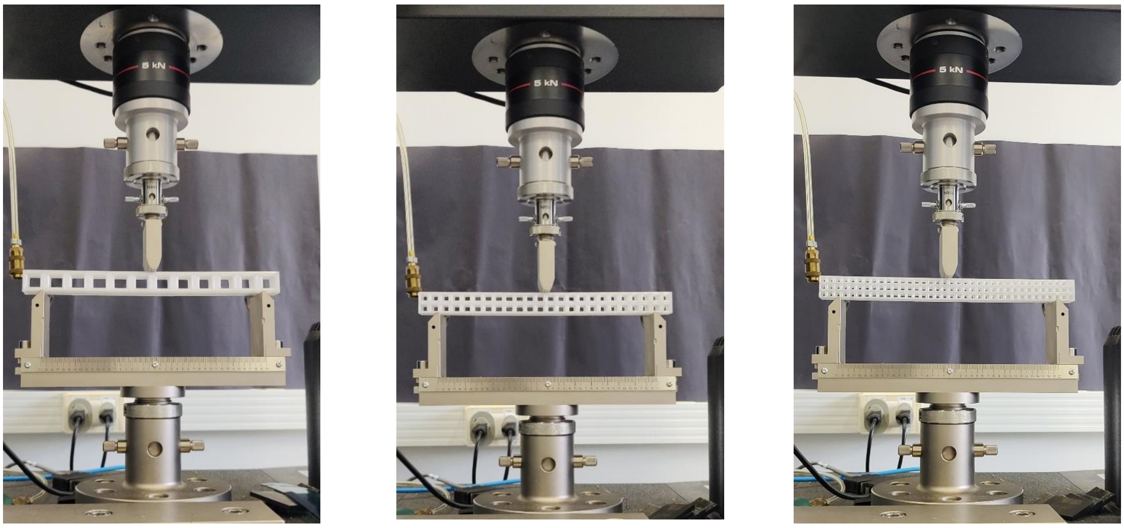

(a) UC Size 1.
(b) UC Size 2.
(c) UC Size 3.

Source: The author.

9.2 Modelling strategies for numerical simulation of the three-point bending test

Computational modelling is carried out through numerical simulations in an in-house FEM code using a computer with an Intel® Xeon® E5-2650 v4 processor, consisting of 24 physical cores (48 virtual cores) and 125 GiB of RAM, which was used to conduct the numerical analyses. Initially, conventional simulations were conducted by full-scale DNS models, where the architected structure is represented in detail through an arrangement of unit cells. Afterwards, coupled multi-scale FE^2 simulations, incorporating first- and second-order computational homogenisation, were performed employing the unit cell model as an RVE descriptive of the underlying architected microstructure.

All simulations were conducted under the assumption of finite strains within a geometrically nonlinear setting. The matrix material was modelled using a hyperelastic constitutive law driven by the Eulerian logarithmic strain tensor, as described in Equations (5.2) and (5.3). The elastic constitutive behaviour is assumed for the architected solids, i.e., inelastic phenomena are not considered in the simulations.

9.2.1 DNS – Direct Numerical Simulations

The geometry of the DNS models for the architected structures consists of an arrangement of periodic unit cells. Four different DNS models of lattice beams were used in the three-point bending numerical tests: (I) DNS model with UC size 1, containing 12 unit cells (12x1x1), (II) DNS model with UC size 2, containing 96 unit cells (24x2x2), (III) DNS model with UC size 3, containing 324 unit cells (36x3x3), and (IV) DNS model with UC size 4, containing 768 unit cells (48×4×4). Therefore, the structures are made of unit cells with different sizes ($l_\mu = 20$ mm, $l_\mu = 10$ mm, $l_\mu = 6.67$ mm and $l_\mu = 5.00$ mm), following the 3D-printed models (see Figures 137 and 139) with the addition of a smaller unit cell size. However, memory limitations of the computer used for processing the numerical simulations did not allow the simulation of the full DNS model with UC size 4, revealing a drawback of full-scale simulations for architected structures with finer unit cell arrangements. Therefore, symmetry conditions on the x-y and y-z planes were imposed on this DNS model to reduce the computational cost, resulting in 192 unit cells (24×4×2).

The H20 element with 8 integration points were used for mesh discretisation of DNS models into finite elements. Figures 144 and 145 illustrate the mesh of the DNS models with UC size 1, for the triangular and square lattice beams, respectively. The details of the finite element meshes for all DNS models are provided in Tables 40 and 41. Regarding the loading programme applied to the lattice beams, a prescribed vertical displacement of $u_0 = 6.0$ mm is imposed in 10 equally-spaced increments, simulating the load cell used in the experimental test.

Figure 144 – Finite element mesh of DNS model with UC size 1 ($l_\mu = 20.00$ mm), for the triangular lattice beam, with $L_x = 240$ mm, $L_s = 200$ mm, and $L_y = L_z = 20$ mm: mesh composed of 8160 elements (H20) and 46274 nodes.

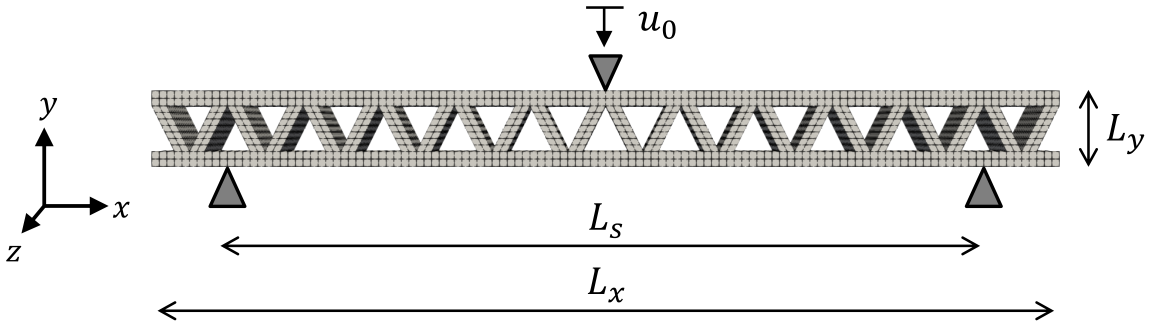

Source: The author.

Table 40 – Mesh data (H20 element) for DNS models composed of triangular cross-section unit cells.

DNS	**Elements**	**Nodes**
Model 1 - Size 1	8160	46274
Model 2 - Size 2	65280	341995
Model 3 - Size 3	220320	1123324
Model 4 - Size 4*	130560	669069

* with symmetry conditions in the x-y and y-z planes

Source: The author.

Figure 145 – Finite element mesh of DNS model with UC size 1 ($l_\mu = 20.00$ mm), for the square lattice beam, with $L_x = 240$ mm, $L_s = 200$ mm, and $L_y = L_z = 20$ mm: mesh composed of 7680 elements (H20) and 41561 nodes.

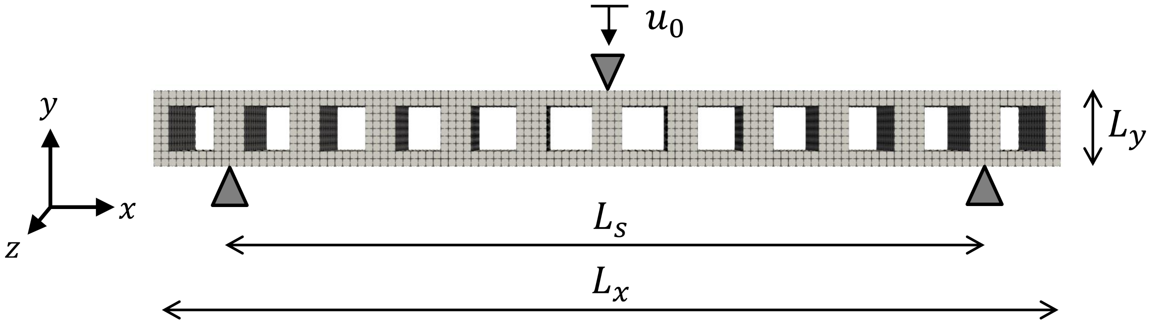

Source: The author.

Table 41 – Mesh data for DNS models composed of square cross-section unit cells.

DNS	**Elements (H20)**	**Nodes**
Model 1 - Size 1	7680	41561
Model 2 - Size 2	61440	304881
Model 3 - Size 3	207360	998761
Model 4 - Size 4*	122880	594841

* with symmetry conditions in the x-y and y-z planes

Source: The author.

9.2.2 FE^2 – Multi-scale simulations based on first- and second-order homogenisation

Coupled multi-scale approaches based on first- and second-order computational homogenisation were also explored for the numerical modelling of the mechanical behaviour of architected structures. Figures 146 and 147 present illustrative schemes of multi-scale modelling for three-point bending tests, incorporating geometry, dimensions, and boundary conditions. It is important to note that the RVE size has no influence on first-order multi-scale simulations. On the other hand, a scale parameter is naturally incorporated into the second-order multi-scale formulation presented by Santos *et al.* (2024). To evaluate the influence of the size effect, six different RVE sizes (equivalent to the unit cell sizes) were considered at second-order multi-scale simulations: (i) Size 1 ($l_\mu = 20.00$ mm), (ii) Size 2 ($l_\mu = 10.00$ mm), (iii) Size 3 ($l_\mu = 6.67$ mm), (iv) Size 4 ($l_\mu = 5.00$ mm), (v) Size 5 ($l_\mu = 3.33$ mm), and (vi) Size 6 ($l_\mu = 2.50$ mm). In this study, the multi-scale simulations enabled the analysis of more RVE sizes for lattice beams compared to DNS models that were limited to sizes 1–4 due to computer memory constraints.

Figure 146 – Multi-scale scheme for determining the homogenised macroscopic behaviour of lattice beams ($L_x = 240$ mm, $L_s = 200$ mm, and $L_y = L_z = 20$ mm) with a triangular cross-section RVE.

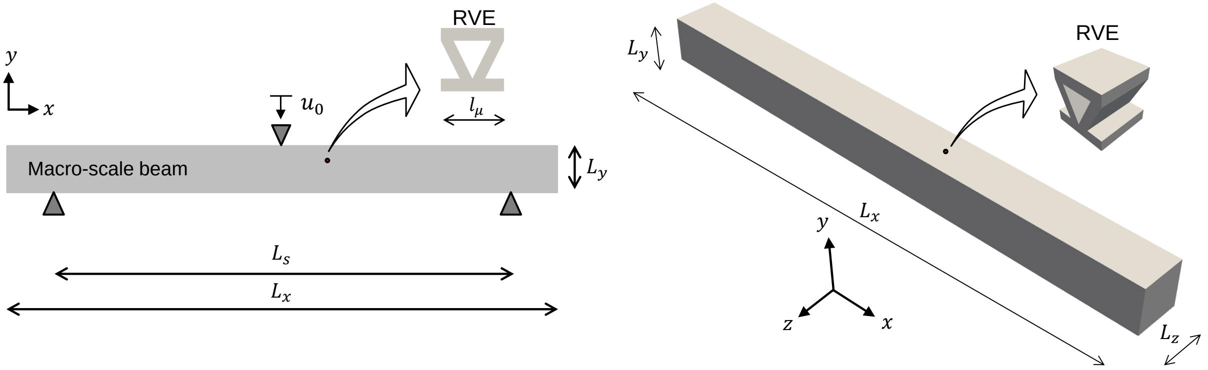

Source: The author.

Figure 147 – Multi-scale scheme for determining the homogenised macroscopic behaviour of lattice beams ($L_x = 240$ mm, $L_s = 200$ mm, and $L_y = L_z = 20$ mm) with a square cross-section RVE.

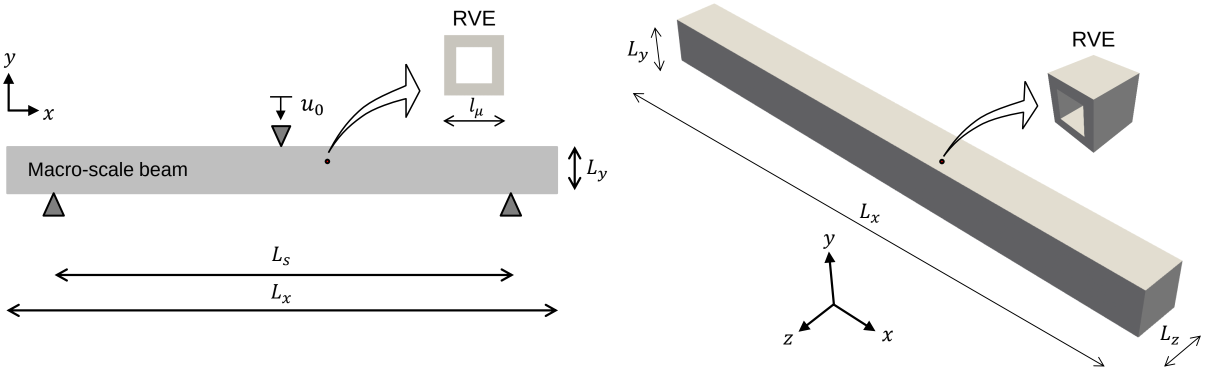

Source: The author.

FE^2 multi-scale analyses require finite element simulations at both the macro-scale and micro-scale. First-order coupled multi-scale analyses are conducted using macro- and micro-level meshes composed of H20 elements. On the other hand, second-order coupled multi-scale analyses require C^1 continuity to address the second-gradient equilibrium problem. Thus, the mixed finite element H20F8L1 was adopted (see more detais in Lopes (2019), Lopes and Pires (2022a)). Furthermore, the micro-scale is still adopted as a classical continuum, allowing to use H20 elements for RVEs in second-order multi-scale analyses. Details of the macroscopic meshes are shown in Figure 148, while the RVE mesh data are presented in Figures 149 and 150. In particular, two meshes are defined at the macro-scale to assess the convergence of the numerical results. The micro-scale meshes have characteristics similar to those defined for the unit cells in the DNS models. A preliminary study using more refined micro-scale meshes revealed minimal impact on the numerical results. In the numerical simulation, the loading program was defined by applying a total prescribed displacement of $u_0 = 6.0$ mm divided into 10 increments.

Figure 148 – Meshes studied at the macro-scale for multi-scale simulations.

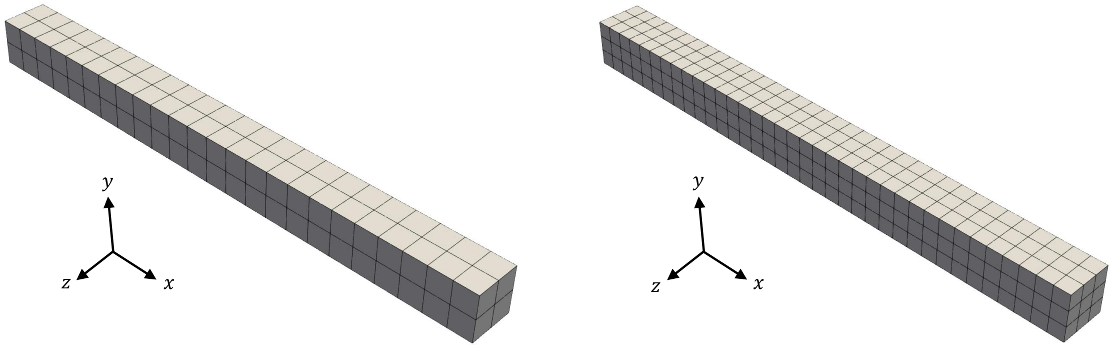

(a) Macro mesh composed of 96 elements (H20 or H20F8L1) and 741 nodes.

(b) Macro mesh composed of 324 elements (H20 or H20F8L1) and 2056 nodes.

Source: The author.

Figure 149 – RVE with a triangular cross-section: geometry and mesh composed of 680 elements (H20) and 4012 nodes).

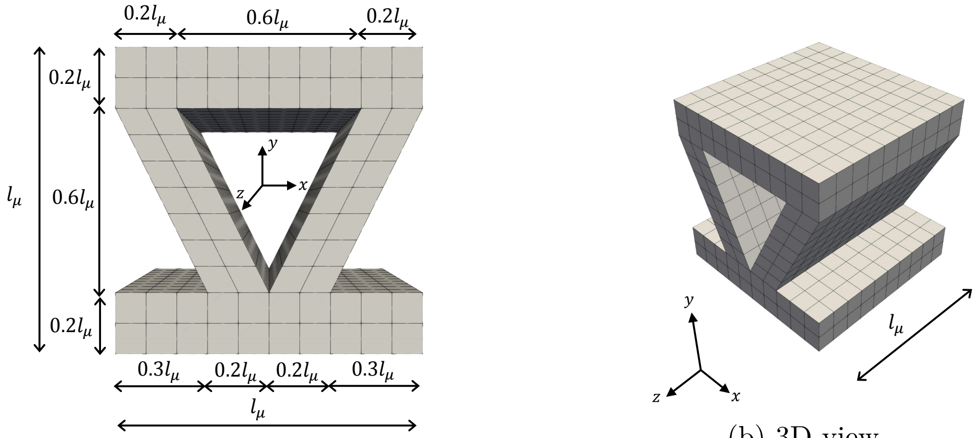

(a) Front view.

(b) 3D view.

Source: The author.

Figure 150 – RVE with a square cross-section: geometry and mesh composed of 640 elements (H20) and 3776 nodes.

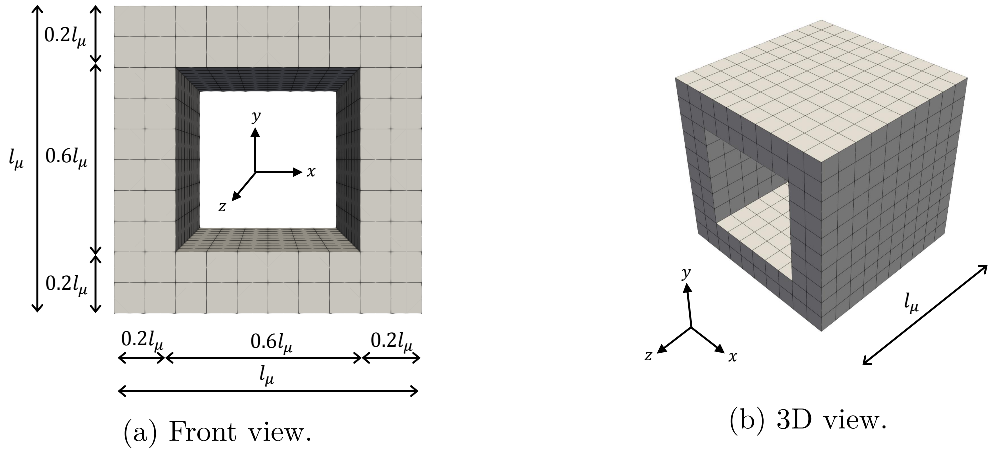

(a) Front view.

(b) 3D view.

Source: The author.

The following multi-scale models were employed in the simulations: (i) first-order approach: uniform traction boundary condition and periodic boundary displacement fluctuations; (ii) second-order approach: minimal constraint and periodic constraint. Since upper bound models are too restrictive, the multi-scale models of linear boundary displacement (first-order theory) and direct constraint (second-order theory) were not explored in this work, contributing to reduce the amount of three-dimensional multi-scale simulations.

9.3 Results

This section presents the experimental and numerical results obtained for three-point bending of lattice beams, with particular focus on size effects. For the experimental results, in addition to the reaction-displacement curves, the failure mode is also analysed. The numerical predictions obtained with DNS are briefly compared with the experimental data before failure. Finally, the FE^2 results are reported for different macroscopic finite element meshes, different formulations (first and second-order homogenisation), and for different RVE boundary conditions.

9.3.1 Experimental results

9.3.1.1 Triangular lattice

Figure 151 depicts the experimental curves of reaction force versus prescribed displacement (R–u_0) for 3D-printed lattice beams with a triangular cross-section. This experimental mechanical behaviour is presented for all the manufactured specimen configurations, with UC sizes 1, 2, and 3. In particular, an approximately linear R–u_0 relationship is observed in the experimental results up to $u_0 = 6$ mm, which justifies the elastic behaviour assumption taken in the numerical models. Moreover, different values of reaction force are observed at the same level of prescribed displacement for each case size. At $u_0 =$ 6 mm, the lattice beam with size 1 has superior stiffness, the structure with size 3 is more flexible. Therefore, the experimental investigation indicates that this type of architected structure exhibits the so-called size effect.

On the other hand, the experimental results up to rupture highlight the complexity of the mechanical behaviour of the lattice beams with a triangular cross-section, manufactured by 3D printing using the FDM technique. In the context of failure analysis, the architected structures of size 1 exhibit superior stiffness and strength, although they show lower ductility. The lattice beams of size 2 display intermediate stiffness, along with lower strength and ductility. Finally, the structures of size 3 exhibit lower stiffness, intermediate strength, and enhanced ductility. Figure 152 shows the lattice beams with a triangular cross-section unit cells near rupture in the three-point bending experimental tests, where the curvature associated with the bending is visible. Furthermore, Figure 153 presents the beams after rupture in the experimental tests. The failure occurs near the centre of the architected structure, where the load cell was positioned to apply the prescribed displacement. At around $u_0 = 10$ mm, the lattice beam of size 3 exhibited local buckling in the region of the load cell, which led to localised deformations and contributed to a more ductile rupture compared to the other cases (size 1 and size 2). It is worth noting that no strain localisation was observed in the regions near the lower supports.

Table 42 shows the average reaction force results at a prescribed displacement of 6 mm. Although only three specimens of each case size were tested in the laboratory, the low standard deviation and coefficient of variation values indicate good representativeness of the results. Therefore, the 3D printing process using the FDM technique provided good reproducibility of the architected structures in terms of mechanical behaviour.

Figure 151 – Experimental results of the mechanical behaviour, considering the reaction force and the prescribed displacement (R - u_0) for triangular-shaped cross-section structures of size 1, size 2, and size 3 (with # indicating the specimen for each structure).

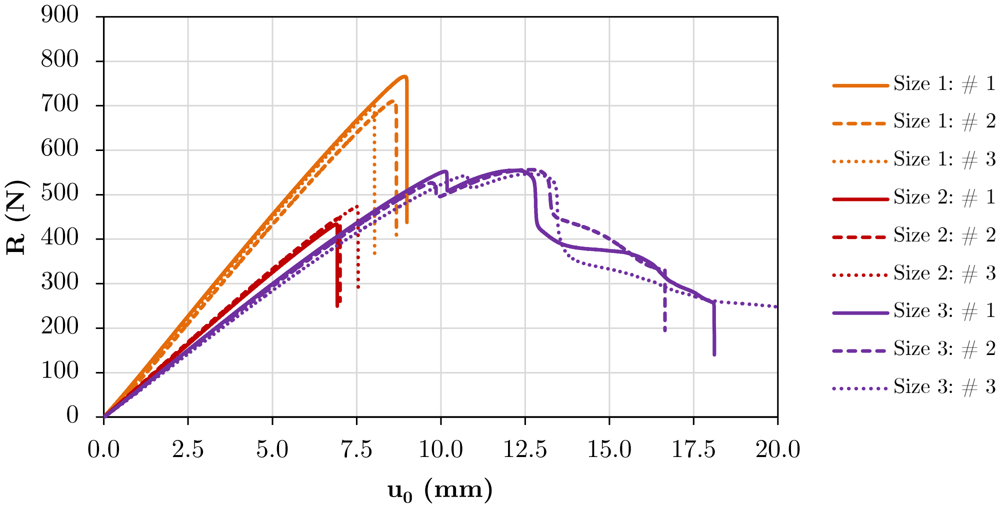

Source: The author.

Figure 152 – Architected structures with triangular-shaped cross-section close to rupture in the three-point bending experimental tests.

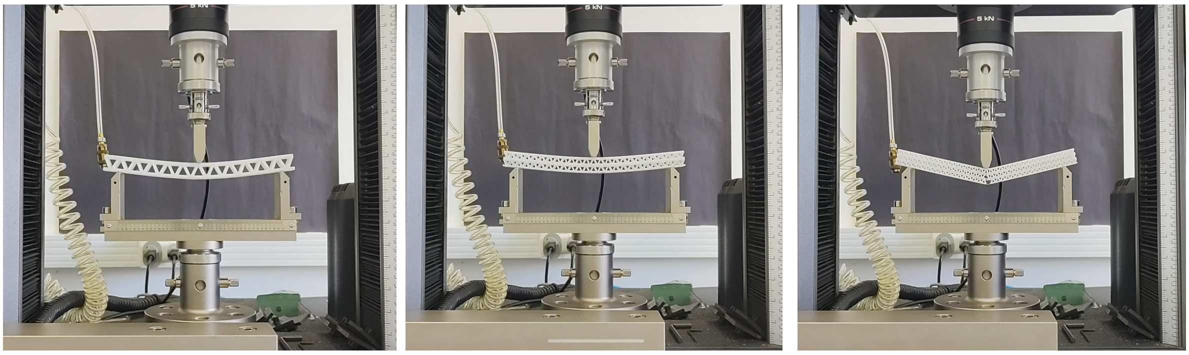

(a) Beam with size 1. (b) Beam with size 2. (c) Beam with size 3.

Source: The author.

Figure 153 – Triangular-shaped cross-section beams after failure in the three-point bending experimental tests.

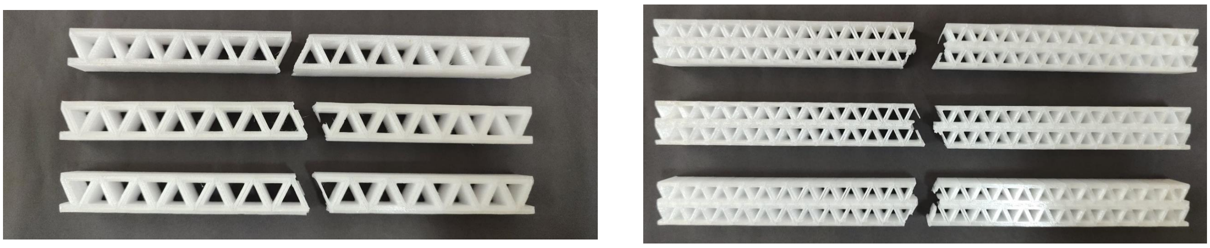

(a) Beams with size 1 broken. (b) Beams with size 2 broken.

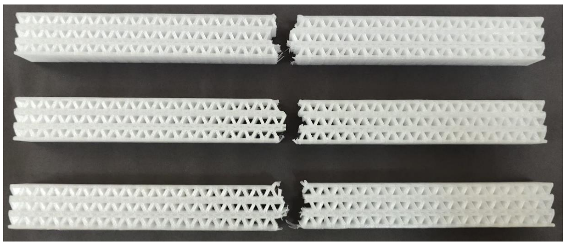

(c) Beams with size 3 broken.

Source: The author.

Table 42 – Averaged experimental reaction force (R), including SD and CV, for triangular-shaped lattice beams considering $u_0 = 6.0$ mm.

Configuration	**Specimen ID △**	$R_{\#}$ **(N)**	R **(N)**	**SD (N)**	**CV**
Size 1	# 1	542.35	532.12	12.42	2.33%
	# 2	518.30			
	# 3	535.71			
Size 2	# 1	386.08	390.68	4.15	1.06%
	# 2	394.12			
	# 3	391.84			
Size 3	# 1	355.96	348.02	9.16	2.63%
	# 2	350.10			
	# 3	337.99			

Source: The author.

9.3.1.2 Square lattice

Figure 154 presents the experimental mechanical behaviour (R versus u_0) of 3D-printed square lattice beams with UC sizes 1, 2, and 3. The size effect is also evident in the lattice beams, as different reaction force values are observed for the same level of prescribed displacement (e.g., see results up to $u_0 = 6$ mm). In summary, decreasing the unit cell size results in architected structures with reduced stiffness, strength, and ductility. The experimental data indicate curves with an approximately linear behaviour between R and u_0. The curvature associated with bending can be observed in Figure 155, which shows the lattice beams nearing rupture during the experimental tests. As shown in Figure 156, the failure occurs near the middle of the architected structures. In this case, no strain localisation was observed in the lower regions of the supports or in the upper region corresponding to the position of the load cell.

Figure 154 – Experimental results of the mechanical behaviour, considering the reaction force and the prescribed displacement (R - u_0) for square-shaped cross-section structures with size 1, size 2 and size 3 (with # denoting the specimen for each structure).

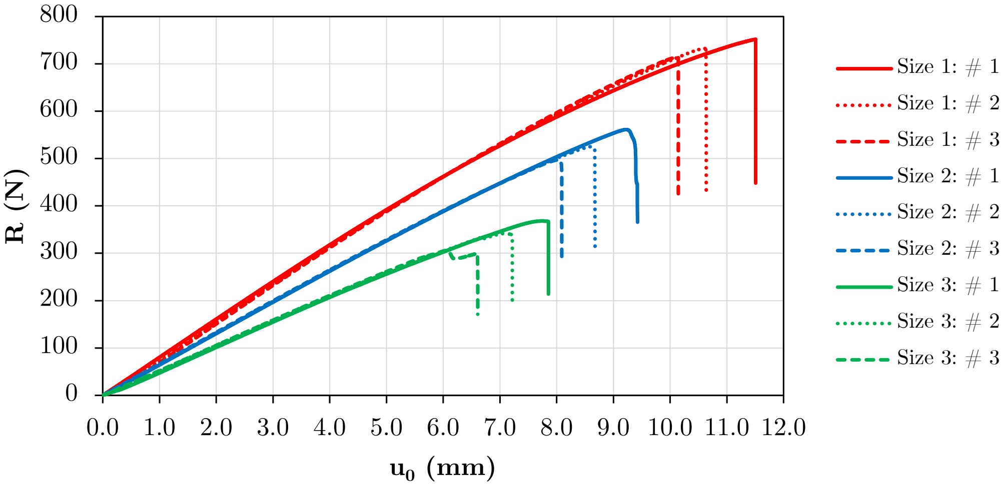

Source: The author.

Figure 155 – Architected structures with square-shaped cross-section close to rupture in the three-point bending experimental tests.

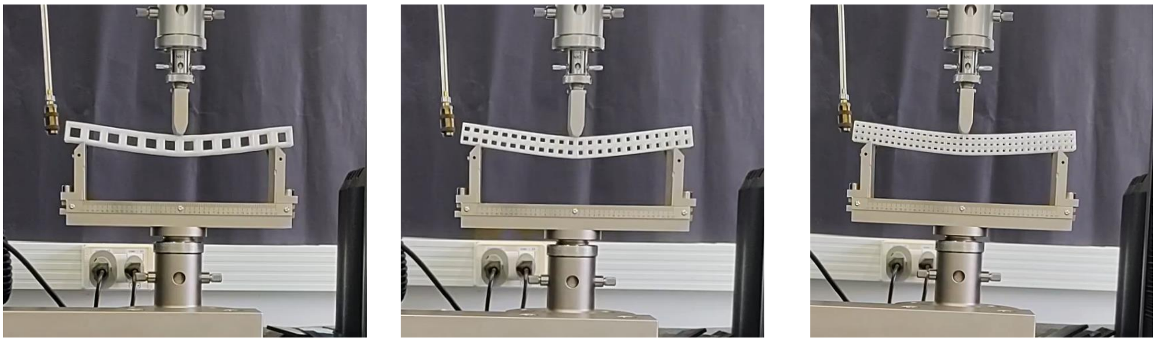

(a) Beam with size 1.
(b) Beam with size 2.
(c) Beam with size 3.

Source: The author.

Figure 156 – Square-shaped cross-section beams after failure in the three-point bending experimental tests.

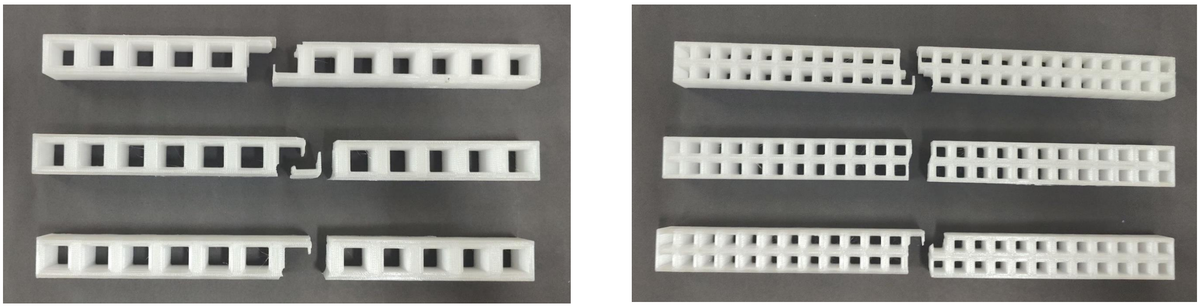

(a) Beams with size 1 broken.

(b) Beams with size 2 broken.

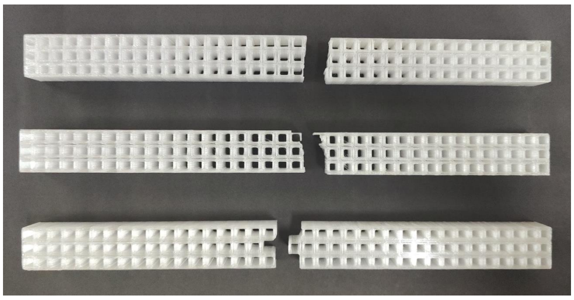

(c) Beams with size 3 broken.

Source: The author.

The average reaction force value at a displacement of 6 mm is presented in Table 43. Similar to the triangular lattice beam, only three specimens have been tested for each size but low scatter is obtained in the results. Hence, good reproducibility of the results is also verified in this case.

Table 43 – Averaged experimental reaction force (R), encompassing SD and CV, for square-shaped lattice beams considering u_0 = 6.0 mm.

Configuration	**Specimen ID □**	$R_{\#}$ (N)	R (N)	**SD (N)**	**CV**
Size 1	# 1	461.97	461.73	0.22	0.05 %
	# 2	461.54			
	# 3	461.69			
Size 2	# 1	388.56	388.97	0.56	0.14 %
	# 2	388.75			
	# 3	389.61			
Size 3	# 1	302.76	304.31	0.94	0.31 %
	# 2	304.45			
	# 3	304.31			

Source: The author.

9.3.2 DNS results

The mechanical behaviour of the DNS models composed of unit cells with triangular and square cross-sections is shown in Figures 157 and 158, respectively. Note that different unit cell sizes result in distinct reaction force values, where the reduction in unit cell size leads to lower reaction force values. Therefore, the size effect is captured through numerical simulations of lattice beams using DNS models. Moreover, the mechanical behaviour demonstrates a linear relationship between the reaction force and the prescribed displacement for all cases, revealing that nonlinear geometric effects are not significant for lattice beams under bending. Finally, it is worth mentioning the high computational cost as a disadvantage of DNS models, particularly associated with memory demand, which made simulations of lattice beams with smaller unit cell lengths unfeasible due to the limitation of the processing computer.

Figure 157 – Mechanical behaviour (R - u_0) for DNS models composed of triangular cross-section unit cells with sizes 1, 2, 3 and 4.

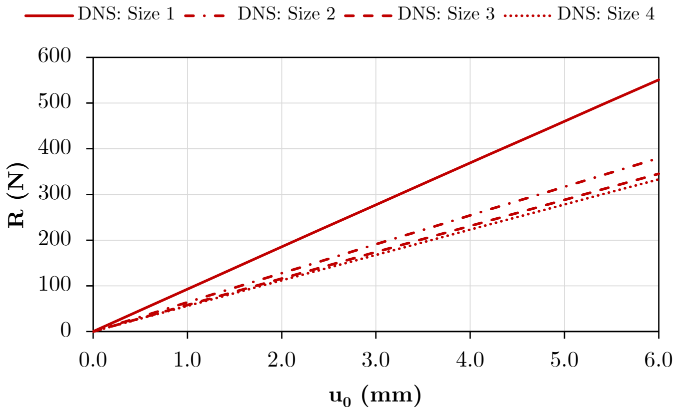

Source: The author.

Figure 158 – Mechanical behaviour (R - u_0) for DNS models composed of square cross-section unit cells with sizes 1, 2, 3 and 4.

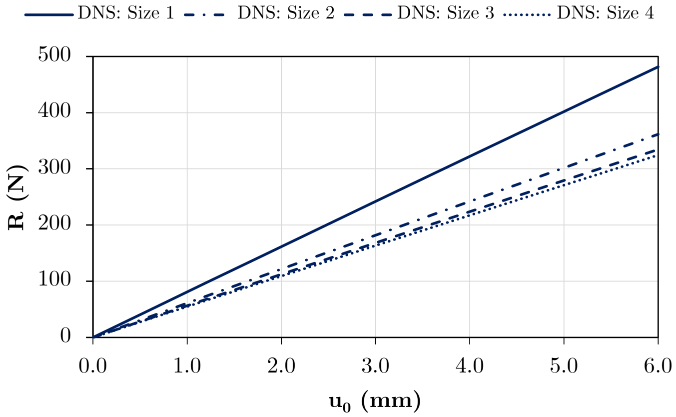

Source: The author.

9.3.3 Multi-scale results

9.3.3.1 Macro-scale mesh convergence

Initially, it is important to assess the convergence of numerical responses in FE^2 multi-scale simulations with respect to the finite element mesh. Tables 44 and 45 present a comparison of the reaction force results for the two investigated macro-scale meshes. In the context of second-order multi-scale simulations, a mesh refinement study was conducted for RVE size 3. Since first-order multi-scale analyses are independent of the RVE length, the mesh refinement investigation of such models is applicable to all RVE sizes. Overall, meshes 1 and 2 yield reaction forces that are in close agreement, as demonstrated by the small relative differences observed between the meshes. Therefore, to reduce the computational cost of the multi-scale analyses, mesh 1 was selected for obtaining the remaining numerical results of the lattice beams under bending.

Table 44 – Mesh refinement study assessing R for beams ($u_0 = 6.0$ mm) composed of RVEs with a triangular cross-section.

	R (N)		
Multi-scale model	**Mesh 1**	**Mesh 2**	**Differences**
Second-order: Periodic - Size 3	386.37	380.56	1.50%
Second-order: Minimal - Size 3	370.64	364.54	1.65%
First-order: Periodic - All sizes	321.47	320.57	0.28%
First-order: Uniform traction - All sizes	269.49	266.72	1.03%

Source: The author.

Table 45 – Mesh refinement study assessing R for beams ($u_0 = 6.0$ mm) of RVEs with a square cross-section.

	R (N)		
Multi-scale model	**Mesh 1**	**Mesh 2**	**Differences**
Second-order: Periodic - Size 3	378.07	374.74	0.88%
Second-order: Minimal - Size 3	186.82	182.54	2.29%
First-order: Periodic - All sizes	314.35	313.41	0.30%
First-order: Uniform traction - All sizes	122.32	122.03	0.23%

Source: The author.

9.3.3.2 Size effect, multi-scale formulation and type of RVE constraint

Figures 159 and 160 show the mechanical behaviour (R - u_0) of the architected structures from multi-scale simulations, obtained with both first and second-order homogenisation, encompassing different RVE sizes and underlying type of constraint. Since the numerical results reveal a linear relationship between R and u_0, geometric nonlinear effects appear to be negligible for the lattice beams under bending. As expected, due to the scale parameter introduced in the formulation, the second-order multi-scale models exhibit mechanical behaviour with a size effect. In summary, increasing the RVE size leads to higher reaction forces for a given level of prescribed displacement. For smaller RVE sizes, the numerical results indicate a convergence of the second-order multi-scale models towards the first-order multi-scale models. The type of microscopic constraint also plays a role, with the uniform traction and minimal constraints providing responses that are more compliant, compared to the periodic conditions. A more detailed analysis is provided in Section 9.4.

Figure 159 – Multi-scale predictions of the mechanical behaviour (R - u_0) of triangular lattice beams with UC sizes 1 to 6.

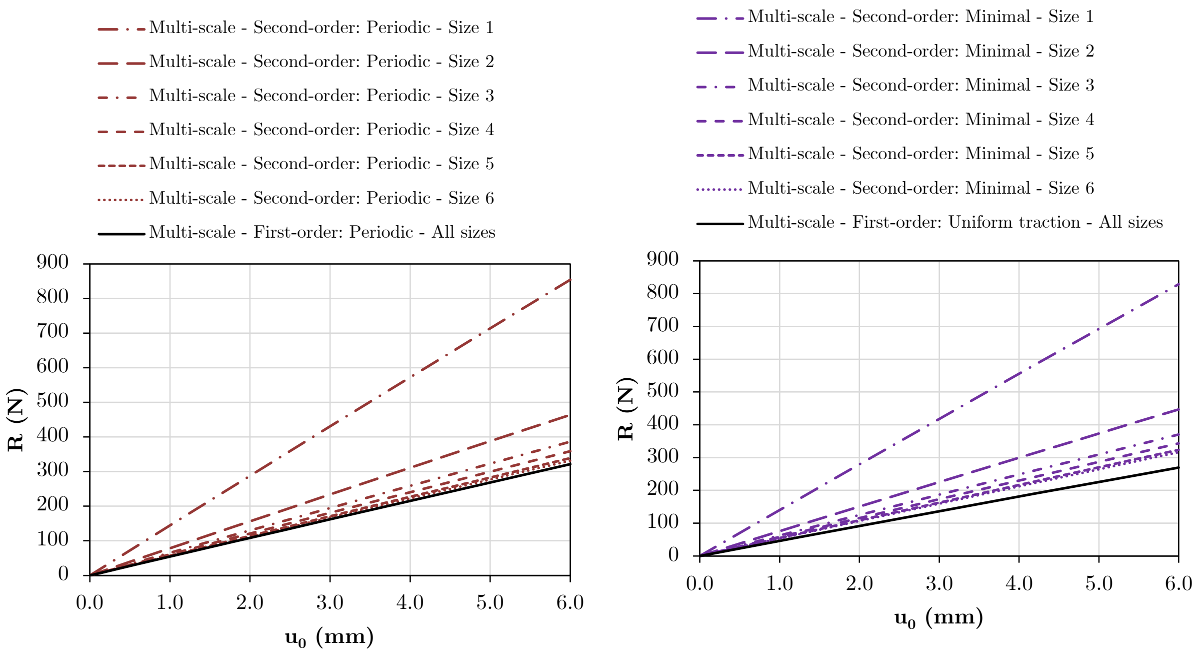

(a) First- and second-order periodic models.

(b) First-order uniform traction model and second-order minimal model.

Source: The author.

Figure 160 – Multi-scale predictions of the mechanical behaviour (R - u_0) of square lattice beams with UC sizes 1 to 6.

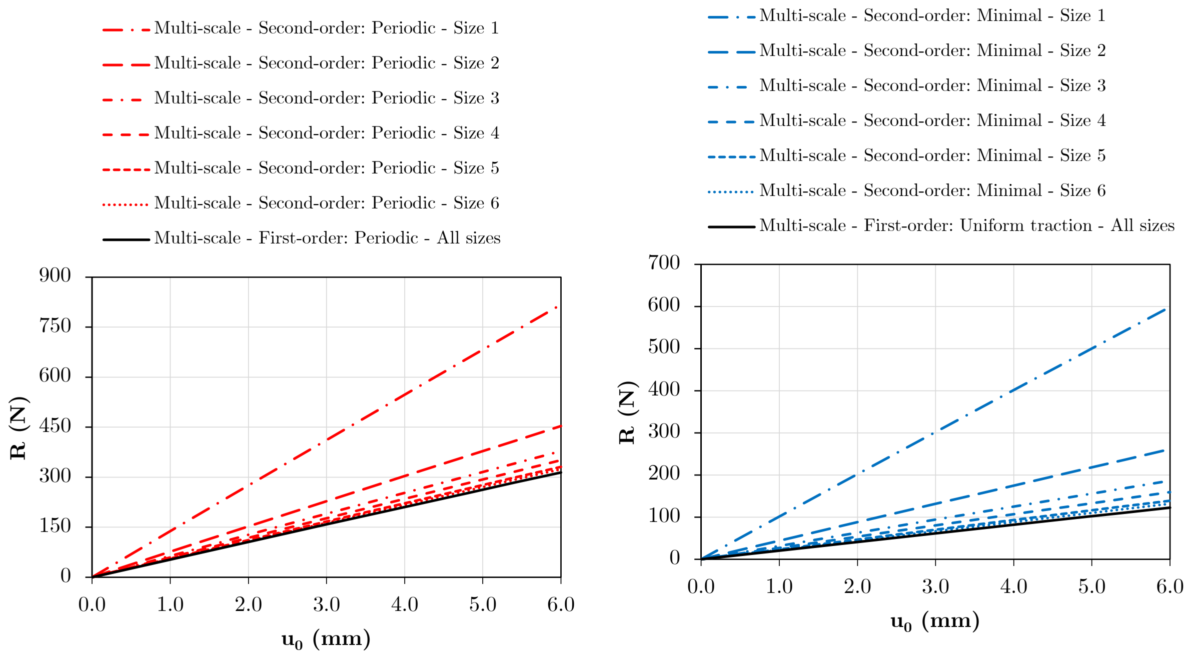

(a) First- and second-order periodic models.

(b) First-order uniform traction model and second-order minimal model.

Source: The author.

9.4 Discussion of the results

9.4.1 Influence of unit cell on the experimentally observed size effects

In this section, the size effects observed in the experimental results are discussed, considering the influence of the lattice structure morphology. To that end, the experimental reaction force obtained for an enforced displacement of 6 mm, in the three-point bending tests, is analysed with respect to unit cell size (R versus unit cell length) and architecture of the lattice structure in Figure 161. It is observed that the triangular lattice beam exhibits a linear relationship between R and the unit cell size, whereas this relationship is non-linear for the square lattice beam. Two possible reasons are hypothesised for this difference: (i) the non-linearity is introduced by the geometry of the unit cell or (ii) it is due to the effects of the manufacturing process, such as some anisotropy caused by the printing directions. The analysis of the numerical results will shed some light on this topic.

Figure 161 – Size effect experimental study (R versus unit cell length) considering $u_0 = 6.0$ mm: triangular and square-shaped lattice beams.

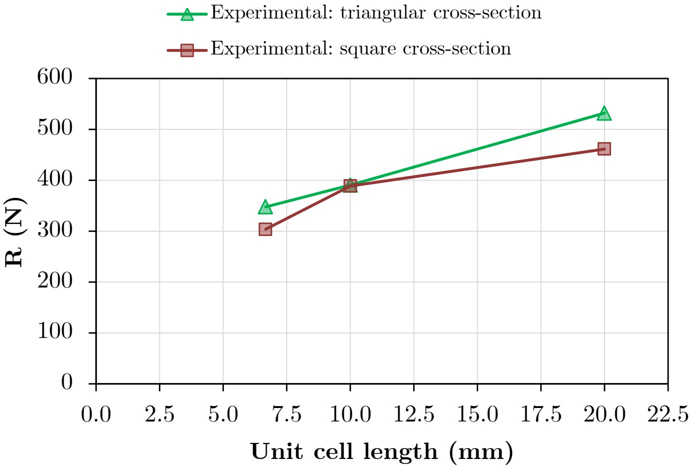

Source: The author.

9.4.2 Comparison of DNS predictions with experimental results

DNS results and experimental data for lattice beams composed of triangular cross-section unit cells are compared in Figure 162, with the reaction obtained at a displacement of 6 mm for different unit cell sizes. Table 46 shows a comparison in more detail, including relative differences in modulus (Differences). The comparative study reveals that the DNS predictions are in close agreement with the experimental data, with relative differences lower than 3.5%, demonstrating the robust predictive capability of the full-scale models to capture the size effect in lattice structures. The relationship between reaction and unit cell size predicted with DNS is approximately linear, as observed in the experiments. Even though for the lowest unit cell size there is no experimental data, the predicted response follows the trend.

Regarding the square lattice beams, DNS results are compared with experimental data in Figure 163 and Table 47. Overall, the numerical results of the DNS models are close to the experimental data, although some differences in responses are observed, with larger relative errors, compared to the triangular lattice. DNS predicts an approximately linear relationship for the size effect, which differs from the experimental results. Therefore, considering the hypotheses introduced in Section 9.4.1, it may be concluded that the non-linear relationship observed in the experiments is not due to the geometrical effects, otherwise these would be captured by the simulation. This may indicate that the manufacturing process significantly influences the experimental investigation of architected structures with different unit cell sizes. Thus, differences in results can be attributed to the anisotropy induced by the 3D printing process, as well as uncertainties arising from material characterisation.

Figure 162 – Size effect study (R versus unit cell length) for triangle cross-section structures considering $u_0 = 6.0$ mm: experimental results versus DNS predictions.

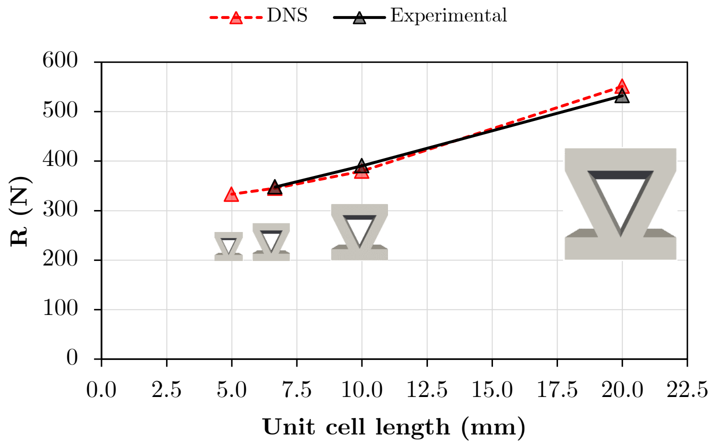

Source: The author.

Figure 163 – Size effect study (R versus unit cell length) for lattice beams with square cross-section considering $u_0 = 6.0$ mm: experimental results versus DNS predictions.

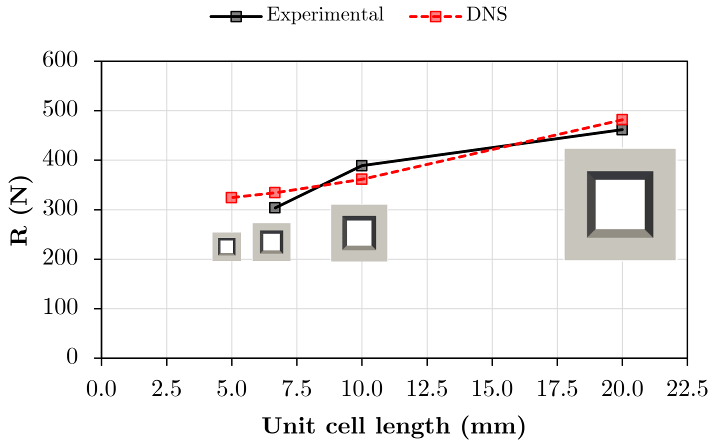

Source: The author.

Table 46 – Comparison of reaction force for triangular cross-section lattice structures considering $u_0 = 6.0$ mm.

	R (N)		Differences
Unit cell	**Experimental (1)**	**DNS model (2)**	**(2) to (1)**
Size 1	532.12	551.03	3.55%
Size 2	390.68	379.59	2.84%
Size 3	348.02	345.39	0.76%
Size 4	–	333.17	–

Source: The author.

Table 47 – Comparison of reaction force for square cross-section lattice structures considering $u_0 = 6.0$ mm.

	R (N)		Differences
Unit cell	**Experimental (1)**	**DNS model (2)**	**(2) to (1)**
Size 1	461.73	481.68	4.32%
Size 2	388.97	361.43	7.08%
Size 3	303.84	334.35	10.04%
Size 4	–	324.45	–

Source: The author.

9.4.3 Multi-scale results: a comparison with experimental data and DNS predictions

Figure 164 and Table 48 show the multi-scale simulation results compared to experimental data and DNS predictions for triangular-shaped cross-section lattice beams. Furthermore, Table 49 presents a more detailed comparative analysis, including the relative differences (in modulus), between the approaches explored in this study. For the visualisation of numerical results, color maps with effective Cauchy stress and displacement magnitude for triangular-shaped cross-section lattice beams with size 3 are shown in Figures 165 and 166, respectively.

Figure 164 – Size effect study (R versus RVE length) for triangular-shaped cross-section architected structures considering $u_0 = 6.0$ mm: comparison of experimental data and DNS results with multi-scale numerical simulation outcomes.

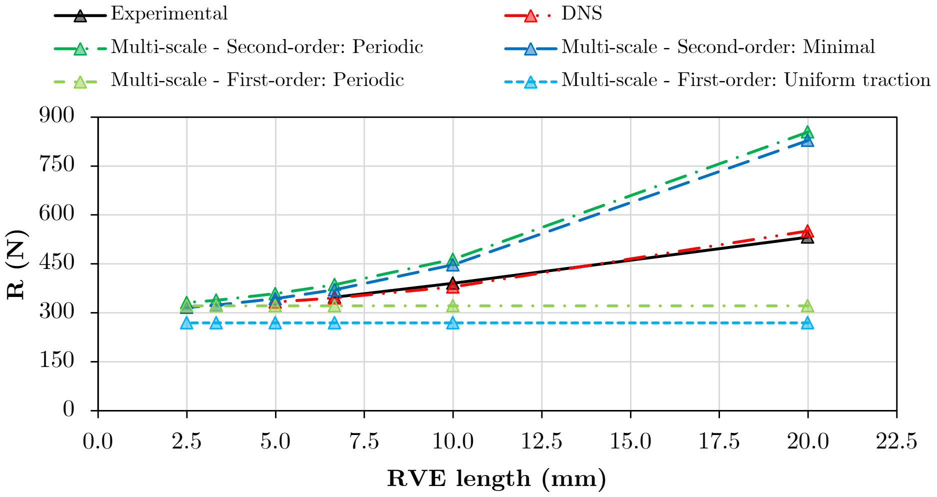

Source: The author.

Table 48 – Comparison of the reaction force (R) associated with RVE size for triangular-shaped lattice beams ($u_0 = 6.0$ mm).

Analysis type	**R (N)**					
	Size 1	**Size 2**	**Size 3**	**Size 4**	**Size 5**	**Size 6**
Experimental	532.12	390.68	348.02	–	–	–
DNS model	551.03	379.59	345.39	333.17	–	–
1^{st}-order: Periodic (Per.)	321.47	321.47	321.47	321.47	321.47	321.47
1^{st}-order: Uniform trac. (Trac.)	269.48	269.48	269.48	269.48	269.48	269.48
2^{nd}-order: Periodic (Per.)	854.41	464.10	386.37	358.64	338.62	331.55
2^{nd}-order: Minimal (Min.)	828.69	447.15	370.64	343.30	323.57	316.61

Source: The author.

Table 49 – Relative differences (in modulus) between multi-scale results, experimental data, and DNS responses for triangular-shaped lattice beams ($u_0 = 6.0$ mm).

	Differences compared to experimental				**Differences compared to DNS**			
	First-order		**Second-order**		**First-order**		**Second-order**	
Size	**Per.**	**Trac.**	**Per.**	**Min.**	**Per.**	**Trac.**	**Per.**	**Min.**
1	39.59%	49.36%	60.57%	55.73%	41.66%	51.09%	55.06%	50.39%
2	17.72%	31.02%	18.79%	14.45%	15.31%	29.01%	22.26%	17.80%
3	7.63%	22.57%	11.02%	6.50%	6.93%	21.98%	11.86%	7.31%
4	–	–	–	–	3.51%	19.12%	7.64 %	3.04%
5	–	–	–	–	–	–	–	–
6	–	–	–	–	–	–	–	–

Source: The author.

Figure 165 – Effective Cauchy stress (MPa) for different computational modeling options for triangular-shaped lattice beams with size 3 considering $u_0 = 6.0$ mm.

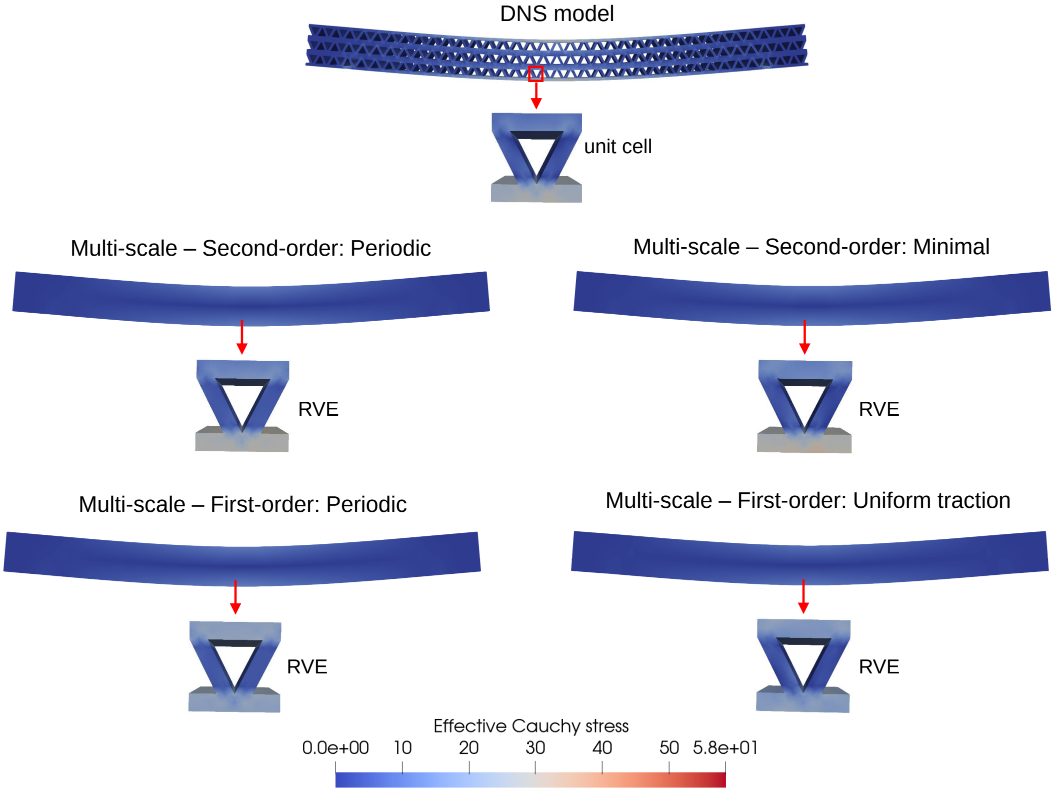

Source: The author.

Figure 166 – Displacement magnitude (mm) for different computational modeling options for triangular-shaped lattice beams with size 3 considering $u_0 = 6.0$ mm.

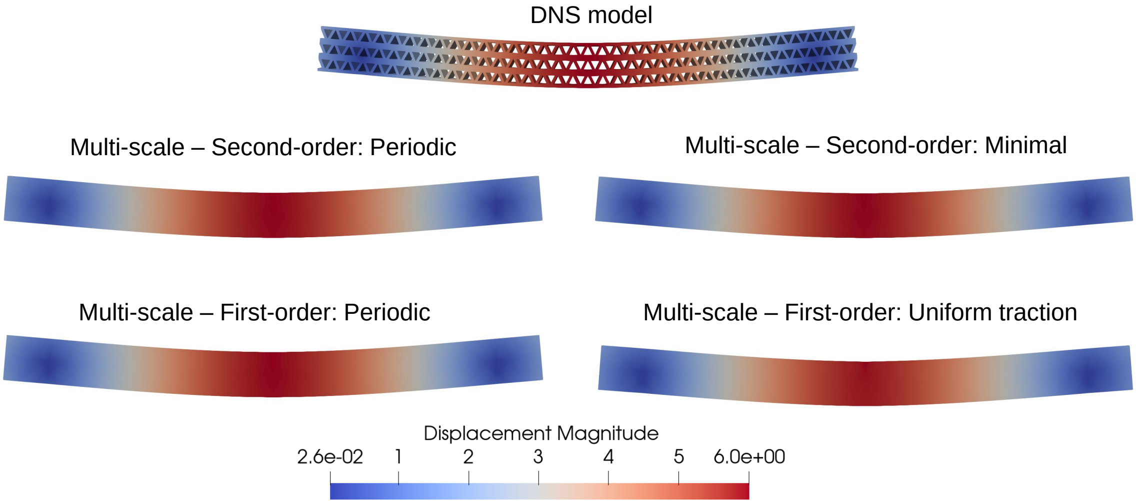

Source: The author.

In addition, taking into account the size effect investigation for square-shaped cross-section lattice beams, a comparative analysis between computational modelling approaches (multi-scale models and DNS models) and experimental data is presented in Figure 167. Numerical values and relative differences (in modulus) between the approaches are detailed in Tables 50 and 51, respectively. Color maps with effective Cauchy stress and displacement magnitude for square-shaped cross-section lattice beams with size 3 are shown in Figures 168 and 169, respectively.

Figure 167 – Size effect study (R versus RVE length) for square-shaped cross-section architected structures considering $u_0 = 6.0$ mm: comparison of experimental data and DNS results with multi-scale numerical simulation outcomes.

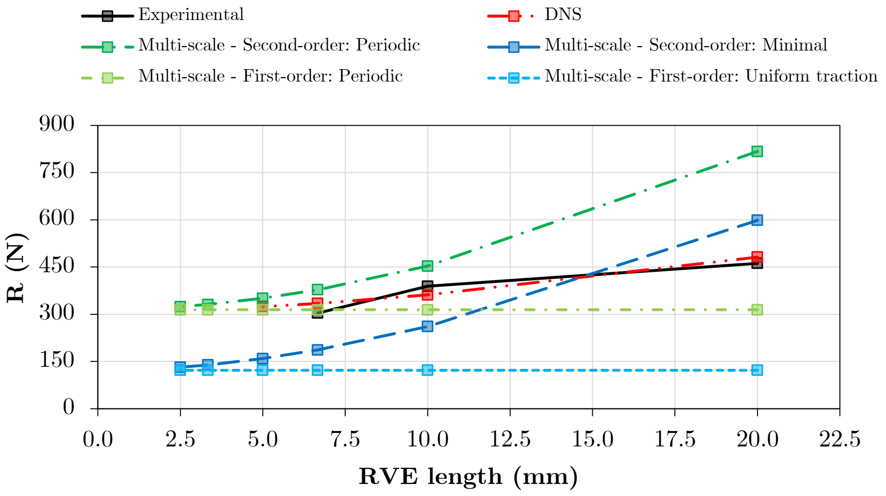

Source: The author.

Table 50 – Comparison of reaction force (R) associated with RVE size for square-shaped lattice beams ($u_0 = 6.0$ mm).

	R (N)					
Analysis type	**Size 1**	**Size 2**	**Size 3**	**Size 4**	**Size 5**	**Size 6**
Experimental	461.73	388.97	303.84	–	–	–
DNS model	481.68	361.43	334.35	324.45	–	–
1^{st}order: Periodic (Per.)	314.35	314.35	314.35	314.35	314.35	314.35
1^{st}order: Uniform trac. (Trac.)	122.32	122.32	122.32	122.32	122.32	122.32
2^{nd}order: Periodic (Per.)	817.22	453.05	378.07	350.90	331.05	323.96
2^{nd}-order: Minimal (Min)	598.71	261.17	186.82	159.34	139.11	131.89

Source: The author.

Table 51 – Relative differences (in modulus) between multi-scale results, experimental data, and DNS responses for square-shaped lattice beams ($u_0 = 6.0$ mm).

	Differences compared to experimental				**Differences compared to DNS**			
	First-order		**Second-order**		**First-order**		**Second-order**	
Size	**Per.**	**Trac.**	**Per.**	**Min.**	**Per.**	**Trac.**	**Per.**	**Min.**
1	31.92%	73.51%	76.99%	29.67%	34.74%	74.61%	69.66%	24.30%
2	19.19%	68.55%	16.47%	32.86%	13.03%	66.16%	25.35%	27.74%
3	3.46%	59.74%	24.43%	38.51%	5.98%	63.42%	13.08%	44.12%
4	–	–	–	–	3.11%	62.30%	8.15%	50.89%
5	–	–	–	–	–	–	–	–
6	–	–	–	–	–	–	–	–

Source: The author.

Figure 168 – Effective Cauchy stress (MPa) for different computational modeling options for square-shaped lattice beams with size 3 considering $u_0 = 6.0$ mm.

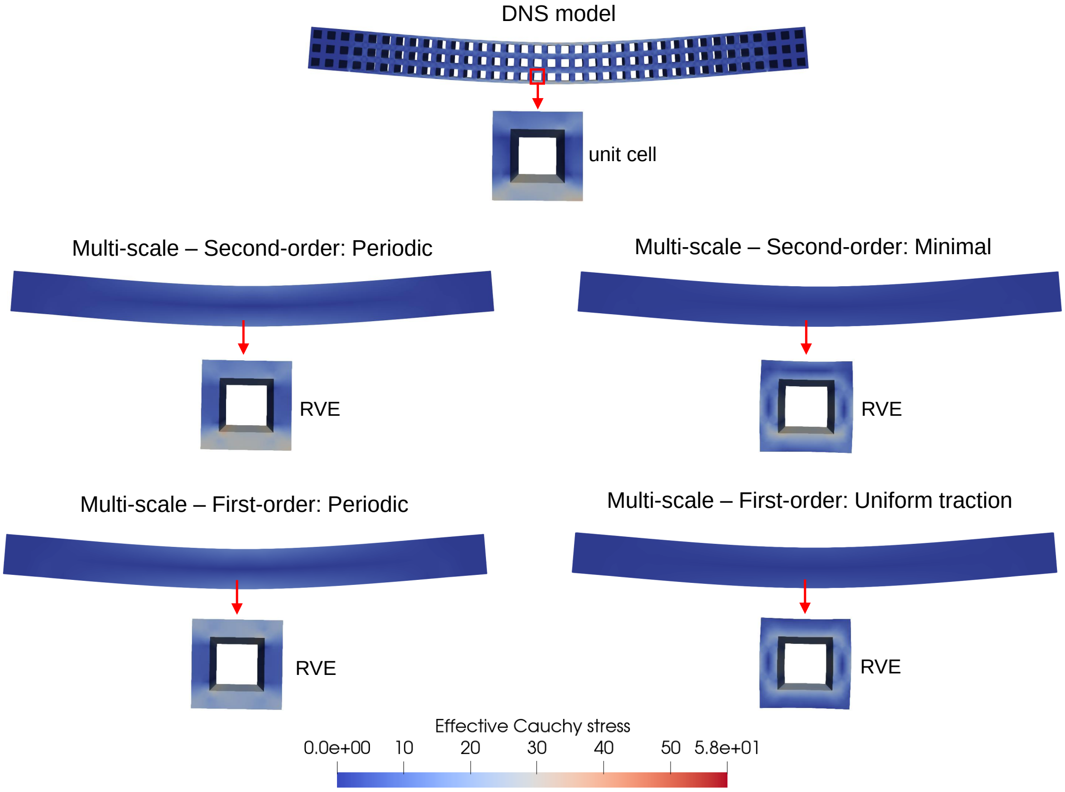

Source: The author.

Figure 169 – Displacement magnitude (mm) for different computational modeling options for square-shaped lattice beams with size 3 considering $u_0 = 6.0$ mm.

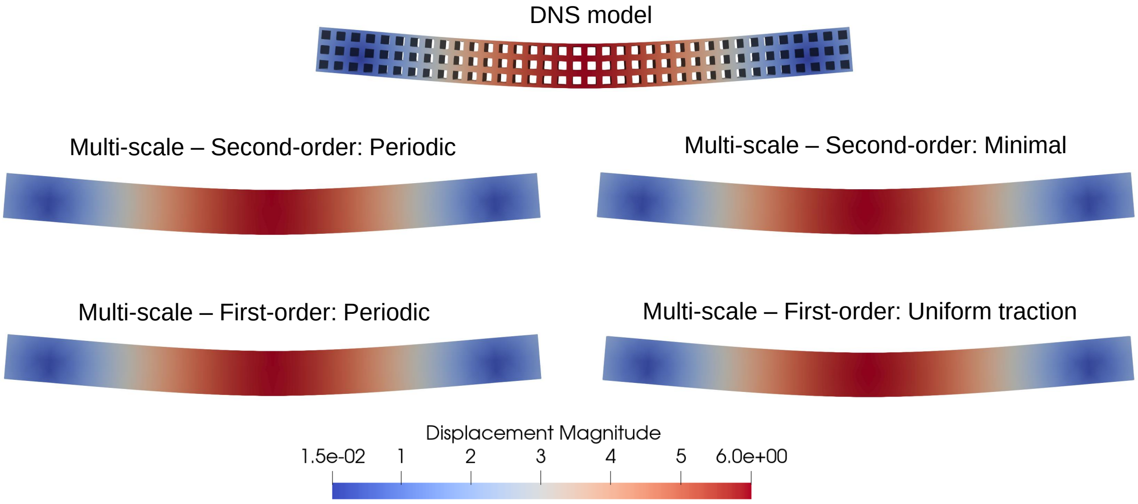

Source: The author.

Second-order multi-scale models capture the size effect, whereas first-order multi-scale models exhibit the same response regardless of the RVE size. Furthermore, it is worth highlighting that second-order multi-scale models (periodic and minimal) converge towards their corresponding first-order multi-scale models (periodic and uniform traction) for smaller RVE sizes.

The RVE morphology played an important role in the comparisons between the multi-scale models. For triangular-shaped cross-section lattice beams, second-order multi-scale models (periodic and minimal) yield similar results. The same conclusion is observed for the first-order multi-scale models (periodic and uniform traction). In fact, Figure 165 indicates a similar distribution of effective Cauchy stresses between the deformed RVEs associated with the different multi-scale models. The RVE with triangular-shaped cross-section contains a significant portion of voids on its external surface, where the boundary conditions are defined. Consequently, the reduced amount of solid material on the RVE outer boundary smoothes the influence of the boundary condition over the effective mechanical behaviour. On the other hand, significant differences are observed between the second-order multi-scale models as well as between the first-order multi-scale models for square-shaped cross-section lattice beams. This can be attributed to the substantial portion of the RVE outer boundary being composed of solid material, which increases sensitivity of the results regarding the boundary conditions. Furthermore, the differences in the distribution of the effective Cauchy stresses for the deformed RVEs (see Figure 168) help explain the discrepancy between the multi-scale models.

Larger RVE lengths result in significant differences between the experimental data and the multi-scale outcomes. For size 1 ($l_\mu = 20.00$ mm), the second-order models overestimate the reaction force, whereas the first-order models underestimate it. This occurs because the RVE length (l_μ) is not sufficiently smaller than the macro-scale characteristic length (L), thereby violating the Principle of Scale Separation. In general, multi-scale models tend to provide results more consistent with experimental data for smaller RVE sizes (size 2 and size 3), indicating that the Principle of Scale Separation is better established for the architected structure. Specifically, the numerical predictions from the second-order minimal multi-scale model are in close agreement with experimental results for triangular-shaped cross-section lattice beams. Although the size effect was not captured, the first-order periodic multi-scale model also provided good results. With regard to lattice beams with a square cross-section, the numerical results from periodic models (first- and second-order) demonstrate better agreement with the experimental data. The curvature direction and smoothness in the numerical responses also suggests that the anisotropy induced by 3D printing influenced the experimental data, where possibly the response for size 3 was excessively flexible. In addition, the minimum constraint model (second-order) and the uniform traction model (first-order) proved to be excessively flexible, failing to yield satisfactory results. Despite the lattice material displaying a size effect, the second-order approach did not show substantial advantages. This suggests that the second-order approach can be more suitable for architected materials exhibiting a pronounced size effect, such as structures with smaller thicknesses. For instance, Santos *et al.* (2024) highlights the significant advantages of the second-order multi-scale approach over the first-order multi-scale strategy in the analysis of thin-walled structures.

The multi-scale strategies provided satisfactory results compared to DNS models for coupled architected structures that adhere to the Principle of Scale Separation. In this context, the numerical results from second-order minimal and first-order periodic multi-scale models are in close agreement with DNS predictions for lattice beams with triangular cross-section. Moreover, this similarity in results is linked to the distribution of effective Cauchy stresses for the deformed RVEs in the multi-scale models and the unit cell results from the DNS model (see Figure 165). Concerning lattice beams with a square cross-section, the numerical results from the periodic multi-scale models (particularly for the first-order approach) were more aligned with the DNS responses for smaller RVE sizes. In this case, the distribution of effective Cauchy stresses in the deformed configuration of the multi-scale periodic RVEs shows good agreement with the unit cell results from the DNS model (see Figure 168).

Finally, it is worth noting that the DNS models were restricted to a size 4 due to computer memory limitations. This emphasises a drawback of DNS models, which may require an excessive number of finite elements to discretize all the unit cells in full-scale models. Unlike DNS models, RVE sizes 5 and 6 were investigated exclusively using multi-scale approaches. Since the macro and micro meshes remain the same in multi-scale simulations, the computational cost of multi-scale models does not increase significantly for smaller RVE sizes. Therefore, multi-scale strategies may offer offer advantages compared to infeasible DNS models due to their high computational cost.

9.5 Partial conclusions

The mechanical behaviour of additively manufactured architected structures under bending displaying size effects has been investigated through experimentation and computational modelling approaches, encompassing DNS finite element models and FE^2 multi-scale simulations based on first- and second-order homogenisation. Lattice beams with different unit cell morphologies were fabricated using the FDM 3D printing technique with a commercially available PETG filament. Material characterisation tests were conducted based on dumbbell-shaped specimens, allowing the determination of the elastic constitutive properties of the thermoplastic polymer.

Regarding the experimentation, the good reproducibility of the 3D-printed lattice beams was confirmed by low coefficient of variation values relative to the experimental data on the mechanical behaviour of the tested architected structures. In general, a mechanical behaviour with approximately elastic response was observed before the failure of the beams under bending. Three-point bending tests revealed the size effects on the mechanical behaviour of lattice beams, where a decrease in unit cell size leads to a reduction of the reaction force in the architected structures. Regarding the size effect study, the lattice beam with triangular cross-sectional unit cells showed an approximately linear relationship between the unit cell size and the reaction force, whereas the lattice beam with square cross-sectional unit cells exhibited a nonlinear behaviour.

DNS predictions showed good agreement with experimental data. Nevertheless, DNS models became unfeasible for lattice beams composed of unit cells with smaller sizes due to the memory limitations of the computer used for performing the numerical simulations. Since a significant number of finite elements are required to obtain the numerical results, full-scale models of architected structures with more refined unit cell arrangements were computationally expensive.

Overall, the main conclusions of the FE^2 multi-scale simulations for modelling the lattice beams under bending can be summarised as follows:

- **RVE-based multi-scale models**: The numerical results for the investigated lattice beam morphologies indicate a sensitivity of the multi-scale models with respect to the solid material portion at the outer boundary of the RVE. The results suggest a larger gap between the predictions of periodic and mininal multi-scale models for the RVE with a higher proportion of solid material on the outer boundary, and a smaller gap for the RVE with a higher proportion of voids on the outer surface. This conclusion was observed in both the second-order and first-order approaches.

- **Size effect**: Second-order multi-scale models capture the size effect in lattice beams, with numerical results converging to the corresponding first-order multi-scale models as the RVE sizes decrease. Despite capturing the size effect, the second-order multi-scale approach can not offer significant advantages compared to the classical first-order multi-scale approach. In general, the second-order strategy tends to over-estimate the effective mechanical behaviour of the architected material for larger RVE sizes. This aspect, combined with thicker lattice beams, can result in stiffer responses when compared to experimental data. On the other hand, second-order framework explored in this work can offer significant advantages for modelling thin-walled architected materials.
- **Applicability**: In summary, the Principle of Scale Separation is a key factor to provide satisfactory results when applying multi-scale approaches. In general, the multi-scale numerical results converge to the experimental data and DNS predictions for smaller RVE sizes, where the Principle of Scale Separation is better established for the lattice beams under bending. Multi-scale strategies enabled the evaluation of smaller RVE sizes without a significant increase in computational cost, offering an advantage over the DNS models that were limited by lack of memory requirements of the processing computer used in the numerical simulations. Furthermore, multi-scale approachs can be a valid modelling option compared to expensive or even unfeasible laboratory experiments, particularly for micro-architected materials that are challenging in terms of manufacturing process.

The numerical results and experimental data show that the combination of additive manufacturing experiments and numerical modelling strategies discussed here represent a path towards the design of innovative micro-architected structures.

10 CONCLUSIONS AND FUTURE WORK

The main contributions and conclusions of the PhD thesis, as well as suggestions for future work, are presented below.

10.1 Main contributions and conclusions

A multi-scale second-order computational homogenisation framework at finite strains, based on the *Method of Multi-scale Virtual Power*, has been proposed for predicting the macroscopic behaviour of natural and architected materials in the presence of voids. The multi-scale kinematics was defined exclusively in the solid part of the RVE, which enables the numerical treatment of RVEs containing voids. A new expression was postulated for the homogenisation of the second-order gradient, accounting for the case with voids intersecting the RVE boundary. The theoretical formulation based on variational considerations provided three different sets of micro-scale kinematic constraints (minimal, periodic, and direct) that were imposed to the RVE by Lagrange multipliers. It was demonstrated that the homogenised stress tensors can be expressed in terms of the Lagrange multipliers.

The discrete micro-scale equilibrium formulation was provided for the minimal, periodic and direct models. The Newton–Raphson scheme was adopted to iteratively solve the non-linear systems of equations at both the micro- and macro-scales. Numerical aspects concerning the micro-scale equilibrium problem were described in detail, including the definition of the micro-scale constraints over the RVE, the homogenisation matrices for obtaining the effective stress tensors, and the derivation of consistent tangents. The discrete formulation was implemented in an in-house finite element code. Quadratic convergence rates achieved in the Newton–Raphson scheme at both the micro- and macro-scales confirmed the consistency of the FE^2 multi-scale strategy.

Regarding analyses conducted solely at the micro-scale, RVEs with different void distributions (internal and/or on outer boundary) were examined using two- and three-dimensional numerical simulations, demonstrating the generality of the formulation for investigation of porous and micro-architected solids. Deformation modes associated with the second-order gradient were imposed on RVEs to verify the capability of the computational strategy in capturing quadratic deformation modes (e.g., bending and torsion). The impact of second-order microscale kinematic constraints on the effective behavior of RVEs was evaluated in several examples. The homogenised response revealed that: (i) the minimal constraint defined a lower bound, (ii) the periodic constraint provided an intermediate response, and (iii) the direct constraint represented an upper bound.

The robustness and predictive capability of the FE^2 second-order multi-scale approach was assessed in several numerical examples carefully investigated through two- or three-dimensional simulations. The second-order approach was compared with first-order homogenisation and DNS finite element models in the numerical analysis of architected structures composed of thin-walled elements. The size effects and/or more complex deformation modes, including second-order modes and coupling mechanisms, were assessed through numerical simulations. In general, the results computed from the coupled second-order multi-scale simulations were close to those provided by DNS models, illustrating the ability of the proposed computational approach to capture size effects and coupling deformation modes in thin-walled architected structures. A computational cost study also indicated potential advantages of the multi-scale strategy over DNS models. Therefore, the developed multi-scale computational framework can be useful in practical applications for designing cellular and lattice structures, as well as mechanical metamaterials to obtain the desired macroscopic behaviour, encompassing remarkable or advanced properties and exotic functionalities.

The developed numerical approaches have been combined with laboratory experiments to study the mechanical behaviour of a novel 3D-printed polymeric metamaterial with tension-induced undulation. The FDM 3D printing process was selected to fabricate the architected structure using an amorphous polymer. Experimental mechanical tests captured tension-induced undulation phenomena, along with strain localisation mechanisms and failure modes in the architected metamaterial. The experimentally defined displacement rates did not have a significant impact on the mechanical testing. Cyclic experimental tests revealed that the metamaterial displays elasto-plastic behaviour. Three-dimensional elasto-plastic finite element simulations, incorporating DNS models and FE^2 first-order periodic multi-scale analyses, were conducted to model the mechanical metamaterial. The constitutive properties were defined based on the experimental characterisation of the feedstock material. In general, the numerical results demonstrated good agreement with the experimental data.

Numerical and experimental analyses were also conducted to investigate size effects in the mechanical behaviour of 3D-printed polymeric architected materials under bending. Lattice beams with different unit cell sizes and morphologies were manufactured using the FDM 3D printing technique with an amorphous polymer. Size effects were captured in the mechanical testing of the structures via three-point bending experiments. Three-dimensional numerical simulations were performed using DNS models and FE^2 multi-scale strategies based on first- and second-order computational homogenisation. The constitutive parameters of the elastic simulations were obtained from characterisation tests of the feedstock material. The comparative analysis of numerical results allowed for the assessment of accurate models to capture size effects, as well as the benefits and limitations of each modelling approach. DNS models have been shown to be suitable for cellular beams with coarser unit cell arrangements but infeasible for structures with finer unit cell arrangements due to computational limitations, particularly related to memory requirements for numerical simulations. The amount of solid material on the outer boundary of the RVE had a significant influence on the comparison between micro-scale constraints. Multi-scale approaches offered potential advantages for simulating architected structures with finer unit cell arrangements, where the Principle of Scale Separation is better established for coupled analyses based on homogenisation. The main advantage of second-order homogenisation over the first-order counterpart lies on its ability to capture size effects, even though these may be overestimated in thick-walled structures. Second-order predictions are more accurate for thin-walled structures displaying size effects.

It is also worth mentioning that coupling different numerical modelling options with 3D printing experiments has proven to be an attractive approach for enhancing the development of architected structures with intricate geometries, including diverse underlying microstructural shapes. In particular, the benefits of each strategy can be combined for the efficient design of these artificial materials. Therefore, this methodology contributes to improving the positive capabilities of architected materials (cellular, lattice, and metamaterials), expanding their potential applications across a wide range of advanced engineering fields.

10.2 Future work

Finally, potential future developments are suggested below:

(a) Comprehensive assessment regarding the influence of the micro-scale constraints derived from the current multi-scale framework to investigate the effective behaviour of architected materials. Some architected structures allow the definition of different RVE morphologies (e.g., cubic and hexagonal geometries). Additionally, RVE morphologies with varying amounts of solid material on the outer boundary can be defined for the same architected structure, influencing the response of micro-scale constraints. Thus, a specific study of micro-scale constraints is valuable to assess their effect in the multi-scale modelling of architected structures, accounting for different loading programmes with complex deformation modes.

(b) Investigation of the quasi-static mechanical behaviour of architected materials governed by inelastic constitutive laws. Non-linear elasticity, visco-elasticity, visco-plasticity, and damage mechanics can be explored to conveniently model metals, polymers, and composites. It is worth mentioning that more advanced constitutive models may require specific characterisation tests. Moreover, higher computational costs will be involved to perform coupled multi-scale numerical simulations with nonlinear constitutive behaviour. Therefore, computational optimisation strategies can be necessary to minimise the high cost of numerical simulations in the context of coupled multi-scale analyses.

(c) Extension of the first- and second-order formulations for dynamic analysis, using the variational theory basis defined by the Method of Multi-scale Virtual Power. This suggestion aligns with the idea that a multi-scale strategy can be employed for the computational modelling of the dynamic behaviour of advanced functional materials designed for impact energy absorption and vibration control, among others engineering problems.

(d) Various multi-scale problems across scales require smaller unit cell dimensions. Thus, another potential investigation involves exploring alternative additive manufacturing strategies to fabricate thin-walled architected structures. In particular, new FDM printers, along with other 3D printing technologies, can be employed for the fabrication of architected structures with complex geometries.

(e) Coupling of topological optimisation strategies and artificial intelligence with the multi-scale framework for the efficient design of architected materials. This integrated approach enables the development of cellular and lattice materials, as well as innovative metamaterials, with a focus on lightweight structures for advanced multifunctional engineering applications, for instance.

REFERENCES

3D LAB - SOLUÇÕES EM IMPRESSÃO 3D. Betim: [s. n.], 2025. Available at: <https://3dlab.com.br/>. Access at: 22 jan. 2025.

ALAVI, S. *et al.* Continualization method of lattice materials and analysis of size effects revisited based on cosserat models. **International Journal of Solids and Structures**, v. 254-255, p. 1–31, 2022.

ALBERDI, R. *et al.* Multi-morphology lattices lead to improved plastic energy absorption. **Materials & Design**, v. 194, p. 1–10, 2020.

ALMESMARI, A. *et al.* Review of additively manufactured polymeric metamaterials: design, fabrication, testing and modeling. **Polymers**, v. 15, n. 19, p. 1–39, 2023.

AMERICAN SOCIETY FOR TESTING AND MATERIALS. **ASTM D638-14**: Standard test method for tensile properties of plastics. West Conshohocken, 2014.

AN, X. *et al.* Three-dimensional chiral meta-plate lattice structures for broad band vibration suppression and sound absorption. **Composites Part B**: Engineering, v. 224, p. 1–10, 2021.

ANDERSEN, M. N.; WANG, F.; SIGMUND, O. On the competition for ultimately stiff and strong architected materials. **Materials & Design**, v. 198, p. 1–15, 2021.

ASKARI, M. *et al.* Additive manufacturing of metamaterials: A review. **Additive Manufacturing**, v. 36, p. 1–36, 2020.

ATAOLLAHI, S. A review on additive manufacturing of lattice structures in tissue engineering. **Bioprinting**, v. 35, p. 1–10, 2023.

AZIZ, A. R. *et al.* Geometrical scaling effects in the mechanical properties of 3d-printed body-centered cubic (BCC) lattice structures. **Polymers**, v. 13, n. 22, p. 1–21, 2021.

BABAEE, S. *et al.* 3D soft metamaterials with negative poisson's ratio. **Advanced Materials**, v. 25, n. 36, p. 5044–5049, 2013.

BAUER, J. *et al.* Nanolattices: An emerging class of mechanical metamaterials. **Advanced Materials**, v. 29, n. 40, p. 1–26, 2017.

BAUER, J.; SCHWAIGER, R.; KRAFT, O. Approaching theoretical strength in glassy carbon nanolattices. **Nature Materials**, v. 15, n. 4, p. 438–443, 2016.

BAUGHMAN, R. H. *et al.* Materials with negative compressibilities in one or more dimensions. **Science**, v. 279, n. 5356, p. 1522–1524, 1998.

BENEDETTI, M. *et al.* Architected cellular materials: A review on their mechanical properties towards fatigue-tolerant design and fabrication. **Materials Science and Engineering: R: Reports**, v. 144, p. 1–40, 2021.

BERTOLDI, K. *et al.* Mechanics of deformation-triggered pattern transformations and superelastic behavior in periodic elastomeric structures. **Journal of the Mechanics and Physics of Solids**, v. 56, n. 8, p. 2642–2668, 2008.

BERTOLDI, K. *et al.* Negative poisson's ratio behavior induced by an elastic instability. **Advanced Materials**, v. 22, n. 3, p. 361–366, 2010.

BHAT, C. *et al.* Additive manufacturing-enabled advanced design and process strategies for multi-functional lattice structures. **Materials**, v. 17, n. 14, p. 1–46, 2024.

BISHOP, J. F. W.; HILL, R. XLVI. a theory of the plastic distortion of a polycrystalline aggregate under combined stresses. **The London, Edinburgh, and Dublin Philosophical Magazine and Journal of Science**, v. 42, p. 414–427, 1951.

BISWAS, R.; POH, L. H.; SHEDBALE, A. S. A micromorphic computational homogenization framework for auxetic tetra-chiral structures. **Journal of the Mechanics and Physics of Solids**, v. 135, p. 1–22, 2020.

BLANCO, P. J. *et al.* The method of multiscale virtual power for the derivation of a second order mechanical model. **Mechanics of Materials**, v. 99, p. 53–67, 2016a.

BLANCO, P. J. *et al.* Variational Foundations and Generalized Unified Theory of RVE-Based Multiscale Models. **Archives of Computational Methods in Engineering**, v. 23, n. 2, p. 191–253, 2016b.

BOURELL, D. *et al.* Materials for additive manufacturing. **CIRP Annals**, v. 66, n. 2, p. 659–681, 2017.

CATCHPOLE-SMITH, S. *et al.* Thermal conductivity of tpms lattice structures manufactured via laser powder bed fusion. **Additive Manufacturing**, v. 30, p. 1–9, 2019.

CHEN, J. *et al.* Fabrication and development of mechanical metamaterials via additive manufacturing for biomedical applications: a review. **International Journal of Extreme Manufacturing**, v. 7, n. 1, p. 1–44, 2024.

CHEN, X. *et al.* A 3D dislocated re-entrant structure with compression-twist coupling effect. **Smart Materials and Structures**, v. 32, n. 5, p. 1–11, 2023. Available at: https://dx.doi.org/10.1088/1361-665X/acc621.

CHEN, X. *et al.* Light-weight shell-lattice metamaterials for mechanical shock absorption. **International Journal of Mechanical Sciences**, v. 169, p. 1–9, 2020.

CHENG, H. *et al.* Mechanical metamaterials made of freestanding quasi-BCC nanolattices of gold and copper with ultra-high energy absorption capacity. **Nature Communications**, v. 14, n. 5356, p. 1–7, 2023.

CHICA, L.; ALZATE, A. Cellular concrete review: New trends for application in construction. **Construction and Building Materials**, v. 200, p. 637–647, 2019.

COSSERAT, E.; COSSERAT, F. **Théorie des corps déformables**. Paris, France: Paris: Librairie Scientifique A. Hermann et Fils, 1909.

CUAN-URQUIZO, E.; SILVA, R. G. Fused Filament Fabrication of cellular, lattice and porous mechanical metamaterials: a review. **Virtual and Physical Prototyping**, v. 18, n. 1, p. 1–40, 2023.

DALELA, S.; BALAJI, P. S.; JENA, D. P. A review on application of mechanical metamaterials for vibration control. **Mechanics of Advanced Materials and Structures**, v. 29, n. 22, p. 3237–3262, 2022.

DUAN, S.; WEN, W.; FANG, D. A predictive micropolar continuum model for a novel three-dimensional chiral lattice with size effect and tension-twist coupling behavior. **Journal of the Mechanics and Physics of Solids**, v. 121, p. 23–46, 2018.

ERINGEN, A.; SUHUBI, E. Nonlinear theory of simple micro-elastic solids: i. **International Journal of Engineering Science**, v. 2, p. 189–203, 1964a.

ERINGEN, A.; SUHUBI, E. Nonlinear theory of simple micro-elastic solids: ii. **International Journal of Engineering Science**, v. 2, p. 389–404, 1964b.

ERINGEN, A. C. Mechanics of micromorphic continua. *In*: KRÖNER, E. (ed.). **Mechanics of Generalized Continua**. Berlin: Springer, 1968. p. 18–35.

FEIJÓO, R. A. *et al.* Novel multiscale models in a multicontinuum approach to divide and conquer strategies. **Computational and Applied Mathematics**, v. 42, p. 1–39, 2023.

FERNANDEZ-CORBATON, I. *et al.* New twists of 3D chiral metamaterials. **Advanced Materials**, v. 31, n. 26, p. 1–7, 2019.

FERRO, C. G. *et al.* Lattice structured impact absorber with embedded anti-icing system for aircraft wings fabricated with additive slm process. **Materials Today Communications**, v. 15, p. 185–189, 2018.

FEYEL, F. Multiscale FE^2 elastoviscoplastic analysis of composite structures. **Computational Materials Science**, v. 16, n. 1, p. 344–354, 1999.

FEYEL, F. A multilevel finite element method (FE^2) to describe the response of highly non-linear structures using generalized continua. **Computer Methods in Applied Mechanics and Engineering**, v. 192, n. 28, p. 3233–3244, 2003.

FEYEL, F.; CHABOCHE, J.-L. FE2 multiscale approach for modelling the elastoviscoplastic behaviour of long fibre SiC/Ti composite materials. **Computer Methods in Applied Mechanics and Engineering**, v. 183, p. 309–330, 2000.

FLECK, V. S. D. N. A.; ASHBY, M. F. Micro-architectured materials: past, present and future. **Proceedings Mathematical Physical & Engineering Sciences**, v. 466, p. 2495–2516, 2010.

FOREST, S. Homogenization methods and the mechanics of generalized continua - part 2. **Theoretical and Applied Mechanics**, v. 28-29, p. 113–143, 2002.

FOREST, S. Micromorphic approach for gradient elasticity, viscoplasticity, and damage. **Journal of Engineering Mechanics**, v. 135, n. 3, p. 117–131, 2009.

FRENZEL, T. *et al.* Large characteristic lengths in 3D chiral elastic metamaterials. **Communications Materials**, v. 2, p. 1–9, 2021.

FRENZEL, T.; KADIC, M.; WEGENER, M. Three-dimensional mechanical metamaterials with a twist. **Science**, v. 358, n. 6366, p. 1072–1074, 2017.

GAO, C. *et al.* Instability-induced pattern transformation in soft metamaterial with hexagonal networks for tunable wave propagation. **Scientific Reports**, v. 8, n. 1, p. 2045–2322, 2018.

GATT, R.; GRIMA, J. N. Negative compressibility. **Physica Status Solidi (RRL) – Rapid Research Letters**, v. 2, n. 5, p. 236–238, 2008.

GEERS, M.; KOUZNETSOVA, V.; BREKELMANS, W. Multi-scale computational homogenization: trends and challenges. **Journal of Computational and Applied Mathematics**, v. 234, n. 7, p. 2175–2182, 2010.

GEERS, M. G. D.; KOUZNETSOVA, V. G.; BREKELMANS, W. A. M. Multiscale first-order and second-order computational homogenization of microstructures towards continua. **International Journal for Multiscale Computational Engineering**, v. 4, p. 371–386, 2003.

GEERS, M. G. D. *et al.* Homogenization methods and multiscale modeling: nonlinear problems. *In*: _____. **Encyclopedia of Computational Mechanics Second Edition**. [*S.l.: s.n.*]: [S. l.]: Wiley, 2017. p. 1–34.

GEERS, M. G. D. *et al.* On a proper account of first- and second-order size effects in crystal plasticity. **Advanced Engineering Materials**, v. 11, n. 3, p. 143–147, 2009.

GIBSON, I.; ROSEN, D.; STUCKER, B. **Additive Manufacturing Technologies: 3D Printing, Rapid Prototyping, and Direct Digital Manufacturing**. Springer New York, 2014. Available at: https://link.springer.com/book/10.1007/978-1-4939-2113-3.

GUO, W. *et al.* Dissipative dual-phase mechanical metamaterial composites via architectural design. **Extreme Mechanics Letters**, v. 48, p. 1–8, 2021.

GUO YANG WU, R. C.-B. L. Y. J. W. Z. B. C. S. Y. P.; WEI, J. Development of strong, stiff and lightweight compression-resistant mechanical metamaterials by refilling tetrahedral wireframes. **Virtual and Physical Prototyping**, v. 19, n. 1, p. 1–18, 2024.

HOSSEINI, S.; NIIRANEN, J. 3D strain gradient elasticity: variational formulations, isogeometric analysis and model peculiarities. **Computer Methods in Applied Mechanics and Engineering**, v. 389, p. 1–21, 2022.

IFTEKAR, S. F. *et al.* Advancements and limitations in 3D printing materials and technologies: a critical review. **Polymers**, v. 15, n. 11, p. 1–23, 2023.

ILTCHEV, A. *et al.* Computational homogenisation of periodic cellular materials: application to structural modelling. **International Journal of Mechanical Sciences**, v. 93, p. 240–255, 2015.

JÄNICKE, R.; STEEB, H. Minimal loading conditions for higher-order numerical homogenisation schemes. **Archive of Applied Mechanics**, v. 82, p. 1075–1088, 2012.

JIANG, H. *et al.* Elastically anisotropic architected metamaterials with enhanced energy absorption. **Thin-Walled Structures**, v. 192, p. 1–11, 2023.

JIAO, P.; ALAVI, A. H. Artificial intelligence-enabled smart mechanical metamaterials: advent and future trends. **International Materials Reviews**, v. 66, n. 6, p. 365–393, 2021.

JIAO, P. *et al.* Mechanical metamaterials and beyond. **Nature Communications**, v. 14, p. 1–17, 2023.

KACZMARCZYK, Ł.; PEARCE, C. J.; BIĆANIĆ, N. Scale transition and enforcement of RVE boundary conditions in second-order computational homogenization. **International Journal for Numerical Methods in Engineering**, v. 74, n. 3, p. 506–522, 2008.

KACZMARCZYK, Ł.; PEARCE, C. J.; BIĆANIĆ, N. Studies of microstructural size effect and higher-order deformation in second-order computational homogenization. **Computers & Structures**, v. 88, n. 23-24, p. 1383–1390, 2010.

KANISHKA, K.; ACHERJEE, B. Revolutionizing manufacturing: a comprehensive overview of additive manufacturing processes, materials, developments, and challenges. **Journal of Manufacturing Processes**, v. 107, p. 574–619, 2023.

KANOUTÉ, P. *et al.* Multiscale methods for composites: a review. **Archives of Computational Methods in Engineering**, v. 16, p. 31–75, 2009.

KHAKALO, S.; BALOBANOV, V.; NIIRANEN, J. Modelling size-dependent bending, buckling and vibrations of 2D triangular lattices by strain gradient elasticity models: Applications to sandwich beams and auxetics. **International Journal of Engineering Science**, v. 127, p. 33–52, 2018.

KLADOVASILAKIS, N. *et al.* Architected materials for additive manufacturing: a comprehensive review. **Materials**, v. 15, n. 17, p. 1–18, 2022.

KLADOVASILAKIS, N.; TSONGAS, K.; TZETZIS, D. Development of novel additive manufactured hybrid architected materials and investigation of their mechanical behavior. **Mechanics of Materials**, v. 176, p. 1–9, 2023.

KORSHUNOVA, N. *et al.* Bending behavior of octet-truss lattice structures: modelling options, numerical characterization and experimental validation. **Materials & Design**, v. 205, p. 1–14, 2021.

KOUZNETSOVA, V. **Computational homogenization for the multi-scale analysis of multi-phase materials**. 2002. Tese (Doutorado) — Technische Universiteit Eindhoven, 2002.

KOUZNETSOVA, V.; BREKELMANS, W. A. M.; BAAIJENS, F. P. T. An approach to micro-macro modeling of heterogeneous materials. **Computational Mechanics**, v. 27, p. 37–48, 2001.

KOUZNETSOVA, V.; GEERS, M.; BREKELMANS, W. Multi-scale constitutive modelling of heterogeneous materials with a gradient-enhanced computational homogenization scheme. **International Journal for Numerical Methods in Engineering**, v. 54, p. 1235–1260, 2002.

KOUZNETSOVA, V.; GEERS, M.; BREKELMANS, W. Multi-scale second-order computational homogenization of multi-phase materials: a nested finite element solution strategy. **Computer Methods in Applied Mechanics and Engineering**, v. 193, n. 48-51, p. 5525–5550, 2004.

KOUZNETSOVA, V. G.; GEERS, M. G. D.; BREKELMANS, W. A. M. Size of a representative volume element in a second-order computational homogenization framework. **International Journal for Multiscale Computational Engineering**, v. 2, n. 4, p. 575–598, 2004.

KUMAR, R. S.; MCDOWELL, D. L. Generalized continuum modeling of 2-D periodic cellular solids. **International Journal of Solids and Structures**, v. 41, n. 26, p. 7399–7422, 2004.

LAKES, R. Foam structures with a negative poisson's ratio. **Science**, v. 235, n. 4792, p. 1038–1040, 1987.

LAKES, R. S. *et al.* Extreme damping in composite materials with negative-stiffness inclusions. **Nature**, v. 410, n. 6828, p. 565–567, 2012.

LARSSON, R.; DIEBELS, S. A second-order homogenization procedure for multi-scale analysis based on micropolar kinematics. **International Journal for Numerical Methods in Engineering**, v. 69, n. 12, p. 2485–2512, 2007.

LEMKALLI, B. *et al.* Mapping of elastic properties of twisting metamaterials onto micropolar continuum using static calculations. **International Journal of Mechanical Sciences**, v. 254, p. 1–8, 2023.

LESIČAR, T.; TONKOVIĆ, Z.; SORIĆ, J. Two-scale computational approach using strain gradient theory at microlevel. **International Journal of Mechanical Sciences**, v. 126, p. 67–78, 2017.

LI, X.; GAO, H. Smaller and stronger. **Nature Materials**, v. 15, p. 373–374, 2016.

LI, X.; YANG, Z.; LU, Z. Design 3D metamaterials with compression-induced-twisting characteristics using shear–compression coupling effects. **Extreme Mechanics Letters**, v. 29, p. 1–8, 2019.

LI, X. *et al.* Microlattice metamaterials with simultaneous superior acoustic and mechanical energy absorption. **Small**, v. 17, n. 24, p. 1–13, 2021.

LI, Z. *et al.* Architected lightweight, sound-absorbing, and mechanically efficient microlattice metamaterials by digital light processing 3D printing. **Virtual and Physical Prototyping**, v. 18, n. 1, p. 1–18, 2023.

LIU, Y. *et al.* Auxetic meta-materials and their engineering applications: a review. **Engineering Research Express**, v. 5, n. 4, p. 1–14, 2023.

LOPES, I. A. R. **Multi-Scale Modelling and Analysis of Multi-Phase Solids Using Second-Order Computational Homogenisation at Finite Strains with Parallel Computing**. 2019. Tese (Doutorado) — Faculdade de Engenharia, Universidade do Porto, 2019.

LOPES, I. A. R.; FERREIRA, B. P.; PIRES, F. M. A. On the efficient enforcement of uniform traction and mortar periodic boundary conditions in computational homogenisation. **Computer Methods in Applied Mechanics and Engineering**, v. 384, p. 1–39, 2021.

LOPES, I. A. R.; PIRES, F. M. A. Formulation and numerical implementation of a variationally consistent multi-scale model based on second-order computational homogenisation at finite strains for quasi-static problems. **Computer Methods in Applied Mechanics and Engineering**, v. 392, p. 1–50, 2022a.

LOPES, I. A. R.; PIRES, F. M. A. An assessment of multi-scale models based on second-order computational homogenisation. **Computers & Structures**, v. 259, p. 1–30, 2022b.

LOPES, I. A. R.; PIRES, F. M. A. A fully second-order homogenization formulation for the multi-scale modeling of heterogeneous materials. **International Journal for Numerical Methods in Engineering**, v. 123, n. 21, p. 5274–5318, 2022c.

LOPES, I. A. R.; PIRES, F. M. A. Unlocking the potential of second-order computational homogenisation: an overview of distinct formulations and a guide for their implementation. **Archives of Computational Methods in Engineering**, v. 29, p. 1339–1393, 2022d.

LOPES, I. A. R.; PIRES, F. M. A.; REIS, F. J. P. A mixed parallel strategy for the solution of coupled multi-scale problems at finite strains. **Computational Mechanics**, v. 61, n. 1-2, p. 157–180, 2018.

LUSCHER, D. J. **A Hierarchical Framework for the Multiscale Modeling of Microstructure Evolution in Heterogeneous Materials**. 2010. Tese (Doutorado) — Georgia Institute of Technology, 2010.

LUSCHER, D. J.; MCDOWELL, D. L.; BRONKHORST, C. A. A second gradient theoretical framework for hierarchical multiscale modeling of materials. **International Journal of Plasticity**, v. 26, n. 8, p. 1248–1275, 2010.

LUSCHER, D. J.; MCDOWELL, D. L.; BRONKHORST, C. A. Essential features of fine scale boundary conditions for second gradient multiscale homogenization of statistical volume elements. **International Journal for Multiscale Computational Engineering**, v. 10, n. 5, p. 461–486, 2012.

MAHMOUD, D.; ELBESTAWI, M. A. Lattice structures and functionally graded materials applications in additive manufacturing of orthopedic implants: a review. **Journal of Manufacturing and Materials Processing**, v. 1, n. 2, 2017.

MANDEL, J. **Plasticité classique et viscoplasticité**. Udine: Springer-Verlag, 1971.

MATOUŠ, K. *et al.* A review of predictive nonlinear theories for multiscale modeling of heterogeneous materials. **Journal of Computational Physics**, v. 330, p. 192–220, 2017.

MEZA, L. R.; DAS, S.; GREER, J. R. Strong, lightweight, and recoverable three-dimensional ceramic nanolattices. **Science**, v. 345, n. 6202, p. 1322–1326, 2014.

MIEHE, C.; KOCH, A. Computational micro-to-macro transitions of discretized microstructures undergoing small strains. **Archive of Applied Mechanics**, v. 72, p. 300–317, 2002.

MINDLIN, R. Second gradient of strain and surface-tension in linear elasticity. **International Journal of Solids and Structures**, v. 1, n. 4, p. 417–438, 1965.

MIZZI, L. *et al.* Mechanical metamaterials with star-shaped pores exhibiting negative and zero Poisson's ratio. **Materials & Design**, v. 146, p. 28–37, 2018.

MOETAZEDIAN, A. *et al.* CONVEX (CONtinuously Varied EXtrusion): a new scale of design for additive manufacturing. **Additive Manufacturing**, v. 37, p. 1–19, 2021.

MOHSENIZADEH, M. *et al.* Additively-manufactured lightweight metamaterials for energy absorption. **Materials & Design**, v. 139, p. 521–530, 2018.

MOLAVITABRIZI, D. *et al.* Second-order homogenization of 3-D lattice materials towards strain gradient media: numerical modelling and experimental verification. **Continuum Mechanics and Thermodynamics**, v. 35, p. 2255–2274, 2023.

MUKHOPADHYAY, T.; ADHIKARI, S. Effective in-plane elastic properties of auxetic honeycombs with spatial irregularity. **Mechanics of Materials**, v. 95, p. 204–222, 2016.

MULLIN, T. Pattern transformation triggered by deformation. **Physical Review Letters**, v. 99, p. 1–4, 2007.

NAZIR, A. *et al.* A state-of-the-art review on types, design, optimization, and additive manufacturing of cellular structures. **The International Journal of Advanced Manufacturing Technology**, v. 104, n. 9, p. 3489–3510, 2019.

NGUYEN, V.-D. *et al.* Imposing periodic boundary condition on arbitrary meshes by polynomial interpolation. **Computational Materials Science**, v. 55, p. 390–406, 2012.

NGUYEN, V. D.; BECKER, G.; NOELS, L. Multiscale computational homogenization methods with a gradient enhanced scheme based on the discontinuous Galerkin formulation. **Computer Methods in Applied Mechanics and Engineering**, v. 260, p. 63–77, 2013.

NGUYEN, V.-D.; NOELS, L. Computational homogenization of cellular materials. **International Journal of Solids and Structures**, v. 51, n. 11-12, p. 2183–2203, 2014.

NGUYEN, V. P.; STROEVEN, M.; SLUYS, L. J. Multiscale continuous and discontinuous modeling of heterogeneous materials: a review on recent developments. **Journal of Multiscale Modelling**, v. 3, p. 229–270, 2011.

NICOLAOU, Z. G.; MOTTER, A. E. Mechanical metamaterials with negative compressibility transitions. **Nature Materials**, v. 11, n. 7, p. 608–613, 2012.

OPGENOORD, M. M. J.; WILLCOX, K. E. Design for additive manufacturing: cellular structures in early-stage aerospace design. **Structural and Multidisciplinary Optimization**, v. 60, n. 2, p. 411–428, 2021.

OTERO, F.; OLLER, S.; MARTINEZ, X. Multiscale computational homogenization: review and proposal of a new enhanced-first-order method. **Archives of Computational Methods in Engineering**, v. 25, n. 2, p. 479–505, 2018.

PAIS, A.; BELINHA, J.; ALVES, J. Advances in computational techniques for bio-inspired cellular materials in the field of biomechanics: Current trends and prospects. **Materials (Basel)**, v. 16, n. 11, p. 1–25, 2023.

PAN, C.; HAN, Y.; LU, J. Design and optimization of lattice structures: a review. **Applied Sciences**, v. 10, n. 18, p. 1–36, 2020.

PERIĆ, D. *et al.* On micro-to-macro transitions for multi-scale analysis of non-linear heterogeneous materials: unified variational basis and finite element implementation. **International Journal for Numerical Methods in Engineering**, v. 87, p. 149–170, 2011.

PHAM, R. D.; HÜTTER, G. Influence of topology and porosity on size effects in stripes of cellular material with honeycomb structure under shear, tension and bending. **Mechanics of Materials**, v. 154, p. 1–12, 2021.

PLOCHER, J.; PANESAR, A. Review on design and structural optimisation in additive manufacturing: Towards next-generation lightweight structures. **Materials & Design**, v. 183, p. 1–20, 2019.

QI, C.; JIANG, F.; YANG, S. Advanced honeycomb designs for improving mechanical properties: A review. **Composites Part B**: Engineering, v. 227, p. 1–24, 2021.

QI, D. *et al.* Innovative 3D chiral metamaterials under large deformation: theoretical and experimental analysis. **International Journal of Solids and Structures**, v. 202, p. 787–797, 2020.

REIS, F.; ANDRADE PIRES, F. M. An adaptive sub-incremental strategy for the solution of homogenization-based multi-scale problems. **Computer Methods in Applied Mechanics and Engineering**, v. 257, p. 164–182, 2013.

REIS, F.; GANGHOFFER, J. Construction of micropolar continua from the asymptotic homogenization of beam lattices. **Computers & Structures**, v. 112-113, p. 354–363, 2012.

RIFAIE, M. A.; ABDULHADI, H.; MIAN, A. Advances in mechanical metamaterials for vibration isolation: a review. **Advances in Mechanical Engineering**, v. 14, n. 3, p. 1–20, 2022.

ROCHA, F. F. *et al.* Multi-scale modelling of arterial tissue: linking networks of fibres to continua. **Computer Methods in Applied Mechanics and Engineering**, v. 341, p. 740–787, 2018.

ROKOŠ, O. *et al.* Micromorphic computational homogenization for mechanical metamaterials with patterning fluctuation fields. **Journal of the Mechanics and Physics of Solids**, v. 123, p. 119–137, 2019.

ROKOš, O. *et al.* Extended micromorphic computational homogenization for mechanical metamaterials exhibiting multiple geometric pattern transformations. **Extreme Mechanics Letters**, v. 37, p. 1–11, 2020.

SAEB, S.; STEINMANN, P.; JAVILI, A. Aspects of computational homogenization at finite deformations: a unifying review from Reuss' to Voigt's bound. **Applied Mechanics Reviews**, v. 68, n. 5, p. 1–33, 2016.

SAJJAD, U. *et al.* Manufacturing and potential applications of lattice structures in thermal systems: A comprehensive review of recent advances. **International Journal of Heat and Mass Transfer**, v. 198, p. 1–33, 2022.

SANTOS, W. F. *et al.* Second-order multi-scale modelling of natural and architected materials in the presence of voids: Formulation and numerical implementation. **Computer Methods in Applied Mechanics and Engineering**, v. 416, p. 1–51, 2023.

SANTOS, W. F. *et al.* Exploring novel mechanical metamaterials: Unravelling deformation mode coupling and size effects through second-order computational homogenisation. **International Journal of Solids and Structures**, v. 292, p. 1–31, 2024.

SANTOS, W. F. *et al.* Analysis of a novel 3D-printed mechanical metamaterial with tension-induced undulation: experimental and numerical investigations. **Under review**, 2025a.

SANTOS, W. F. *et al.* Three-point bending of 3D-printed polymer architected materials with size effects: manufacturing, testing and numerical modelling. **Under review**, 2025b.

SARHIL, M. *et al.* Size-effects of metamaterial beams subjected to pure bending: on boundary conditions and parameter identification in the relaxed micromorphic model. **Computational Mechanics**, v. 72, p. 1091–1113, 2023.

SAVIO, G. *et al.* Geometric modeling of cellular materials for additive manufacturing in biomedical field: a review. **Applied Bionics and Biomechanics**, v. 2018, n. 1, p. 1–14, 2018.

SCHAEDLER, T. A. *et al.* Ultralight metallic microlattices. **Science**, v. 334, n. 6058, p. 962–965, 2011.

SCHMIDT, F. *et al.* Computational homogenization of higher-order continua. **International Journal for Numerical Methods in Engineering**, v. 123, n. 11, p. 2499–2529, 2022.

SETHI3D - IMPRESSORAS 3D. Campinas: [s. n.], 2025. Available at: https://www.sethi3d.com.br/. Access at: 22 jan. 2024.

SMEETS, B. J. *et al.* Structural testing of a shear web attachment point on a composite lattice cylinder for aerospace applications. **Composites Part B**: Engineering, v. 212, p. 1–12, 2021.

SONG, J. *et al.* Octet-truss cellular materials for improved mechanical properties and specific energy absorption. **Materials & Design**, v. 173, p. 1–13, 2019.

SOUZA, F.; ALLEN, D.; KIM, Y.-R. Multiscale model for predicting damage evolution in composites due to impact loading. **Composites Science and Technology**, v. 68, n. 13, p. 2624–2634, 2008.

SOUZA, F. V.; ALLEN, D. H. Multiscale modeling of impact on heterogeneous viscoelastic solids containing evolving microcracks. **International Journal for Numerical Methods in Engineering**, v. 82, n. 4, p. 464–504, 2010.

SOUZA NETO, E. *et al.* An RVE-based multiscale theory of solids with micro-scale inertia and body force effects. **Mechanics of Materials**, v. 80, p. 136–144, 2015.

SPADACCINI, C. M. Additive manufacturing and processing of architected materials. **MRS Bulletin**, v. 44, n. 10, p. 782–788, 2019.

SU, Y.; WU, X.; SHI, J. A novel 3D printable multimaterial auxetic metamaterial with reinforced structure: Improved stiffness and retained auxetic behavior. **Mechanics of Advanced Materials and Structures**, v. 29, n. 3, p. 408–418, 2022.

SURJADI, J. U. *et al.* Mechanical metamaterials and their engineering applications. **Advanced Engineering Materials**, v. 21, n. 3, p. 1–37, 2019.

SYAM, W. P. *et al.* Design and analysis of strut-based lattice structures for vibration isolation. **Precision Engineering**, v. 52, p. 494–506, 2018.

TAY, C. S. L. Y. Y.; LANKARANI, H. M. A finite element analysis of high-energy absorption cellular materials in enhancing passive safety of road vehicles in side-impact accidents. **International Journal of Crashworthiness**, Taylor & Francis, v. 19, n. 3, p. 288–300, 2014.

TEKOGLU, C.; ONCK, P. R. Size effects in the mechanical behavior of cellular materials. **Journal of Materials Science**, v. 40, n. 22, p. 5911–5917, 2005.

TERADA, K.; KIKUCHI, N. A class of general algorithms for multi-scale analyses of heterogeneous media. **Computer Methods in Applied Mechanics and Engineering**, v. 190, p. 5427–5464, 2001.

TILLEY, R. *et al.* 3D printed metamaterials for energy absorption in motorsport applications. **International Journal of Automotive Technology**, v. 25, n. 6, p. 1529–1540, 2024.

TIWARI, A. K.; PRATAPA, P. P.; SANTHANAM, M. Lattice concrete: 3D printed periodic cellular structures through selective cement hydration. **Journal of Building Engineering**, v. 86, p. 1–18, 2024.

URIBE-LAM CECILIA D. TREVIñO-QUINTANILLA, E. C.-U. E.; OLVERA-SILVA, O. Use of additive manufacturing for the fabrication of cellular and lattice materials: a review. **Materials and Manufacturing Processes**, v. 36, n. 3, p. 257–280, 2021.

VAN BREE, S. *et al.* A Newton solver for micromorphic computational homogenization enabling multiscale buckling analysis of pattern-transforming metamaterials. **Computer Methods in Applied Mechanics and Engineering**, v. 372, p. 1–25, 2020.

VAZIC, B.; NEWELL, P. Towards the design of nature-inspired materials: Impact of complex pore morphologies via higher-order homogenization. **Mechanics of Materials**, v. 181, p. 1–11, 2023.

WANG, E. *et al.* Lightweight metallic cellular materials: a systematic review on mechanical characteristics and engineering applications. **International Journal of Mechanical Sciences**, v. 270, p. 1–55, 2024.

WANG, H. *et al.* A review on the mechanical metamaterials and their applications in the field of biomedical engineering. **Frontiers in Materials**, v. 10, p. 1–17, 2023.

WANG, L.; LIU, H.-T. 3D compression–torsion cubic mechanical metamaterial with double inclined rods. **Extreme Mechanics Letters**, v. 37, p. 1–8, 2020.

WANG, Q. *et al.* Lightweight mechanical metamaterials with tunable negative thermal expansion. **Physical Review Letters**, v. 117, p. 1–6, 2016.

WANG, Y. *et al.* Achieving the theoretical limit of strength in shell-based carbon nanolattices. **Proceedings of the National Academy of Sciences**, v. 119, n. 34, p. 1–11, 2022.

WEEGER, O. Numerical homogenization of second gradient, linear elastic constitutive models for cubic 3D beam-lattice metamaterials. **International Journal of Solids and Structures**, v. 224, p. 1–16, 2021.

WU, L. *et al.* Second-order computational homogenisation enhanced with non-uniform body forces for non-linear cellular materials and metamaterials. **Computer Methods in Applied Mechanics and Engineering**, v. 407, p. 1–42, 2023b.

WU, W. *et al.* Mechanical design and multifunctional applications of chiral mechanical metamaterials: A review. **Materials & Design**, v. 180, p. 1–13, 2019.

WU, Y. *et al.* Additively manufactured materials and structures: a state-of-the-art review on their mechanical characteristics and energy absorption. **International Journal of Mechanical Sciences**, v. 246, p. 1–62, 2023a.

XU, W. *et al.* General assembly rules for metamaterials with scalable twist effects. **International Journal of Mechanical Sciences**, v. 259, p. 1–11, 2023.

YANG, H. *et al.* Verification of asymptotic homogenization method developed for periodic architected materials in strain gradient continuum. **International Journal of Solids and Structures**, v. 238, p. 1–19, 2022.

YANG, H. *et al.* Determination of metamaterial parameters by means of a homogenization approach based on asymptotic analysis. **Continuum Mechanics and Thermodynamics**, v. 32, p. 1251–1270, 2020.

YANG, H. *et al.* Mechanical properties of hierarchical lattice via strain gradient homogenization approach. **Composites Part B**: Engineering, v. 271, p. 1–25, 2024.

YANG, H.; MÜLLER, W. H. Size effects of mechanical metamaterials: a computational study based on a second-order asymptotic homogenization method. **Archive of Applied Mechanics**, v. 91, p. 1037–1053, 2021.

YANG, H. *et al.* Effective strain gradient continuum model of metamaterials and size effects analysis. **Continuum Mechanics and Thermodynamics**, v. 35, p. 775–797, 2021.

YAVAS, D. *et al.* Design and fabrication of architected multi-material lattices with tunable stiffness, strength, and energy absorption. **Materials & Design**, v. 217, p. 1–13, 2022.

YIN, H. *et al.* Review on lattice structures for energy absorption properties. **Composite Structures**, v. 304, p. 1–40, 2023.

YODER, M.; THOMPSON, L.; SUMMERS, J. Size effects in lattice structures and a comparison to micropolar elasticity. **International Journal of Solids and Structures**, v. 143, p. 245–261, 2018.

YU, X. *et al.* Mechanical metamaterials associated with stiffness, rigidity and compressibility: A brief review. **Progress in Materials Science**, v. 94, p. 114–173, 2018.

YVONNET, J.; AUFFRAY, N.; MONCHIET, V. Computational second-order homogenization of materials with effective anisotropic strain-gradient behavior. **International Journal of Solids and Structures**, v. 191-192, p. 434–448, 2020.

ZHANG, J. *et al.* Enhancing specific energy absorption of additively manufactured titanium lattice structures through simultaneous manipulation of architecture and constituent material. **Additive Manufacturing**, v. 55, p. 1–16, 2022.

ZHANG, Q. *et al.* A three-dimensional compression-torsion metamaterial based on the three-period minimum surface theory. **Composite Structures**, v. 324, p. 1–17, 2023.

ZHANG, Q.; SUN, Y. Novel metamaterial structures with negative thermal expansion and tunable mechanical properties. **International Journal of Mechanical Sciences**, v. 261, p. 1–25, 2024.

ZHANG, X. *et al.* A novel 3D chiral metamaterial with overall compression-twist properties. **Advanced Engineering Materials**, v. 26, n. 23, p. 2401613, 2024.

ZHANG, X. *et al.* Lightweight, flaw-tolerant, and ultrastrong nanoarchitected carbon. **Proceedings of the National Academy of Sciences**, v. 116, n. 14, p. 6665–6672, 2019.

ZHANG, X. *et al.* Design, fabrication, and mechanics of 3d micro-/nanolattices. **Small**, v. 16, n. 15, p. 1–19, 2020.

ZHANG, X. Y. *et al.* A novel auxetic metamaterial with enhanced mechanical properties and tunable auxeticity. **Thin-Walled Structures**, v. 174, p. 1–13, 2022.

ZHENG, B.-B. *et al.* A novel metamaterial with tension-torsion coupling effect. **Materials & Design**, v. 171, p. 1–9, 2019.

ZHENG, X. *et al.* Ultralight, ultrastiff mechanical metamaterials. **Science**, v. 344, n. 6190, p. 1373–1377, 2014.

ZHMAYLO, M. *et al.* Finite element homogenization and experimental evaluation of additively manufactured lattice metamaterials. **Journal of the Brazilian Society of Mechanical Sciences and Engineering**, v. 45, p. 1–18, 2023.

ZHONG, R. *et al.* A novel three-dimensional mechanical metamaterial with compression-torsion properties. **Composite Structures**, v. 226, p. 1–6, 2019.

ZHOU, L. *et al.* Additive manufacturing: a comprehensive review. **Sensors**, v. 24, n. 9, p. 1–44, 2024.

ZIEMKE, P. *et al.* Tailoring the characteristic length scale of 3d chiral mechanical metamaterials. **Extreme Mechanics Letters**, v. 32, p. 1–6, 2019.

APPENDIX

APPENDIX A – HOMOGENISATION OF THE DEFORMATION DESCRIPTORS FOR A CONSTANT FLUCTUATION FIELD

A.1 Homogenisation of the first gradient for a constant fluctuation field

The homogenisation of the first macro-deformation gradient is given by Equation (3.11). As shown in Subsection 3.1.4, the definition of micro-deformation gradient (Equation 3.7) inserted in Equation (3.11) yields

$$\int_{\partial\Omega_\mu^{s,b}} \tilde{\boldsymbol{u}} \otimes \boldsymbol{N} dA - \int_{\partial\Omega_\mu^{s,b}} \tilde{\boldsymbol{u}} \otimes \bar{\boldsymbol{N}} dA = \boldsymbol{0}, \tag{A.1}$$

i.e., a similar expression to Equation (3.21).

The enforcement of a constant displacement fluctuation field (i.e., $\tilde{\boldsymbol{u}} = \boldsymbol{c}$) in Equation (A.1) yields in

$$\boldsymbol{c} \otimes \int_{\partial\Omega_\mu^{s,b}} \left(\boldsymbol{N} - \bar{\boldsymbol{N}}\right) dA = \boldsymbol{0}. \tag{A.2}$$

Finally, Equation A.2 can be simplified by eliminating the constant term $\boldsymbol{c}$:

$$\int_{\partial\Omega_\mu^{s,b}} \left(\boldsymbol{N} - \bar{\boldsymbol{N}}\right) dA = \boldsymbol{0}. \tag{A.3}$$

A.2 Homogenisation of the second gradient for a constant fluctuation field

The expression for homogenisation of the second macro-deformation gradient is postulated in Equation (3.14). As demonstrated in Subsection 3.1.4, Equation (3.7) can be explored to insert the gradient of the displacement field into Equation (3.14), resulting in

$$\int_{\partial\Omega_\mu^{s,b}} \tilde{\boldsymbol{u}} \otimes \boldsymbol{N} \otimes \boldsymbol{Y} dA \cdot \boldsymbol{J}^{-1} - \int_{\partial\Omega_\mu^{s,b}} \tilde{\boldsymbol{u}} \otimes \bar{\bar{\boldsymbol{X}}} dA \cdot \boldsymbol{J}^{-1} - \int_{\Omega_\mu^s} \tilde{\boldsymbol{u}} dV \otimes \boldsymbol{J}^{-1} = \boldsymbol{0}, \tag{A.4}$$

i.e., a rewritten version of Equation (3.27).

Thus, the imposition of $\tilde{\boldsymbol{u}} = \boldsymbol{c}$ (constant displacement fluctuation field) in Equation (A.4) leads to

$$\boldsymbol{c} \otimes \int_{\partial\Omega_\mu^{s,b}} \left(\boldsymbol{N} \otimes \boldsymbol{Y} - \bar{\bar{\boldsymbol{X}}}\right) dA \cdot \boldsymbol{J}^{-1} - \boldsymbol{c} \otimes \int_{\Omega_\mu^s} dV \boldsymbol{J}^{-1} = \boldsymbol{0}. \tag{A.5}$$

Regarding the last term of Equation (A.5), the second-order identity tensor $\boldsymbol{I}$ can be conveniently explored as $\boldsymbol{J}^{-1} = \boldsymbol{I} \cdot \boldsymbol{J}^{-1}$, enabling us to obtain

$$\boldsymbol{c} \otimes \left[\int_{\partial\Omega_\mu^{s,b}} \left(\boldsymbol{N} \otimes \boldsymbol{Y} - \bar{\bar{\boldsymbol{X}}}\right) dA - \int_{\Omega_\mu^s} dV \boldsymbol{I}\right] \cdot \boldsymbol{J}^{-1} = \boldsymbol{0}, \tag{A.6}$$

which can be simplified as

$$\int_{\partial\Omega_\mu^{s,b}} \left(\boldsymbol{N} \otimes \boldsymbol{Y} - \bar{\bar{\boldsymbol{X}}}\right) dA - V^s \boldsymbol{I} = \boldsymbol{0}. \tag{A.7}$$

EESC • USP